



**Universidad de Valladolid**



**PROGRAMA DE DOCTORADO EN FÍSICA**

**FACULTAD DE CIENCIAS**

**DEPARTAMENTO DE FÍSICA DE LA MATERIA  
CONDENSADA, CRISTALOGRAFÍA Y MINERALOGÍA**

**TESIS DOCTORAL:**

**Structural Characterization of Solid Cellular Polymers by  
X-ray Tomography and Light Scattering**

Presentada por Saúl Pérez Tamarit para optar al grado de  
Doctor por la Universidad de Valladolid

Dirigida por:

Dr. Eusebio Solórzano

Dr. Miguel Ángel Rodríguez Pérez



Valladolid, Noviembre de 2018













<b>Introducción en Castellano .....</b>	<b>15</b>
<b>Marco de la Tesis.....</b>	<b>20</b>
<b>Objetivos.....</b>	<b>23</b>
<b>Desafíos.....</b>	<b>24</b>
<b>Principales Novedades .....</b>	<b>26</b>
<b>Estructura de la Tesis.....</b>	<b>27</b>
<b>Referencias.....</b>	<b>35</b>

## Chapter 1

<b>Introduction.....</b>	<b>39</b>
<b>1.1 Framework of this Thesis .....</b>	<b>44</b>
<b>1.2 Objectives .....</b>	<b>47</b>
<b>1.3 Challenges .....</b>	<b>48</b>
<b>1.4 Main Novelties .....</b>	<b>50</b>
<b>1.5 Structure of this thesis.....</b>	<b>51</b>
<b>References .....</b>	<b>59</b>

## Chapter 2

<b>Basic Concepts on Cellular Materials.....</b>	<b>63</b>
<b>2.1 Cellular Structure .....</b>	<b>65</b>
2.1.1 <i><math>\mu</math>-structure model .....</i>	65
2.1.2 <i>Microscopic descriptors.....</i>	67
<b>2.2 Foaming Dynamics .....</b>	<b>76</b>
2.2.1 <i>Cells formation .....</i>	76
2.2.2 <i>Degeneration of the cellular structure .....</i>	78
<b>2.3 Materials .....</b>	<b>80</b>
2.3.1 <i>Polyurethane (PU) and Reactive Foaming.....</i>	80
2.3.2 <i>Polyethylene (PE), poly-methyl methacrylate (PMMA) and Gas Dissolution Foaming .....</i>	83
2.3.3 <i>Polystyrene (PS) and Extrusion Foaming .....</i>	85
2.3.4 <i>Nanosilica Aerosil R812 .....</i>	87
<b>References .....</b>	<b>88</b>

## Chapter 3

<b>X-ray Imaging and Image Analysis .....</b>	<b>91</b>
<b>3.1 X-ray imaging fundamentals .....</b>	<b>93</b>
3.1.1 X-ray generation.....	94
3.1.2 X-ray-matter interaction .....	98
3.1.3 X-ray detection .....	102
<b>3.2 X-ray Computed micro Tomography (<math>\mu</math>-CT).....</b>	<b>104</b>
3.2.1 Acquisition .....	105
3.2.2 Projection correction.....	107
3.2.3 Sinograms.....	109
3.2.4 Reconstruction.....	110
<b>3.3 <math>\mu</math>-CT device at CellMat.....</b>	<b>118</b>
3.3.1 X-ray Source.....	118
3.3.2 Flat Panel detector .....	119
<b>3.4 Synchrotron facilities .....</b>	<b>112</b>
3.4.1 Bessy II. BAMline .....	112
3.4.2 Diamond Light Source. I13 .....	123
3.4.3 Swiss Light Source (SLS). TOMCAT .....	125
<b>3.5 Image analysis software .....</b>	<b>127</b>
3.5.1 ImageJ/Fiji .....	127
3.5.2 Octopus.....	127
3.5.3 Avizo Fire/Amira.....	128
<b>3.6 Image processing .....</b>	<b>129</b>
3.6.1 Conventional features characterization .....	129
3.6.2 Advanced features characterization .....	130
<b>References.....</b>	<b>133</b>

## Chapter 4

### **X-ray Tomography Studies on Cellular Polymers..... 137**

#### **4.1 Multi-scale inspection of the cellular structure ..... 139**

“Multi-scale tomographic analysis of polymeric foams: A detailed study of the cellular structure” ..... 141

#### **4.2 Corrugation influence on physical properties ..... 159**

“Effect of solid phase corrugation on the thermo-mechanical properties of low density flexible cellular polymers” ..... 161

#### **4.3 4D monitoring of the foaming process..... 175**

“In-situ understanding of pore nucleation and growth in polyurethane foams by using real-time synchrotron X-ray tomography” ..... 177

**References ..... 187**

## Chapter 5

### **Theory of Light Scattering Applied to Cellular Materials..... 189**

#### **5.1 Light Scattering..... 192**

5.1.1 *Single and Multiple scattering* ..... 193

#### **5.2 Principles of Light Scattering..... 195**

5.2.1 *Rayleigh Scattering* ..... 196

5.2.2 *Mie Theory* ..... 198

5.2.3 *Geometric Scattering*..... 201

5.2.4 *Diffusion Approximation* ..... 201

#### **5.3 Modelling the Light Scattering on Cellular Materials ..... 204**

5.3.1 *Aqueous foams* ..... 205

5.3.2 *Solid cellular polymers*..... 207

5.3.3 *Nanocellular polymers* ..... 208

#### **5.4 Practical aspects of implementation ..... 210**

5.4.1 *Transmission measurements setup* ..... 210

5.4.2 *Methodological details*..... 212

5.4.3 *Systematic studies*..... 213

**References ..... 216**

## Chapter 6

### **Light Scattering in Solid Cellular Polymers..... 219**

#### **6.1 Solution of the Diffusion Approximation equation .....221**

“Efficient prediction of cell size in solid polymeric foams by numerically solving the diffusion approximation of light scattering equation” ..... 223

#### **6.2 Novel theoretical modelling in solid cellular polymers .....237**

“Semi-empirical modified light scattering model for cell size characterization of solid cellular polymers” ..... 239

#### **6.3 Characterization of the cellular anisotropy.....249**

“Light transmission as a novel tool for the characterization of cell anisotropy in cellular polymers” ..... 251

**References.....259**

## Chapter 7

### **X-ray Tomography and Light Scattering in Non-Conventional/Nanocellular Polymers..... 261**

#### **7.1 Nano-tomography applied to non-conventional cellular polymers.....263**

7.1.1 *Zernike phase contrast X-ray transmission microscopy (TXM)* ..... 263

7.1.2 *Scanning coherent diffraction imaging (ptychography)* ..... 266

“First 3D characterization of non-conventional cellular polymers by means of X-ray ptycho-tomography” ..... 269

#### **7.2 Light Scattering in nanocellular polymers. Transparency .....277**

“Light transmission in nanocellular polymers: Are semi-transparent cellular polymers possible?” ..... 279

**References.....285**

## Chapter 8

### **Conclusions and Perspectives..... 287**

#### **8.1 Conclusions.....289**

#### **8.2 Perspectives .....293**



## **Annex**

### **Other Applications of X-ray Imaging Techniques ..... 295**

#### **A.1 Cell size determination in X-ray transmission images..... 297**

“Fast Fourier Transform procedures applied to X-ray transmission images” ..... 299

#### **A.2 Quantification of additive dispersion in polymers using X-ray**

##### **Tomography ..... 313**

“Novel quantification methods of fillers dispersion in polymer composites based on high resolution synchrotron X-ray  $\mu$ -CT” ..... 315

##### **References ..... 331**



# **Introducción en Castellano**



Los materiales celulares son estructuras bifásicas en las cuales una fase gaseosa que puede ser tanto continua como discontinua está dispersa en una fase continua de líquido o sólido [1]. Estos materiales han atraído mucha atención en los últimos tiempos debido a multitud de factores. La presencia de gas en el seno de la matriz sólida se traduce en una reducción de densidad en comparación a los materiales sólidos de partida [2]. Además, los materiales celulares extienden el rango de las propiedades físicas correspondientes de los materiales sólidos de partida (mostrado en la Figura 1) por lo tanto expandiendo también el rango de aplicaciones en las cuales pueden ser empleados.

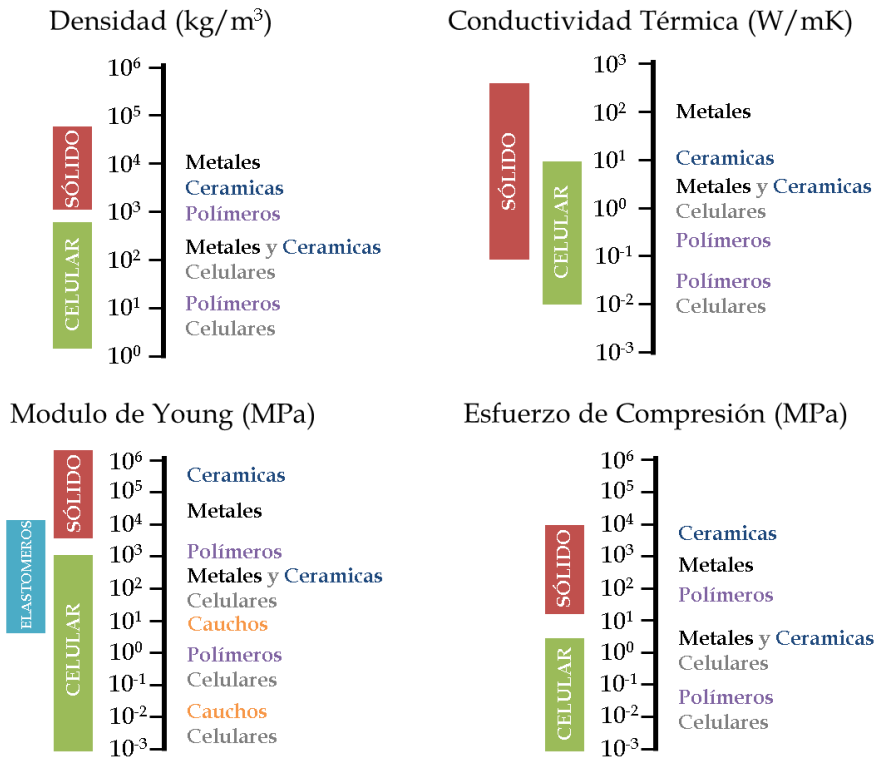


**Figura 1.** Propiedades físicas de los materiales celulares y de los sólidos de partida.

Estos materiales muestran bajas propiedades de transferencia térmica, como puede ser la conductividad térmica, gran capacidad de absorción de energía así como excelentes rigidez y resistencia y además, dependiendo de su estructura celular, increíbles

propiedades de absorción acústica. De hecho, algunos materiales en la naturaleza presentan estructura celular interna y con propiedades increíbles como pueden ser el corcho, la madera, el coral o el hueso. Los materiales celulares creados por el hombre tienden a imitar aquellos de la naturaleza desarrollando procesos de producción que permitan controlar la estructura, fabricando así a medida materiales capaces de cumplir con requerimientos específicos. Por ello, los materiales celulares tienen un gran presente y un futuro prometedor en sectores industriales y tecnológicos tales como el aeronáutico, la automoción, la construcción, el confort, el empaquetado, las energías renovables, la biotecnología, el sector médico, etc. [3, 4] El tipo de material celular más representativo usa los polímeros o plásticos como material sólido de partida (llamados entonces polímeros celulares o espumas poliméricas). Para mostrar la importancia de estos materiales, se espera un consumo de polímeros celulares de 25.3 MT en 2019 [5], lo que representa casi el 10% en peso del consumo global de plásticos (y más del 50% del volumen total consumido) [6].

Entre todas las matrices poliméricas, el poliuretano (PU), el poliestireno (PS), el cloruro de polivinilo (PVC) y las poliolefinas (PO) son habitualmente consideradas en la producción de polímeros celulares aunque es importante incidir que el PU y el PS abarcan el 80% del consumo global de polímeros celulares [7] (como se muestra en la Figura 2).

### Consumo de Polímeros Celulares

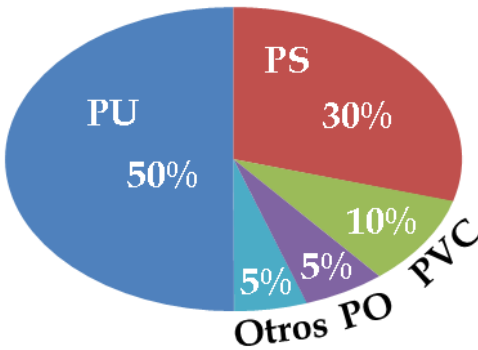


**Figura 2.** Importancia relativa de varios materiales empleados para fabricar polímeros celulares.

Los materiales celulares basados en PU son principalmente usados como aislantes térmicos (tanto en edificación como en refrigeradores) y como relleno de confort en asientos. Por otra parte, las espumas de PS destacan en aplicaciones tanto de empaquetado (usando poliestireno expandido, EPS) como de aislamiento térmico (en este caso usando poliestireno extruido, XPS). Además de ello, los materiales celulares basados en PVC son básicos en aplicaciones estructurales y de perfilería. Finalmente, las espumas de poliolefinas tienen gran importancia en los mercados de empaquetado, aislamiento térmico y confort [8].

En las últimas décadas, se han llevado a cabo estudios teóricos y experimentales estudiando la tríada de relaciones proceso-estructura-propiedades en los materiales celulares para optimizar el rendimiento y extender aún más el rango de aplicación de estos materiales. Se ha avanzado enormemente en este campo gracias al desarrollo de técnicas de caracterización no destructivas (NDT, por sus siglas en inglés) que permiten caracterizar los materiales sin alterar su estructura. La mayoría de ellas se basan en la interacción radiación-materia (ya sea con radiación visible, infrarrojo, rayos-X, etc.) y en el análisis de la señal recibida para obtener características particulares de los materiales testeados.

Teniendo en cuenta este concepto, esta tesis doctoral se ha enfocado en el uso de dos de estas técnicas, **Tomografía de rayos-X** y **Light Scattering**, para llevar a cabo una caracterización detallada de materiales celulares poliméricos.

Este capítulo introductorio está dividido en cuatro secciones explicando la estructura de esta investigación. La primera sección muestra el marco científico en el cual la tesis se ha desarrollado. Después, se describen los objetivos principales, seguidos de los retos que ha habido que superar para completar la investigación. Finalmente, se describen brevemente los contenidos de cada capítulo para resumir al final tanto las publicaciones científicas como las comunicaciones en conferencias derivadas de esta tesis doctoral.

### Marco de la Tesis

Esta tesis es parte de la investigación centrada en materiales celulares desarrollada en el Laboratorio de Materiales Celulares (CellMat) de la Universidad de Valladolid [9]. El director de este laboratorio es el Prof. Dr. Miguel Ángel Rodríguez Pérez, uno de los directores de esta tesis doctoral.

El Prof. Dr. José Antonio de Saja, junto al Prof. Dr. Miguel Ángel Rodríguez Pérez fundaron el Laboratorio CellMat en 1999 después de la defensa de la tesis doctoral de Miguel Ángel Rodríguez Pérez, centrada en el estudio de propiedades térmicas y mecánicas de materiales celulares basados en poliolefinas [10]. En los primeros años, la investigación en CellMat se orientó hacia la caracterización de las propiedades físicas de materiales celulares de ese tipo, dando como resultado varias tesis doctorales y publicaciones científicas [11-22] y alcanzando gran comprensión sobre la relación entre la estructura y las propiedades físicas de polímeros celulares. Después de varios años, la investigación se extendió también a la producción de varios materiales para entender mejor la relación proceso-estructura [23-26]. Además de ello, una línea de investigación centrada en la producción y el estudio de espumas basadas en aluminio se inició estos años colateralmente [27-34]. Finalmente, en los últimos años se ha invertido gran esfuerzo en desarrollar técnicas no convencionales que proporcionan conocimiento adicional tanto de la estructura celular como de los procesos de espumado [35-43]. El principal promotor de algunas de estas técnicas fue el co-director de esta tesis doctoral, Dr. Eusebio Solórzano.

Hoy en día, la investigación en CellMat se divide en cinco grandes líneas de investigación. Estas líneas son espumas de poliuretano [36, 42, 44-46], nanocompuestos celulares [35, 36, 44, 47-49], materiales celulares multifuncionales [50-52], materiales celulares basados en bioplásticos [53-60] y polímeros nanocelulares [61-67]. Todas ellas incluyen la producción, caracterización estructural y modelizado de las propiedades físico-químicas para cubrir aplicaciones específicas (Figura 3) dado que uno de los objetivos principales de este laboratorio es la transferencia de conocimiento desde la Universidad a la Industria.



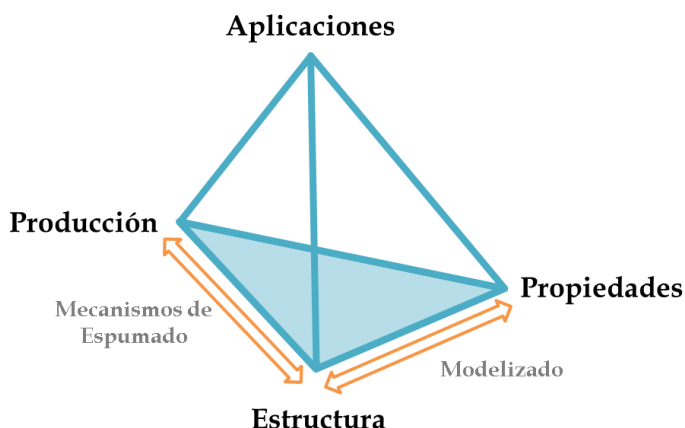


**Figura 3.** Tetraedro de los materiales correspondiente a la investigación en materiales celulares.

La investigación llevada a cabo durante esta tesis doctoral trata de profundizar en el desarrollo y aplicación de técnicas de caracterización no convencionales centrándose en las NDT.

Por una parte, la micro-Tomografía computarizada ( $\mu$ -CT, por sus siglas en inglés) es una técnica de caracterización ampliamente utilizada dado que ofrece la posibilidad de obtener información del objeto escaneado en tres dimensiones [68-72].

La aplicación de esta técnica en el laboratorio CellMat comenzó con la investigación realizada por el Dr. Samuel Pardo Alonso, como parte de su tesis doctoral centrada en estudiar tanto los procesos de espumado como la estructura de los polímeros celulares usando técnicas de imagen por rayos-X (radioscopía y tomografía respectivamente) [36]. La investigación correspondiente a esta tesis doctoral ha permitido mejorar los resultados previos y desarrollar nuevos protocolos de análisis de imagen, proporcionando nuevos conocimientos en las relaciones proceso-estructura-propiedades en los materiales celulares. Adicionalmente, los resultados proporcionados por la Tomografía de rayos-X han servido como referencia para verificar la validez de la otra técnica principal desarrollada en esta tesis doctoral, el Light Scattering.

Por otra parte, el desarrollo de una técnica de caracterización nueva que permita obtener resultados en 3D de una manera rápida, simple y sobre todo barata va a resultar siempre de gran interés para la comunidad científica. Teniendo en cuenta esta premisa, Light Scattering, usada ampliamente en el caso de materiales celulares en base acuosa [73], ha sido adaptada y aplicada en esta tesis doctoral en materiales celulares en base sólida obteniendo resultados prometedores.

Finalmente, una vez que ambas técnicas se aplicaron en materiales celulares convencionales, ha sido posible aplicarlas a los novedosos y prometedores polímeros nanocelulares, una nueva clase de materiales celulares con propiedades mejoradas [74].

## Objetivos

Esta tesis tiene como objetivo establecer técnicas no destructivas para la caracterización detallada de una amplia gama de polímeros celulares.

Para este fin, por una parte, la **Tomografía de rayos-X** fue seleccionada para obtener tanto la información básica sobre la fase gaseosa como la descripción detallada de características avanzadas correspondientes a la fase sólida de los materiales celulares, y estudiar su influencia en sus propiedades. Además de ello, su influencia en las propiedades térmicas y mecánicas de los materiales celulares ha sido analizada.

Por otra parte, se ha desarrollado una nueva metodología para la caracterización rápida de parámetros básicos de la estructura celular como el tamaño de celda y la anisotropía, basándose en el **Light Scattering**.

Estas técnicas han sido aplicadas y optimizadas para el caso de polímeros celulares convencionales (tamaño de celda entre 200 y 1000  $\mu\text{m}$ ) basados en PU, PS y PE y consecuentemente con diferente arquitectura celular. Adicionalmente, un objetivo adicional de esta tesis fue realizar experimentos tanto de Tomografía como de Light Scattering por primera vez en polímeros nanocelulares basados en polimetilmetacrilato (PMMA) con tamaños de celda en el rango de los nanómetros (30-1000 nm).

Los objetivos de esta tesis doctoral pueden ser resumidos como sigue:

*"Profundizar el análisis detallado de la estructura de los polímeros celulares mediante Tomografía de rayos X y su influencia en las propiedades físicas"*

*"Desarrollar una técnica de caracterización nueva para polímeros celulares sólidos basada en Light Scattering"*

*"Caracterizar polímeros nanocelulares por primera vez usando ambas técnicas"*

Para completar dichos objetivos, varios desafíos que ha habido que superar durante esta tesis se describen a continuación.

### Desafíos

Varios aspectos técnicos fueron propuestos para alcanzar los objetivos previamente comentados:

- Diseñar, adaptar y optimizar el sistema de Tomografía de rayos-X del laboratorio CellMat para poder realizar experimentos con tamaño de pixel efectivo de 2.5  $\mu\text{m}$  con contraste óptimo en polímeros celulares de baja densidad.
- Diseñar y construir un sistema específico para la realización de los experimentos de Light Scattering que permitiera poder testar materiales con características muy variadas (densidad y tamaño de celda).

Además, se ha necesitado resolver multitud de aspectos metodológicos durante esta tesis doctoral:

- Desarrollar nuevas metodologías de análisis de imagen para obtener una descripción detallada de la estructura celular de los polímeros celulares. Particularmente, nos hemos centrado en los parámetros correspondientes a la fase sólida, que no han sido aún estudiados en profundidad, tales como el reparto de material sólido entre las distintas partes de la estructura, el espesor de la fase sólida o la corrugación de la misma.
- Desarrollar una metodología experimental novedosa para realizar y analizar los experimentos de Light Scattering de polímeros celulares sólidos.
- Seleccionar una colección adecuada de polímeros celulares basados en PU, PE y PS que permitan verificar la validez de las técnicas y metodologías desarrolladas.

Por ultimo pero no por ello menos importante, los principales temas a destacar desde el punto de vista científico son los siguientes:

- Estudiar la morfología de la estructura de los polímeros celulares en 3D mediante Tomografía de rayos-X. Estos materiales están compuestos por elementos de bajo peso atómico, y además, con sólo 3-5% de volumen sólido. Por lo tanto, la absorción de rayos-X es muy baja, comprometiendo el contraste/calidad de los

volúmenes reconstruidos. Una selección cuidadosa de los parámetros de experimento sirvió para optimizar el contraste en los experimentos realizados de Tomografía de rayos-X.

- Determinar la influencia en las propiedades mecánicas y térmicas de los polímeros celulares de nuevos parámetros estructurales correspondientes a la fase sólida de estos materiales.
- Desarrollar un modelo que permita describir el fenómeno de Light Scattering en los polímeros celulares sólidos.
- Evaluar como las particularidades del proceso de espumado (como la presencia o ausencia de agentes nucleantes) pueden alterar la estructura de los materiales celulares mientras éstos espuman.

### Principales Novedades

Las principales novedades de esta tesis doctoral sobre la literatura científica actual pueden ser resumidas como sigue:

- El establecimiento de protocolos de análisis de imagen nuevos que permitan cuantificar las características de la fase sólida mediante Tomografía de rayos-X alcanzando así una descripción global de la estructura bifásica de los materiales celulares.
- El estudio de la influencia de la corrugación de la estructura sólida de estos materiales en el esfuerzo de colapso y el coeficiente de expansión térmica de polímeros celulares flexibles.
- La visualización y cuantificación de la nucleación y crecimiento celular en polímeros celulares en 3D usando Tomografía de rayos-X de sincrotrón en tiempo real.
- El desarrollo tanto de una nueva metodología experimental como de un modelo teórico para caracterizar los polímeros celulares sólidos mediante Light Scattering con grandes resultados en cuanto a la medida del tamaño de celda y la anisotropía.
- La visualización en 3D de la estructura de polímeros no convencionales y nanocelulares por primera vez utilizando técnicas de Tomografía de rayos-X con resolución nanométrica.
- La aplicación de Light Scattering a polímeros nanocelulares, lo que permitió establecer el primer indicio sobre la posibilidad de fabricar polímeros nanocelulares transparentes a la luz visible.

## Estructura de la Tesis

Esta tesis doctoral ha sido escrita en el formato de un *compendio de publicaciones*. Los resultados experimentales presentados se apoyan en 10 artículos científicos, 3 de los cuales ya publicados y el resto pendientes de publicación (tabla 1). También se abordan las comunicaciones en conferencias nacionales e internacionales (tabla 2) así como los proyectos de investigación desarrollados durante esta investigación (tabla 3). Actividades adicionales llevadas a cabo tales como otras publicaciones científicas o estancias en centros de investigación extranjeros también se detallan a continuación (tabla 4).

Esta tesis está constituida por ocho capítulos y un anexo. Después de los dos primeros capítulos introductorios, los cinco siguientes están divididos en tres bloques (Tomografía de rayos-X, Light Scattering y la aplicación de ambas técnicas en polímeros celulares no convencionales/nanocelulares) con estructura piramidal (Figura 4). Finalmente, como octavo y último capítulo de la tesis se presentan las conclusiones de este trabajo.



**Figura 4.** Estructura de esta tesis doctoral.

Adicionalmente, esta tesis cumple con todos los requerimientos para ser acreditada con la **Mención Internacional**.

El **Capítulo 1** introduce los principales conceptos sobre esta investigación así como el marco científico, los objetivos y los hitos.

El **Capítulo 2** revisa los principales conceptos sobre la estructura celular, introduciendo un modelo nuevo multicomponente de la estructura celular y además incluyendo la definición de varios parámetros nuevos. Además, se detallan ideas básicas sobre los mecanismos (tanto de generación como de degeneración celular) involucrados en el proceso de espumado.

El **Capítulo 3** proporciona una visión general sobre los conceptos básicos relacionados con la formación de imagen con rayos-X, centrándose más en el caso de la Tomografía. Se presentan los pasos y factores clave necesarios para obtener resultados optimizados. Además, se realiza una descripción breve de todos los sistemas de rayos-X utilizados así como de los softwares de análisis de imagen considerados.

El **Capítulo 4** presenta los principales resultados de esta tesis doctoral en el tema de la Tomografía de rayos-X. Para comenzar, se presenta una descripción detallada de la estructura celular de dos tipos de polímero celular a dos niveles de resolución (*un artículo*). Después de ello, se modelizan las propiedades termo-mecánicas de una colección de polímeros celulares flexibles incluyendo el efecto de la corrugación celular (*un artículo*). Por último, se estudia mediante tomografía rápida de rayos-X el proceso de espumado de dos sistemas de PU (*un artículo*).

El **Capítulo 5** incluye el desarrollo de la teoría de Light Scattering para el estudio de materiales celulares, discutiendo las principales teorías de scattering (Rayleigh, Mie) y la aproximación al caso de sistemas acuosos. Finalmente, los se detallan aspectos prácticos que ha sido necesario superar para la aplicación de esta técnica para la caracterización de polímeros celulares sólidos.

El **Capítulo 6** representa entonces el proceso experimental seguido en esta investigación para alcanzar el resultado final sobre el Light Scattering como técnica válida para la caracterización de polímeros celulares sólidos. Para este fin, la ecuación de Light Scattering fue resuelta numéricamente (*un artículo*) para obtener el modelo modificado que permite obtener el tamaño de celda directamente de medidas de scattering (*un artículo*). Para terminar, se presentan los resultados que corroboran que la anisotropía celular puede ser medida mediante este tipo de técnicas (*un artículo*).



El **Capítulo 7** resume los primeros resultados tanto de Tomografía de rayos-X (*un artículo*) como de Light Scattering (*un artículo*) aplicado a polímeros celulares no convencionales/nanocelulares.

Finalmente, el **Capítulo 8** resume las conclusiones de esta investigación y propone posibilidades para el trabajo futuro. Hay también **un anexo** que incluye otros usos prácticos de la imagen por rayos-X (*dos artículos*).

La Figura 5 muestra el resumen de capítulos y publicaciones científicas de las que se compone esta tesis doctoral.



**Figura 5.** Resumen de capítulos y publicaciones científicas contenidas en esta tesis.

**Tabla 1**

No.	Publicaciones Científicas	Cp.
1	S. Pérez-Tamarit, E. Solórzano, A. Hilger, I. Manke and M. A. Rodríguez-Perez	4
	Multi-scale tomographic analysis of polymeric foams: A detailed structural analysis <i>European Polymer Journal</i> 109 (2018) 169-178	
2	S. Pérez-Tamarit, E. Solórzano, A. Hilger, I. Manke and M. A. Rodríguez-Perez	4
	Effect of solid phase corrugation on the thermo-mechanical properties of low density flexible cellular polymers <i>Materials and Design</i> (enviado)	
3	S. Pérez-Tamarit, E. Solórzano, S. Pardo-Alonso, R. Mokso and M. A. Rodríguez-Pérez	4
	Monitoring of pore nucleation and growth in cellular polymers by real-time synchrotron X-ray tomography: Modelling of the involved physical mechanisms <i>Physical Review Letters</i> (enviado)	
4	S. Pérez-Tamarit, E. Solórzano and M. A. Rodríguez-Perez	6
	Efficient prediction of cell size in solid polymeric foams by numerically solving the diffusion approximation of light scattering equation <i>Colloid and Surfaces A</i> 534 (2017) 130-137	
5	S. Pérez-Tamarit, E. Solórzano and M. A. Rodríguez-Perez	6
	Semi-empirical modified light scattering model for cell size characterization of solid cellular polymers <i>Colloid and Surfaces A</i> (enviado)	
6	S. Pérez-Tamarit, E. Solórzano and M. A. Rodríguez-Perez	6
	Light transmission as a novel tool for the characterization of cell anisotropy in cellular polymers <i>Materials Letters</i> (enviado)	
7	S. Pérez-Tamarit, P. Cimavilla, J. Martín-de León, V. Bernardo, E. Solórzano, D. Batey, S. Cipiccia, C. Rau and M. A. Rodríguez-Perez	7
	First 3D inspection of nanocellular polymers by means of X-ray ptucho-tomography <i>Macromolecular Communications</i> (enviado)	
8	S. Pérez-Tamarit, B. Notario, E. Solórzano and M. A. Rodríguez-Perez	7
	Light transmission in nanocellular polymers: Are semi-transparent cellular polymers possible? <i>Materials Letters</i> 210 (2018) 39-41	
9	S. Pérez-Tamarit, E. Solórzano, A. Kaestner and M. A. Rodríguez-Perez	Anexo
	Fast Fourier Transform procedures applied to X-ray transmission images <i>Microscopy and Microanalysis</i> (enviado)	
10	S. Pérez-Tamarit, E. Solórzano, E. Laguna-Gutierrez, A. Hilger, I. Manke and M. A. Rodríguez-Perez	Anexo
	Novel quantification methods of fillers dispersion in polymer composites based on high resolution synchrotron X-ray $\mu$ -CT <i>Polymer</i> (enviado)	

Tabla 2

Comunicaciones en Conferencias Científicas
<u>S. Pérez Tamarit</u> , B. Notario, E. Solórzano, M. A. Rodríguez-Perez
Cell size determination by means of light scattering methodologies in micro and nanoporous foams (ORAL)
VII Escuela Europea de Nanociencia Molecular (ESMolNa 2014), Valencia (España), Octubre 2014
<u>S. Pérez-Tamarit</u> , E. Solórzano, M. A. Rodríguez-Perez, A. Salonen and W. Drenkham
Modified light scattering models in solid polymeric foams (ORAL)
X Conferencia Europea en Espumas y Aplicaciones (EuFoam 2014), Salónica (Grecia), Julio 2014
<u>S. Pérez-Tamarit</u> , E. Solórzano, A. Kaestner and M. A. Rodríguez-Perez
Cell size determination by means of FFT in X-ray transmission images (POSTER)
X Conferencia Europea en Espumas y Aplicaciones (EuFoam 2014), Salónica (Grecia), Julio 2014
<u>E. Solórzano</u> , E. Laguna-Gutiérrez, S. Pérez-Tamarit, A. Kaestner, J. Pinto and M. A. Rodríguez-Perez
Polymer foam evolution characterized by time-resolved neutron radiography (ORAL)
X Conferencia Europea en Espumas y Aplicaciones (EuFoam 2014), Salónica (Grecia), Julio 2014
<u>S. Pérez-Tamarit</u> , E. Solórzano, A. Hilger, I. Manke and M. A. Rodríguez-Perez
Solid-phase structural characterization in polymeric foams: Synchrotron micro-CT in the limits of resolution (ORAL)
II Conferencia Internacional en Tomografía de Materiales y Estructuras (ICTMS 2015), Quebec (Canadá) Julio 2015
<u>J. Martín-de León</u> , V. Bernardo, S. Pérez-Tamarit, E. Solórzano and M. A. Rodríguez-Perez
Nanocellular foams fabrication methods by gas dissolution process (POSTER)
IX Conferencia Internacional en Metales Porosos y Espumas Metálicas (Metfoam 2015), Barcelona (España), Septiembre 2015
<u>V. Bernardo</u> , J. Martín-de León, S. Pérez-Tamarit, E. Solórzano and M. A. Rodríguez-Perez
Cellular structure, properties and applications of nanoporous materials (POSTER)
IX Conferencia Internacional en Metales Porosos y Espumas Metálicas (Metfoam 2015), Barcelona (España), Septiembre 2015
<u>S. Pérez-Tamarit</u> , V. Bernardo, J. Martín-de León, E. Solórzano and M. A. Rodríguez-Perez
Characterization of the solid phase of cellular materials by means of x-ray micro-CT (POSTER)
IX Conferencia Internacional en Metales Porosos y Espumas Metálicas (Metfoam 2015), Barcelona (España), Septiembre 2015
<u>S. Pérez-Tamarit</u> , E. Solórzano and M. A. Rodríguez-Perez
A numerical approach for solving the light scattering model applied to solid polymeric foams (ORAL)
XI Conferencia Europea en Espumas y Aplicaciones (EuFoam 2016), Dublín (Irlanda), Julio 2016
<u>S. Pérez-Tamarit</u> , B. Notario, E. Solórzano and M. A. Rodríguez-Perez
Towards transparent nano-cellular polymeric foams (POSTER)
XI Conferencia Europea en Espumas y Aplicaciones (EuFoam 2016), Dublín (Irlanda), Julio 2016

<u>S. Pérez-Tamarit</u> , E. Solórzano, E. Laguna-Gutierrez, B. Notario, A. Hilger, I. Manke and M. A. Rodriguez-Perez
Characterization of fillers dispersion in composites and nanocomposites by means of synchrotron X-ray micro-tomography ( <b>ORAL</b> )
XIV Reunión del Grupo Especializado de Polímeros (GEP 2016), Burgos (España) Septiembre 2016
<u>S. Pérez-Tamarit</u> , E. Solórzano, S. Pardo-Alonso, R. Mokso and M. A. Rodriguez-Perez
Pore Nucleation and growth in cellular polymers analysed by time resolved synchrotron $\mu$ -CT ( <b>ORAL</b> )
III Conferencia Internacional en Tomografía de Materiales y Estructuras (ICTMS 2017), Lund (Suecia) Junio 2017
<u>S. Pérez-Tamarit</u> , E. Solórzano, E. Laguna-Gutierrez, B. Notario, A. Hilger, I. Manke and M. A. Rodriguez-Perez
Novel quantification methods of fillers dispersion in polymer composites and nanocomposites based on high resolution synchrotron X-ray $\mu$ -CT ( <b>POSTER</b> )
III Conferencia Internacional en Tomografía de Materiales y Estructuras (ICTMS 2017), Lund (Suecia) Junio 2017
<u>S. Pérez-Tamarit</u> , E. Solórzano, A. Hilger, I. Manke and M. A. Rodriguez-Perez
Multiscale analysis of cellular polymers ( <b>POSTER</b> )
VIII Conferencia en Tomografía Computarizada Industrial (iCT 2018), Wels (Austria) Febrero 2018
<u>S. Pérez-Tamarit</u> , E. Solórzano, A. Hilger, I. Manke and M. A. Rodriguez-Perez
Determination of solid phase corrugation ratio of polymeric foams ( <b>POSTER</b> )
VIII Conferencia en Tomografía Computarizada Industrial (iCT 2018), Wels (Austria) Febrero 2018
<u>S. Pérez-Tamarit</u> , E. Solórzano and M. A. Rodriguez-Perez
Characterization of the cellular architecture of solid polymeric foams by means of optical light transmission measurements ( <b>ORAL</b> )
XII Conferencia Europea en Espumas y Aplicaciones (EuFoam 2018), Lieja (Bélgica), Julio 2018
<u>S. Pérez-Tamarit</u> , P. Cimavilla, J. Martín-de León, V. Bernardo, E. Solórzano and M. A. Rodriguez-Perez
X-ray tomographic homogeneity inspection in nanocellular polymers produced using different foaming conditions ( <b>POSTER</b> )
XII Conferencia Europea en Espumas y Aplicaciones (EuFoam 2018), Lieja (Bélgica), Julio 2018
<u>P. Cimavilla</u> , S. Pérez-Tamarit, M. Santiago-Calvo and M. A. Rodriguez-Perez
In-situ physicochemical analysis of the foaming process of aerogel-rigid polyurethane composite foams ( <b>ORAL</b> )
XII Conferencia Europea en Espumas y Aplicaciones (EuFoam 2018), Lieja (Bélgica), Julio 2018
<u>P. Cimavilla</u> , S. Pérez-Tamarit, E. Solórzano, A. Hilger, I. Manke and M. A. Rodriguez-Perez
Novel subresolution tomographic methods for quantifying fraction of mass in Plateau borders of solid polymeric foams ( <b>POSTER</b> )
XII Conferencia Europea en Espumas y Aplicaciones (EuFoam 2018), Lieja (Bélgica), Julio 2018
<u>D. Batey</u> , S. Cipiccia, X. Shi, S. Williams, K. Wanelik, A. Wilson, S. Pérez-Tamarit, P. Cimavilla, M. A. Rodríguez-Pérez and C. Rau
Coherence Branch at I13, DLS: The Multiscale, Multimodal, Ptycho-tomographic End Station ( <b>ORAL</b> )
XIV Conferencia Internacional en Microscopía de rayos-X (XRM 2018), Saskatoon (Canadá), Agosto 2018

C. Rau, M. Storm, S. Marathe, A. J. Bodey, S. Cipiccia, D. Batey, X. Shi, M-C. Zdora, I. Zanette, S. Pérez-Tamarit, P. Cimavilla, M. A. Rodríguez-Pérez, F. Doring and C. David
Multi-Scale Imaging at the Coherence and Imaging Beamline I13 at Diamond (ORAL)
XIV Conferencia Internacional en Microscopía de rayos-X (XRM 2018), Saskatoon (Canadá), Agosto 2018

### Tabla 3

Proyectos de Investigación
Desarrollo y fabricación en continuo de aislantes térmicos avanzados basados en polímeros nanocelulares
Neadfoam: Aditivos innovadores para espumas con mejores prestaciones de aislamiento térmico y comportamiento frente al fuego
Desarrollo de bandejas de espuma de poliestireno extruido con baja densidad y propiedades mejoradas

### Tabla 4

Estancias en otros centros de Investigación
XXXIV Berlin School on Neutron Scattering
Helmholtz Zentrum, Berlin (Alemania) 13-21 de Marzo de 2014
Synchrotron tomography of polymer foams: in the limits of resolution ( <i>Campaña de Experimentación</i> )
Sincrotrón BESSY II, Berlín (Alemania) 5-8 de Junio de 2014
In-situ characterization of the foaming behaviour and exfoliation of nanoclays in nanocomposites using combined white-beam X-ray radiography & diffraction ( <i>Campaña de Experimentación</i> )
Sincrotrón BESSY II, Berlín (Germany) 7-10 de Mayo de 2015
In-situ study of nanoclay exfoliation of polymeric nanocomposites during foaming with azodicarbonamide ( <i>Campaña de Experimentación</i> )
Sincrotrón BESSY II, Berlín (Alemania) 3-9 de Octubre de 2016
Multiscale investigation of nanocellular polymers with synchrotron based tomography
Sincrotrón Diamond Light Source, Oxford (Reino Unido) Septiembre-Diciembre de 2017
<b>Estancia de Investigación de la Tesis Doctoral</b>
Multiscale investigation of nanocellular polymers with synchrotron based tomography ( <i>Campaña de Experimentación</i> )
Sincrotrón Diamond Light Source, Oxford (Reino Unido) 18-21 de Enero de 2018

### Otras Publicaciones Científicas

E. Solórzano, E. Laguna-Gutiérrez, S. Pérez-Tamarit, A. Kaestner and M. A. Rodríguez-Pérez
Polymer foam evolution characterized by time-resolved neutron radiography
<i>Colloids and Surfaces A</i> 473 (2015) 46-54
M. Santiago-Calvo, S. Pérez-Tamarit, J. Tirado-Medavilla, F. Villafañe and M. A. Rodríguez-Pérez
Infrared expandometry: A novel methodology to monitor the expansion kinetics of cellular materials produced with exothermic foaming mechanisms
<i>Polymer Testing</i> 66 (2018) 383-393

---

D. Batey, S. Cipiccia, X. Shi, S. Williams, K. Wanelik, A. Wilson, S. Pérez-Tamarit, P. Cimavilla,  
M. A. Rodríguez-Pérez and C. Rau

---

Coherence Branch at I13, DLS: The Multiscale, Multimodal, Ptycho-tomographic End Station

---

*Microscopy and Microanalysis* 24 (2018) 40-41

---

C. Rau, M. Storm, S. Marathe, A. J. Bodey, S. Cipiccia, D. Batey, X. Shi, M-C. Zdora, I. Zanette, S. Pérez-Tamarit,  
P. Cimavilla, M. A. Rodríguez-Pérez, F. Doring and C. David

---

Multi-Scale Imaging at the Coherence and Imaging Beamline I13 at Diamond

---

*Microscopy and Microanalysis* 24 (2018) 254-255

---

## Referencias

- [1] L.J. Gibson, M.F. Ahsby, *Cellular Solids: Structure and Properties*, Pergamon Press, Oxford, England, 1988.
- [2] A. Cunningham, N.C. Hilyard, *Low Density Cellular Plastics: Physical Basis of Behaviour*, Ed. Chapman and Hall, London, 1994.
- [3] M.A. Rodríguez- Perez, J.I. Velasco, D. Arencón, O. Almanza, J.A. De Saja, Mechanical characterization of closed-cell polyolefin foams, *Journal of Applied Polymer Science*, 75 (2000) 156-166.
- [4] E. Solórzano, M.A. Rodríguez- Perez, *Polymer Foams: Advanced Structural Materials in Transportation*, in: D. Lehmhus, M. Busse, A. Herrmann, K. Kayvantash (Eds.) *Structural Materials and Processes in Transportation*, Wiley 2013.
- [5] *The Future of Polymer Foams to 2019*, 2014.
- [6] [www.plasticseurope.es](http://www.plasticseurope.es).
- [7] <http://www.plastemart.com>.
- [8] D. Klempner, K.C. Frish, *Handbook of Polymeric Foams and Foam Technology*, in: Hanser (Ed.), 1991.
- [9] <http://cellmat.es/>.
- [10] M.A. Rodríguez- Perez, *Propiedades Térmicas y Mecánicas de espumas de poliolefinas*, PhD Thesis, University of Valladolid, 1999.
- [11] J.I. González-Peña, *Efecto de tratamientos térmicos en bloques de espuma de polietileno de baja densidad fabricados mediante moldeo por compresión*, PhD Thesis, University of Valladolid, 2006.
- [12] J.L. Ruiz-Herrero, *Impacto y Fluencia en espumas con base polietileno*, PhD Thesis, University of Valladolid, 2004.
- [13] O. Almanza, *Caracterización y modelización de las propiedades térmicas y mecánicas de espumas con base polietileno*, PhD Thesis, University of Valladolid, 2000.
- [14] L.O. Arcos y Rábago, *Propiedades térmicas y mecánicas en espumas de poliolefinas fabricadas en un proceso de moldeo por compresión*, PhD Thesis, University of Valladolid, 2002.
- [15] M.L. Álvarez Láinez, *Propiedades térmicas, mecánicas y acústicas de espumas de poliolefina de celda abierta*, PhD Thesis, University of Valladolid, 2007.
- [16] F. Hidalgo González, *Diseño optimizado de los parámetros de proceso en la fabricación de espumas de poliolefina reticulada mediante moldeo por compresión*, PhD Thesis, University of Valladolid, 2008.
- [17] R.A. Campo-Arnáiz, *Aplicación de técnicas espectroscópicas al estudio de la morfología polimérica, propiedades térmicas y de emisión de espumas de baja densidad con base poliolefina*, PhD Thesis, University of Valladolid, 2011.
- [18] M.A. Rodríguez- Perez, O. Alonso, J. Souto, J.A. De Saja, Thermal Conductivity of Physically Crosslinked Closed Cell Polyolefin Foams, *Polymer Testing*, 16 (1997) 287-298.
- [19] C. Saiz-Arroyo, M.A. Rodríguez-Pérez, J. Tirado, A. López-Gil, J.A. de Saja, Structure-property relationships of medium-density polypropylene foams, *Polymer International*, 62 (2013) 1324-1333.
- [20] O. Almanza, L.O. Arcos y Rábago, M.A. Rodríguez- Perez, Structure-Property relationships in polyolefin foams, *Journal of Macromolecular Science, Part B*, 40 (2001) 603-613.
- [21] M.A. Rodríguez- Perez, S. Díez-Gutiérrez, J.A. De Saja, The recovery behaviour of crosslinked closed cell polyolefin foams, *Polymer Engineering and Science*, 38 (1998) 831-837.
- [22] M.A. Rodríguez-Perez, M. Álvarez-Láinez, J.A. de Saja, Microstructure and physical properties of open-cell polyolefin foams, *Journal of Applied Polymer Science*, 114 (2009) 1176-1186.

- [23] C. Saiz-Arroyo, Fabricación de materiales celulares mejorados basados en poliolefinas. Relación procesado-composición-estructura-propiedades, PhD Thesis, University of Valladolid, 2012.
- [24] O. Almanza, M.A. Rodríguez- Perez, J.A. De Saja, The microstructure of polyethylene foams produced by a nitrogen solution process, *Polymer*, 42 (2001) 7117-7126.
- [25] M.A. Rodríguez- Perez, O. Almanza, J.L. Ruiz-Herrero, J.A. De Saja, The effect of processing on the structure and properties of crosslinked closed cell polyethylene foams, *Cellular Polymers*, 27 (2008) 179-200.
- [26] M.A. Rodríguez- Perez, O. Almanza, J.A. De Saja, Anomalous thickness increase in crosslinked closed cell polyolefin foams during heat treatments, *Journal of Applied Polymer Science*, 73 (1998) 2825-2835.
- [27] J.A. Reglero Ruiz, Production and characterization of aluminium foams: Applications in the aeronautical sector, PhD Thesis, University of Valladolid, 2007.
- [28] E. Solórzano, Aluminium foams: Foaming process, cellular structure and properties, PhD Thesis, University of Valladolid, 2008.
- [29] J. Lázaro Nebreda, Optimization of the cellular structure of aluminium foams, PhD Thesis, University of Valladolid, 2014.
- [30] E. Solórzano, M.A. Rodríguez-Perez, J.A. de Saja, Thermal Conductivity of Cellular Metals Measured by the Transient Plane Sour Method, *Advanced Engineering Materials*, 10 (2008) 371-377.
- [31] E. Solórzano, M.A. Rodríguez-Perez, J.A. Reglero, J.A. de Saja, Mechanical Behaviour of Internal Reinforced Aluminium Foams, *Advanced Engineering Materials*, 9 (2007) 955-958.
- [32] J. Lázaro, E. Laguna-Gutiérrez, E. Solórzano, M.A. Rodríguez-Pérez, Effect of Microstructural Anisotropy of PM Precursors on the Characteristic Expansion of Aluminum Foams, *Metallurgical and Materials Transactions B*, 44 (2013) 984-991.
- [33] J. Lázaro, E. Solórzano, J.A. de Saja, M.A. Rodríguez-Pérez, Early anisotropic expansion of aluminium foam precursors, *Journal of Materials Science*, 48 (2013) 5036-5046.
- [34] J. Lázaro, E. Solórzano, M.A. Rodríguez Pérez, F. García-Moreno, Pore connectivity of aluminium foams: effect of production parameters, *Journal of Materials Science*, 50 (2015) 3149-3163.
- [35] E. Laguna Gutiérrez, Understanding the foamability of complex polymeric systems by using extensional rheology, PhD Thesis, University of Valladolid, 2016.
- [36] S. Pardo-Alonso, X-ray imaging applied to the characterization of polymer foams' cellular structure and its evolution, PhD Thesis, University of Valladolid, 2014.
- [37] E. Solórzano, S. Pardo-Alonso, J.A. de Saja, M.A. Rodríguez-Perez, X-ray radiography in-situ studies in thermoplastic polymer foams, *Colloids and Surfaces A: Physicochemical and Engineering aspects*, 438 (2013) 167-173.
- [38] E. Solórzano, S. Pardo-Alonso, J.A. de Saja, M.A. Rodríguez-Pérez, Study of aqueous foams evolution by means of X-ray radiography, *Colloids and Surfaces A: Physicochemical and Engineering Aspects*, 438 (2013) 159-166.
- [39] S. Pardo-Alonso, E. Solórzano, S. Estravís, M.A. Rodríguez-Perez, J.A. de Saja, In situ evidence of the nanoparticle nucleating effect in polyurethane-nanoclay foamed systems, *Soft Matter*, 8 (2012) 11262.
- [40] M.M. Bernal, S. Pardo-Alonso, E. Solórzano, M.A. Lopez-Machado, R. Verdejo, M.A. Rodríguez- Perez, Effect of carbon nanofillers on flexible polyurethane foaming from a chemical and physical perspective, *RSC Advances*, 4 (2014).
- [41] E. Solórzano, J. Pinto, S. Pardo, F. Garcia-Moreno, M.A. Rodríguez-Perez, Application of a microfocus X-ray imaging apparatus to the study of cellular polymers, *Polymer Testing*, 32 (2013) 321-329.
- [42] M. Santiago-Calvo, S. Pérez-Tamarit, J. Tirado-Mediavilla, F. Villafañe, M.A. Rodríguez-Pérez, Infrared expandometry: A novel methodology to monitor the expansion kinetics of



cellular materials produced with exothermic foaming mechanisms, *Polymer Testing*, 66 (2018) 383-393.

[43] E. Solórzano, M. Antunes, C. Saiz-Arroyo, M.A. Rodríguez-Pérez, J.I. Velasco, J.A. de Saja, Optical expandometry: A technique to analyze the expansion kinetics of chemically blown thermoplastic foams, *Journal of Applied Polymer Science*, 125 (2012) 1059-1067.

[44] S. Estravís Sastre, Cellular nanocomposites based on rigid polyurethane and nanoclays: fabrication, characterization and modeling of the mechanical and thermal properties, PhD Thesis, University of Valladolid, 2014.

[45] S. Estravís, J. Tirado-Mediavilla, M. Santiago-Calvo, J.L. Ruiz-Herrero, F. Villafañe, M.Á. Rodríguez-Pérez, Rigid polyurethane foams with infused nanoclays: Relationship between cellular structure and thermal conductivity, *European Polymer Journal*, 80 (2016) 1-15.

[46] M. Santiago-Calvo, V. Blasco, C. Ruiz, R. París, F. Villafañe, M.Á. Rodríguez-Pérez, Synthesis, characterization and physical properties of rigid polyurethane foams prepared with poly(propylene oxide) polyols containing graphene oxide, *European Polymer Journal*, 97 (2017) 230-240.

[47] J. Escudero Arconada, Polyolefin based cellular materials. Development of new production routes and optimization of barrier and mechanical properties by the addition of nanoclays, PhD Thesis, University of Valladolid, 2016.

[48] S. Román Lorza, Production and characterization of flame retardant halogen-free polyolefin based cellular materials, PhD Thesis, University of Valladolid, 2010.

[49] F. Silva-Bellucci, Preparation and characterization of multifunctional nanocomposites by adding paramagnetic ferroelectric nanoparticles to natural rubber films, PhD Thesis, University of Valladolid, Sao Paulo State University, 2013.

[50] J. Lobos Martín, Improving the stiffness and strength of porous materials by enhancement of the matrix microstructure and cellular morphology, PhD Thesis, University of Valladolid, 2013.

[51] M. Dumon, J.A. Reglero Ruiz, J. Pinto, M.A. Rodríguez-Pérez, M.A. Tallon, J.M. Pedros, M. Cloutet, P. Viot, Block copolymer-assisted microcellular supercritical CO<sub>2</sub> foaming of Polymers and Blends, *Cellular Polymers*, 31 (2012) 207-221.

[52] J.A. Reglero Ruiz, C. Saiz-Arroyo, M. Dumon, M.A. Rodríguez-Pérez, L. Gonzalez, Production, cellular structure and thermal conductivity of microcellular (methyl methacrylate)-(butyl acrylate)-(methyl methacrylate) triblock copolymers, *Polymer International*, 60 (2011) 146-152.

[53] D. Velasco Nieto, Development of cellular biomaterials based on EVA, PLA and PHB, production and characterization, PhD Thesis, University of Valladolid, 2017.

[54] A. López Gil, Development of environmentally friendly cellular polymers for packing and structural applications. Study of the relationship cellular structure-mechanical properties, PhD Thesis, University of Valladolid, 2016.

[55] H. Ventura Casellas, Development of new lightweight green composites reinforced with nonwoven structures of flax fibers, PhD Thesis, Polytechnic University of Catalonia and University of Valladolid, 2017.

[56] L. Oliveira-Salmazo, Foaming kinetics and cellular structure control of materials based on natural rubber and polyolefins, PhD Thesis, University of Valladolid and Sao Paulo State University, 2015.

[57] M.A. Rodríguez-Pérez, R.D. Simoes, S. Roman-Lorza, M. Alvarez-Lainez, C. Montoya-Mesa, C.J.L. Constantino, J.A. de Saja, Foaming of EVA/starch blends: Characterization of the structure, physical properties, and biodegradability, *Polymer Engineering & Science*, 52 (2012) 62-70.

[58] M.A. Rodríguez-Pérez, R.D. Simoes, C.J.L. Constantino, J.A. de Saja, Structure and physical properties of EVA/starch precursor materials for foaming applications, *Journal of Applied Polymer Science*, 121 (2011) 2324-2330.

- [59] A. Lopez-Gil, F. Silva-Bellucci, D. Velasco, M. Ardanuy, M.A. Rodriguez-Perez, Cellular structure and mechanical properties of starch-based foamed blocks reinforced with natural fibers and produced by microwave heating, *Industrial Crops and Products*, 66 (2015) 194-205.
- [60] L. Oliveira-Salmazo, A. Lopez-Gil, F. Silva-Bellucci, A.E. Job, M.A. Rodriguez-Perez, Natural rubber foams with anisotropic cellular structures: Mechanical properties and modeling, *Industrial Crops and Products*, 80 (2016) 26-35.
- [61] J. Pinto, Fabrication and characterization of nanocellular polymeric materials from nanostructured polymers, PhD Thesis, University of Valladolid and University of Bordeaux, 2014.
- [62] B. Notario Collado, Fabrication and characterization of the physical properties of nanocellular polymers: The transition from the micro to the nanoscale, PhD Thesis, University of Valladolid, 2016.
- [63] B. Notario, J. Pinto, E. Solorzano, J.A. de Saja, M. Dumon, M.A. Rodríguez-Pérez, Experimental validation of the Knudsen effect in nanocellular polymeric foams, *Polymer*, 56 (2015) 57-67.
- [64] B. Notario, J. Pinto, M.A. Rodríguez-Pérez, Towards a new generation of polymeric foams: PMMA nanocellular foams with enhanced physical properties, *Polymer*, 63 (2015) 116-126.
- [65] V. Bernardo, J. Martín-de León, E. Laguna-Gutiérrez, M.A. Rodríguez-Pérez, PMMA-sepiolite nanocomposites as new promising materials for the production of nanocellular polymers, *European Polymer Journal*, 96 (2017) 10-26.
- [66] J. Pinto, B. Notario, R. Verdejo, M. Dumon, S. Costeux, M.A. Rodriguez-Perez, Molecular confinement of solid and gaseous phases of self-standing bulk nanoporous polymers inducing enhanced and unexpected physical properties, *Polymer*, 113 (2017) 27-33.
- [67] J. Martín-de León, V. Bernardo, M. Rodríguez-Pérez, Low Density Nanocellular Polymers Based on PMMA Produced by Gas Dissolution Foaming: Fabrication and Cellular Structure Characterization, *Polymers*, 8 (2016) 265.
- [68] S. Pardo-Alonso, E. Solórzano, L. Brabant, P. Vanderniepen, M. Dierick, L. Van Hoorebeke, M.A. Rodriguez- Perez, 3D Analysis of the progressive modification of the cellular architecture in polyurethane nanocomposite foams via X-ray microtomography, *European Polymer Journal*, 49 (2013) 999-1006.
- [69] M.D. Montminy, A.R. Tannenbaum, C.W. Macosko, The 3D structure of real polymer foams, *Journal of colloid and interface science*, 280 (2004) 202-211.
- [70] Y. Ma, R. Pyrz, M.A. Rodriguez-Perez, J. Escudero, J.C. Rauhe, X. Su, X-ray microtomographic study of nanoclay-polypropylene foams, *Cellular Polymers*, 30 (2011) 95-110.
- [71] J. Lambert, I. Cantat, R. Delannay, A. Renault, F. Graner, J.A. Glazier, I. Veretennikov, P. Cloetens, Extraction of relevant physical parameters from 3D images of foams obtained by X-ray tomography, *Colloids and Surfaces A: Physicochemical and Engineering Aspects*, 263 (2005) 295-302.
- [72] A. Elmoutaouakkil, G. Fuchs, P. Bergounhon, F. Peyrin, Three-dimensional quantitative analysis of polymer foams from synchrotron radiation x-ray microtomography, *Journal of Physics D: Applied Physics*, 36 (2003) A37-A43.
- [73] I. Cantat, S. Cohen-Addad, F. Elias, F. Graner, R. Höhler, O. Pitois, F. Rouyer, A. Saint-Jalmes, *Foams Structure and Dynamics*, Oxford University Press 2013.
- [74] B. Notario, J. Pinto, M.A. Rodriguez-Perez, Nanoporous polymeric materials: A new class of materials with enhanced properties, *Progress in Materials Science*, 78-79 (2016) 93-139.

Chapter 1

# Introduction



## 1. Introduction

Cellular materials are biphasic structures in which a continuous or discontinuous gas phase is dispersed in a continuous liquid or solid phase [1]. These materials have focused a lot of attention in recent decades due to several interesting factors. The presence of the gas phase within the structure provides density reduction in comparison to the solids [2]. In addition, cellular materials extend the range of physical properties of the respective solid precursors (as shown in Figure 1-1) thus expanding the application capabilities of these materials.

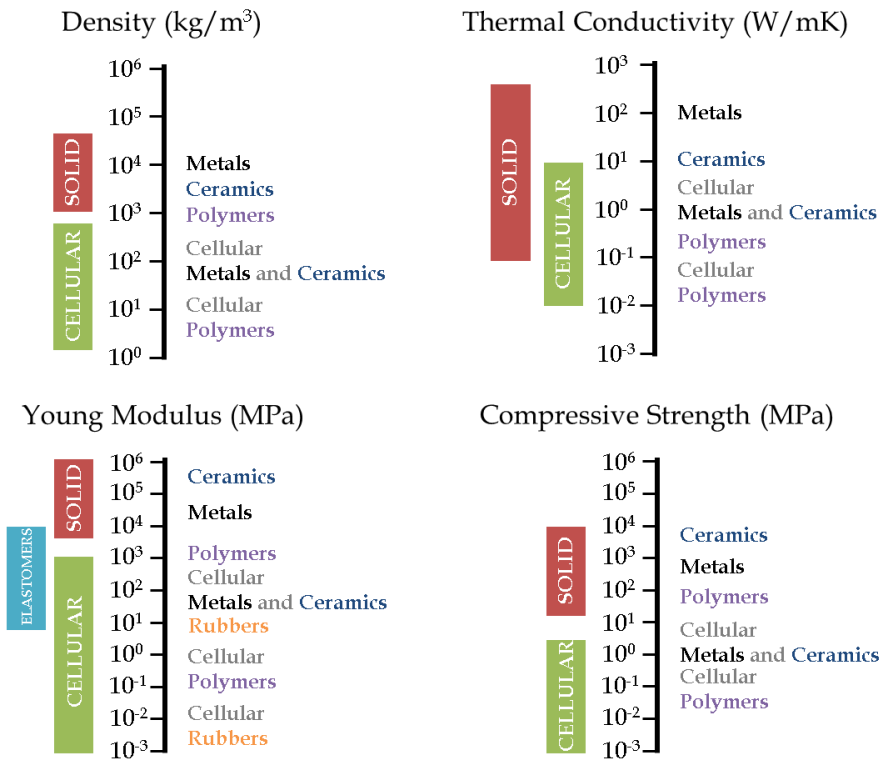


**Figure 1-1.** Comparative properties of solid and cellular materials.

They exhibit extremely low thermal transport properties, as for instance a low thermal conductivity, high energy absorption capability as well as excellent stiffness and strength and depending on their cellular structure excellent acoustic absorption properties. In fact, some materials in nature present an internal cellular structure with impressive properties such as cork, wood, coral or bone. The man-made cellular

materials tend to imitate those from nature by developing production processes that allow controlling the final structure and thus fabricating tailored materials to specific requirements. For this reason, cellular materials have a great present and a promising future in important technological sectors such as aeronautic, automotive, building, cushioning, packaging, renewal energies, biotechnology, medical, etc. [3, 4] The most representative kind of cellular materials are based on polymers as the constituent solid phase (so-called cellular polymers or polymeric foams). To show the importance of this type of materials, it is expected that the polymer foam market will consume 25.3 MT by 2019 [5], representing almost 10 wt.% of the global consumption of plastics (and more than 50 % of the total consumption volume) [6].

Among all the existing polymeric matrixes, polyurethane (PU), polystyrene (PS), polyvinyl chloride (PVC) and polyolefins (PO) are the most employed for the production of cellular polymers although it is important to remark that cellular products based on PU and PS are about 80% of total cellular polymers world-wide consumption [7] (as shown in Figure 1-2).

### Cellular Polymers Consumption

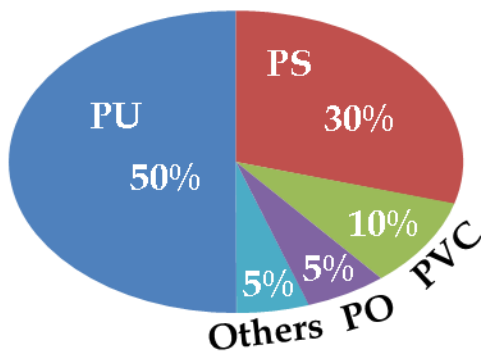


**Figure 1-2.** Representative importance of various raw materials used in the production of cellular polymers.

PU cellular materials are widely used as thermal insulators (buildings and refrigerators) and as fillers for seats. On the other hand, PS foams stand out in both

packaging (expanded polystyrene, EPS) and insulation (extruded polystyrene, XPS) applications. In addition, PVC cellular materials are basic for profiles and structural applications. Finally, PO foams gain importance in the packaging, buoyancy thermal insulation and cushioning markets [8].

In recent decades, both theoretical and empirical studies have been carried out concerning the so-called process-structure-properties relationships in cellular materials in order to optimize the performance and further extend the range of application of these materials. One important contribution to this task is the development and application of non-destructive techniques (NDT) for the characterization of materials without altering their structure. Most of them are based on the interaction of the material with radiation (visible, infrared, X-rays, etc.) and on the analysis of the subsequent signal to determine particular characteristics of the tested materials.

In the framework of this concept this thesis is focused on the use of two NDT techniques, **X-ray Tomography** and **Light Scattering**, to perform a detailed characterization of solid cellular polymers.

This chapter is divided in four sections explaining the structure of the investigation. The first one mainly shows the scientific framework in which this investigation has been developed. After that, the principal objectives of the investigation are addressed followed by the main challenges that have been necessary to overcome in order to complete the investigation. Finally, the contents of each chapter are shortly described and the scientific articles and contributions to conferences derived from this thesis are summarized.

### 1.1 Framework of this Thesis

This investigation is part of the research focused on cellular materials developed in the Cellular Materials Laboratory (CellMat) of the University of Valladolid [9]. This laboratory is led by Prof. Dr. Miguel Ángel Rodríguez Pérez, one of the supervisors of this PhD thesis.

CellMat Laboratory was founded in 1999 by Prof. Dr. José Antonio de Saja and Prof. Dr. Miguel Ángel Rodríguez Pérez after the PhD thesis defended by Miguel Ángel Rodríguez Pérez focused on the thermal and mechanical properties of cellular polymers based on polyolefins [10]. During the first years, the research performed at CellMat was oriented on the characterization of the physical properties of such kind of cellular polymers resulting in several PhD thesis and publications [11-22] and reaching a high understanding of the structure-properties relationship in cellular polymers. After a few years, the research was extended also to the production of several types of cellular materials in order to understand better the process-structure relationship [23-26]. Furthermore, in this period a collateral research focused on the production and characterization of cellular materials based on aluminium was established [27-34]. Finally, in the last years the development of non-conventional characterization techniques has engaged a great effort in order to provide further knowledge of both cellular structure and foaming mechanisms [35-43]. The main promoter of some of these techniques was the co-director of this thesis, Dr. Eusebio Solórzano.

Nowadays, the research at CellMat is established on five areas of technological application. These topics are polyurethane foams [36, 42, 44-46], cellular nanocomposites [35, 36, 44, 47-49], multifunctional cellular materials [50-52], bioplastic cellular materials [53-60] and nanocellular polymers [61-67]. All these topics include the production, structural characterization and modelling of the physicochemical properties to cover specific applications (Figure 1-3) since one of the principal aims of this laboratory is the technological transfer from University to Industry.



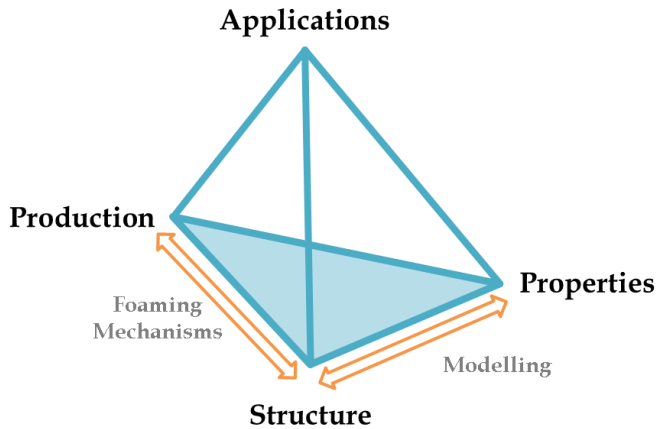


**Figure 1-3.** Materials tetrahedron for the research on cellular materials.

The research accomplished in this thesis intends to deepen in the development and application of non-conventional techniques for the characterization of cellular polymers focusing on NDT.

On the one hand, computed micro-tomography ( $\mu$ -CT) is an extensively used technique for the materials characterization since it offers the possibility of resolving objects in three dimensions [68-72].

The application of this technique in CellMat for the structural characterization of cellular polymers was started by Dr. Samuel Pardo Alonso, as part of his PhD thesis focused on both the study of foaming mechanisms and structure of cellular polymers by X-ray imaging techniques (radioscopy and tomography respectively) [36]. In the research presented in this thesis, an improvement and development of novel image analysis protocols for X-ray tomography results have permitted to go further in the understanding of the process-structure-properties relationships of cellular materials. Additionally, X-ray tomography has been used as reference technique to verify the reliability of the other main technique used during this PhD thesis, Light Scattering.

On the other hand, the development of a novel characterization technique allowing a fast, simple and relatively inexpensive 3D characterization of solid cellular polymers would be always of great interest for the cellular materials community. Regarding

these insights, Light Scattering, extensively used in the case of aqueous foams [73], has been suitably adapted and applied in this thesis to the case of solid cellular polymers obtaining promising results.

Finally, once both techniques were properly established for conventional cellular materials, it was possible to apply both to novel promising materials such as nanocellular polymers, a new class of cellular materials with enhanced properties [74].

### 1.2 Objectives

This thesis is aimed at establishing non-destructive techniques for the detailed characterization of a wide range of cellular polymers.

To this end, on one hand, **X-ray tomography** has been selected to obtain from the basic structural information of the gas phase to the detailed description of advanced features concerning the solid phase and study its influence on their properties. In addition, the influence of the parameters describing the solid phase on the thermal and mechanical properties has been analysed.

On the other hand, a novel methodology for the fast and reliable characterization of basic structural parameters of cellular polymers such as cell size and anisotropy has been developed based on **Light Scattering**.

These techniques have been optimized for conventional cellular polymers with cell sizes ranging 200-1000  $\mu\text{m}$ , based on PU, PS and PE with different cellular architectures. In addition, one additional objective of this investigation is to perform both tomographic and light scattering tests for the first time in nanocellular polymers based on poly-methyl methacrylate (PMMA) with cell sizes ranging the nanoscale (30-1000 nm).

The general purposes of this PhD thesis can be summarized as follows:

*"Deepen into the detailed analysis of the structure of cellular polymers by means of X-ray  $\mu$ -CT and its influence on physical properties"*

*"Develop a novel characterization technique for solid cellular polymers based on Light Scattering"*

*"Characterize nanocellular polymers by using both techniques for the first time"*

For the final consecution of the aforementioned goals several scientific, technical and methodological challenges are described in detail in the following section.

### 1.3 Challenges

Various technical aspects were proposed with the aim of achieving the objectives previously described:

- To design, adapt and optimize the tomography system at CellMat Laboratory to obtain tomographic reconstructions with up to 2.5  $\mu\text{m}$  effective pixel size with optimum contrast for low density cellular polymers.
- To design and build a specific system for the characterization of cellular polymers of a wide range of characteristics (density, cell size) by means of Light Scattering.

Furthermore, during this PhD thesis it has been necessary to overcome several methodological aspects:

- To develop novel methodologies based on image analysis to obtain a detailed description of the cellular structure of cellular polymers. In particular, we have focused our attention on non well-studied parameters of the solid phase of these materials such as the repartition of material throughout the solid skeleton, the solid material thickness distribution and the quantification of the corrugation of the structure.
- To develop a novel experimental methodology to perform and analyse the Light Scattering experiments in solid cellular polymers.
- To select a suitable collection of conventional cellular polymers based on PU, PE and PS that allow verifying the reliability of the developed techniques and methodologies.

Last but not least, from a scientific perspective, the main topics to highlight are:

- To study the morphology of cellular polymers structure in 3D by means of X-ray  $\mu\text{-CT}$ . These materials are low X-ray absorbing materials with only 2-5% of solid volume in the material. Therefore, the X-ray absorption is reduced to the minimum compromising the contrast in the final reconstructed volumes. A careful

selection of the experiment parameters has served for the contrast optimization on the X-ray tomography performed experiments.

- To determine the influence of novel structural descriptors of the solid phase on mechanical and thermal properties of cellular polymers.
- To develop a model to describe Light Scattering in solid cellular polymers including the key characteristics of cellular polymers.
- To evaluate how the particularities of the foaming process such as the presence/absence of external nucleating agents may alter the structure of the cellular materials while foaming.

### 1.4 Main Novelties

The main novelties of this thesis over current scientific literature could be summarized as follows:

- The establishment of novel image analysis protocols for the quantification of features corresponding to the solid phase of cellular materials by means of X-ray tomography reaching a global description of the biphasic structure of cellular materials.
- The study of the influence of solid phase corrugation in both collapse stress and thermal expansion coefficient of flexible cellular polymers.
- The visualization and quantification of cell nucleation and growth in cellular polymers in 3D by using real time synchrotron X-ray Tomography.
- The development of both a novel methodology and theoretical model to enable the characterization of solid cellular polymers by means of Light Scattering methodologies with great results concerning the measurement of cell size and anisotropy.
- The 3D structure visualization of non-conventional/nanocellular polymers for the first time by using synchrotron based X-ray nanotomography techniques.
- The application of Light Scattering technique to nanocellular polymers establishing the first evidence about the possibility of manufacturing nanocellular polymers transparent to visible light.

### 1.5 Structure of this thesis

This thesis is written in the format of a *compendium of publications*. The presented experimental results are supported by 10 scientific articles, 3 of them already published and the rest pending of publication (table 1-1). Communications in national and international conferences (table 1-2) and research projects developed during the time of this investigation (table 1-3) are also addressed. Additional activities developed during this investigation such as other scientific publications or stays at foreign research facilities are summarized (table 1-4).

The structure of this thesis is developed over eight chapters and one annex. After the two first introductory chapters, the following five are divided in three blocks (X-ray Tomography, Light Scattering and application of both techniques on non-conventional ocellular polymers) with pyramidal structure (Figure 1-4). Finally, the conclusions of the investigation are presented as the eighth and last chapter of this thesis.

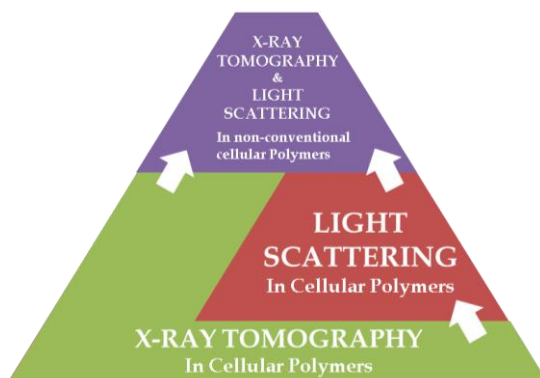


**Figure 1-4.** Schematic view of the structure of this thesis.

Moreover, this thesis fulfils the necessary requirements to be accredited with the **International Mention**.

**Chapter 1** introduces the main insights about this investigation as well as the scientific framework and the main objectives and milestones.

**Chapter 2** deals with a revision of the main concepts related to the structure of cellular materials introducing a new multicomponent model of the cellular structure, including the definition of several new advanced descriptors. In addition, basic ideas about the involved mechanisms (cell generation and degeneration processes) occurring during foaming are addressed.

**Chapter 3** provides a general overview of the basic concepts of X-ray imaging focused on the case of X-ray  $\mu$ -CT. The different steps and key factors to obtain optimized tomographic results are presented. Furthermore, a brief description of the different X-ray facilities in which the experimental work of this thesis has been carried out is included as well as the employed image analysis softwares and processing protocols.

**Chapter 4** presents the main results of this thesis concerning X-ray  $\mu$ -CT. Firstly, a detailed tomographic characterization of two sets of cellular polymers combining two sets of tomographies with different spatial resolutions is presented (*one paper*). After that, the thermo-mechanical properties of one of the precedents cellular polymers collection have been suitably modelled including the effect of the corrugation in the structure (*one paper*). Finally, the foaming process of two PU systems is studied by means of time-resolved X-ray  $\mu$ -CT (*one paper*).

**Chapter 5** includes the development of Light Scattering theory for the study of cellular materials, discussing the basis of the existing theories of scattering (Rayleigh, Mie) and the deduction/approach to aqueous system solution. Finally, the practical aspects of implementation that have been overcome for the final application in solid cellular polymers are addressed.

**Chapter 6** represents then the experimental process followed in this investigation to reach the final result about the Light Scattering as an effective tool for the characterization of solid cellular polymers. To this end, firstly the Light Scattering equation is solved numerically due to its own particularities (*one paper*) to reach finally the modification of the model that allows the characterization of solid cellular polymers (*one paper*). Finally, the results concerning the cellular anisotropy measurements by this technique are addressed (*one paper*).



## 1. Introduction

**Chapter 7** summarizes the first results concerning both X-ray nano-Tomography (n-CT) novel techniques (*one paper*) and Light Scattering application in non-conventional/nanocellular polymers (*one paper*).

Finally, **chapter 8** summarizes the most remarkable conclusions of this investigation and it proposes topics for further work. There is also **one annex** including other practical uses of X-ray imaging techniques (*two papers*).

Figure 1-5 shows the summary of the chapters and scientific publications contributing to this investigation.

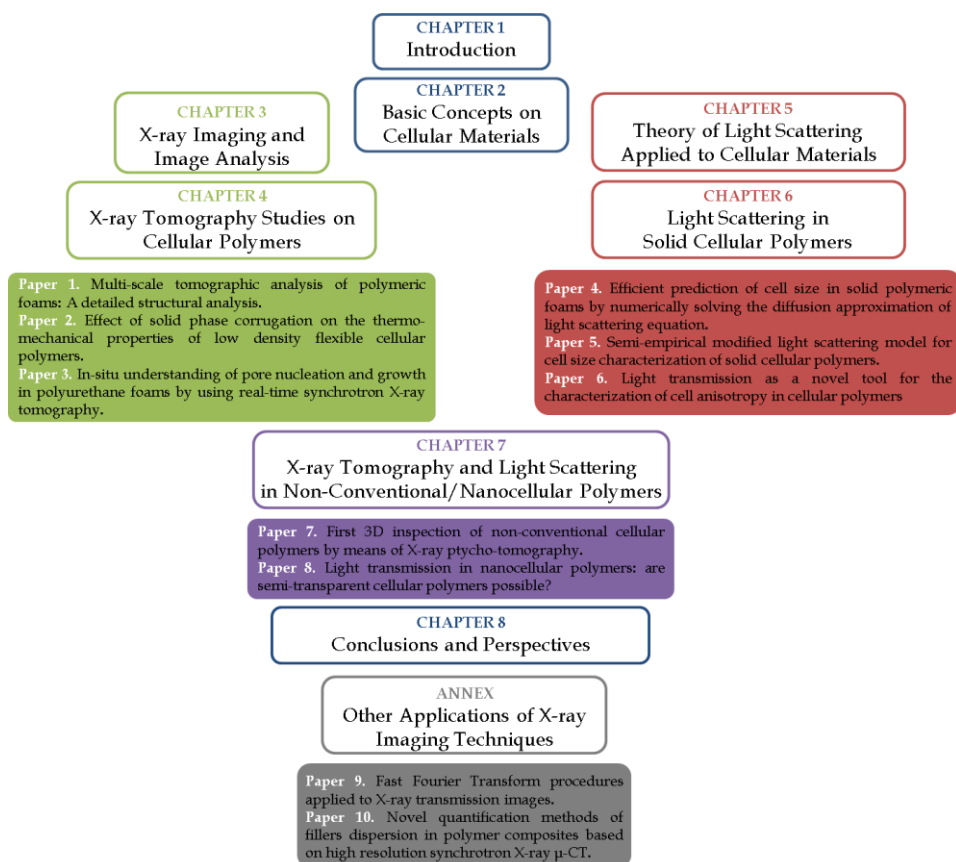


**Figure 1-5.** Summary of the chapters and scientific publications contributing to this thesis.

Table 1-1

No.	Scientific Publications	Ch.
1	S. Pérez-Tamarit, E. Solórzano, A. Hilger, I. Manke and M. A. Rodríguez-Perez Multi-scale tomographic analysis of polymeric foams: A detailed structural analysis <i>European Polymer Journal</i> 109 (2018) 169-178	4
2	S. Pérez-Tamarit, E. Solórzano, A. Hilger, I. Manke and M. A. Rodríguez-Perez Effect of solid phase corrugation on the thermo-mechanical properties of low density flexible cellular polymers <i>Materials and Design</i> (submitted)	4
3	S. Pérez-Tamarit, E. Solórzano, S. Pardo-Alonso, R. Mokso and M. A. Rodríguez-Pérez Monitoring of pore nucleation and growth in cellular polymers by real-time synchrotron X-ray tomography: Modelling of the involved physical mechanisms <i>Physical Review Letters</i> (submitted)	4
4	S. Pérez-Tamarit, E. Solórzano and M. A. Rodríguez-Perez Efficient prediction of cell size in solid polymeric foams by numerically solving the diffusion approximation of light scattering equation <i>Colloid and Surfaces A</i> 534 (2017) 130-137	6
5	S. Pérez-Tamarit, E. Solórzano and M. A. Rodríguez-Perez Semi-empirical modified light scattering model for cell size characterization of solid cellular polymers <i>Colloid and Surfaces A</i> (submitted)	6
6	S. Pérez-Tamarit, E. Solórzano and M. A. Rodríguez-Perez Light transmission as a novel tool for the characterization of cell anisotropy in cellular polymers <i>Materials Letters</i> (submitted)	6
7	S. Pérez-Tamarit, P. Cimavilla, J. Martín-de León, V. Bernardo, E. Solórzano, D. Batey, S. Cipiccia, C. Rau and M. A. Rodríguez-Perez First 3D inspection of nanocellular polymers by means of X-ray ptucho-tomography <i>Macromolecular Communications</i> (submitted)	7
8	S. Pérez-Tamarit, B. Notario, E. Solórzano and M. A. Rodríguez-Perez Light transmission in nanocellular polymers: Are semi-transparent cellular polymers possible? <i>Materials Letters</i> 210 (2018) 39-41	7
9	S. Pérez-Tamarit, E. Solórzano, A. Kaestner and M. A. Rodríguez-Perez Fast Fourier Transform procedures applied to X-ray transmission images <i>Microscopy and Microanalysis</i> (submitted)	Annex
10	S. Pérez-Tamarit, E. Solórzano, E. Laguna-Gutierrez, A. Hilger, I. Manke and M. A. Rodríguez-Perez Novel quantification methods of fillers dispersion in polymer composites based on high resolution synchrotron X-ray $\mu$ -CT <i>Polymer</i> (submitted)	Annex

**Table 1-2**

Scientific Communications in Conferences	
<u>S. Pérez Tamarit</u> , B. Notario, E. Solórzano, M. A. Rodríguez-Pérez	
Cell size determination by means of light scattering methodologies in micro and nanoporous foams (ORAL)	
VII European School on Molecular Nanoscience (ESMoI Na 2014), Valencia (Spain), October 2014	
<u>S. Pérez-Tamarit</u> , E. Solórzano, M. A. Rodríguez-Pérez, A. Salonen and W. Drenkham	
Modified light scattering models in solid polymeric foams (ORAL)	
X European Conference on Foams and Applications (EuFoam 2014), Thessaloniki (Greece), July 2014	
<u>S. Pérez-Tamarit</u> , E. Solórzano, A. Kaestner and M. A. Rodríguez-Pérez	
Cell size determination by means of FFT in X-ray transmission images (POSTER)	
X European Conference on Foams and Applications (EuFoam 2014), Thessaloniki (Greece), July 2014	
<u>E. Solórzano</u> , E. Laguna-Gutiérrez, S. Pérez-Tamarit, A. Kaestner, J. Pinto and M. A. Rodríguez-Pérez	
Polymer foam evolution characterized by time-resolved neutron radiography (ORAL)	
X European Conference on Foams and Applications (EuFoam 2014), Thessaloniki (Greece), July 2014	
<u>S. Pérez-Tamarit</u> , E. Solórzano, A. Hilger, I. Manke and M. A. Rodríguez-Pérez	
Solid-phase structural characterization in polymeric foams: Synchrotron micro-CT in the limits of resolution (ORAL)	
II International Conference on Tomography of Materials and Structures (ICTMS 2015), Quebec city (Canada) July 2015	
<u>J. Martín-de León</u> , V. Bernardo, S. Pérez-Tamarit, E. Solórzano and M. A. Rodríguez-Pérez	
Nanocellular foams fabrication methods by gas dissolution process (POSTER)	
IX International Conference on Porous Metals and Metallic Foams (Metfoam 2015), Barcelona (Spain), September 2015	
<u>V. Bernardo</u> , J. Martín-de León, S. Pérez-Tamarit, E. Solórzano and M. A. Rodríguez-Pérez	
Cellular structure, properties and applications of nanoporous materials (POSTER)	
IX International Conference on Porous Metals and Metallic Foams (Metfoam 2015), Barcelona (Spain), September 2015	
<u>S. Pérez-Tamarit</u> , V. Bernardo, J. Martín-de León, E. Solórzano and M. A. Rodríguez-Pérez	
Characterization of the solid phase of cellular materials by means of x-ray micro-CT (POSTER)	
IX International Conference on Porous Metals and Metallic Foams (Metfoam 2015), Barcelona (Spain), September 2015	
<u>S. Pérez-Tamarit</u> , E. Solórzano and M. A. Rodríguez-Pérez	
A numerical approach for solving the light scattering model applied to solid polymeric foams (ORAL)	
XI European Conference on Foams and Applications (EuFoam 2016), Dublin (Ireland), July 2016	
<u>S. Pérez-Tamarit</u> , B. Notario, E. Solórzano and M. A. Rodríguez-Pérez	
Towards transparent nano-cellular polymeric foams (POSTER)	
XI European Conference on Foams and Applications (EuFoam 2016), Dublin (Ireland), July 2016	

<u>S. Pérez-Tamarit</u> , E. Solórzano, E. Laguna-Gutierrez, B. Notario, A. Hilger, I. Manke and M. A. Rodriguez-Perez
Characterization of fillers dispersion in composites and nanocomposites by means of synchrotron X-ray micro-tomography ( <b>ORAL</b> )
XIV Reunión del Grupo Especializado de Polímeros (GEP 2016), Burgos (Spain) September 2016
<u>S. Pérez-Tamarit</u> , E. Solórzano, S. Pardo-Alonso, R. Mokso and M. A. Rodriguez-Perez
Pore Nucleation and growth in cellular polymers analysed by time resolved synchrotron $\mu$ -CT ( <b>ORAL</b> )
III International Conference on Tomography of Materials and Structures (ICTMS 2017), Lund (Sweden) June 2017
<u>S. Pérez-Tamarit</u> , E. Solórzano, E. Laguna-Gutierrez, B. Notario, A. Hilger, I. Manke and M. A. Rodriguez-Perez
Novel quantification methods of fillers dispersion in polymer composites and nanocomposites based on high resolution synchrotron X-ray $\mu$ -CT ( <b>POSTER</b> )
III International Conference on Tomography of Materials and Structures (ICTMS 2017), Lund (Sweden) June 2017
<u>S. Pérez-Tamarit</u> , E. Solórzano, A. Hilger, I. Manke and M. A. Rodriguez-Perez
Multiscale analysis of cellular polymers ( <b>POSTER</b> )
VIII Conference on Industrial Computed Tomography (iCT 2018), Wels (Austria) February 2018
<u>S. Pérez-Tamarit</u> , E. Solórzano, A. Hilger, I. Manke and M. A. Rodriguez-Perez
Determination of solid phase corrugation ratio of polymeric foams ( <b>POSTER</b> )
VIII Conference on Industrial Computed Tomography (iCT 2018), Wels (Austria) February 2018
<u>S. Pérez-Tamarit</u> , E. Solórzano and M. A. Rodriguez-Perez
Characterization of the cellular architecture of solid polymeric foams by means of optical light transmission measurements ( <b>ORAL</b> )
XII European Conference on Foams and Applications (EuFoam 2018), Liege (Belgium), July 2018
<u>S. Pérez-Tamarit</u> , P. Cimavilla, J. Martín-de León, V. Bernardo, E. Solórzano and M. A. Rodriguez-Perez
X-ray tomographic homogeneity inspection in nanocellular polymers produced using different foaming conditions ( <b>POSTER</b> )
XII European Conference on Foams and Applications (EuFoam 2018), Liege (Belgium), July 2018
<u>P. Cimavilla</u> , S. Pérez-Tamarit, M. Santiago-Calvo and M. A. Rodriguez-Perez
In-situ physicochemical analysis of the foaming process of aerogel-rigid polyurethane composite foams ( <b>ORAL</b> )
XII European Conference on Foams and Applications (EuFoam 2018), Liege (Belgium), July 2018
<u>P. Cimavilla</u> , S. Pérez-Tamarit, E. Solórzano, A. Hilger, I. Manke and M. A. Rodriguez-Perez
Novel subresolution tomographic methods for quantifying fraction of mass in Plateau borders of solid polymeric foams ( <b>POSTER</b> )
XII European Conference on Foams and Applications (EuFoam 2018), Liege (Belgium), July 2018
<u>D. Batey</u> , S. Cipiccia, X. Shi, S. Williams, K. Wanelik, A. Wilson, S. Pérez-Tamarit, P. Cimavilla, M. A. Rodríguez-Pérez and C. Rau
Coherence Branch at I13, DLS: The Multiscale, Multimodal, Ptycho-tomographic End Station ( <b>ORAL</b> )
XIV International Conference on X-Ray Microscopy (XRM 2018), Saskatoon (Canada), August 2018

## 1. Introduction

C. Rau, M. Storm, S. Marathe, A. J. Bodey, S. Cipiccia, D. Batey, X. Shi, M-C. Zdora, I. Zanette, S. Pérez-Tamarit, P. Cimavilla, M. A. Rodríguez-Pérez, F. Doring and C. David  
Multi-Scale Imaging at the Coherence and Imaging Beamline I13 at Diamond (ORAL)  
XIV International Conference on X-Ray Microscopy (XRM 2018), Saskatoon (Canada), August 2018

**Table 1-3**

Research Projects
Desarrollo y fabricación en continuo de aislantes térmicos avanzados basados en polímeros nanocelulares
Neadfoam: Aditivos innovadores para espumas con mejores prestaciones de aislamiento térmico y comportamiento frente al fuego
Desarrollo de bandejas de espuma de poliestireno extruido con baja densidad y propiedades mejoradas

**Table 1-4**

Stays in Other Research Facilities
XXXIV Berlin School on Neutron Scattering
Helmholtz Zentrum, Berlin (Germany) 13 <sup>th</sup> -21 <sup>st</sup> March 2014
Synchrotron tomography of polymer foams: in the limits of resolution ( <i>Experimentation campaign</i> )
BESSY II Synchrotron, Berlín (Germany) 5 <sup>th</sup> -8 <sup>th</sup> June 2014
In-situ characterization of the foaming behaviour and exfoliation of nanoclays in nanocomposites using combined white-beam X-ray radiography & diffraction ( <i>Experimentation campaign</i> )
BESSY II Synchrotron, Berlín (Germany) 7 <sup>th</sup> -10 <sup>th</sup> May 2015
In-situ study of nanoclay exfoliation of polymeric nanocomposites during foaming with azodicarbonamide ( <i>Experimentation campaign</i> )
BESSY II Synchrotron, Berlín (Germany) 3 <sup>rd</sup> -9 <sup>th</sup> October 2016
Multiscale investigation of nanocellular polymers with synchrotron based tomography
Diamond Light Source, Oxford (United Kingdom) September-December 2017
<b>PhD Research Stay</b>
Multiscale investigation of nanocellular polymers with synchrotron based tomography ( <i>Experimentation campaign</i> )
Diamond Light Source, Oxford (United Kingdom) 18 <sup>th</sup> -21 <sup>st</sup> January 2018

## Other Scientific Publications

E. Solórzano, E. Laguna-Gutiérrez, S. Pérez-Tamarit, A. Kaestner and M. A. Rodríguez-Pérez  
Polymer foam evolution characterized by time-resolved neutron radiography  
*Colloids and Surfaces A* 473 (2015) 46-54  
M. Santiago-Calvo, S. Pérez-Tamarit, J. Tirado-Medavilla, F. Villafañe and M. A. Rodríguez-Pérez  
Infrared expandometry: A novel methodology to monitor the expansion kinetics of cellular materials produced with exothermic foaming mechanisms  
*Polymer Testing* 66 (2018) 383-393

---

D. Batey, S. Cipiccia, X. Shi, S. Williams, K. Wanelik, A. Wilson, S. Pérez-Tamarit, P. Cimavilla,  
M. A. Rodríguez-Pérez and C. Rau

---

Coherence Branch at I13, DLS: The Multiscale, Multimodal, Ptycho-tomographic End Station

---

*Microscopy and Microanalysis* 24 (2018) 40-41

---

C. Rau, M. Storm, S. Marathe, A. J. Bodey, S. Cipiccia, D. Batey, X. Shi, M-C. Zdora, I. Zanette, S. Pérez-Tamarit,  
P. Cimavilla, M. A. Rodríguez-Pérez, F. Doring and C. David

---

Multi-Scale Imaging at the Coherence and Imaging Beamline I13 at Diamond

---

*Microscopy and Microanalysis* 24 (2018) 254-255

---

### References

---

- [1] L.J. Gibson, M.F. Ahsby, *Cellular Solids: Structure and Properties*, Pergamon Press, Oxford, England, 1988.
- [2] A. Cunningham, N.C. Hilyard, *Low Density Cellular Plastics: Physical Basis of Behaviour*, Ed. Chapman and Hall, London, 1994.
- [3] M.A. Rodríguez- Perez, J.I. Velasco, D. Arencón, O. Almanza, J.A. De Saja, Mechanical characterization of closed-cell polyolefin foams, *Journal of Applied Polymer Science*, 75 (2000) 156-166.
- [4] E. Solórzano, M.A. Rodríguez- Perez, *Polymer Foams: Advanced Structural Materials in Transportation*, in: D. Lehmhus, M. Busse, A. Herrmann, K. Kayvantash (Eds.) *Structural Materials and Processes in Transportation*, Wiley 2013.
- [5] *The Future of Polymer Foams to 2019*, 2014.
- [6] [www.plasticseurope.es](http://www.plasticseurope.es).
- [7] <http://www.plastemart.com>.
- [8] D. Klempner, K.C. Frish, *Handbook of Polymeric Foams and Foam Technology*, in: Hanser (Ed.), 1991.
- [9] <http://cellmat.es/>.
- [10] M.A. Rodríguez- Perez, *Propiedades Térmicas y Mecánicas de espumas de poliolefinas*, PhD Thesis, University of Valladolid, 1999.
- [11] J.I. González-Peña, *Efecto de tratamientos térmicos en bloques de espuma de polietileno de baja densidad fabricados mediante moldeo por compresión*, PhD Thesis, University of Valladolid, 2006.
- [12] J.L. Ruiz-Herrero, *Impacto y Fluencia en espumas con base polietileno*, PhD Thesis, University of Valladolid, 2004.
- [13] O. Almanza, *Caracterización y modelización de las propiedades térmicas y mecánicas de espumas con base polietileno*, PhD Thesis, University of Valladolid, 2000.
- [14] L.O. Arcos y Rábago, *Propiedades térmicas y mecánicas en espumas de poliolefinas fabricadas en un proceso de moldeo por compresión*, PhD Thesis, University of Valladolid, 2002.
- [15] M.L. Álvarez Láinez, *Propiedades térmicas, mecánicas y acústicas de espumas de poliolefina de celda abierta*, PhD Thesis, University of Valladolid, 2007.
- [16] F. Hidalgo González, *Diseño optimizado de los parámetros de proceso en la fabricación de espumas de poliolefina reticulada mediante moldeo por compresión*, PhD Thesis, University of Valladolid, 2008.
- [17] R.A. Campo-Arnáiz, *Aplicación de técnicas espectroscópicas al estudio de la morfología polimérica, propiedades térmicas y de emisión de espumas de baja densidad con base poliolefina*, PhD Thesis, University of Valladolid, 2011.
- [18] M.A. Rodríguez- Perez, O. Alonso, J. Souto, J.A. De Saja, Thermal Conductivity of Physically Crosslinked Closed Cell Polyolefin Foams, *Polymer Testing*, 16 (1997) 287-298.
- [19] C. Saiz-Arroyo, M.A. Rodríguez-Pérez, J. Tirado, A. López-Gil, J.A. de Saja, Structure-property relationships of medium-density polypropylene foams, *Polymer International*, 62 (2013) 1324-1333.
- [20] O. Almanza, L.O. Arcos y Rábago, M.A. Rodríguez- Perez, Structure-Property relationships in polyolefin foams, *Journal of Macromolecular Science, Part B*, 40 (2001) 603-613.
- [21] M.A. Rodríguez- Perez, S. Díez-Gutiérrez, J.A. De Saja, The recovery behaviour of crosslinked closed cell polyolefin foams, *Polymer Engineering and Science*, 38 (1998) 831-837.
- [22] M.A. Rodríguez-Perez, M. Álvarez-Láinez, J.A. de Saja, Microstructure and physical properties of open-cell polyolefin foams, *Journal of Applied Polymer Science*, 114 (2009) 1176-1186.

- [23] C. Saiz-Arroyo, Fabricación de materiales celulares mejorados basados en poliolefinas. Relación procesado-composición-estructura-propiedades, PhD Thesis, University of Valladolid, 2012.
- [24] O. Almanza, M.A. Rodríguez- Perez, J.A. De Saja, The microstructure of polyethylene foams produced by a nitrogen solution process, *Polymer*, 42 (2001) 7117-7126.
- [25] M.A. Rodríguez- Perez, O. Almanza, J.L. Ruiz-Herrero, J.A. De Saja, The effect of processing on the structure and properties of crosslinked closed cell polyethylene foams, *Cellular Polymers*, 27 (2008) 179-200.
- [26] M.A. Rodríguez- Perez, O. Almanza, J.A. De Saja, Anomalous thickness increase in crosslinked closed cell polyolefin foams during heat treatments, *Journal of Applied Polymer Science*, 73 (1998) 2825-2835.
- [27] J.A. Reglero Ruiz, Production and characterization of aluminium foams: Applications in the aeronautical sector, PhD Thesis, University of Valladolid, 2007.
- [28] E. Solórzano, Aluminium foams: Foaming process, cellular structure and properties, PhD Thesis, University of Valladolid, 2008.
- [29] J. Lázaro Nebreda, Optimization of the cellular structure of aluminium foams, PhD Thesis, University of Valladolid, 2014.
- [30] E. Solórzano, M.A. Rodríguez-Perez, J.A. de Saja, Thermal Conductivity of Cellular Metals Measured by the Transient Plane Source Method, *Advanced Engineering Materials*, 10 (2008) 371-377.
- [31] E. Solórzano, M.A. Rodríguez-Perez, J.A. Reglero, J.A. de Saja, Mechanical Behaviour of Internal Reinforced Aluminium Foams, *Advanced Engineering Materials*, 9 (2007) 955-958.
- [32] J. Lázaro, E. Laguna-Gutiérrez, E. Solórzano, M.A. Rodríguez-Pérez, Effect of Microstructural Anisotropy of PM Precursors on the Characteristic Expansion of Aluminum Foams, *Metallurgical and Materials Transactions B*, 44 (2013) 984-991.
- [33] J. Lázaro, E. Solórzano, J.A. de Saja, M.A. Rodríguez-Pérez, Early anisotropic expansion of aluminium foam precursors, *Journal of Materials Science*, 48 (2013) 5036-5046.
- [34] J. Lázaro, E. Solórzano, M.A. Rodríguez Pérez, F. García-Moreno, Pore connectivity of aluminium foams: effect of production parameters, *Journal of Materials Science*, 50 (2015) 3149-3163.
- [35] E. Laguna Gutiérrez, Understanding the foamability of complex polymeric systems by using extensional rheology, PhD Thesis, University of Valladolid, 2016.
- [36] S. Pardo-Alonso, X-ray imaging applied to the characterization of polymer foams' cellular structure and its evolution, PhD Thesis, University of Valladolid, 2014.
- [37] E. Solórzano, S. Pardo-Alonso, J.A. de Saja, M.A. Rodríguez-Perez, X-ray radiography in-situ studies in thermoplastic polymer foams, *Colloids and Surfaces A: Physicochemical and Engineering aspects*, 438 (2013) 167-173.
- [38] E. Solórzano, S. Pardo-Alonso, J.A. de Saja, M.A. Rodríguez-Pérez, Study of aqueous foams evolution by means of X-ray radiography, *Colloids and Surfaces A: Physicochemical and Engineering Aspects*, 438 (2013) 159-166.
- [39] S. Pardo-Alonso, E. Solórzano, S. Estravís, M.A. Rodríguez-Perez, J.A. de Saja, In situ evidence of the nanoparticle nucleating effect in polyurethane-nanoclay foamed systems, *Soft Matter*, 8 (2012) 11262.
- [40] M.M. Bernal, S. Pardo-Alonso, E. Solórzano, M.A. Lopez-Machado, R. Verdejo, M.A. Rodríguez- Perez, Effect of carbon nanofillers on flexible polyurethane foaming from a chemical and physical perspective, *RSC Advances*, 4 (2014).
- [41] E. Solórzano, J. Pinto, S. Pardo, F. Garcia-Moreno, M.A. Rodríguez-Perez, Application of a microfocus X-ray imaging apparatus to the study of cellular polymers, *Polymer Testing*, 32 (2013) 321-329.
- [42] M. Santiago-Calvo, S. Pérez-Tamarit, J. Tirado-Mediavilla, F. Villafañe, M.A. Rodríguez-Pérez, Infrared expandometry: A novel methodology to monitor the expansion kinetics of



cellular materials produced with exothermic foaming mechanisms, *Polymer Testing*, 66 (2018) 383-393.

[43] E. Solórzano, M. Antunes, C. Saiz-Arroyo, M.A. Rodríguez-Pérez, J.I. Velasco, J.A. de Saja, Optical expandometry: A technique to analyze the expansion kinetics of chemically blown thermoplastic foams, *Journal of Applied Polymer Science*, 125 (2012) 1059-1067.

[44] S. Estravís Sastre, Cellular nanocomposites based on rigid polyurethane and nanoclays: fabrication, characterization and modeling of the mechanical and thermal properties, PhD Thesis, University of Valladolid, 2014.

[45] S. Estravís, J. Tirado-Mediavilla, M. Santiago-Calvo, J.L. Ruiz-Herrero, F. Villafañe, M.Á. Rodríguez-Pérez, Rigid polyurethane foams with infused nanoclays: Relationship between cellular structure and thermal conductivity, *European Polymer Journal*, 80 (2016) 1-15.

[46] M. Santiago-Calvo, V. Blasco, C. Ruiz, R. París, F. Villafañe, M.Á. Rodríguez-Pérez, Synthesis, characterization and physical properties of rigid polyurethane foams prepared with poly(propylene oxide) polyols containing graphene oxide, *European Polymer Journal*, 97 (2017) 230-240.

[47] J. Escudero Arconada, Polyolefin based cellular materials. Development of new production routes and optimization of barrier and mechanical properties by the addition of nanoclays, PhD Thesis, University of Valladolid, 2016.

[48] S. Román Lorza, Production and characterization of flame retardant halogen-free polyolefin based cellular materials, PhD Thesis, University of Valladolid, 2010.

[49] F. Silva-Bellucci, Preparation and characterization of multifunctional nanocomposites by adding paramagnetic ferroelectric nanoparticles to natural rubber films, PhD Thesis, University of Valladolid, Sao Paulo State University, 2013.

[50] J. Lobos Martín, Improving the stiffness and strength of porous materials by enhancement of the matrix microstructure and cellular morphology, PhD Thesis, University of Valladolid, 2013.

[51] M. Dumon, J.A. Reglero Ruiz, J. Pinto, M.A. Rodríguez-Pérez, M.A. Tallon, J.M. Pedros, M. Cloutet, P. Viot, Block copolymer-assisted microcellular supercritical CO<sub>2</sub> foaming of Polymers and Blends, *Cellular Polymers*, 31 (2012) 207-221.

[52] J.A. Reglero Ruiz, C. Saiz-Arroyo, M. Dumon, M.A. Rodríguez-Pérez, L. Gonzalez, Production, cellular structure and thermal conductivity of microcellular (methyl methacrylate)-(butyl acrylate)-(methyl methacrylate) triblock copolymers, *Polymer International*, 60 (2011) 146-152.

[53] D. Velasco Nieto, Development of cellular biomaterials based on EVA, PLA and PHB, production and characterization, PhD Thesis, University of Valladolid, 2017.

[54] A. López Gil, Development of environmentally friendly cellular polymers for packing and structural applications. Study of the relationship cellular structure-mechanical properties, PhD Thesis, University of Valladolid, 2016.

[55] H. Ventura Casellas, Development of new lightweight green composites reinforced with nonwoven structures of flax fibers, PhD Thesis, Polytechnic University of Catalonia and University of Valladolid, 2017.

[56] L. Oliveira-Salmazo, Foaming kinetics and cellular structure control of materials based on natural rubber and polyolefins, PhD Thesis, University of Valladolid and Sao Paulo State University, 2015.

[57] M.A. Rodríguez-Pérez, R.D. Simoes, S. Roman-Lorza, M. Alvarez-Lainez, C. Montoya-Mesa, C.J.L. Constantino, J.A. de Saja, Foaming of EVA/starch blends: Characterization of the structure, physical properties, and biodegradability, *Polymer Engineering & Science*, 52 (2012) 62-70.

[58] M.A. Rodríguez-Pérez, R.D. Simoes, C.J.L. Constantino, J.A. de Saja, Structure and physical properties of EVA/starch precursor materials for foaming applications, *Journal of Applied Polymer Science*, 121 (2011) 2324-2330.

- [59] A. Lopez-Gil, F. Silva-Bellucci, D. Velasco, M. Ardanuy, M.A. Rodriguez-Perez, Cellular structure and mechanical properties of starch-based foamed blocks reinforced with natural fibers and produced by microwave heating, *Industrial Crops and Products*, 66 (2015) 194-205.
- [60] L. Oliveira-Salmazo, A. Lopez-Gil, F. Silva-Bellucci, A.E. Job, M.A. Rodriguez-Perez, Natural rubber foams with anisotropic cellular structures: Mechanical properties and modeling, *Industrial Crops and Products*, 80 (2016) 26-35.
- [61] J. Pinto, Fabrication and characterization of nanocellular polymeric materials from nanostructured polymers, PhD Thesis, University of Valladolid and University of Bordeaux, 2014.
- [62] B. Notario Collado, Fabrication and characterization of the physical properties of nanocellular polymers: The transition from the micro to the nanoscale, PhD Thesis, University of Valladolid, 2016.
- [63] B. Notario, J. Pinto, E. Solorzano, J.A. de Saja, M. Dumon, M.A. Rodríguez-Pérez, Experimental validation of the Knudsen effect in nanocellular polymeric foams, *Polymer*, 56 (2015) 57-67.
- [64] B. Notario, J. Pinto, M.A. Rodríguez-Pérez, Towards a new generation of polymeric foams: PMMA nanocellular foams with enhanced physical properties, *Polymer*, 63 (2015) 116-126.
- [65] V. Bernardo, J. Martín-de León, E. Laguna-Gutiérrez, M.Á. Rodríguez-Pérez, PMMA-sepiolite nanocomposites as new promising materials for the production of nanocellular polymers, *European Polymer Journal*, 96 (2017) 10-26.
- [66] J. Pinto, B. Notario, R. Verdejo, M. Dumon, S. Costeux, M.A. Rodriguez-Perez, Molecular confinement of solid and gaseous phases of self-standing bulk nanoporous polymers inducing enhanced and unexpected physical properties, *Polymer*, 113 (2017) 27-33.
- [67] J. Martín-de León, V. Bernardo, M. Rodríguez-Pérez, Low Density Nanocellular Polymers Based on PMMA Produced by Gas Dissolution Foaming: Fabrication and Cellular Structure Characterization, *Polymers*, 8 (2016) 265.
- [68] S. Pardo-Alonso, E. Solórzano, L. Brabant, P. Vanderniepen, M. Dierick, L. Van Hoorebeke, M.A. Rodriguez- Perez, 3D Analysis of the progressive modification of the cellular architecture in polyurethane nanocomposite foams via X-ray microtomography, *European Polymer Journal*, 49 (2013) 999-1006.
- [69] M.D. Montminy, A.R. Tannenbaum, C.W. Macosko, The 3D structure of real polymer foams, *Journal of colloid and interface science*, 280 (2004) 202-211.
- [70] Y. Ma, R. Pyrz, M.A. Rodriguez-Perez, J. Escudero, J.C. Rauhe, X. Su, X-ray microtomographic study of nanoclay-polypropylene foams, *Cellular Polymers*, 30 (2011) 95-110.
- [71] J. Lambert, I. Cantat, R. Delannay, A. Renault, F. Graner, J.A. Glazier, I. Veretennikov, P. Cloetens, Extraction of relevant physical parameters from 3D images of foams obtained by X-ray tomography, *Colloids and Surfaces A: Physicochemical and Engineering Aspects*, 263 (2005) 295-302.
- [72] A. Elmoutaouakkil, G. Fuchs, P. Bergounhon, F. Peyrin, Three-dimensional quantitative analysis of polymer foams from synchrotron radiation x-ray microtomography, *Journal of Physics D: Applied Physics*, 36 (2003) A37-A43.
- [73] I. Cantat, S. Cohen-Addad, F. Elias, F. Graner, R. Höhler, O. Pitois, F. Rouyer, A. Saint-Jalmes, *Foams Structure and Dynamics*, Oxford University Press 2013.
- [74] B. Notario, J. Pinto, M.A. Rodriguez-Perez, Nanoporous polymeric materials: A new class of materials with enhanced properties, *Progress in Materials Science*, 78-79 (2016) 93-139.

## Chapter 2

# **Basic Concepts on Cellular Materials**



This chapter describes the basic concepts related to the structural description of cellular materials, as well as the main notions about foaming mechanisms required to understand the contents included in the following chapters. In addition, the materials involved in this investigation are presented as well as a description of the foaming process to produce them.

### 2.1 Cellular structure

Cellular materials are structures constituted by two phases, a continuous solid (or liquid) skeleton and a continuous or discontinuous gas phase dispersed on it [1-3]. The solid phase is generally called matrix. It is possible to find cellular materials based on a large variety of matrixes such as polymers, metals, wood, etc... According to the particular structural features cellular materials can be classified in three groups: lattice materials, engineered materials and foams. This investigation is focused on foams and more precisely on polymeric foams since they are one of the main topics covered by the research carried out at CellMat. These cellular materials are produced (or foamed) from the liquid/softened state using a blowing agent that produces cellular structures with a completely stochastic morphology and topology.

#### 2.1.1 *$\mu$ -structure model*

It is possible to distinguish different elements in the two mentioned phases (Figure 2-1). The main component characterizing any kind of cellular material are the cells, also called pores or bubbles indistinctively that are the principal constituent of the gas phase when the density is low. Cells could be geometrically described according to a polyhedral modelling.

On the other hand, the topology of the solid phase of low density cellular materials permits distinguishing two main constituents, cell walls (or films) and struts (or Plateau borders). Cell walls are the polyhedron faces separating two contiguous cells whereas vertexes and edges together form the cellular struts, considered the main skeleton of the cellular structure.

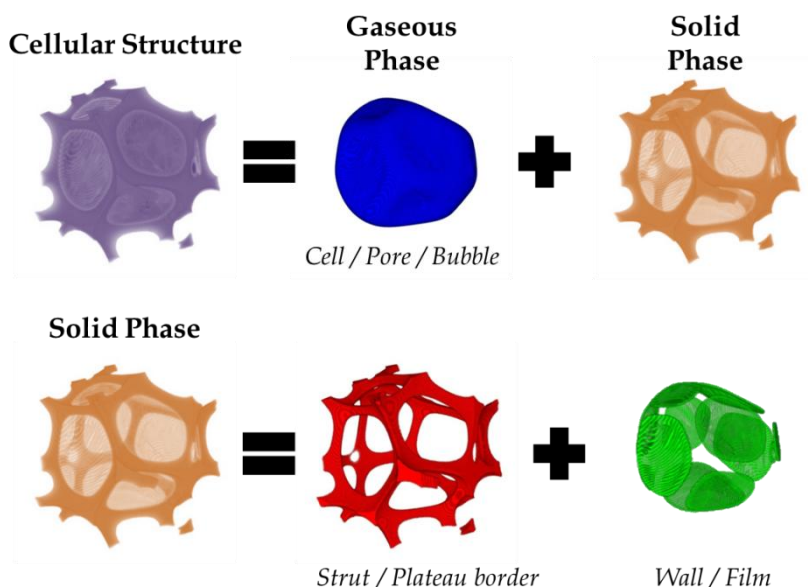


**Figure 2-1.** Conventional model of cellular structures.

As it is well known, physical properties of cellular materials such as thermal conductivity, stiffness, permeability, acoustic absorption strongly depends on microstructure [1-3]. However, a description of gaseous phase is not enough to explain many of these properties. For this reason, the characterization of the features corresponding to the solid phase, typically not considered nowadays in the literature, is of vital importance. For example, obviating the influence of presence/absence of cell walls, the mechanical performance of such kind of materials for a fixed relative density is strongly dominated by the cell wall thickness. The thicker is the cell wall thickness, the higher is the material stiffness.

The first and principal feature of cellular materials is their density [1-3]. The introduction of gas into the solid matrix leads to a weight reduction and thus a density reduction. However, in order to eliminate the influence of the matrix density it is more commonly used the so-called **relative density** ( $\rho_r$ ) defined as the ratio between the cellular material density ( $\rho_f$ ) and the density of the solid precursor ( $\rho_s$ ) (Equation 2-1). It is also called solid fraction depending on the aggregate state of the matrix.

$$\rho_r = \frac{\rho_f}{\rho_s} \quad \text{Equation 2-1}$$

According to its relative density, cellular materials can be classified in three great groups: **low density** ( $\rho_r < 0.3$ ), **medium density** ( $0.3 \leq \rho_r \leq 0.6$ ) and **high density** cellular materials ( $\rho_r > 0.6$ ). Linked to relative density, **porosity** ( $\psi$ ) or void fraction is defined as the fraction of the volume of voids over the total volume of material (Equation 2-2).

$$\psi = 1 - \rho_r \quad \text{Equation 2-2}$$

Another parameter related with relative density and normally employed when dealing with cellular materials is the **expansion ratio** ( $ER$ ) calculated as the inverse value of the relative density (Equation 2-3). It indicates the volume ratio reached by the foamed materials, or more precisely, how many times the precursor material has been expanded during foaming.

$$ER = \frac{1}{\rho_r} \quad \text{Equation 2-3}$$

### 2.1.2 Microscopic descriptors

This section deals with the description of the main descriptors concerning the microstructure of cellular materials. As these materials are biphasic, in this section the descriptors are classified accordingly.

- *Gaseous Phase*

The **average cell size** ( $\phi$ ) is one of the most representative parameters of the cellular structure. A lot of definitions of this parameter are possible but the most typical refers to mean diameter of the corresponding cell.

In fact, another classification of cellular materials can be addressed regarding their mean cell size (Figure 2-2). **Nanocellular materials** are those with cell size lower than  $0.3 \mu\text{m}$ , **sub-microcellular materials** are characterized by cell sizes ranging  $0.3\text{--}1 \mu\text{m}$ ,

**microcellular materials** are those with cell sizes between 1-10  $\mu\text{m}$  and finally **conventional cellular materials** have cell sizes higher than 10  $\mu\text{m}$ .

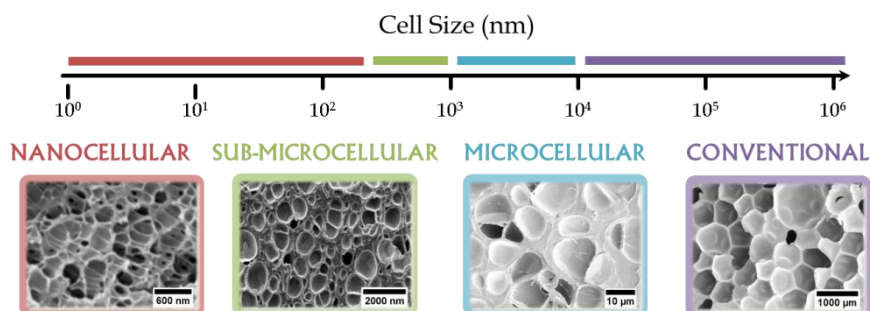


**Figure 2-2.** Schematic view of cell size range classification of cellular materials.

In practice, two main procedures are considered in order to determine this parameter. The first one consists on calculating the size of the three main axis of the equivalent ellipsoid. The average value of these three values is considered as the mean cell size. On the other hand, the mean cell size calculated as the equivalent diameter is that one obtained from an equivalent sphere containing the same volume as the considered cell. In fact, the two values are identical in spherical pores.

Cell size is a key parameter for properties such as thermal conductivity, toughness and ultimate mechanical properties. For this reason, some of the most important research topics nowadays directly focus on reducing the cell size to the micro-scale (microcellular materials) and nanoscale (sub-microcellular and nanocellular materials).

Finally, it is important to mention that the mean cell size is not enough to accurately characterize the gaseous phase of cellular materials. Cell size distribution can also strongly alter the physical properties since the resulting cellular structures can be homogeneous or highly inhomogeneous even if the average value of cell size is not modified (Figure 2-3). The influence of the cellular homogeneity on the physical properties of a cellular material is an analysed topic. In general, it has been found that non-uniform distribution of the cell sizes has in general a detrimental effect on the



properties of the material [2]. In this case the solid mass is not homogenously distributed which favours the appearance of cracks in the weaker areas [1].

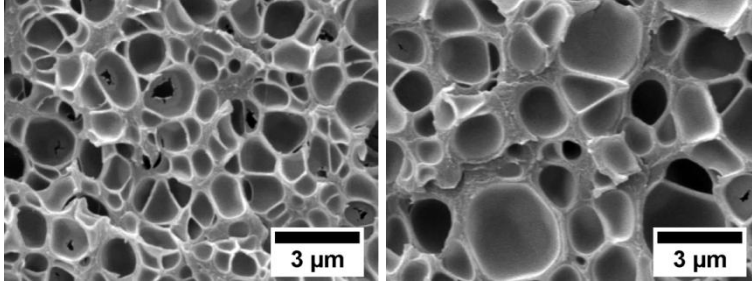


**Figure 2-3.** Micrographs of two cellular polymers with homogeneous –left- and inhomogeneous –right- cellular structure.

The standard deviation ( $SD$ ) (Equation 2-4) or most recently the normalised standard deviation ( $NSD$ ) (Equation 2-5), which permits eliminating the effect of mean cell size, are the numerical parameters that should be taken into account when comparing different structures [4].

$$SD = \sqrt{\sum_{i=1}^n \frac{(\phi_i - \phi)^2}{n}} \quad \text{Equation 2-4}$$

$$NSD = SD / \phi \quad \text{Equation 2-5}$$

Where  $n$  is the total number of cells,  $\phi_i$  is the diameter of each cell, and  $\phi$  is the mean cell size. The smaller is the value of  $NSD$ , the more homogeneous is the cellular structure.

**Cell density** ( $N_v$ ) is defined as the number of pores per unit volume and is typically calculated using both mean cell size and relative density (Equation 2-6).

$$N_v = \frac{6}{\pi \phi^3} (1 - \rho_r) \quad \text{Equation 2-6}$$

However, in order to compare two cellular materials with different relative densities is more adequate to introduce the **cell nucleation density** ( $N_0$ ) which is closely related with cell density (Equation 2-7).

$$N_0 = \frac{N_v}{\rho_r} \quad \text{Equation 2-7}$$

Due to the cubic dependence of cell density with mean cell size, reducing cell size dramatically increases cell density if the relative density remains constant (Figure 2-4). Focusing on the average cell size classification of cellular materials shown before, cell density is around  $10^{14}$ ,  $10^{11}$ ,  $10^8$  and  $10^6$  cells $^{-3}$  for nanocellular, sub-microcellular, microcellular and conventional materials respectively [5-7]. Cell density is one of the most representative parameters of any cellular structure since it combines the influence of both cell size and relative density. In addition, it is crucial to understand the cellular structure evolution during the foaming processes. In our case, cell density is directly obtained in X-ray Tomography due to the 3D outputs of this technique.

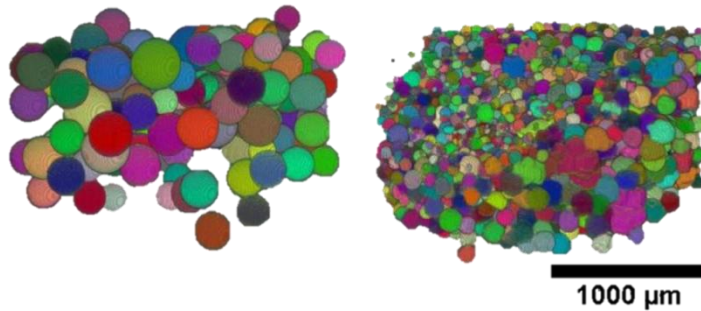


**Figure 2-4.** Tomographic 3D rendering of two cellular materials with similar relative density but different cell density.

In order to justify the directionality of physical properties, **cell anisotropy** ( $R_i$ ) is typically considered. It is defined as the mean cell size in that direction divided by the average cell size in the perpendicular plane (Equation 2-8). However, depending on processing peculiarities, cells are typically elongated along preferential directions (Figure 2-5) [8, 9] and therefore it is useful to identify some of them with the typical directions of a Cartesian reference system [1, 2, 10]. On the other hand, the **pore orientation** is typically described considering the two angles that form the main axis of the equivalent ellipsoid with the reference system in the 3D space.

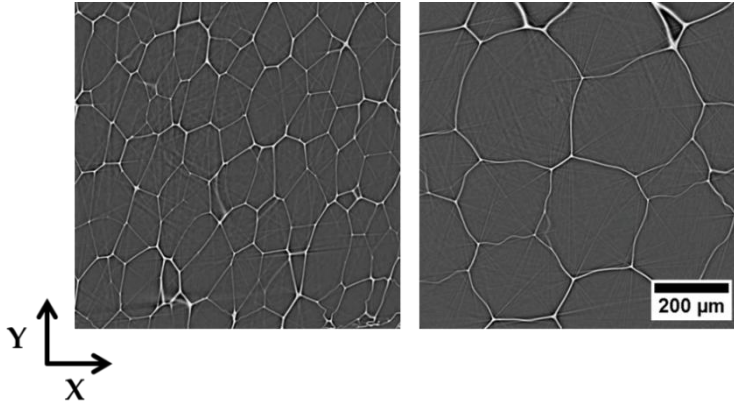


**Figure 2-5.** Tomographic slices showing a slightly anisotropic cellular PS in the Y direction and an isotropic cellular PE.

$$R_i = \frac{2\phi_i}{\phi_j + \phi_k}; \quad i \neq j \neq k \quad \text{Equation 2-8}$$

The topological information of the cellular structure is provided by the **coordination number** ( $n_i$ ). It indicates the average number of neighbouring cells, that is close connected with the cell packing and cell shape in cellular materials. At this respect, a lot of possible cell topologies are possible in 3D space from tetrahedrons, triangular prisms, cubes, octahedrons, pentagonal dodecahedrons, etc... [1]. However, only few packing geometries are admissible for the minimisation of the energy. In 1873 Plateau deduced that the rhombic dodecahedron, polyhedron containing 12 faces with rhombic shape, was the most energy efficient single unit. Few years later (1887) Kelvin minimizes further the involved energy by using the tetrakaidekahedron cells (14 faces, 6 quadrilateral and 8 hexagonal), but with slightly curved surfaces [11]. In 1994 Weaire and Phelan minimized even more this energy by employing 14-sided polyhedrons made up of 12 curved pentagonal and 2 hexagonal plane faces [12].

Coordination number is, in addition, linked with other descriptors of the cellular structure like cell size distribution. For example, a wider cell size distribution should be linked to a higher average coordination number since large cells will be surrounded by many smaller neighbours.

**Open cell content (OC)** is defined as the gas volume fraction of interconnected cells in the material. It is calculated typically using gas pycnometry that allows determining the displaced volume of the sample ( $V_p$ ) considering the geometric volume of the sample ( $V$ ) and also the volume of cells in the surface of the sample ( $V_s$ ) (ASTM 6226-10, Equation 2-9) [13]. The grade of this parameter (ranging 0-1) allows establishing the classification of cellular materials between purely open and closed-cell materials (Figure 2-6).

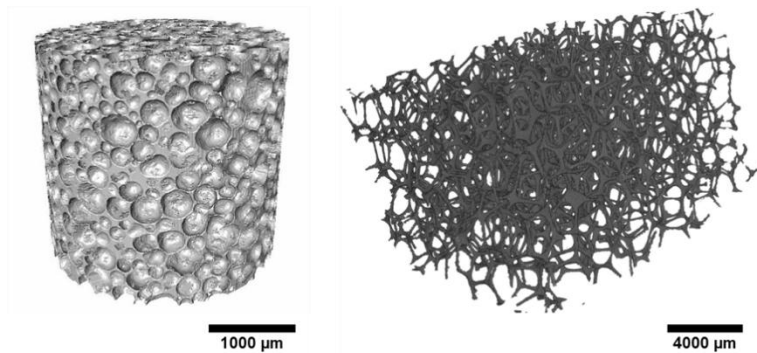


**Figure 2-6.** 3D rendering of two cellular materials. Closed cell cellular epoxy –left- and open cell cellular PU –right-.

$$OC = \frac{V - V_p - V_s}{V(1 - \rho_r)} \quad \text{Equation 2-9}$$

**Closed cell** materials are characterized by the absence of interconnected cells and therefore open cell content is 0 and in **open cell materials** the open cell content is close to 1. In this case, it is important to mention that the interconnection of cells is possible either by the total absence of cell walls in the structure or by the presence of holes in the cell walls. In fact, size, concentration and shape of holes in the cellular structure have a influence on several physical properties of cellular materials. However, gas pycnometry is not able to discriminate between these two situations, becoming tomography one of the only possible solutions for the characterization of the holes in the cell walls.

### ○ Solid Phase

The principal solid phase descriptor of cellular materials is the **structure thickness**. Several algorithms have been developed nowadays for the quantification of thickness in 3D [14]. One of the most used is called **Local Thickness Algorithm** [15-17], that assign to each point of the entity under study the diameter of the greatest sphere entirely enclosed within the entity and centred in the selected point.

Once the algorithm is implemented, it is possible to obtain material thickness distributions on the analysed volume (Figure 2-7). For low density cellular materials, the typical material thickness distribution contains two differentiated peaks corresponding to the two mentioned parts of the solid phase, struts (thicker part peak) and walls (thinner part peak). Furthermore, depending on the characteristics of the cellular architecture the two peaks can be well separated or highly overlapped.

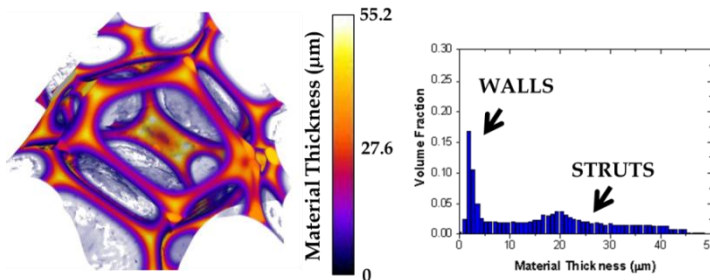


**Figure 2-7.** 3D rendering of a cell of a PU foam showing the calculated material thickness along the structure –left- and the resulting material thickness distribution –right-.

Analysing the materials thickness distribution it is possible to calculate the mean **cell wall thickness** ( $\delta$ ), the **strut thickness** ( $\xi$ ) and the **average thickness** of the structure ( $t$ ). All these thicknesses are crucial to understand physical properties of cellular materials such as stiffness [18] or thermal conductivity [19]. A detailed characterization of these non-well studied features has been carried out in low density cellular polymers during this research by using high resolution X-ray Tomography (Chapter 4).

As mentioned, it is possible to discern two parts in the solid structure of cellular materials: struts (Plateau borders) and cell walls (films). Consequently, the repartition of matrix material between the two parts is crucial to understand many physical properties of these materials such as collapse stress [20, 21] or thermal conductivity [19, 22]. For this reason, the **fraction of material in the struts** ( $f_s$ ) is introduced as the ratio between the amount of material located in struts and the total amount of matrix material in the structure (Equation 2-10).

$$f_s = \frac{m_{struts}}{m_{struts} + m_{walls}} \quad \text{Equation 2-10}$$

Up to now, several 2D methods have been conventionally employed assimilating the cross section of the struts both to an equivalent circle [23] or triangle [10] and then estimating the value of  $f_s$  assuming a determined pore geometry (typically pentagonal dodecahedron). However, 3D methods that allow classifying directly both parts of the structure (Figure 2-8) provide a direct quantification of this parameter. This part of the research in this thesis is focused on the development of image analysis protocols for the accurate characterization of  $f_s$  and its influence on physical properties of cellular materials (Chapter 4).

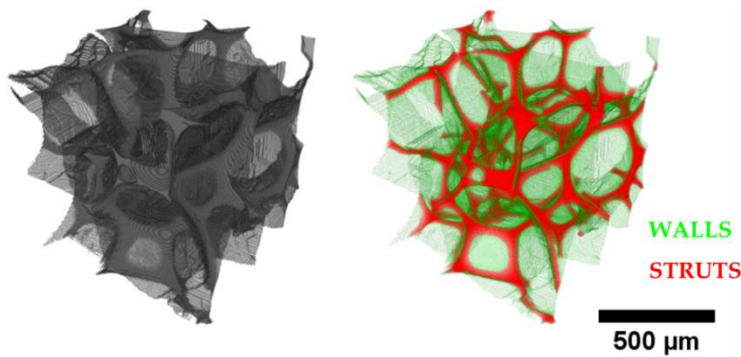


**Figure 2-8.** Separation of the typical structure of a cellular PU -left- in its two constituents, walls (green) and struts (red) -right-.

Finally, cellular materials may present a corrugated cellular structure, i.e. the cell walls and/or the struts are not flat (Figure 2-9). The **structure corrugation** has been

already studied in the literature [24, 25], even using tomographic methods [26]. However, its influence on physical properties has been scarcely analysed and modelled. In this investigation, once characterized by tomographic methods, its influence on both collapse stress and thermal expansion coefficient of flexible cellular polymers has been studied (**Chapter 4**).

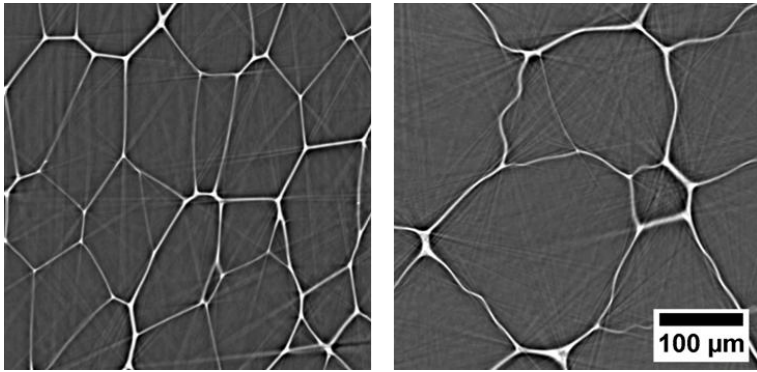


**Figure 2-9.** Tomography slices of two cellular materials with flat -left- and corrugated -right- cellular structure.

## 2.2 Foaming dynamics

Most cellular materials are produced by the expansion of a gaseous phase dispersed on the liquid matrix. The foaming process is comprised by three steps: cells formation, growth and stabilisation in which several mechanisms take place: nucleation, growth, drainage, coalescence and coarsening (Figure 2-10). It is possible to separate them into two groups, those corresponding to the **cells generation** (nucleation/growth) and those promoting the **degeneration of the cellular structure** (drainage/coalescence/coarsening).

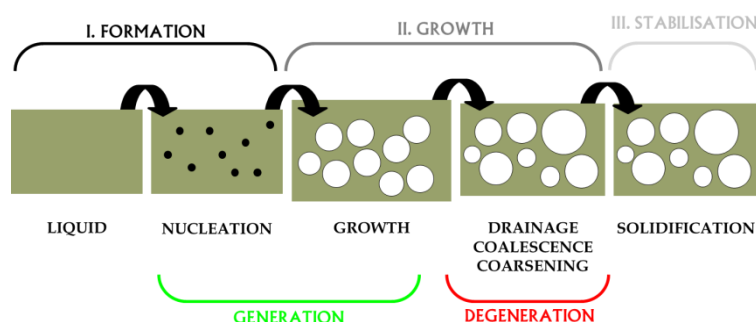


**Figure 2-10.** Main stages of cellular materials formation.

The information about what happened during the foaming process of cellular materials is crucial to understand their final structure since a stronger nucleation can be compensated by a coalescence of the bubbles. For this reason, it is important to study intermediate stages (with either *in-situ* or *ex-situ* techniques).

### 2.2.1 Cells formation

**Nucleation** is the process leading the formation of cells within the liquid matrix. This mechanism initiates the formation of nanometric areas in the early stages of the foaming process as a consequence of a thermodynamical instability in the gas-liquid interphase. Then, due to pressure inhomogeneties these points are able to grow forming the cells of the material. It is one of the key parameters in order optimize the production of cellular materials since suitable nucleation steps usually lead to



successful foaming processes. Two types of nucleation possibilities are considered in the literature: homogeneous and heterogeneous nucleation.

The **homogeneous nucleation** involves the pore formation without the presence of impurities in the liquid-gas system. The classical nucleation theory establishes the **homogeneous nucleation rate** ( $N_{hom}$ ) as a function of the Gibbs free energy or cell activation energy ( $\Delta G_{hom}$ ), temperature ( $T$ ) and other factors related to the process kinetics such as the concentration of gas molecules ( $C_{hom}$ ) and the frequency factor of the gas molecules ( $f_{hom}$ ) [27-29] (Equation 2-11).

$$N_{hom} = C_{hom} f_{hom} \exp\left(-\frac{\Delta G_{hom}}{k_B T}\right) \quad \text{Equation 2-11}$$

Further, in this case the cell activation energy is calculated as a function of the pressure difference between gas and liquid ( $\Delta p$ ) and surface tension ( $\sigma$ ) (Equation 2-12).

$$\Delta G_{hom} = \frac{16\pi\sigma^3}{3\Delta p^2} \quad \text{Equation 2-12}$$

On the other hand, **heterogeneous nucleation** takes place with impurities in the liquid-gas mixture. In this situation the cells are created preferably on the solid-liquid interphase of these impurities reducing the activation energy by a factor ( $f$ ) depending on the geometry of the impurities and the contact angle between particle and matrix [30](Equation 2-13). Therefore these impurities in the system act as nucleation agents. In fact, the addition of foreign particles to the cellular material matrix prior foaming is a typical strategy to control the cellular structure of foamed materials [31-34].

$$\Delta G_{het} = f \Delta G_{hom} \quad \text{Equation 2-13}$$

The **nucleation rate in heterogeneous** systems ( $N_{het}$ ) is similar to the previous case, but with different factors related with the process such as the concentration of nucleation sites ( $C_{het}$ ) and the frequency of gas molecules joining the nucleus ( $f_{het}$ ) [28, 35] (Equation 2-14).

$$N_{hom} = C_{het} f_{het} \exp\left(-\frac{\Delta G_{hom}}{k_B T}\right) \quad \text{Equation 2-14}$$

Once the cells are nucleated they are able to **grow** resulting in the macroscopic expansion of the material. According to classical nucleation theory only cells with a radius greater than the critical radius ( $R_c$ ) tends to grow whereas the smaller cells collapse redistributing their gas into the molten matrix. Surface tension ( $\sigma$ ) and pressure difference ( $\Delta p$ ) are again involved into the critical radius determination (Equation 2-15).

$$R_c = \frac{2\sigma}{\Delta p} \quad \text{Equation 2-15}$$

This process continues until the stabilization of the cellular structure [2]. From the theoretical point of view, some of the current theoretical models explain the cells growth considering the expansion of an individual cell into a Newtonian fluid with constant viscosity [36, 37]. In this model, the cell growing rate ( $dR/dt$ ) is related to bubble radius ( $R$ ), the viscosity of the matrix ( $\eta$ ), the surface tension ( $\sigma$ ) and internal and external pressures of the cell ( $p_i$  and  $p_o$ ) (Equation 2-16).

$$\frac{dR}{dt} = R \left( \frac{p_i - p_o - 2\sigma/R}{4\eta} \right) \quad \text{Equation 2-16}$$

### 2.2.2 Degeneration of the cellular structure

Prior the stabilization of the structure it can be degenerated by several mechanisms such as drainage, coalescence and coarsening.

**Drainage** takes place during foaming at a microscopic level as the liquid phase drains out of equilibrium in the thin films separating cells. It is caused by capillary forces that produce transport of the liquid material from the cell walls towards the struts. Consequently the cell walls are thinned and both coarsening and coalescence are favoured [38].

The rupture of a film separating two consecutive cells is called **coalescence**. It is the result of an excessive thinning of cell walls and subsequent loss of strength to resist

the expansion of the cells, generating a bigger cell from two (or more) smaller ones [30, 39, 40]. This mechanism is mainly dominated by the surface tension of the liquid-gas system and thermodynamically favoured since the total surface of cells is reduced by coalescence [41].

Finally, **coarsening** consist on the diffusion of gas from smaller cells to larger ones due to pressure differences. The lower is the volume of the cell, the higher is the pressure inside it. As a result, the larger cell grows and the smaller cell becomes even smaller and could even disappear [3, 38].

### 2.3 Materials

In this section, a description of the materials selected for this investigation as well as the foaming process to produce them is addressed. Three different types of cellular polymers based on different matrices (PU, PE and PS) were considered whereas nanocellular polymers based on PMMA as solid matrix were also used. In addition, the characteristic of the selected nanosilica (Aerosil R812) to evaluate the effect of nucleating agents in the foaming process are finally addressed.

#### 2.3.1 Polyurethane (PU) and Reactive Foaming

**Polyurethane (PU) foams** are the most extensively used and well-known cellular polymers, representing more than half of the global market of foams [42]. These materials are produced by the chemical reaction of two main components, polyol and isocyanate, being the main example of the so-called **reactive foaming** process [2, 43]. In this foaming process, two simultaneous reactions take place, gelling and blowing reactions. Figure 2-11 shows the typical reaction for water-blown PU foams, in which water is used as blowing agent. A mixing process of the three components, in which the main parameters are stirring time and rate (rpm), is required to promote both reactions.

In the gelling reaction urethane groups are created due to the isocyanate ( $R-N=C=O$ ) and hydroxyl ( $-OH$ ) groups present on the polyol component. On the other hand, blowing reaction forms carbamic acid from isocyanate ( $R-N=C=O$ ) and water ( $H_2O$ ). This acid decomposes in amine ( $RNH_2$ ) and  $CO_2$  thus creating the cells. Furthermore, the created amine is able to react with isocyanate resulting in urea groups [44].

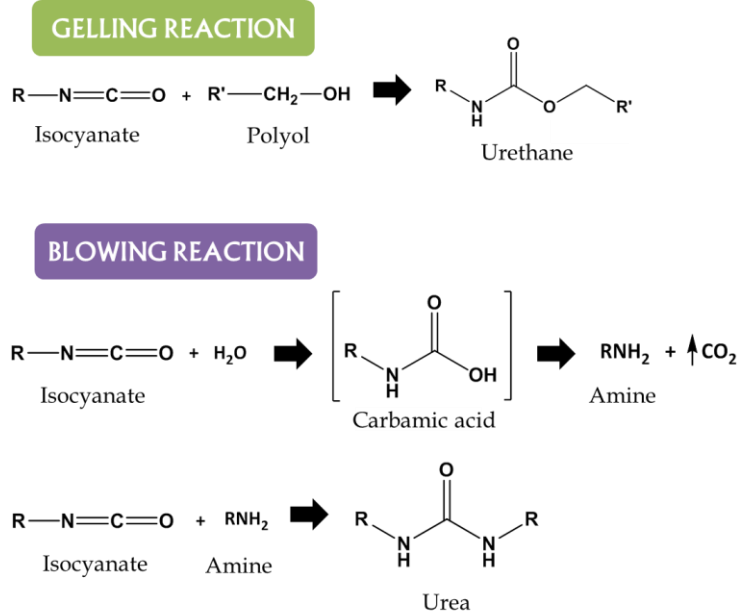


**Figure 2-11.** Chemical reactions involved in the reactive foaming of PU.

The structure of PU foams is the result of these two chemical reactions. These materials own pentagonal dodecahedron shape cells. In addition, depending on the conditions of the foaming process (free or in mould) different cells anisotropy could appear. From the point of view of the solid phase, due to semisolid material drainage prior the gelling of the structure, PU foams concentrate a high amount of solid material in the struts, resulting in high values of  $f_s$  ( $>0.6$ ) and therefore very thin cell walls (1-2  $\mu\text{m}$ ) (Figure 2-12).

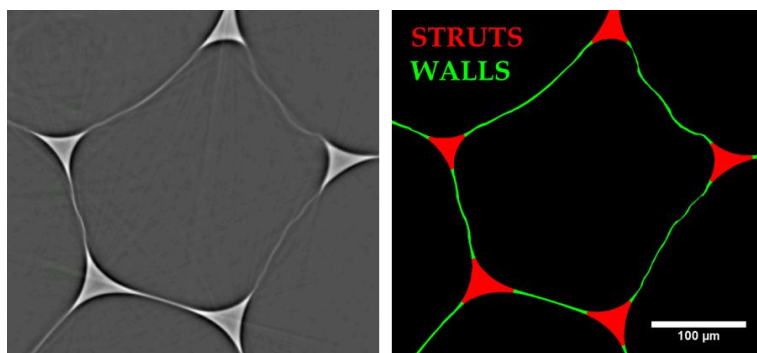


**Figure 2-12.** Tomographic slice –left- and separation in walls and struts –right- of a PU foam with  $f_s$  of 0.7.

For this investigation a commercial PU formulation from BASF was selected (Elastopor® H). The polyol component, Elastopor® H 1501/1 ( $1.07 \text{ gcm}^{-3}$ ), is a mixture of polyols, catalysts, stabilizers and water. The isocyanate, IsoPMDI 92140 ( $1.23 \text{ gcm}^{-3}$ ), is a diphenylmethane diisocyanate. By using four different commercial polyol blends with different amounts of water samples with different densities were produced ( $30\text{--}100 \text{ kgm}^{-3}$ ). In addition, using different mixing conditions different cell sizes were obtained ( $350\text{--}800 \text{ μm}$ ). As a result, a complete chart of materials with independent density and cell sizes were manufactured and used for developing this investigation (Table 2-1).

**Table 2-1.** List of PU samples produced during this research using 4 different formulations and 4 different mixing conditions (16 samples in total).

	Formulation 1	Formulation 2	Formulation 3	Formulation 4
	Density ~ 30 kg/m <sup>3</sup>	Density ~ 55 kg/m <sup>3</sup>	Density ~ 70 kg/m <sup>3</sup>	Density ~ 100 kg/m <sup>3</sup>
<b>Mixing conditions 1</b>				
(12s, 800 rpm)	✓	✓	✓	✓
Cell size ~ 800 µm				
<b>Mixing conditions 2</b>				
(16s, 1000 rpm)	✓	✓	✓	✓
Cell size ~ 600 µm				
<b>Mixing conditions 3</b>				
(20s, 1200 rpm)	✓	✓	✓	✓
Cell size ~ 500 µm				
<b>Mixing conditions 4</b>				
(25s, 2000 rpm)	✓	✓	✓	✓
Cell size ~ 350 µm				

### 2.3.2 Polyethylene (PE), poly-methyl methacrylate (PMMA) and Gas Dissolution Foaming

**Polyethylene (PE)** is the most common polyolefin, formed by simple repetition of the ethylene (-CH<sub>2</sub>-) group. In particular, low density polyethylene (LDPE) shows low density (910 kgm<sup>-3</sup>), chemical stability and mechanical strength and is frequently selected as base polymer in foaming for multiple purposes [45]. It is a semicrystalline thermoplastic polymer with approx. 40% of crystallinity.

**Polymethyl methacrylate (PMMA)** is an amorphous thermoplastic polymer, optically transparent, with density of 1180 kgm<sup>-3</sup> often used in sheet form as a lightweight or shatter-resistant alternative to glass. It is a strong, tough and lightweight material with very good impact strength.

Both materials could be foamed by the so-called **gas dissolution foaming** [5, 46]. This foaming process consists on several steps (Figure 2-13):

**Step I. Saturation:** the polymer is placed inside a pressure vessel under controlled gas pressure and temperature. The gas diffuses into the polymer, occupying the free space between the polymer chains [5, 47-49]. This stage usually ends when the polymer sample is completely saturated by surrounding gas.

**Step II. Desorption:** gas pressure is released, and the sample enters into a supersaturated state. The polymer starts to release the excess of gas, either by diffusion to the outside or by the formation of discontinuities/voids inside the matrix. These voids will act as nuclei for the cells formation [35].

**Step III. Foaming:** when the saturated sample reaches a temperature over or close to its glass transition temperature ( $T_g$ ) for PMMA or the melting temperature ( $T_m$ ) for PE the cell growth and then sample expansion takes place.

In this process, the variation of the different processing parameters permits controlling the final structure of the produced materials (density and cell size).

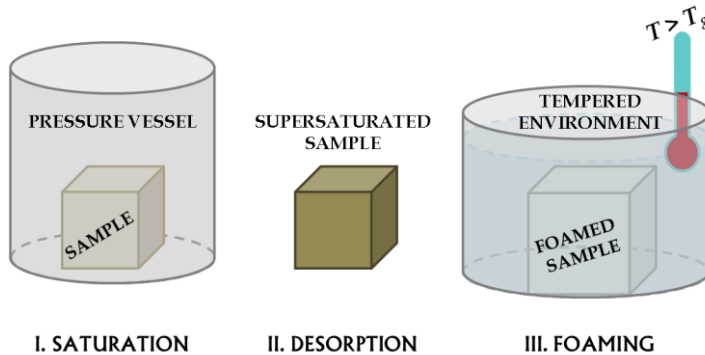


**Figure 2-13.** Gas dissolution foaming scheme.

For this investigation a collection of commercial low density cellular polyethylene samples produced by the company Zotefoams (UK) [50] were considered (density 15-60 kgm<sup>-3</sup>, cell size 300-800  $\mu$ m). These materials are produced using N<sub>2</sub> as blowing agent. Cell geometry in this case is tetrakaidecahedral with isotropic cells. In addition, the solid material is distributed throughout the structure more homogeneously than



in the case of PU foams, achieving therefore low-medium values of  $f_s$  (0.2-0.4) owing also thin cell wall thickness (2-4  $\mu\text{m}$ ) (Figure 2-14).

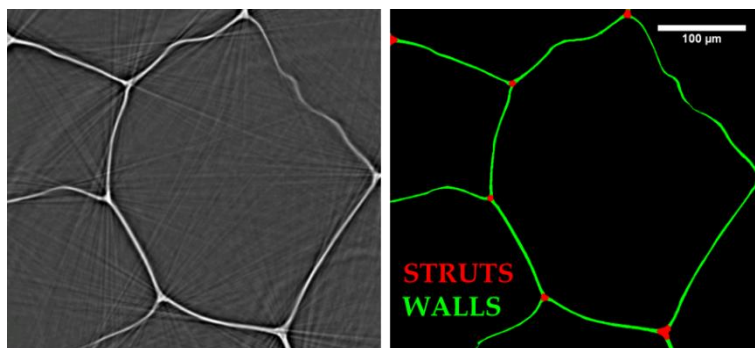


**Figure 2-14.** Tomographic slice -left- and separation in walls and struts -right- of a typical LDPE foam with  $f_s$  0.3.

On the other hand, for the nanocellular polymers considered in this investigation a PMMA (Plexiglas® V825) from Altuglas-Arkema (France) was used as raw material. The foamed specimens manufactured present relative densities around 0.4-0.8 and cell sizes from 25 nm to a few microns. The exact shape of the pores in this type of materials is still unknown. However, it has been proven that the anisotropy of the pores is linked with the anisotropy of the solid precursor [51, 52]. Regarding the solid phase, 2D microscopy studies have shown that  $f_s$  is proportional to relative density for constant cell size [5].

### 2.3.3 Polystyrene (PS) and Extrusion Foaming

Finally, **polystyrene (PS)** is an aromatic amorphous thermoplastic polymer produced from the monomer styrene with density of  $1050 \text{ kgm}^{-3}$ . It is clear, hard and brittle and one of the most widely used plastics. Among all its uses, foaming is one of the most important. Both expanded polystyrene (EPS) and extruded polystyrene (XPS) are manufactured nowadays mainly for insulation applications. EPS is fabricated by the sintering in a mould of pre-expanded PS beads whereas XPS is produced following the so-called **extrusion foaming**.

This is a continuous process working under similar principles of solid polymer extrusion [2, 41]. It allows producing simple geometries (pipes, sheets, etc...) of low and high density foams. However, temperature and pressure need to be controlled with care due to the presence of reactive and flammable gases acting as blowing agents. This process is composed by several steps: polymer melting, blowing agent injection and dissolution into the molten polymer, cooling of the blowing agent-molten polymer mixture to a temperature close to the glass transition temperature of the base polymer and pressure drop at the die which allows expansion. This pressure drop allows cell nucleation, followed by the sample expansion reaching stabilisation of the resultant cellular structure by cooling and solidification. The extrusion foaming can use a single extruder or tandem extruders. This last case permits manufacturing cellular materials with very low density.

In this investigation two similar commercial XPS samples (density  $35 \text{ kgm}^{-3}$ , cell size around  $250 \text{ }\mu\text{m}$ ) have been considered. Cells in this material are typically oriented in the thickness direction. These kind of materials reaches ultra-low values of  $f_s$  ( $<0.2$ ) with very thin ( $\sim 1 \text{ }\mu\text{m}$ ) flat cell walls and almost uniform material thickness distributions (Figure 2-15).

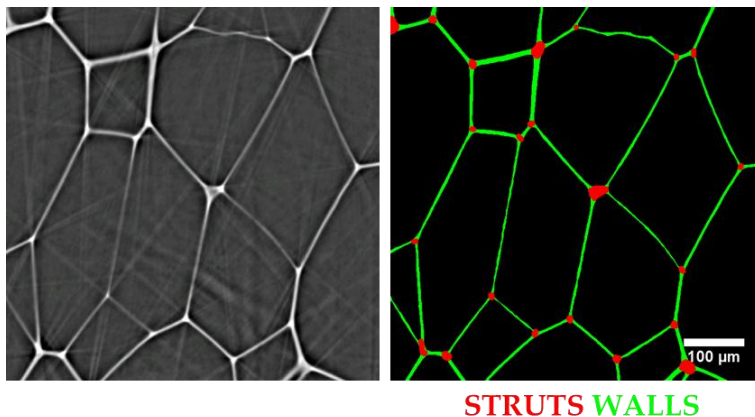


**Figure 2-15.** Tomographic slice -left- and separation in walls and struts -right- of PS foam with  $f_s$  0.15.

### 2.3.4 Nanosilica Aerosil R812

These hydrophobic-fumed silica (pyrogenic silicon dioxide) post-treated with hexamethyldisilazane (90% of hydrophobic surface) [53] were provided by Evonik Industries (Germany). The nanometric silica powder has an extremely low density and high surface area. In fact, the specific surface area for this particle ranges 230-290 m<sup>2</sup>/g. Due to the post-treatment only a small fraction of the surface hydroxyl groups are free. Its three-dimensional structure may result in viscosity increase when used as reinforcing additive.

## References

- [1] L.J. Gibson, M.F. Ahsby, *Cellular Solids: Structure and Properties*, Pergamon Press, Oxford, England, 1988.
- [2] D. Klemptner, K.C. Frisch, *Handbook of polymeric foams and foam technology*, Passavia Druckerei GmbH Passau 1991.
- [3] D. Weaire, S. Hutzler, *The physics of foams*, First Edition ed. 2001.
- [4] M.A. Rodríguez- Pérez, O. Alonso, A. Duijens, J.A. De Saja, Thermal expansion of crosslinked closed-cell polyethylene foams, *Journal of Polymer Science Part B: Polymer Physics*, 36 (1998) 2587-2596.
- [5] J. Martín-de León, V. Bernardo, M. Rodríguez-Pérez, Low Density Nanocellular Polymers Based on PMMA Produced by Gas Dissolution Foaming: Fabrication and Cellular Structure Characterization, *Polymers*, 8 (2016) 265.
- [6] C. Saiz-Arroyo, M.A. Rodríguez-Pérez, J. Tirado, A. López-Gil, J.A. de Saja, Structure-property relationships of medium-density polypropylene foams, *Polymer International*, 62 (2013) 1324-1333.
- [7] E. Laguna-Gutierrez, R. Van Hooghten, P. Moldenaers, M.A. Rodríguez-Pérez, Understanding the foamability and mechanical properties of foamed polypropylene blends by using extensional rheology, *Journal of Applied Polymer Science*, 132 (2015) 42430.
- [8] V. Bernardo, E. Laguna-Gutierrez, A. Lopez-Gil, M.A. Rodríguez-Pérez, Highly anisotropic crosslinked HDPE foams with a controlled anisotropy ratio: Production and characterization of the cellular structure and mechanical properties, *Materials & Design*, 114 (2017) 83-91.
- [9] L. Oliveira-Salmazo, A. Lopez-Gil, F. Silva-Bellucci, A.E. Job, M.A. Rodríguez-Pérez, Natural rubber foams with anisotropic cellular structures: Mechanical properties and modeling, *Industrial Crops and Products*, 80 (2016) 26-35.
- [10] A. Cunningham, N.C. Hilyard, *Low Density Cellular Plastics: Physical Basis of Behaviour*, Ed. Chapman and Hall, London, 1994.
- [11] D. Weaire, Kelvin's ideal foam structure, *Journal of Physics: Conference Series*, 158 (2009) 012005.
- [12] D. Weaire, R. Phelan, A counter-example to Kelvin's conjecture on minimal surfaces, *Philosophical Magazine Letters*, 69 (1994) 107-110.
- [13] A. D6226-15, *Annual Book of ASTM standards*, 2015.
- [14] H. Haidar, J.S. Soul, Measurement of cortical thickness in 3D brain MRI data: validation of the Laplacian method, *Journal of neuroimaging : official journal of the American Society of Neuroimaging*, 16 (2006) 146-153.
- [15] T. Hildebrand, P. Rüeggsegger, A new method for the model-independent assessment of thickness in three-dimensional images, *Journal of Microscopy*, 185 (1997) 67-75.
- [16] T. Stammberger, F. Eckstein, K.-H. Englmeier, M. Reiser, Determination of 3D cartilage thickness data from MR imaging: Computational method and reproducibility in the living, *Magnetic Resonance in Medicine*, 41 (1999) 529-536.
- [17] R. Dougherty, K.H. Kunzelmann, Computing Local Thickness of 3D Structures with ImageJ, *Microscopy and Microanalysis*, 13 (2007).
- [18] M.A. Rodríguez- Pérez, O. Almanza, J.L. Ruiz-Herrero, J.A. De Saja, The effect of processing on the structure and properties of crosslinked closed cell polyethylene foams, *Cellular Polymers*, 27 (2008) 179-200.
- [19] R.A. Campo-Arnáiz, M.A. Rodríguez-Pérez, B. Calvo, J.A. de Saja, Extinction coefficient of polyolefin foams, *Journal of Polymer Science Part B: Polymer Physics*, 43 (2005) 1608-1617.
- [20] A.N. Gent, A.G. Thomas, Mechanics of foamed elastic materials, *Rubber Chemistry and Technology*, 36 (1963) 597-610.

- [21] N.J. Mills, A. Gilchrist, The effects of heat-transfer and Poissons Ratio on the compressive response of closed-cell polymer foams, *Cellular Polymers*, 16 (1997) 87-109.
- [22] O.A. Almanza, M.A. Rodriguez- Perez, J.A. de Saja, Prediction of the Radiation Term in the Thermal conductivity of crosslinked closed cell polyolefin foams, *Journal of Polymer Science Part B: Polymer Physics*, 38 (2000) 993-1004.
- [23] J. Kuhn, H.P. Ebert, M.C. Arduini-Schuster, D. Büttner, J. Fricke, Thermal transport in polystyrene and polyurethane foam insulations, *International Journal of Heat and Mass Transfer*, 35 (1992) 1795-1801.
- [24] A.E. Simone, L.J. Gibson, The effects of cell face curvature and corrugations on the stiffness and strength of metallic foams, *Acta Materialia*, 46 (1998) 3929-3935.
- [25] J.L. Grenestedt, Influence of wavy imperfections in cell walls on elastic stiffness of cellular solids, *Journal of the Mechanics and Physics of Solids*, 46 (1998) 29-50.
- [26] S. Pardo-Alonso, E. Solorzano, J. Vicente, L. Brabant, M.L. Dierick, I. Manke, A. Hilger, E. Laguna, M.A. Rodriguez-Perez, muCT-Based Analysis of the Solid Phase in Foams: Cell Wall Corrugation and other Microscopic Features, *Microscopy and Microanalysis*, 21 (2015) 1361-1371.
- [27] R.B. McClurg, Design criteria for ideal foam nucleating agents, *Chemical Engineering Science*, 59 (2004) 5779-5786.
- [28] J.S. Colton, Nucleation of microcellular foam: Theory and practice, *Polymer Engineering & Science*, 27 (1987) 500-503.
- [29] J.S. Colton, The Nucleation of Microcellular Foams in Semicrystalline Thermoplastics, *Materials and Manufacturing Processes*, 4 (1989) 253-262.
- [30] N.S. Ramesh, D.H. Rasmussen, G.A. Campbell, The heterogeneous nucleation of microcellular foams assisted by the survival of microvoids in polymers containing low glass transition particles. Part I: Mathematical modeling and numerical simulation, *Polymer Engineering & Science*, 34 (1994) 1685-1697.
- [31] V. Bernardo, J. Martín-de León, E. Laguna-Gutiérrez, M.Á. Rodríguez-Pérez, PMMA-sepiolite nanocomposites as new promising materials for the production of nanocellular polymers, *European Polymer Journal*, 96 (2017) 10-26.
- [32] S. Estravís, J. Tirado-Mediavilla, M. Santiago-Calvo, J.L. Ruiz-Herrero, F. Villafañe, M.Á. Rodríguez-Pérez, Rigid polyurethane foams with infused nanoclays: Relationship between cellular structure and thermal conductivity, *European Polymer Journal*, 80 (2016) 1-15.
- [33] E. Laguna-Gutierrez, C. Saiz-Arroyo, J.I. Velasco, M.A. Rodriguez-Perez, Low density polyethylene/silica nanocomposite foams. Relationship between chemical composition, particle dispersion, cellular structure and physical properties, *European Polymer Journal*, 81 (2016) 173-185.
- [34] J. Lobos, S. Iasella, M.A. Rodriguez-Perez, S.S. Velankar, Improving the stability of polylactic acid foams by interfacially adsorbed particles, *Polymer Engineering & Science*, 56 (2016) 9-17.
- [35] J.S. Colton, N.P. Suh, The nucleation of microcellular thermoplastic foam with additives: Part I: Theoretical considerations, *Polymer Engineering and Science*, 27 (1987) 485-492.
- [36] R.D. Patel, Bubble growth in a viscous Newtonian liquid, *Chemical Engineering Science*, 35 (1980) 2352-2356.
- [37] M. Favelukis, R.J. Albalak, Bubble growth in viscous newtonian and non-newtonian liquids, *The Chemical Engineering Journal*, 63 (1996) 149-155.
- [38] I. Cantat, S. Cohen-Addad, F. Elias, F. Graner, R. Höhler, O. Pitois, F. Rouyer, A. Saint-Jalmes, *Foams Structure and Dynamics*, Oxford University Press 2013.
- [39] M.M. Bernal, S. Pardo-Alonso, E. Solórzano, M.A. Lopez-Machado, R. Verdejo, M.A. Rodriguez- Perez, Effect of carbon nanofillers on flexible polyurethane foaming from a chemical and physical perspective, *RSC Advances*, 4 (2014).

- [40] S. Pardo-Alonso, E. Solórzano, S. Estravís, M.A. Rodríguez-Pérez, J.A. de Saja, In situ evidence of the nanoparticle nucleating effect in polyurethane-nanoclay foamed systems, *Soft Matter*, 8 (2012) 11262.
- [41] S.T. Lee, C.B. Park, *Foam Extrusion: Principles and Practice*, CRC Press 2000.
- [42] [www.smithersrapra.com/news/2014/may/polymer-foam-market-to-consume-25-3-million-tonnes](http://www.smithersrapra.com/news/2014/may/polymer-foam-market-to-consume-25-3-million-tonnes).
- [43] G. Oertel, *Polyurethane Handbook* 2nd ed, New York, 1993.
- [44] S. Tan, T. Abraham, D. Ference, C.W. Macosko, Rigid polyurethane foams from a soybean oil-based Polyol, *Polymer*, 52 (2011) 2840-2846.
- [45] L. Garrido, L. Ibarra, C. Marco, *Ciencia y Tecnología de Materiales Poliméricos. Volumen II*, Instituto de Ciencia y Tecnología de Polímeros-CSIC 2004.
- [46] M.A. Rodríguez-Pérez, Crosslinked Polyolefin Foams: Production, Structure, Properties, and Applications, *Advances in Polymer Science*, 184 (2005) 97-126.
- [47] G.S. K, B.E. J, Generation of microcellular polymers using supercritical CO<sub>2</sub>, *Cellular Polymers*, 12 (1993) 251-274.
- [48] S. Costeux, CO<sub>2</sub>-Blown Nanocellular Foams, *Journal of Applied Polymer Science*, 131 (2014) 41293.
- [49] O. Almanza, M.A. Rodríguez-Pérez, J.A. De Saja, The microstructure of polyethylene foams produced by a nitrogen solution process, *Polymer*, 42 (2001) 7117-7126.
- [50] <https://www.zotefoams.com/>.
- [51] B. Notario, J. Pinto, E. Solorzano, J.A. de Saja, M. Dumon, M.A. Rodríguez-Pérez, Experimental validation of the Knudsen effect in nanocellular polymeric foams, *Polymer*, 56 (2015) 57-67.
- [52] B. Notario, J. Pinto, M.A. Rodríguez-Pérez, Towards a new generation of polymeric foams: PMMA nanocellular foams with enhanced physical properties, *Polymer*, 63 (2015) 116-126.
- [53] M. Santiago-Calvo, J. Tirado-Mediavilla, J.L. Ruiz-Herrero, M.Á. Rodríguez-Pérez, F. Villafañe, The effects of functional nanofillers on the reaction kinetics, microstructure, thermal and mechanical properties of water blown rigid polyurethane foams, *Polymer*, 150 (2018) 138-149.

## Chapter 3

# **X-ray Imaging and Image Analysis**





Scientific imaging aims at obtaining qualitative and quantitative information becoming therefore an useful tool in topics such as biology, physics, chemistry, materials science, etc... [1-3]. In this collection of techniques, both source and detection systems are required. Typically, imaging comprises any type of radiation-matter interaction (reflexion, refraction, absorption...).

Among all the possibilities, X-rays are one of the most suitable radiation sources for scientific purposes. Due to the penetration power of X-rays they permit the non-destructive inspection of the internal structure of materials. In addition, in the particular case of imaging the existence of both lab-scale X-ray sources and large synchrotron facilities offer the possibility of performing a wide variety of experiments [4, 5].

This chapter deals with the principal concepts required to understand the principles of X-ray Imaging and its application to conduct X-ray Tomography experiments. Firstly, the ins and outs about the generation of X-rays, their interaction with matter and final detection with imaging purposes are presented. Once these preliminary concepts are adequately described, a detailed explanation of X-ray Tomography is developed, from projection acquisition (the first step) to the correction of artefacts on the reconstructed slices (the last step of the process). Further, the particularities of the X-ray equipment designed and assembled at CellMat laboratory are cited and discussed followed by a brief summary of the beamlines in which part of the experimentation of this thesis has been carried out. Finally, both the different softwares used and the image analysis protocols developed during this investigation are presented.

#### 3.1 X-ray imaging fundamentals

Wilhelm Conrad Roentgen discovered X-rays in 1895 [6, 7]. Few months later the first commercial X-ray sources were fabricated. This electromagnetic radiation ranges from  $10^{-8}$  m (so-called soft X-rays) to  $10^{-11}$  m (hard X-rays). Consequently, the energy of this radiation ranges from 100 eV up to 2 MeV (in the frontier with  $\gamma$ -rays) (Figure 3-1). For imaging purposes typical X-ray energies are located in the range 5-150 keV,

excluding industrial applications in which a higher penetration power is required thus increasing the energy up to 6-9 MeV.

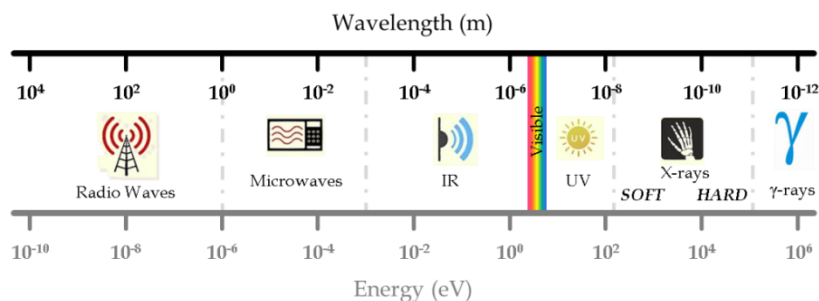


**Figure 3-1.** Energy and wavelength of the electromagnetic spectrum.

## 3.1.1 X-ray generation

The first step to carry out X-ray imaging consists on the production of the radiation. In this sense, two main mechanisms are able to generate X-rays.

On one hand, the excitation of atoms in elements with high atomic number (typically tungsten) by a high energy beam of charged particles provokes a subsequent de-excitation in form of X-rays emission. In this process two types of X-ray generated can be distinguished: characteristic radiation and bremsstrahlung radiation (Figure 3-2).

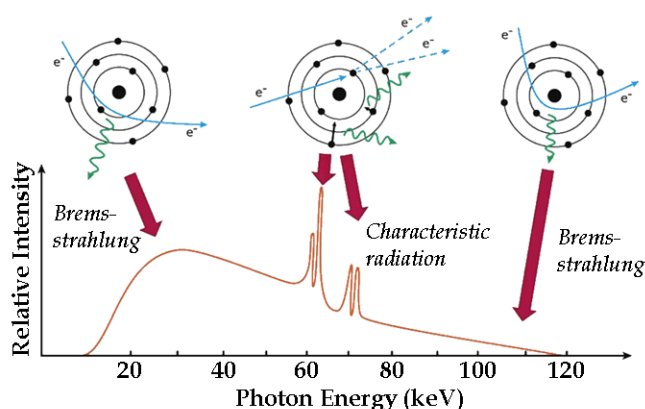


**Figure 3-2.** Two types of generated X-rays and typical emission X-rays spectrum.

### 3. X-ray Imaging and Image Analysis

Characteristic radiation is generated when a high energy electron collides with an inner shell electron provoking the ejection of the latter from the tungsten atom leaving a “hole” in the inner layer. This is filled then by an outer shell electron with a loss of energy emitted as an X-ray photon. In contrast, when an electron passes near the nucleus it is slowed and its path is deflected. Energy lost in this process is then emitted as a bremsstrahlung (braking radiation) X-ray photon. As a result of characteristic and bremsstrahlung radiation generation, a spectrum of X-ray energy is produced.

On the other hand, it is well known that accelerated charged particles emit radiation of different wavelengths depending of the magnitude of the acceleration. This mechanism is typically accomplished maintaining high energy electrons in circular trajectories. In this case, the centripetal acceleration suffered by the charged particles is the responsible of the generation of X-rays that are emitted tangentially to the electrons trajectory (Figure 3-3). This process generates a broad X-ray spectrum that depends on the magnitude of the acceleration.

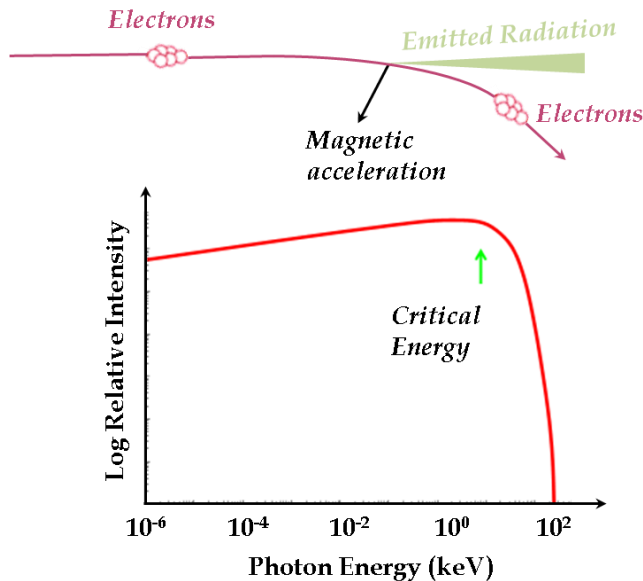


**Figure 3-3.** Schematic representation of X-ray generation of accelerated charged particles and resulting X-rays spectrum.

In the following paragraphs a description of the two great groups of X-ray generation systems (X-ray compact sources (tubes) and synchrotron large facilities) is addressed.

### ○ *Conventional Laboratory X-ray Sources*

The main working principle of this kind of X-ray radiation generator is the strike of free electrons against a metal target thanks to a high voltage. In 1913 Coolidge source was invented. In this design the electron source was an incandescent filament. In this case the target (anode) was inside a glass tube under vacuum which allowed increasing the tube current and consequently the density of photons emitted. In addition, in this setup the acceleration voltage was tuneable and therefore the energy of the beam. In fact, some of the actual compact X-ray tubes are still working under this principle including improved components. The main limitation on this kind of X-ray source was the heat generated into the target that might lead to the anode melting. To overcome this issue, different cooling systems were implemented until the establishment of the rotating anode. This improvement permitted distributing the generated heat and thus increasing the power of the X-ray sources (kW).

Furthermore, due to the intrinsic conic geometry of the generated beam in these systems, depending on the spot size blurring artefacts could appear limiting the spatial resolution. For this reason, in order to improve the spatial resolution the main goal has been downsizing the focus area and thus reducing the size of the blurring area (Figure 3-4).

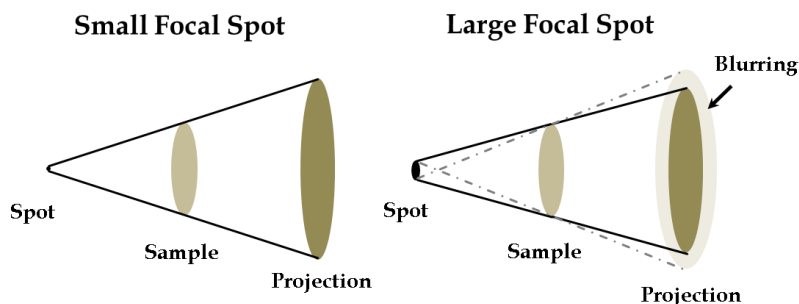


**Figure 3-4.** Effect of focal spot size on spatial resolution for cone-beam configuration.

Mini, micro and sub-micro (nano) focus sources are nowadays available focusing the electrons onto a reduced zone of the target. As a consequence, the intensity current decreases proportionally to the spot area reducing the available number of photons. Latest developments to increase the X-ray flux in micro and nanofocus sources are basically focused on targets with improved heat dissipation. In this sense, liquid anode technology is based on liquid metal target continuously circulating providing optimum thermal dissipation and thus powerful X-rays from a quasi-punctual source.

- *Synchrotron Sources*

Alternatively, as mentioned before, X-rays can be generated in synchrotrons. A synchrotron machine exists to accelerate electrons to extremely high energy and then make them change direction periodically. The resulting X-rays are emitted (Figure 3-3) as dozens of thin beams, each directed toward a beamline next to the accelerator. The electrons are kept in the Storage Ring in which they circle for hours close to the speed of light. The tube is maintained at very low pressure (approx.  $10^{-9}$  mbar) in order to avoid undesired collisions. The electrons pass through several types of magnets in their trajectory producing X-rays (Figure 3-5). On one hand, **Undulators** (short period) and **Wrigglers** (large period) are magnetic structures made up of a complex array of small magnets and force the electrons to follow an undulating trajectory. The radiation emitted at each consecutive bend overlaps and interferes with that from other bends. This generates a much more focused, or brilliant, beam of radiation than that generated by a single magnet roughly in proportion to the number of magnets [8]. Also, the photons emitted are concentrated at certain energies (called the fundamental and harmonics). The gap between the rows of magnets can be changed to fine-tune the wavelength of the X-rays in the beam. On the other hand, **Bending Magnets** (Figure 3-5) bend the electrons into their racetrack orbit. However, as the electrons are deflected from their straight path when passing through these magnets, they emit a spray of X-rays tangentially to the plane of the electron beam. The synchrotron light from a bending magnet covers a wide and continuous spectrum, from microwaves to hard X-rays, and it is much less focused, or brilliant, than the fine beam of X-rays from an Undulator or Wiggler.

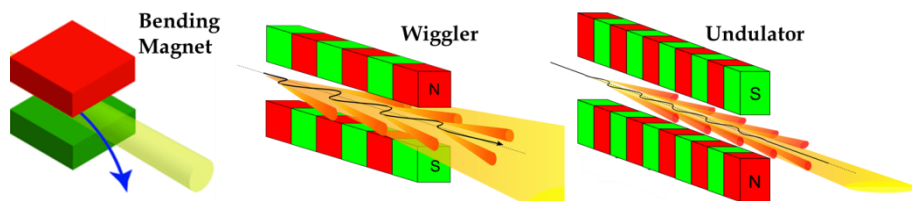


**Figure 3-5.** Different magnetic devices present on synchrotron facilities.

During the last decades a large number of synchrotron facilities have been built across the world. Synchrotrons have been developed from first to third generation rapidly increasing brilliance of these radiation sources [9-11].

Furthermore, X-rays are generated in synchrotrons far from the sample position leading to quasi-parallel configurations avoiding the influence of the focal spot size and enabling high resolution experiments using lenses to obtain small effective pixel sizes. In addition, even smaller pixel sizes can be achieved by using X-rays microscopes that allow reducing further the effective pixel size (nm) focusing the X-ray beam.

### 3.1.2 X-ray-matter interaction

The interaction of X-rays with matter is linked to the complex refractive index ( $n$ ) of the involved materials, with real and imaginary parts containing the principal parameters dominating phase and absorption contrast respectively (Equation 3-1) [12].

$$n = 1 - \delta + i\beta \rightarrow \begin{cases} \mu = \frac{4\pi\beta}{\lambda} \\ \phi = \frac{2\pi\delta}{\lambda} \end{cases} \quad \text{Equation 3-1}$$

Where  $\mu$  is the attenuation coefficient,  $\phi$  is the phase shift and  $\lambda$  is the radiation wavelength. Absorption is represented as the attenuation in the intensity of the X-ray wave when passing through the material whereas phase contrast provokes a phase shift on it (Figure 3-6). Comparing the magnitude of both contributions, phase contrast generate 10-1000 times more signal, but requires coherent illumination [13-

15]. This fact is employed for either reducing the radiation dose or increasing the sensitivity.

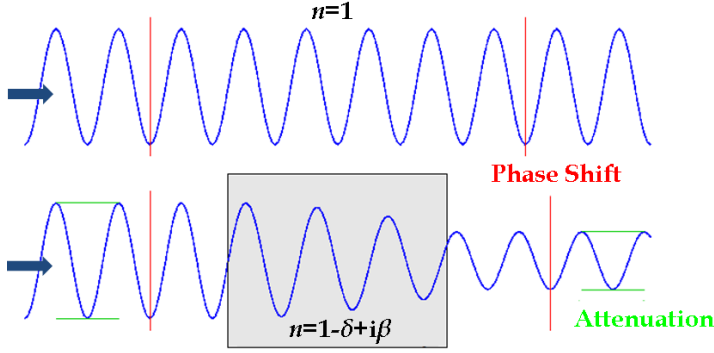


**Figure 3-6.** Attenuation and phase shift of X-ray wave propagating in medium with complex index of refraction.

#### ○ Absorption

Absorption contrast imaging is the most common imaging technique. An absorption contrast image is essentially a shadowgraph, the contrast being generated by the different attenuating power of materials and their thicknesses in the sample. The physical fundamentals of radiation absorption are based on Beer-Lambert law (Equation 3-2). This expression predicts the attenuation of incident monochromatic X-ray radiation by an exponential function of the linear absorption coefficient ( $\mu$ ), the element concentration ( $c$ ) and the thickness ( $t$ ). In case of heterogeneous materials and/or polychromatic X-rays, an effective attenuation coefficient ( $\mu_{eff}$ ) is usually considered. In addition, in order to eliminate the influence of material density, the mass attenuation coefficient,  $\mu_m$ , is introduced ( $\mu_m = \mu_{eff}/c$ ).

$$I = I_0 \exp(-\mu_{eff} ct) = I_0 \exp(-\mu_m t) \quad \text{Equation 3-2}$$

The attenuation coefficient varies with incident energy and basically with atomic numbers of elements in scanned object (Figure 3-7). On one hand, the lower is the energy of X-rays, the higher is the attenuation coefficient and therefore also the X-ray absorption. On the other hand, roughly speaking, materials with high atomic number

such as metals stop X-ray radiation, whereas materials with low atomic number (oxygen, carbon, hydrogen, nitrogen...) are almost transparent to X-rays.

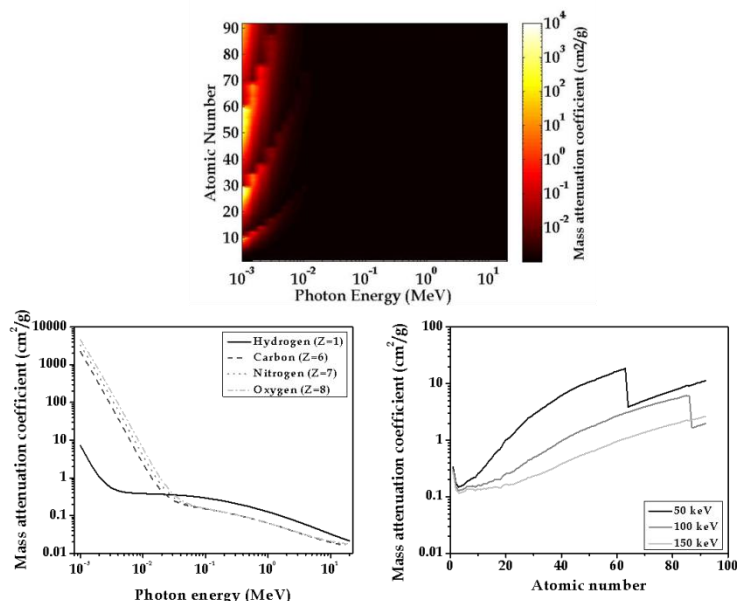


**Figure 3-7.** Dependence of mass attenuation coefficient with both atomic number and incident radiation energy. General view –up- and particular cases –down-.

## ○ Phase contrast

The phase of the waves travelling through the sample contributes to the modulation of the detected intensity in an X-ray phase-contrast imaging system. It is not possible to directly measure the phase of electromagnetic waves at optical frequencies and above, however, phase effects can play a significant role in the image formation also in the hard X-ray regime. Phase-contrast imaging techniques exploit the phase perturbations introduced by the sample to modulate the intensity recorded at the image receptor [16]. The simplest approach is the so-called **Free-space Propagation** [17-19] (Figure 3-8). According to this approach, the introduction of an appropriate distance between the sample and the detection system ( $R_2$ ) can be sufficient to make phase effects detectable. This phenomenon for a pure phase object is interpreted in terms of Fresnel diffraction (Equation 3-3).



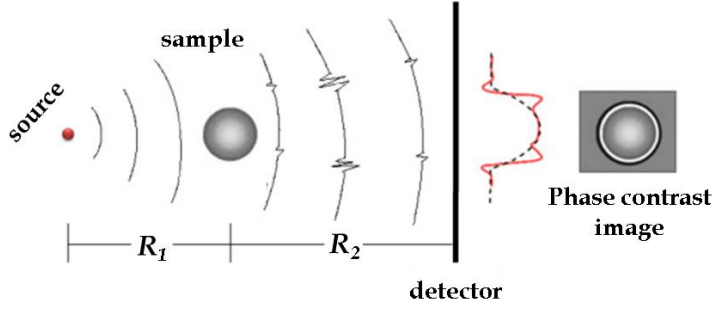


**Figure 3-8.** Schematic of the Free-space Propagation phase contrast.

$$I = \frac{I_0}{M^2} \left[ 1 + \frac{R_2 \lambda}{2\pi M} \nabla^2 \phi \right] \quad \text{Equation 3-3}$$

Where  $M=(R_1+R_2)/R_1$  is the geometrical magnification and  $R_1$  is the distance between source and sample,  $\phi$  is the phase shift and  $\lambda$  the radiation wavelength. The contrast from a pure phase object vanishes when  $R_2 \rightarrow 0$  and the phase term is directly proportional to the propagation distance  $R_2$ . In addition, the monochromaticity of the radiation is not essential for this type of imaging. A necessary condition, however, is that the radiation must have a certain degree of spatial coherence [15, 20] (Equation 3-4).

$$l_c = \frac{\lambda R_1}{\sigma_s^2 \sqrt{2 \log 2}} \quad \text{Equation 3-4}$$

where  $\sigma_s$  is the standard deviation of the source intensity distribution. The coherence length ( $l_c$ ) has to be comparable to or larger than the inverse spatial frequency of the feature of interest [21] in order to obtain significant phase contrast. In practice this means that the source has to be small or that the object must be placed at large distance  $R_1$  from it. Another requirement is that the imaging system must have spatial resolution high enough to not wash out the interference fringes.

The intensity projection image will contain a mixture of contributions from both the absorption and the phase shifts in the sample. Other experimental parameters, like the X-ray energy, the geometrical magnification, the radiation coherence and the system resolution, determine the modulation of intensity at the detector. The process that

calculates phase and amplitude at the exit surface of the sample is called **phase retrieval** [22, 23]. Quantitative retrieval algorithms are also a fundamental component for accurate three-dimensional reconstructions [24]. The determination of both amplitude and phase requires more than a single measurement (by changing either the propagation distance or the energy) unless some constraints can be imposed on the sample.

Other imaging techniques using phase contrast are interferometry [25], analyser based imaging [26] and edge illumination [27]. The latter has been investigated in recent years as a possible way forward for the translation of phase-sensitive imaging techniques into mainstream applications by using two different apertures (or masks), before and after the sample even in conventional X-ray systems [28, 29]. The first mask allows separating the polychromatic beam in series of independent beamlets. Combined to the second mask, this technique has negligible spatial or temporal coherence requirements [30] providing high sensitivity on laboratory implementations.

### *3.1.3 X-ray detection*

Once the X-ray radiation passes through the object, the last step of the imaging process consists on collecting the transmitted radiation and converting it into a readable signal. Nowadays, there are a lot of detection systems depending on the required application. In particular, X-ray detectors for imaging purposes can be divided in two groups depending on the used technology for the conversion of X-rays to electrical signals (intensity currents) representing the X-rays intensity distribution (Figure 3-9). On one hand, in indirect detection a scintillating material converts X-ray photons into visible light by luminescence process. Then, a secondary system (CCD, photodiode) converts the visible photons into electrical current intensities. This detection principle is predominantly used in X-ray imaging since the energy response of the detector can be easily optimized varying the scintillating material and its thickness. In addition, the great variety of detector of light in the visible range permits selecting the best option in each case. Some common scintillating materials are

### 3. X-ray Imaging and Image Analysis

ceramics, phosphor (P), silicium (Si), cesium iodide (CsI), etc. One of the main disadvantages of this detection technique is that spectral information is lost and the light scattering inside the scintillator strongly limits the resolution. Doping scintillators with rare earths or fluorescent ions permits increasing the quantum efficiency of the scintillator (emit more light photons per X-ray photon) and therefore reducing scintillator thickness improving the final image quality. Typical examples of such kind of scintillator materials are Cerium-doped Lutetium Yttrium Orthosilicate (LYSO), Cadmium Tungstate (CWO) and Gadolinium Oxysulfide (GOS). On the other hand, the direct detection is based on materials that convert directly the X-rays to intensity currents (sensitive layers or photoconductors) such as amorphous selenium or Cadmium Telluride (CdTe). This mechanism counts every single photon and its energy avoiding light scattering of indirect detection, increasing quantum efficiency and maintaining the spectral information, but the X-ray flux needs to be low in order to match the frame rate of the used electronics avoiding in this way the overlap of photons in the acquired signal.

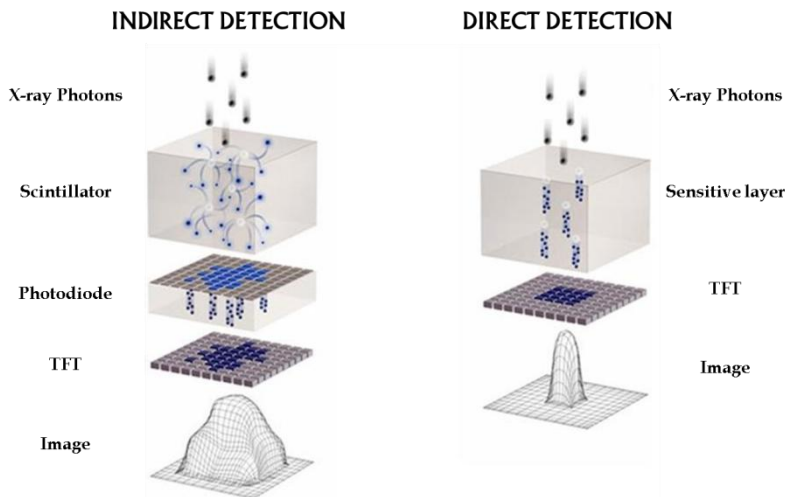


**Figure 3-9.** Scheme of main steps of X-ray detection for indirect and direct detection systems.

### 3.2 X-ray Computed micro Tomography ( $\mu$ -CT)

X-ray tomography, also known as CT (Computed Tomography) is a non-destructive technique which provides 3D information of materials [31]. The micro-structure characterization must be carried out at the relevant scale. X-ray Tomography permits the inspection from centimetres to few microns, the so-called micro-Tomography ( $\mu$ -CT). It is consequently very attractive in materials science to study the structure of materials. X-ray tomography is employed in several research topics besides materials science such as in medicine, in paleontology, archeology [32-34].

Nowadays, X-ray tomography can really compete with classical optical and electronic microscopy techniques due to several reasons:

- The technique is non invasive and there is no need for sample preparation like polishing or metal deposition.
- Very brittle samples can be easily handled.
- In situ tests can be monitored on the tomography stage (depending on resolution and kind of test).
- Spatial resolution is up to 1  $\mu$ m in lab-scale equipments and ever further in novel devices.
- And the most important is obtaining representative data in 3D.

The general concept of X-ray tomography is an extension of classical X-ray radiography, and is based on the attenuation of the X-ray beam through the specimen. X-ray radiography provides only a projection of the sample volume on one single plane. X-ray tomography overcomes this disadvantage by combining the information from hundreds of radiographs, each being recorded with different orientation of the sample in front of the detector. The variation of X-ray attenuation in the volume of the sample can be reconstructed by combining a sufficient number of radiographs with an appropriate algorithm. The data is obtained in the form of a 3D array of voxels, for

which the grey-level of each voxel describes the calculated X-ray attenuation at that position. A detailed description of all the involved steps in the tomography process (Figure 3-10) is addressed hereinafter.

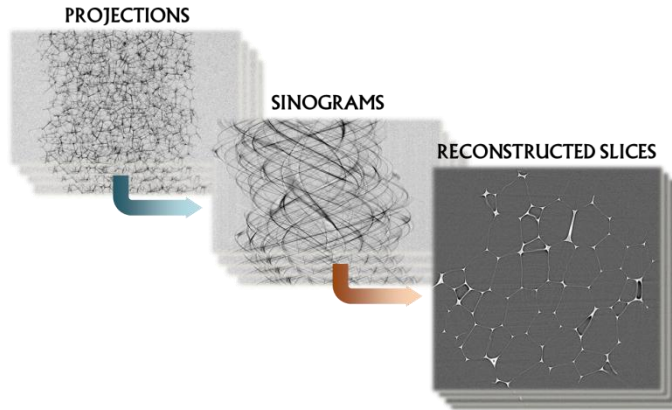


**Figure 3-10.** Main steps of the tomography process. Projections acquisition, sinograms generation and reconstruction.

#### 3.2.1 Acquisition

The first step of every tomography experiment is the **acquisition** of the so-called projections, each of the radiographs of the scanned sample at different angles. It is the crucial step since optimum raw data leads to suitable reconstructed results. To this purpose, several parameters play an important role: beam conditions (voltage and current), detector exposure time, number of projections and the acquisition mode (single projection or multiple projection integration).

Firstly, depending on the characteristics of the scanned sample (geometrical dimensions and constituents) mainly voltage but also current should be adapted to achieve the maximum contrast in every projection using as a consequence most of the dynamical range of the detector. In this sense, several efforts have been carried out in order to establish simple criterion to select suitable illumination conditions. One of the most representative methods is the following [35]. Considering an irregular sample, the normalized transmissivity (defined as the intensity divided by the intensity

without sample) on the thickest part of the sample ( $T_n^{thick}$ ) should be always below 0.37 and on the thinnest part of the sample ( $T_n^{thin}$ ) should be above 0.37. In addition, in an ideal case both values should be related (Equation 3-6).

$$T_n^{thick} \ln(T_n^{thick}) = T_n^{thin} \ln(T_n^{thin}) \quad \text{Equation 3-6}$$

The second parameter affecting final quality of projections is the exposure time on the detector [36]. Increasing exposure time typically increases the image contrast. However, in addition to the extension of experiment time, increasing exposure time could provoke the grey level saturation on the detector. To solve this issue and maintain the good contrast the common practice is the integration (sum or average) of several identical radiographs with moderate exposure time to form each projection. As a result, since the noise in the images is random contrast becomes optimized.

Finally, it has been broadly studied the influence of the number of projections on the final reconstructed volume [37]. As the number of projection increases, more angular information is available thus facilitating the final reconstruction without unexpected noise (Figure 3-11).

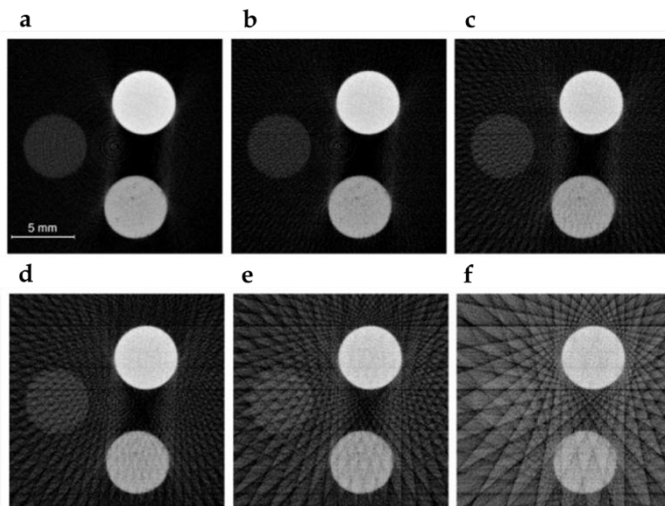


**Figure 3-11.** Six CT reconstructions of Perspex, aluminium and plaster cylindrical samples reducing the number of projections. a) 180 b) 90 c) 60 d) 45 e) 30 and f) 18.

However, depending on the magnification (or effective pixel size) and due to blurring distortions we have found that the optimum number of projections starts at 250-300 for  $M=1$  to 1200-1500 for  $M=20$  for  $360^\circ$  rotation scanning. The number of projections is theoretically defined as  $\pi x N/2$  where  $N$  is the number of horizontal pixels of the detector, roughly 1.5 times the number of detector row pixels for  $180^\circ$  scans, and  $\pi x N$  for  $360^\circ$  scans since with that number of projections the Fourier space is filled along radial lines (Fourier Slice Theorem) [38, 39].

#### 3.2.2 Projection correction

There are still several artefacts to consider and correct prior to continue the tomography reconstruction: irregularities on the detector and changes in illumination conditions during the acquisition of projections.

- *Defective pixel*

Assuming an expected linear response of the detecting system with radiation excitation a defective pixel can be defined as the one deviating from linearity. A good criterion is identifying those above or below certain threshold (90-98%). Two different kind of defective pixels are identified: dead pixels (without response) and hot pixels (excessive response or without excitation). They can appear individually or forming defective lines. These pixels are corrected from the image by software manipulations of the proper acquisition software by interpolation.

- *Background and Shading*

Background and Shading corrections are used in order to correct the beam profile and scintillator, taper or detector imperfections. In addition, they are necessary to correct various detector imperfections, among which dark current, read-out noise and ADC offset (Figure 3-12). To this end two different sets of images (with the same acquisition parameters) are always acquired in addition to the tomography projections: background images (also called darkfields, dark images or offset images) and open beam images (also called flatfields or beam profile images). Background intensity ( $I_B$ )

is subtracted to remove floor noise from the image intensity ( $I$ ). Then normalization is done by flatfield ( $I_F$ ) with the background subtraction, the so-called shading image. This shading image should represent the sensitivity variation of the system, which you want to account for (Equation 3-7). Several background and flatfields are acquired and then averaged to improve the results. In systems with beam stabilization problems, collections of both correction images should be acquired during the tomography scan process.

$$I_{corrected} = \frac{I - I_B}{I_F - I_B} \quad \text{Equation 3-7}$$

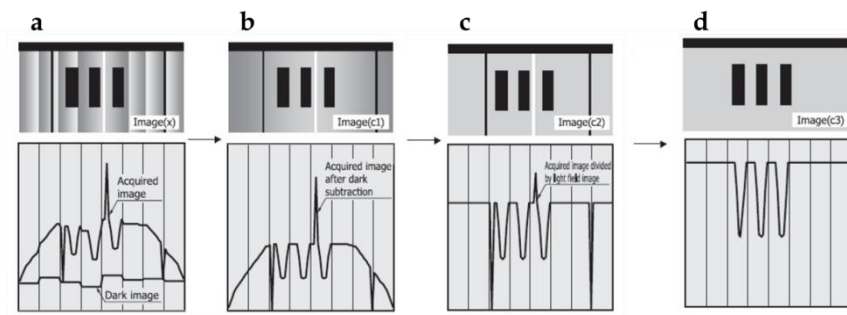


**Figure 3-12.** Application of different corrections on test image. a) Pure image b) image after background correction c) image divided by flatfield image and d) image corrected with both background and shading corrections.

○ *Intensity normalization*

The intensity normalization is carried out if the source intensity is not perfectly stable. The easiest way to perform this correction is selecting a region on the detector free of sample shadow during the whole tomography process. The average intensity of this region is used to calculate an arbitrary value of the source intensity evolution with time. This region should be selected with care since scattering of radiation from the object can influence the background signal.



- *Spot filter*

The spot filter is a median filter (changing the intensity value of one pixel by the median value of the neighbour pixels) acting on those pixels that deviate more than a certain level from the neighbouring pixels.

- *Ring filter*

Inaccurate corrected defective pixels provoke the apparition of rings into the final reconstruction slices. For these reason, this type of filter is denominated ring filter. In it, a combination of median and mean filters is applied in the projections. The level of these filters must be selected carefully since a level that is too high can overcorrect and introduce new rings.

#### 3.2.3 Sinograms

The next step of the tomography process consists on the generation of the so-called sinograms, the Radon transform of the scanned object and the base of the tomography reconstruction algorithms. Sinograms are the image principle encoding in tomographic reconstruction and consist on a visualization of the projections represented in other coordinate system. Considering an object represented as a function  $f(x, y)$ , it is projected in the detector as a projection  $p(s, \phi)$ . Changing the space from  $(x, y)$  to  $(s, \phi)$  projections are transformed into sinograms (Figure 3-13).

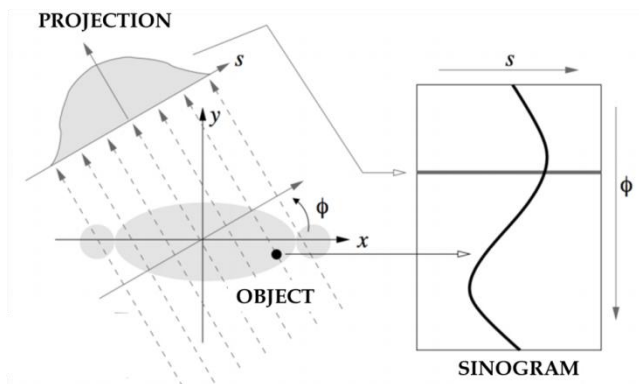


**Figure 3-13.** Basic example of transformation between projections and sinograms.

### 3.2.4 Reconstruction

The reconstruction is the last step of the tomography process that allows obtaining the slices of the scanned object. In each slice (or in the whole volume) a distribution of the linear attenuation coefficients  $\mu(x,y,z)$  of the sample is determined. This can be accomplished mainly in two ways:

- *Direct analytical inversion*: solve  $N$  equations with  $N$  unknowns simultaneously providing an exact solution.
- *Iterative reconstruction*: minimizing the error after comparison between original projection and the pseudo-projection provided by the reconstruction.

The first one (found in 1917) is numerically impractical due to the finite number of detector points available. For this reason novel theorems dealing with these constraints have been developed over the years being the origin of one of the most used nowadays algorithms, the so-called Filtered Back Projection (FBP) [40, 41]. On the other hand, Statistical Iterative Reconstruction (SIR) has been developed due to its accuracy mainly in applications in which it is required minimizing the radiation dose to the sample (and therefore number of projections) [42, 43].

Independently of the considered algorithm, the reconstruction process is accomplished following the steps below:

- The raw projection images coming from the detector are first filtered using a spot filter.
- These filtered images are then normalised by flat field (integrated if possible) and background images. In addition, the intensity changes from source are adequately corrected.
- The obtained images are now reordered in order to generate the sinograms.

### 3. X-ray Imaging and Image Analysis

- In addition, fine details such as adjustment of the exact centre of rotation or deviations on the detector (tilt and skew angles) (Figure 3-14), can be modified prior the final reconstruction of the object.

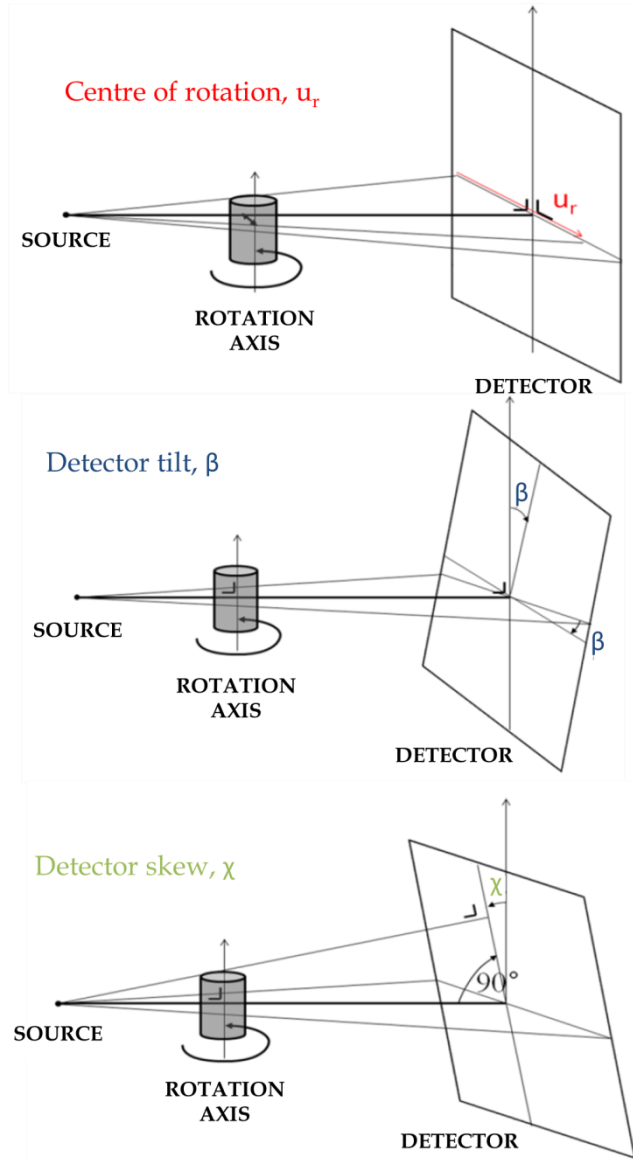


**Figure 3-14.** Fine adjustments prior the reconstruction in tomography.

○ Filtered Back Projection (FBP)

The Fourier Slice Theorem resulted essential to solve the reconstruction equation system. It states that the reconstruction of the object from its projections is possible by using Fourier transforms as long as the number of projections (angles) fills the Fourier space along radial lines. Collecting projections from 0° to 180° can fill the entire Fourier space, but in cone-beam geometry 360° are covered to minimize the distortions induced in the projections due to beam geometry and thus improving the final reconstruction. Finally, the scanned object is recovered by the inverse Fourier transform. In order to exemplify these statements we can consider a 2D object as the cross section of a 3D object and the following definitions:

$f(x,y)$	2D Object
$R[f(\rho, \phi)]$	1D projection of $f(x,y)$ at angle $\phi$ (Sinogram – Radon Transform)
$F[f(v, \phi)]$	2D Fourier transform of $f(x,y)$ in polar coordinates
$F_p([Rf(v, \phi)])$	1D Fourier transform of the projection $Rf(\rho, \phi)$ in polar coordinates at angle $\phi$

Hence, the Fourier Slice Theorem states that the Fourier transform of the sinogram is linked to the Fourier transform of the original projection (Figure 3-15) (Equation 3-8).

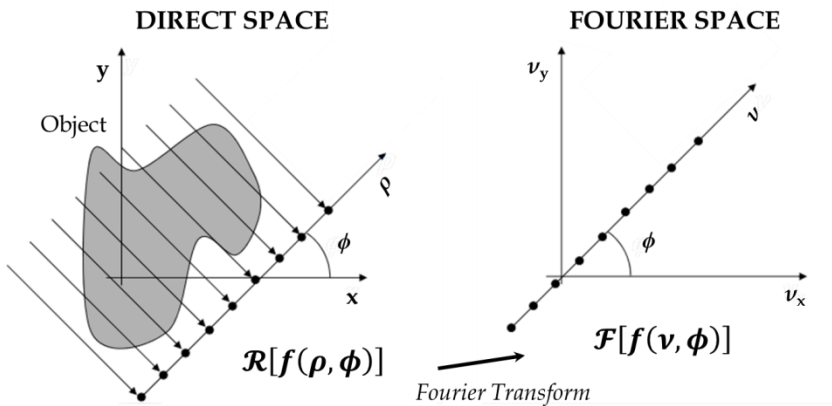


**Figure 3-15.** Schematic representation of the main statement of Fourier Slice Theorem.

$$\mathcal{F}_\rho\{\mathcal{R}[f(v, \phi)]\} = \mathcal{F}[f(v, \phi)] \quad \text{Equation 3-8}$$

From this theorem, the bases of the **Filtered Back Projection (FBP)** algorithm are easily derived. In this algorithm, the spreading and sum (Back Projection) over the full Fourier space (over 180°) of the inverse Fourier transforms of the sinograms, adequately filtered with a high-pass filter in order to suppress background and thus enhance sample contrast, permit the reconstruction of the scanned object (Equation 3-9).

$$f(x, y) = \frac{1}{2\pi} \int_{-\pi}^{\pi} \mathcal{F}_\rho^{-1}[\mathcal{F}_\rho\{\mathcal{R}[f(v, \phi)]\} \#(v)] d\phi \quad \text{Equation 3-9}$$

**FDK** (Feldkamp, Davies and Kress) reconstruction algorithm is the mainstream method in practice to develop FBP reconstructions [44] mainly in cone-beam configurations.

#### ○ *Statistical Iterative Reconstruction (SIR)*

The iterative reconstruction algorithm first synthesizes forward projection and mathematically compares and corrects the actual measurement with the measured projection at the detector. The technique then iterates this comparison and correction step to achieve close proximity between actual and measured projections. These algorithms incorporate a better statistical noise model, which uses noise information in the measured projection data to accurately model the behaviour of attenuated photons and electronic noise (referred to as photon and noise statistics, respectively). These algorithms also include accurate mathematical information of actual focal spot size, detector size and shape, and image voxel shape (referred to as the system optics). Inconsistencies in the projection measurement owing to limited photon statistics and electronic noise are corrected with multiple iterations. The forward projection and multiple iterative corrections lead to increase in reconstruction time (100 times higher than FBP) but help to lower image noise and artefacts [45].

A pure iterative reconstruction technique includes mathematical probability likelihood functions to compute a more accurate noise model as well as a forward

model or a projector, which is mathematically more complex and accurate. These algorithms also incorporate prior functions, which take into account prior appropriate information about the image reconstruction and the CT imaging system such as actual focal spot size, image voxel model, exact detector size, raw data statistics, and the desired image behaviour. These techniques compute a cost function to include all of the above inputs and perform the optimal number of iterations to generate a final desired CT image as output under a convergence criterion or after a predetermined number of iterations is performed (Figure 3-16) [46].

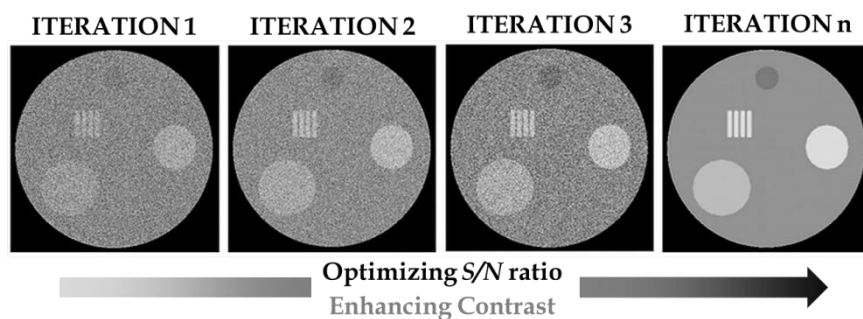


**Figure 3-16.** Several iterations on the iterative reconstruction of a test sample until the convergence criterion is reached.

Finally, comparing the two mentioned reconstruction algorithms FBP permits obtaining reconstructed information without very specific computation requirements. Moreover, reconstruction process is accomplished in moderate computation times (few seconds in GPU). However, in order to achieve ideal results a lot of projections are required therefore increasing the radiation dose in the sample. On the other hand, SIR allows obtaining very good results with few raw information, but requiring more computation power and reconstruction time.

### ○ *Reconstruction artefacts*

Some specific artefacts occurring in X-ray Tomography are briefly described in the following paragraphs. Ring artefacts, beam hardening, metal and scattering artefacts

are addressed. There are strategies to solve them that imply the slice modification both before and after the reconstruction process [47].

**Ring artefacts** result from pixel deviation due to miss-calibration. This is usually caused by imperfections in the scintillating detectors [48] (Figure 3-17). They are concentric rings centre around the rotation axis. They can be corrected by filtering the image during the reconstruction process. In some cases, an additional correction after the reconstruction process is required to avoid this artefact. The reconstructed slices are translated to polar coordinates, in which ring artefacts become vertical stripes. Then, a stripe-wavelet filter is applied in order to suppress the lines. Finally, the images are retranslated to the Cartesian space to recover the original image, but without rings [49].

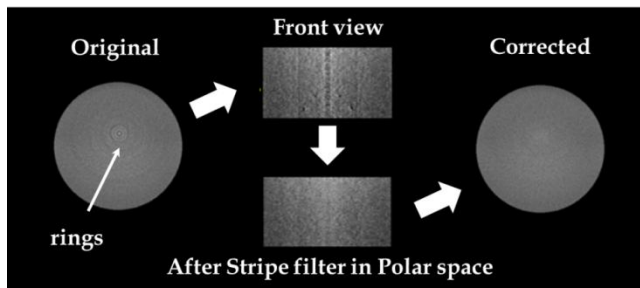


**Figure 3-17.** Ring artefacts and typical protocol to post-process the reconstructed slices to correct them.

Beam hardening is the result of the dependence with energy of attenuation coefficient when using polychromatic illumination [50, 51] (Figure 3-18). Since the attenuation coefficient is higher for low energies, low energy photons are attenuated by samples more frequently than high energy ones. As a consequence, the transmitted beam contains a higher proportion of high energy photons. The effect is conceptually similar to a high-pass filter. Beam hardening may result in two characteristic artefacts: streaking (dark bands) and cupping. Streaking artefact appears as multiple dark streaking bands positioned between two dense objects whereas cupping artefact refers to a falsely bright appearance along the periphery of an object. Since higher energy photons are less attenuated by tissue, the beam will be less attenuated versus identical

tissue near the skin entry site. If uncorrected during CT reconstruction, these differences in expected attenuation profile lead to a peripherally dense appearance.

Beam hardening is usually corrected by using filters of an attenuating substance (often metallic) that harden the beam before it reaches the sample. In addition, there are image methods that substitute every value of the natural logarithm of the sinograms ( $s$ ) with the corresponding value of a 5<sup>th</sup> polynomial whose four parameters ( $a_i$ ) can be adjusted (Equation 3-10).

$$s' = s + a_0s^2 + a_1s^3 + a_2s^4 + a_3s^5 \quad \text{Equation 3-10}$$

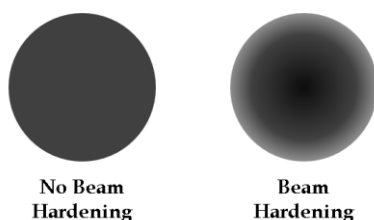


**Figure 3-18.** Schematic view of a cylindrical sample with and without Beam Hardening artefact (cupping).

In the presence of high attenuation objects, the reconstruction algorithms such as FBP give rise to streak and star artefacts, condensed as **metal artefacts** [52] (Figure 3-19). The metal artefact reduction (MAR) algorithms can be divided mainly in two classes: the projection completion based methods and the statistically based iterative methods that interpolates the missing data using the neighbouring projections.

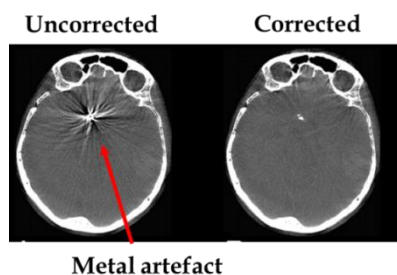


**Figure 3-19.** Metal artefact and corresponding corrected slice.



Finally, the additional share of scattered X-rays during the acquisition of projections may result in increased measured intensities, since the scattered intensities add to the primary intensity. As a result, in the final reconstruction an underestimation on the attenuation coefficient takes place, known as **scattering artefact** [53]. The reconstructed error is dependent on the object and is proportional to the amount of scatter present. Scatter causes streak artefacts in the reconstruction that are very similar to those caused by beam hardening.

### 3.3 $\mu$ -CT device at CellMat

The X-ray system of CellMat laboratory was built as part of a previous PhD. Thesis [54]. The critical elements are the X-ray tube (microfocus L10101 from Hamamatsu photonics, Japan) and flat panel detector (C7940DK-02 also from Hamamatsu). Both elements were carefully selected since polymers are low absorbing materials. To overcome this constraint, low energy X-rays are required in order to guarantee enough contrast in the images. For this reason, the spectral response of the selected detector should be focused on the low energy range to maximize the sensibility and efficiency. Moreover, dimensions of cellular structure are in the order of microns and therefore high spatial resolution is also relevant, needing small focus spot size and small pixel size in the detector. In addition, tomography experiments are carried out by locating a high precision rotation stage (DT-65 N from PI miCos, Germany) between source and detector.

#### 3.3.1 X-ray Source

A closed air-cooled micro-focus X-ray source is the X-ray generator. The main technical characteristics of the X-ray source are summarized in table 3-1. In this tube an ultrafine electron beam strikes on a tungsten target in high vacuum atmosphere. The tungsten anode, irradiated by the electrons, produces X-rays. X-rays come out the source through a Beryllium 150  $\mu\text{m}$ -thick window forming an X-ray cone-beam of  $39^\circ$  of aperture. The micro-focus spot size of 5  $\mu\text{m}$  tends to slightly broaden as electron acceleration voltage or current become increased up to a maximum of 20  $\mu\text{m}$ . Nevertheless, the spot size remains in its minimum size for values below 40% of its maximum power (20 W). In addition, the maximum intensity is limited by the produced voltage (Figure 3-20).

**Table 3-1.** Technical characteristics of Hamamatsu L10101 X-ray source

Spot size ( $\mu\text{m}$ )	5-20
Voltage (kV)	20-100
Current ( $\mu\text{A}$ )	0-200
Maximum output power (W)	20

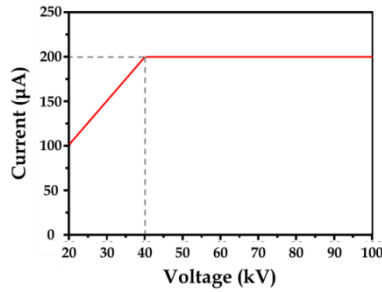


**Figure 3-20.** Maximum output power curve of the X-ray source.

#### 3.3.2 Flat Panel detector

This high resolution detector is composed by a matrix of  $2240 \times 2344$  pixels<sup>2</sup> with a pixel size of  $50 \mu\text{m}$  (therefore  $111.50 \times 117.20 \text{ mm}^2$ ). The digital output is a 12 bits depth resolution (4096 real grey levels) with maximum acquisition velocity up to 9 fps working at  $4 \times 4$  binning mode. In this detector, the CsI scintillator layer is directly grown over the CMOS detector. In this way the light transmission is maximized reducing light scattering resulting in high sensibility of the detected X-rays. It is important that the diameter of the grown scintillator material is smaller or similar than CMOS pixel size. Further, the detector area is covered by a 1 mm-thick carbon fibre plate. The communication between detector and CPU is accomplished using a frame grabber (Dalsa-Coreco, USA).

X-ray tube and detector are located in front of each other inside a lead shielded cabinet (Figure 3-21).

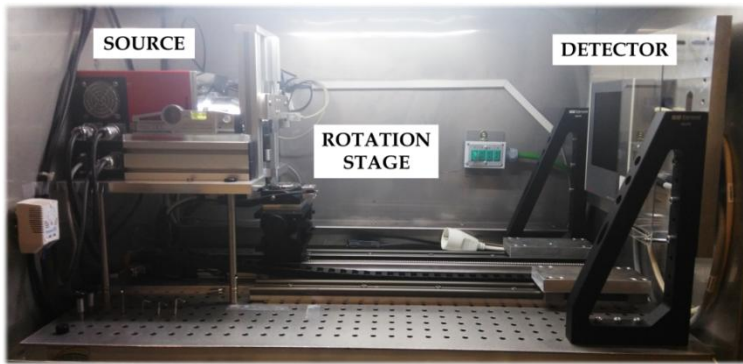


**Figure 3-21.** X-ray system at CellMat laboratory.

Due to the conical spread of the X-ray beam, source-detector distance ( $SDD$ ) could be in the range 0.3-1.2 m. In our case, due to the spatial limitations marked by the cabinet,  $SDD$  is commonly fixed at 580 mm, becoming a compromise distance for all the involved factors such as beam intensity decay and apparition of artefacts. Thanks to a linear stage the scanned object could be placed at any position between source and detector thus changing the optical magnification factor ( $M$ ). Magnification factor is calculated considering the distances between source and detector ( $SDD$ ) and source and scanned object ( $SOD$ ) (Equation 3-11).

$$M = \frac{SDD}{SOD} \quad \text{Equation 3-11}$$

As magnification increases sample position in reference to the rotation axis plays a more important role. In addition, wobble of the rotation stage (and thus of the rotation axis) can become into a horizontal sample displacement during the scan that increases with vertical distance between rotation stage and sample position. These two facts can preclude the correct reconstruction of the tomography.

During this thesis, in order to avoid these two constrains and enhance the X-ray Tomography results the X-ray system has been optimized. On one hand, the position of the sample in the X-ray beam can be adjusted in height by a specific Z lab-jack that maintains constant and reduced the distance between sample and rotation stage, reducing therefore the wobble problems. On the other hand, the sample can be easily

### 3. X-ray Imaging and Image Analysis

placed on the centre of rotation by an X-Y micrometre table connected to the rotation stage (Figure 3-22).

These two updates in the X-ray system permit nowadays performing with ease and optimum contrast X-ray tomography at CellMat Laboratory with an effective pixel size of  $2.5\ \mu\text{m}$ .

Finally, all the functions corresponding to all the devices (source, detector, motors of the linear and rotation stage, etc.) have been counted in a unique application developed under LabView framework.

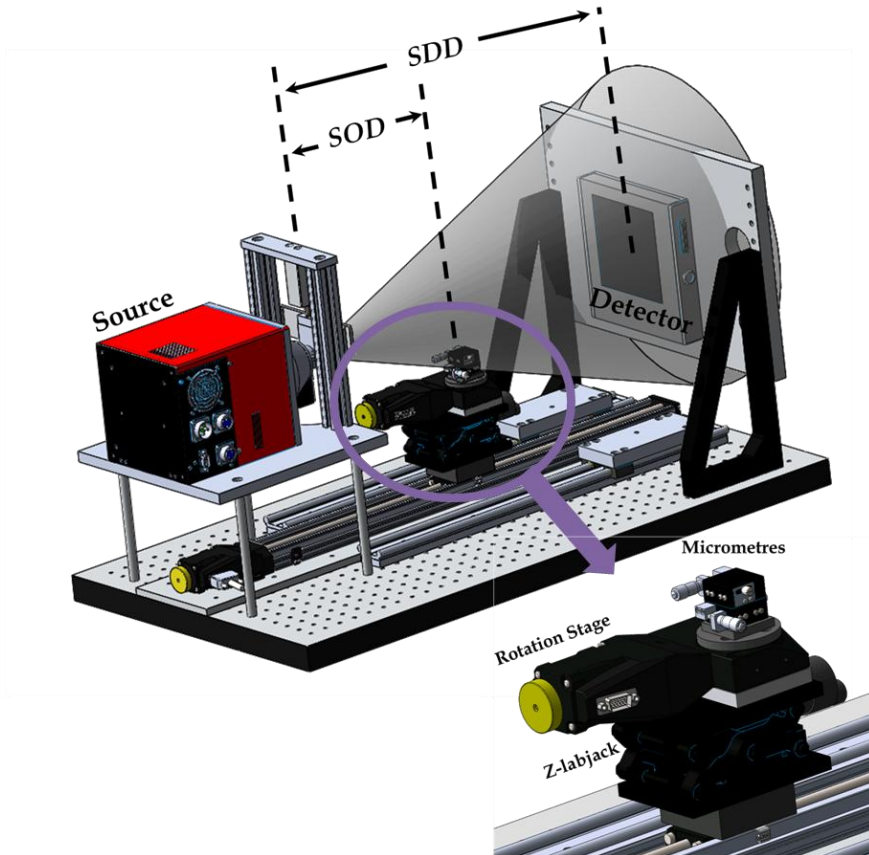


**Figure 3-22.** 3D rendering of the X-ray system indicating the distances required to calculate optical magnification and focused zone of the Z-labjack and positioning micrometres.

### **3.4 Synchrotron facilities**

Due to the limitations both in spatial and temporal resolutions offered by the X-ray tubes nowadays, part of the experimental work corresponding to this thesis was accomplished in synchrotron facilities such as Bessy II (Berlin, Germany), Diamond (Oxford, United Kingdom) or SLS (Villigen, Switzerland). In these facilities, due to the high brilliance, coherence and parallel geometry of the X-ray beam, experiments with extremely improved temporal and spatial resolutions are possible (up to 20 tomographies per second and effective pixel sizes in the nanometer range respectively). In the following paragraphs a brief description of the beamlines dedicated to imaging purposes of these synchrotrons is addressed.

#### *3.4.1 Bessy II. BAMline*

The beamline dedicated to imaging (among other purposes) in Bessy II synchrotron is called BAMline [55]. The synchrotron light coming from the superconducting 7 T wavelength shifter insertion device ( $10^{12}$  photons/s mrad<sup>2</sup> mm<sup>2</sup> 0.1%BW) can be monochromatized with a double multilayer monochromator (DMM) and/or a double crystal monochromator (DCM). Several polished metal foils placed in front of the DMM are used to absorb low energy X-rays improving monochromaticity (Figure 3-23). Several scintillating options are also available in this beamline (CWO, BGO, LuAG:Eu, LSO:Ce). Each scintillator screen (material and thickness) is carefully selected and used depending on the energy and type of performed experiment. Finally, light photons are collected by a great variety of CCD chips, selected also for optimizing the range of wavelength generated by the used scintillator. In our case, a collection of 20 tomographies of a great variety of materials, both solid and foamed, was performed with 0.44  $\mu\text{m}$  of effective pixel size. To this end, a PCO 4000 camera was used employing a 20x optical magnification system between scintillator and camera. The tomographies were acquired maintaining the sample-to-detector distance in 9 mm in order to reduce as much as possible phase contrast. The X-ray energy was fixed at 9.8 keV to maximize the attenuation of the X-rays. This fact, in conjunction with a high number of projections (2200 covering 180°) and long exposure time of the

projections (3000 ms) allowed us obtaining high spatial resolution tomographies in which is possible to clearly discern with valuable contrast even the thinnest parts of the solid phase of the scanned cellular polymers (**Chapter 4**).

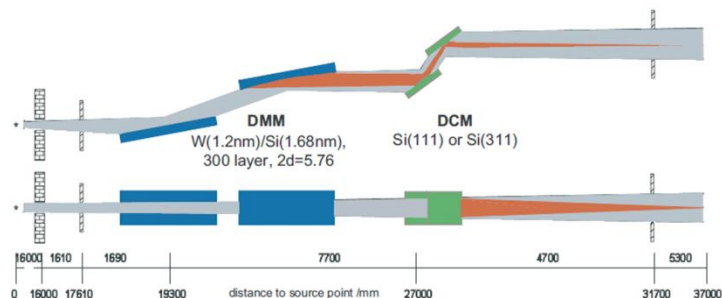


**Figure 3-23.** Layout of the X-ray beam path at BAMline (top: side view, bottom: top view) [55].

#### 3.4.2 Diamond Light Source. I13

The second synchrotron is Diamond Light Source in Oxford, United Kingdom in which a 3 months stay has took place. The beamline focused on imaging (and coherence) experiments is called I13 [56] (Figure 3-24). Diamond is a 3rd generation synchrotron operating at 3 GeV energy. I13 is located in one of the long straight sections of the storage ring, providing space for two insertion devices dedicated independently to the two branches (coherence and imaging). The brilliance (around  $10^{19}$ - $10^{20}$  photons/s  $\text{mm}^2$   $0.1\% \text{BW}$ ) can be significantly increased, especially at higher photon energies reducing the ID (undulator) gap (until 5 mm).

The divergence of the X-ray beam is  $50 \times 25 \text{ mrad}^2$  and its minimal size is about  $400 \times 12 \mu\text{m}^2$  and the length of the beamline (250m) provide parallel and coherent illumination to both beamlines. The deflecting optics (mirrors and monochromators) are placed horizontally to minimise deterioration of coherent beam. The energy of the beam is tuneable in the range 6-40 keV. For both branches the experimental floor is completely isolated from the building. Between hall floor, the concrete walls of the hutches and the experimental floor plate is a gap, the experimental floor plate is placed on concrete piles. Other peripheral such as air conditioning is isolated from the hutch, too. The

stability of the experimental floor in respect to the Diamond ring building is recorded with an autocollimator and a hydrostatic levelling system.

The imaging station is dedicated to micro- and nano-imaging with resolution up to 50nm. For micro-imaging the base technique is the in-line phase contrast with spatial resolutions up to 0.33  $\mu\text{m}$ . Adapted sample environments can be installed on separate experimental tables. It is for example possible to study samples under stress, pressure and at high or low temperatures. Improved spatial resolution is achieved by swapping a hard X-ray microscope (TXM) into the experimental setup similar to a visible light microscope. A condenser of the X-rays is matched to the aperture (order sorting aperture, OSA). After that, the X-rays pass through the sample reaching the Fresnel Zone Plate (FZP) acting as objective lens that allows increasing the spatial resolution up to 50 nm. Locating then a phase ring between FZP and detector marks the bases for the so-called Zernike phase contrast imaging [57, 58]. The details of this technique are summarized in Chapter 7.

On the other hand, the coherence branch is dedicated for imaging with the highest achievable resolution. For coherent X-ray diffraction (CXRD) and coherent diffraction imaging (CDI) the achievable resolution is neither limited by the detector nor by the X-ray optics. Under coherent illumination the sample produces a diffraction pattern at large distances (far field). Original structure and pattern are related through Fourier transformation and the object is reconstructed through iterative methods. The coherence length and therefore the illuminated field can be modified over a large range (1-200  $\mu\text{m}$ ) and can be further increased by scanning the focussing optic. The entire object is reconstructed then by a technique known in literature as “ptychography” (or scanning coherent diffraction imaging) [59-61]. A detailed description of this technique is included in the corresponding paper (**Chapter 7**).

During the research stay, both Zernike phase contract and ptychography tomography experiments were performed for the structural characterization, for the first time in 3D, of nanocellular polymers using effective pixel sizes around 100 nm.



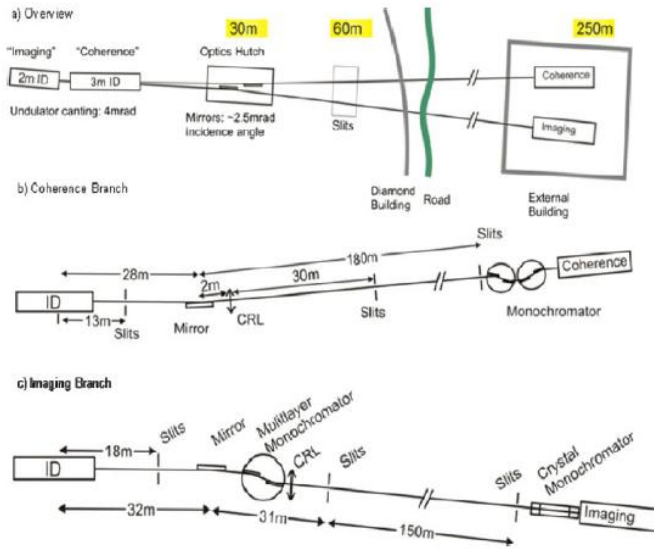


**Figure 3-24.** Layout of the two branches of I13 beamline [56].

#### 3.4.3 Swiss Light Source (SLS). TOMCAT

TOMCAT beamline offers a synchrotron radiation instrument for fast non-invasive, high resolution, quantitative investigations on diverse samples [62]. Dynamic processes can be followed in 3D here thanks to the new ultrafast tomographic endstation with sub-second temporal resolution thanks to the in-house developed GigaFrost system [63]. The X-rays source is a synchrotron beam from 2.9T superbend and the sample is placed 25 m far from it. Focal spot size is  $53 \times 16 \mu\text{m}^2$  and the photon flux is  $10^{13}$  photons/s 0.1% BW at 8 keV. This high flux is one of the main requirements to perform ultrafast scans. This is necessary to achieve successful tomogram reconstruction in a very short time. Absorption and phase contrast imaging are available at TOMCAT with isotropic voxel size ranging from 0.16 up to 11 microns with an energy range of 8-45 keV of monochromatic beam. Phase contrast is obtained with simple edge-enhancement, propagation-based techniques or through grating interferometry. In addition, the hard X-ray full-field microscope setup delivers a pixel size of 80 nm for microscopic samples (FOV  $50 \times 50 \mu\text{m}^2$ ). In addition, different endstations permit performing different kinds of experiments such as elevated

temperature *in-situ* Tomographic Microscopy, differential phase contrast imaging or nanotomography.

For fast tomographic applications, the rotation axis and detector system are of extreme importance. Synchronization between axis rotation and detector acquisition is crucial. In this case the maximum rotation speed of the high-precision stage is 600 rpm and by that the limit of the tomographic acquisition speed is set to 20 Hz (or tomographies per second). Typical acquisition times for a single tomogram are below 1s and complete tomographic sequences are usually on the order of few minutes. In this case, the *in-situ* evolution of the pore nucleation and growth in polyurethane nanocomposites (**Chapter 4**) was performed thanks to the 4D (3D+time) experiments carried out in the tomography endstation of TOMCAT (Figure 3-25).

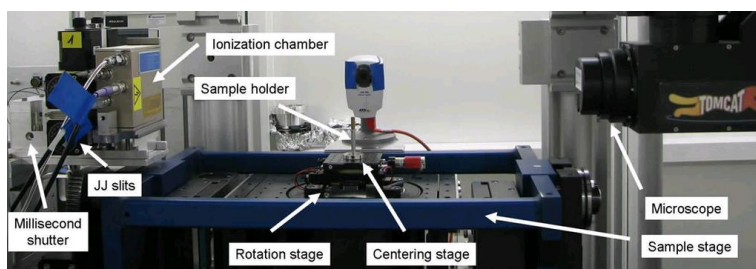


**Figure 3-25.** Endstation dedicated to Tomography in TOMCAT beamline.

## 3.5 Image analysis software

The analysis concerning the image processing of this thesis was accomplished using both commercial and open-source packages for image analysis. Each of them owns specific advantages and disadvantages. For this reason, a combination of all of them offers the perfect tools to achieve the specific goals of every steps of the image analysis. It is always necessary to keep in mind that a compromise between final quality, computing capabilities of the used machine and computation time optimization is always considered prior the selection of a specific software package.

### 3.5.1 *ImageJ/Fiji*

ImageJ/Fiji is an open source image processing package, bundling a lot of preinstalled plugins which facilitate scientific image analysis [64, 65]. It is an extensively used tool in comparison to closed commercial packages due to its versatility. In addition, it permits developing automated analysis macros enabling fast processing workflows. It was the basic tool during this investigation for filtering and binarizing, but recently also used for the analysis of the involved features (explained in the next section).

### 3.5.2 *Octopus*

During this investigation, two separated software packages developed by XRE NV (prior Inside Matters, Gent, Belgium) were used. On one hand, Octopus Reconstruction, which is one of the leading packages for reconstruction of tomography data [66]. It combines high performance reconstruction routines for parallel, fan and cone beam data with advanced artefact reduction methods and an intuitive graphical user interface. The Octopus reconstruction package was initially developed for the reconstruction of parallel beam neutron tomography data, and has evolved to one of the most versatile and performing packages for the processing of tomography data acquired in almost any geometry. All the reconstructions of the in-house  $\mu$ -CT were performed using Octopus Reconstruction.

On the other hand Octopus Analysis, formerly known as Morpho+ was used at the start of the thesis for the morphological analysis of the tomograms. It is a powerful 3D analysis software package due to its intuitive and user-friendly interface which provides quick access to the powerful algorithms implemented in the package and allows for a complete 3D analysis of very large datasets (>8 gigavoxel) [67].

### 3.5.3 *Avizo Fire/Amira*

Avizo/Amira is a general purpose commercial software application for scientific and industrial data visualization and analysis developed by FEI Visualization Sciences Group [68]. It enables to perform interactive visualization and computation on 3D data sets. It includes a large amount of different kernels for filtering, object separation algorithms, quantification tools and rendering for visualization. This software was used in this investigation for the computing of surface curvatures on high resolution  $\mu$ -CT and for visualization purposes.

## 3.6 Image processing

Finally, to obtain quantifiable information of the acquired data it is required to perform specific image processing protocols onto the tomographic data. As the structure of cellular materials is characterized by a multi-scaled architecture (solid+gaseous phases), the developed protocols have considered the analysed phase (or scale). As a result, parameters concerning gaseous phase (conventional parameters) and solid phase (advanced parameters) are analysed separately, as explained hereinafter.

### 3.6.1 Conventional features characterization

The analysis of the gaseous phase of cellular materials by means of X-ray  $\mu$ -CT has been broadly performed within the literature [69-72]. It is accomplished following several steps aiming at the end of the process to extract quantitative data about the gas phase of these materials such as cell size, anisotropy, etc... (Figure 3-26).

- An edge preserving filter (typically median) is applied in order to enhance the contrast between gas and solid phase in the images.
- Thresholding and binarization allows separating the solid material from gaseous phase background. In low density cellular materials, as the cell walls are commonly extremely thin, the spatial resolution employed is not high enough to correctly binarize these parts of the structure.
- As a consequence, a watershed based algorithm is required in order to separate artificially joined gaseous phase thus creating digital walls that permit obtaining separated pores to analyse.
- Prior the 3D analysis of the cells, cells touching the border edges of the volume considered are eliminated in order to improve the results statistics.
- Finally, several quantitative parameters are evaluated for every remaining single pore.

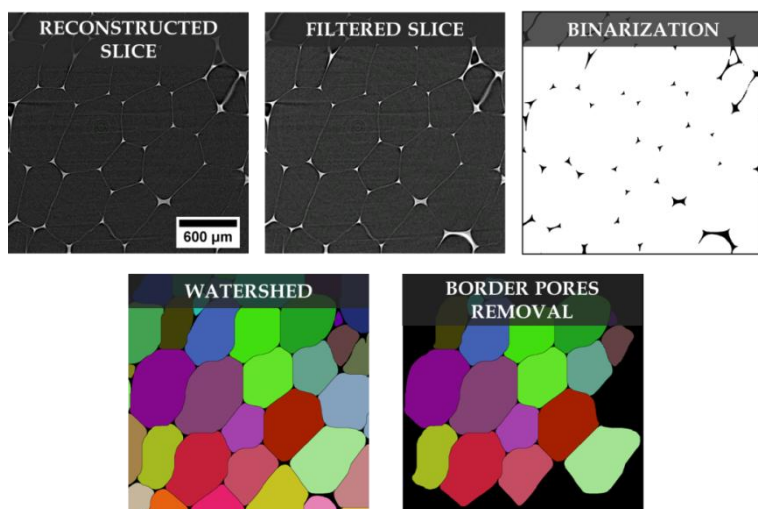


**Figure 3-26.** Visualization of the main steps of the image analysis protocol for the gas phase characterization by  $\mu$ -CT.

As a result of this workflow several parameters can be extracted of the 3D images.

- The ratio of the gaseous phase volume fraction and the total volume, i.e., porosity.
- The cell size of the pores by means of the equivalent diameter procedure.
- The anisotropy and orientation of the pores using the bounding box approach and the equivalent ellipsoid.
- The neighbourhood distribution of the pores that enables characterizing their 3D geometry.

### 3.6.2 Advanced features characterization

High resolution  $\mu$ -CT opens the possibility to reconstruct even the cell wall in low density cellular polymers. As a result, advanced features of the solid phase, not widely studied in the literature, can be accurately characterized. In this sense, few studies have been carried out considering several criterions to separate the two constituents of the solid phase: cell walls and struts. The two main ways are the de-structuration by a succession of erosions-dilations in 3D [73] and a solid classification

algorithm in with the inertia moment of each pixel is calculated considering its neighbourhood to discriminate between the two mentioned constituents [74]. However, in this thesis, the determination of the local thickness has been considered as a key point to extract the basic parameters of the solid phase such as the fraction of material in the struts or the thickness of the different constituents (Figure 3-27).

After filtering and binarizing (as well as in the previous case) an Euclidean transform local thickness algorithm allows assigning to every pixel belonging to the solid phase a thickness value corresponding to the diameter of the maximum sphere self-contained in that phase and centred in that pixel [75]. As a result, material thickness distributions can be obtained typically containing two separate peaks, each of them corresponding to the main constituents of the solid phase (Figure 3-27).

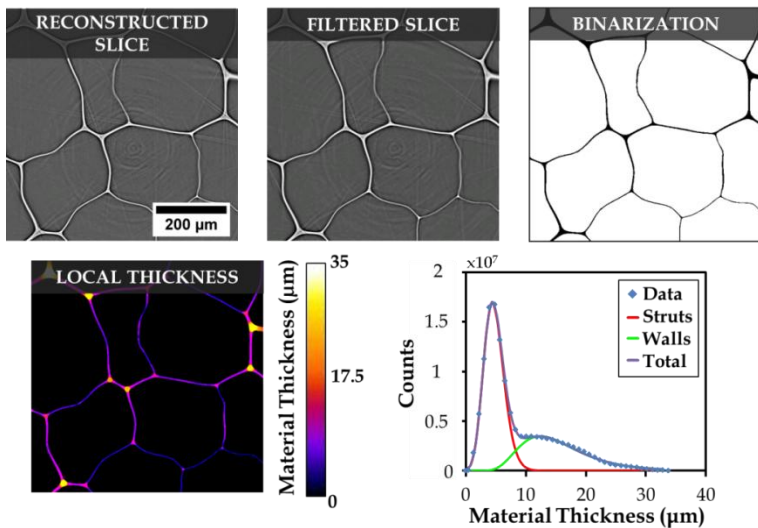


**Figure 3-27.** Main steps in the imaging analysis protocol for the characterization of the parameters concerning the solid phase.

After that, by analysing the relative area of the two peaks the fraction of material in each zone of the solid skeleton can be calculated. In addition, from every thickness distribution (cell walls, struts and total) the average thickness can be determined obtaining then the mean cell wall thickness, strut thickness and total structure average thickness.

During this research, additional image analysis protocols have been developed to quantify specific features in X-ray Tomography. A detailed description of all these methodologies is included in the corresponding papers of the next chapter (**Chapter 4**).



## References

- [1] J. Banhart, *Advanced tomographic methods in materials research and engineering*, Oxford University Press 2008.
- [2] J. Ohser, K. Schloditz, *3D Images of Materials Structures: Processing and Analysis*, Wiley-VCH Verlag GmbH & Co. KGaA 2010.
- [3] J.C. Russ, *The Image Processing Handbook*, CRC Press 2002.
- [4] K.-H. Ng, M.M. Rehani, X ray imaging goes digital: Digital imaging brings benefits but also demands changes in ways of working, *British Medical Journal*, 333 (2006) 765-766.
- [5] J.A. Rowlands, Material change for X-ray detectors, *Nature*, 550 (2017) 47-48.
- [6] H. Waters, *The First X-ray*, 1895, *The Scientist*, (2011).
- [7] W.C. Röntgen, A new kind of rays, *Nature*, 53 (1896) 274-276.
- [8] A.P. Hitchcock, J.J. Neville, Some applications of synchrotron light to physics and chemistry, *Physics in Canada*, 55 (1999) 191-198.
- [9] G.C. Baldwin, D.W. Kerst, Origin of synchrotron radiation, *Physics Today*, 28 (1975) 9-11.
- [10] H. Wilnick, S. Doniach, *Synchrotron Radiation Research*, Springer-Verlag US 1980.
- [11] K. Codling, Atomic and molecular physics using synchrotron radiation - the early years, *Journal of Synchrotron Radiation*, 4 (1997) 316-333.
- [12] M. Endrizzi, X-ray phase-contrast imaging, *Nuclear Instruments and Methods in Physics Research Section A: Accelerators, Spectrometers, Detectors and Associated Equipment*, 878 (2018) 88-98.
- [13] A. Momose, Recent Advances in X-ray Phase Imaging, *Japanese Journal of Applied Physics*, 44 (2005) 6355-6367.
- [14] A. Snigirev, I. Snigireva, V. Kohn, S. Kuznetsov, I. Schelokov, On the possibilities of x-ray phase contrast microimaging by coherent high-energy synchrotron radiation, *Review of Scientific Instruments*, 66 (1995) 5486-5492.
- [15] P.R.T. Munro, K. Ignatyev, R.D. Speller, A. Olivo, Source size and temporal coherence requirements of coded aperture type x-ray phase contrast imaging systems, *Optics Express*, 18 (2010) 19681-19692.
- [16] P.C. Diemoz, A. Bravin, P. Coan, Theoretical comparison of three x-ray phase contrast imaging techniques: propagation-based imaging, analyzer-based imaging and grating interferometry, *Optics Express*, 20 (2012) 2789-2805.
- [17] P. Coan, E. Pagot, S. Fiedler, P. Cloetens, J. Baruchel, A. Bravin, Phase-contrast X-ray imaging combining free space propagation and Bragg diffraction, *Journal of Synchrotron Radiation*, 12 (2005) 241-245.
- [18] A. Olivo, L. Rigon, S.J. Vinnicombe, K.C. Cheung, M. Ibison, R.D. Speller, Phase contrast imaging of breast tumours with synchrotron radiation, *Applied radiation and isotopes : including data, instrumentation and methods for use in agriculture, industry and medicine*, 67 (2009) 1033-1041.
- [19] X.-j. Guo, X.-l. Liu, C. Ni, B. Liu, S.-m. Huang, M. Gu, Improving image quality of x-ray inline phase contrast imaging using an image restoration method, *Optics Express*, 19 (2011) 23460-23468.
- [20] M. Born, E. Wolf, *Principles of Optics: Electromagnetic Theory of Propagation, Interference and Diffraction of Light*, Pergamon 1980.
- [21] A. Pogany, D. Gao, S.W. Wilkins, Contrast and resolution in imaging with a microfocus x-ray source, *Review of Scientific Instruments*, 68 (1997) 2774-2782.
- [22] K.A. Nugent, T.E. Gureyev, D.F. Cookson, D. Paganin, Z. Barnea, Quantitative phase imaging using hard X-rays, *Physical Review Letters*, 77 (1996) 2961-2964.
- [23] T.E. Gureyev, S.W. Wilkins, On x-ray phase imaging with a point source, *Optical Society of America A*, 15 (1998) 579-585.

- [24] A.V. Bronnikov, Reconstruction formulas in phase-contrast tomography, *Optics Communications*, 171 (1999) 239-244.
- [25] U. Bonse, M. Hart, An X-Ray Interferometer, *Applied Physics Letters*, 6 (1965) 155-156.
- [26] P. Suortti, J. Keyriläinen, W. Thomlinson, Analyser-based x-ray imaging for biomedical research, *Journal of Physics D: Applied Physics*, 46 (2013) 494002.
- [27] A. Olivo, F. Arfelli, G. Cantatore, R. Longo, R.H. Menk, S. Pani, M. Prest, P. Poropat, L. Rigon, G. Tromba, E. Vallazza, E. Castelli, An innovative digital imaging set-up allowing a low-dose approach to phase contrast applications in the medical field, *Medical physics*, 28 (2001) 1610-1619.
- [28] A. Olivo, R. Speller, A coded-aperture technique allowing x-ray phase contrast imaging with conventional sources, *Applied Physics Letters*, 91 (2007) 074106.
- [29] G.K. Kallon, M. Wesolowski, F.A. Vittoria, M. Endrizzi, D. Basta, T.P. Millard, P.C. Diemoz, A. Olivo, A laboratory based edge-illumination x-ray phase-contrast imaging setup with two-directional sensitivity, *Applied Physics Letters*, 107 (2015) 204105.
- [30] M. Endrizzi, F.A. Vittoria, G. Kallon, D. Basta, P.C. Diemoz, A. Vincenzi, P. Delogu, R. Bellazzini, A. Olivo, Achromatic approach to phase-based multi-modal imaging with conventional X-ray sources, *Opt Express*, 23 (2015) 16473-16480.
- [31] L. Salvo, P. Cloetens, E. Maire, S. Zabler, J.J. Blandin, J.Y. Buffiere, W. Ludwig, E. Boller, D. Bellet, C. Josserrond, X-ray micro-tomography an attractive characterisation technique in materials science, *Nuclear Instruments and Methods in Physics Research Section B*, 200 (2003) 273-286.
- [32] L. Babout, X-ray tomography imaging: a necessary tool for materials science, *Automatyka*, 10 (2006).
- [33] E. Maire, P.J. Withers, Quantitative X-ray tomography, *International Materials Reviews*, 59 (2013) 1-43.
- [34] J.H. Kinney, Q.C. Johnson, U. Bonse, M.C. Nichols, R.A. Saroyan, R. Nusshardt, R. Pahl, J.M. Brase, Three-dimensional X-ray computed tomography in materials science, *MRS Bulletin*, 13 (1988) 13-18.
- [35] M. Vopálensky, D. Vavrik, I. Kumpova, Optimization of the X-ray tube voltage with respect to the dynamical resolution in radiography and tomography, 8th Conference on Industrial TomographyWels (Austria), 2018.
- [36] D. Tilak Raju, K. Shanthi, Analysis on X-ray parameters of exposure by measuring X-ray tube voltage and time of exposure, *The International Journal of Engineering and Science*, 3 (2014) 69-73.
- [37] A.N. van Daatselaar, P.F. van der Stelt, J. Weenen, Effect of number of projections on image quality of local CT, *Dento maxillo facial radiology*, 33 (2004) 361-369.
- [38] R.N. Bracewell, Numerical Transforms, *Science*, 248 (1990).
- [39] D.H. Garces, W.T. Rhodes, N.M. Peña, Projection-slice theorem: a compact notation, *Journal of Optical Society of America A*, 28 (2011) 766-769.
- [40] J.P. Guedon, Y. Bizais, Bandlimited and Haar filtered back-projection reconstructions, *IEEE transactions on medical imaging*, 13 (1994) 430-440.
- [41] M.J. Flynn, Y. Chen, J. Hsieh, J.Y. Lo, J.A. Baker, J.T. Dobbins Iii, Gaussian frequency blending algorithm with matrix inversion tomosynthesis (MITS) and filtered back projection (FBP) for better digital breast tomosynthesis reconstruction, 6142 (2006) 61420E.
- [42] A.C. Silva, H.J. Lawder, A. Hara, J. Kujak, W. Pavlicek, Innovations in CT dose reduction strategy: application of the adaptive statistical iterative reconstruction algorithm, *AJR. American journal of roentgenology*, 194 (2010) 191-199.
- [43] J. Tang, B.E. Nett, G.H. Chen, Performance comparison between total variation (TV)-based compressed sensing and statistical iterative reconstruction algorithms, *Phys Med Biol*, 54 (2009) 5781-5804.

- [44] L. Li, K. Kang, Z. Chen, The FDK algorithm with an expanded definition domain for cone-beam reconstruction preserving oblique line integrals, *Journal of X-Ray Science and Technology*, 14 (2006) 217-233.
- [45] H. Zhang, J. Huang, J. Ma, Z. Bian, Q. Feng, H. Lu, Z. Liang, W. Chen, Iterative reconstruction for x-ray computed tomography using prior-image induced nonlocal regularization, *IEEE Transactions on Biomedical Engineering*, 61 (2014) 2367-2378.
- [46] J.A. Seibert, Iterative reconstruction: how it works, how to apply it, *Pediatric radiology*, 44 Suppl 3 (2014) 431-439.
- [47] R. Schulze, U. Heil, D. Gross, D.D. Bruellmann, E. Dranischnikow, U. Schwanecke, E. Schoemer, Artefacts in CBCT: a review, *Dento maxillo facial radiology*, 40 (2011) 265-273.
- [48] Y. Kyriakou, D. Prell, W.A. Kalender, Ring artifact correction for high-resolution micro CT, *Phys Med Biol*, 54 (2009) N385-391.
- [49] B. Münch, P. Trtik, F. Marone, M. Stampanoni, Stripe and ring artifact removal with combined wavelet-Fourier filtering, *Optics Express*, 17 (2009).
- [50] R.A. Brooks, G. Di Chiro, Beam hardening in X-ray Reconstructive Tomography, *Physics in Medicine and Biology*, 21 (1976) 390-398.
- [51] K. Remeysen, R. Swennen, Beam hardening artifact reduction in microfocus computed tomography for improved quantitative coal characterization, *International Journal of Coal Geology*, 67 (2006) 101-111.
- [52] D. Prell, Y. Kyriakou, T. Struffert, A. Dorfler, W.A. Kalender, Metal artifact reduction for clipping and coiling in interventional C-arm CT, *AJNR. American journal of neuroradiology*, 31 (2010) 634-639.
- [53] J.H. Siewerdsen, M.J. Daly, B. Bakhtiar, D.J. Moseley, S. Richard, H. Keller, D.A. Jaffray, A simple, direct method for x-ray scatter estimation and correction in digital radiography and cone-beam CT, *Medical physics*, 33 (2006) 187-197.
- [54] S. Pardo-Alonso, X-ray imaging applied to the characterization of polymer foams' cellular structure and its evolution, PhD Thesis, University of Valladolid, 2014.
- [55] A. Rack, S. Zabler, B.R. Müller, H. Riesemeier, G. Weidemann, A. Lange, J. Goebbels, M. Hentschel, W. Görner, High resolution synchrotron-based radiography and tomography using hard X-rays at the BAMline (BESSY II), *Nuclear Instruments and Methods in Physics Research Section A: Accelerators, Spectrometers, Detectors and Associated Equipment*, 586 (2008) 327-344.
- [56] C. Rau, U. Wagner, Z. Pešić, A. De Fanis, Coherent imaging at the Diamond beamline I13, *physica status solidi (a)*, 208 (2011) 2522-2525.
- [57] C. Holzner, M. Feser, S. Vogt, B. Hornberger, S.B. Baines, C. Jacobsen, Zernike phase contrast in scanning microscopy with X-rays, *Nature Physics*, 6 (2010) 883-887.
- [58] F. Zernike, How I Discovered Phase Contrast, *Science*, 121 (1955).
- [59] P. Thibault, A. Menzel, Reconstructing state mixtures from diffraction measurements, *Nature*, 494 (2013) 68-71.
- [60] J.M. Rodenburg, A.C. Hurst, A.G. Cullis, B.R. Dobson, F. Pfeiffer, O. Bunk, C. David, K. Jefimovs, I. Johnson, Hard-x-ray lensless imaging of extended objects, *Phys Rev Lett*, 98 (2007) 034801.
- [61] D.J. Batey, T.B. Edo, C. Rau, U. Wagner, Z.D. Pešić, T.A. Waigh, J.M. Rodenburg, Reciprocal-space up-sampling from real-space oversampling in x-ray ptychography, *Physical Review A*, 89 (2014).
- [62] U. Bonse, M. Stampanoni, A. Groso, A. Isenegger, G. Mikuljan, Q. Chen, A. Bertrand, S. Henein, R. Betemps, U. Frommherz, P. Böhler, D. Meister, M. Lange, R. Abela, Trends in synchrotron-based tomographic imaging: the SLS experience, 6318 (2006) 63180M.
- [63] R. Mokso, C.M. Schleputz, G. Theidel, H. Billich, E. Schmid, T. Celcer, G. Mikuljan, L. Sala, F. Marone, N. Schlumpf, M. Stampanoni, GigaFRoST: the gigabit fast readout system for tomography, *J Synchrotron Radiat*, 24 (2017) 1250-1259.

- [64] M.D. Abràmoff, P.J. Magalhaes, J. Sunanda, Image Processing with ImageJ, *Biophotonics International*, 11 (2004) 36-42.
- [65] C.A. Schneider, W.S. Rasband, K.W. Eliceiri, NIH Image to ImageJ: 25 years of image analysis, *Nature Methods*, 9 (2012) 671-675.
- [66] M. Dierick, B. Masschaele, L.V. Hoorebeke, Octopus, a fast and user-friendly tomographic reconstruction package developed in LabView®, *Measurement Science and Technology*, 15 (2004) 1366-1370.
- [67] J. Vlassenbroeck, M. Dierick, B. Masschaele, V. Cnudde, L. Van Hoorebeke, P. Jacobs, Software tools for quantification of X-ray microtomography at the UGCT, *Nuclear Instruments and Methods in Physics Research Section A: Accelerators, Spectrometers, Detectors and Associated Equipment*, 580 (2007) 442-445.
- [68] <https://www.fei.com/software/amira-avizo/>.
- [69] A. Elmoutaouakkil, L. Salvo, E. Maire, G. Peix, 2D and 3D characterization of metal foams using x-ray tomography, *Advanced Engineering Materials*, 4 (2002) 803-807.
- [70] J. Lambert, I. Cantat, R. Delannay, A. Renault, F. Graner, J.A. Glazier, I. Veretennikov, P. Cloetens, Extraction of relevant physical parameters from 3D images of foams obtained by X-ray tomography, *Colloids and Surfaces A: Physicochemical and Engineering Aspects*, 263 (2005) 295-302.
- [71] Y. Ma, R. Pyrz, M.A. Rodriguez-Perez, J. Escudero, J.C. Rauhe, X. Su, X-ray microtomographic study of nanoclay-polypropylene foams, *Cellular Polymers*, 30 (2011) 95-110.
- [72] M.D. Montminy, A.R. Tannenbaum, C.W. Macosko, New Algorithms for 3-D Imaging and Analysis of Open-Celled Foams, *Journal of Cellular Plastics*, 37 (2001) 501-515.
- [73] S. Pardo-Alonso, E. Solórzano, L. Brabant, P. Vanderniepen, M. Dierick, L. Van Hoorebeke, M.A. Rodriguez- Perez, 3D Analysis of the progressive modification of the cellular architecture in polyurethane nanocomposite foams via X-ray microtomography, *European Polymer Journal*, 49 (2013) 999-1006.
- [74] S. Pardo-Alonso, E. Solorzano, J. Vicente, L. Brabant, M.L. Dierick, I. Manke, A. Hilger, E. Laguna, M.A. Rodriguez-Perez,  $\mu$ CT-Based Analysis of the Solid Phase in Foams: Cell Wall Corrugation and other Microscopic Features, *Microscopy and Microanalysis*, 21 (2015) 1361-1371.
- [75] T. Hildebrand, P. Rügsegger, A new method for the model-independent assessment of thickness in three-dimensional images, *Journal of Microscopy*, 185 (1997) 67-75.

## Chapter 4

# **X-ray Tomography Studies on Cellular Polymers**



This Chapter summarizes the experimental work carried out during this investigation in order to extract information about cellular polymers using X-ray Tomography and developed specific image analysis protocols. This investigation tends to continue the precedent work carried out at CellMat Laboratory using this technique [1, 2].

There are three different papers included below studying on one hand the ex-situ final structure of low density cellular polymers and its relationship with both specific conditions of the foaming process and the final physical properties of the foams. On the other hand, the 4D (3D+time) inspection of a polymer foam formation is carried out using the most advanced real-time tomography capabilities and facilities.

### 4.1 Multi-scale inspection of the cellular structure

The first work entitled **“Multi-scale tomographic analysis of polymeric foams: A detailed study of the cellular structure”** addresses the study of the structure of two collections of low density cellular polymers (PE and PU foams). Considering the thin cell walls of such kind of cellular materials a correct visualization of both phases (solid and gaseous) is only accomplished using X-ray  $\mu$ -CT at two different spatial resolutions. In our case, lab-scale tomography at 5  $\mu\text{m}$  of effective pixel size allowed us investigating the main characteristics of the gaseous phase such as the cell size and cell size distribution, anisotropy, neighbour distribution or cell density. Moreover, a collection of high spatial resolution (at 0.438  $\mu\text{m}$  effective pixel size) tomographies carried out at Bessy II synchrotron permitted us evaluating advanced descriptors of the solid phase such as cell wall thickness or faction of material in the struts. To this purpose, an innovative procedure based on the determination of the local thickness distribution of the solid phase in 3D along the structure of the foams has been developed and implemented on the high resolution tomographies.

The 3D analysis investigates the particular structural differences due to the characteristics of the corresponding foaming types of the two analysed foam collections. It is shown within the paper that depending on the foaming process the cell size, homogeneity of the cell size distribution, cell geometry, fraction of material

in the struts and cell wall thickness is different, even for materials with similar relative density. Firstly, PE foams own cells with tetrakaidecaedral geometry, homogeneous distributions of cell size and the material uniformly distributed in the whole structure (and thus low-medium fraction of material in the struts). Opposite, PU foams have pentagonal dodecahedron cells with broader distributions of cell size. In addition, PU foams concentrate almost the totality of the mass in the struts and consequently the fraction of mass in the struts is near to one and the mean cell wall thickness is reduced (in the order of 2  $\mu\text{m}$ ).



European Polymer Journal 109 (2018) 169-178  
<https://doi.org/10.1016/j.europolymj.2018.09.047>

## Multi-scale tomographic analysis of polymeric foams: A detailed study of the cellular structure

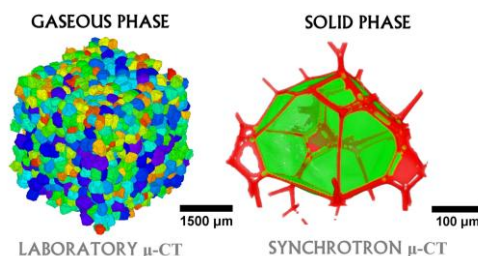
S. Pérez-Tamarit<sup>a,\*</sup>, E. Solórzano<sup>a</sup>, A. Hilger<sup>b</sup>, I. Manke<sup>b</sup>, M.A. Rodríguez-Pérez<sup>a</sup>

<sup>a</sup> CellMat Laboratory, University of Valladolid, Paseo de Belén 7 47011, Spain

<sup>b</sup> Helmholtz-Zentrum Berlin für Materialien und Energie, Lise-Meitner-Campus, Hahn-Meitner-Platz 1 14109, Berlin, Germany.

\* Corresponding author: [saul.perez@fmc.uva.es](mailto:saul.perez@fmc.uva.es)

Tel.: +34 983 423572; fax: +34 983 433192



### Abstract

This manuscript presents a detailed characterization of the cellular structure of two types of polymeric foams by non-destructive multi-scale X-ray computed microtomography. This comparative study is conducted in two different polymeric materials –rigid polyurethane foams and cross-linked low density polyethylene foams-. Based on this technique and using 3D image analysis, conventional descriptors of the foams gaseous phase (cell size distribution, mean cell size and anisotropy ratio) are characterized at a standard voxel size of 5 microns. Complementarily, 0.4 microns voxel size synchrotron X-ray tomography data sets have been used to characterize, using a new image analysis approach, features of the solid phase of the foams (fraction of mass in the struts and thickness of the different entities of the solid architecture: struts and walls). The presented methodology, based on multi-scale tomographic analysis, allows obtaining a better understanding of the connection between foaming process and cellular structure and is important to gain knowledge on the structure-properties relationships for these materials.

**Keywords:** X-ray tomography; Imaging; Polyurethane; Polyethylene; Polymeric foams characterization.

## 1. Introduction

From the structural point of view, solid cellular materials and foams consist on a gaseous phase which is dispersed throughout a solid continuous phase [1]. Solid foams are cellular materials produced by the foaming process of a liquid that is then cured/solidified. The solid architecture, local topology and cell organization determine the final physical -mechanical, thermal, acoustic...- properties of the foam [2-4].

The gaseous phase is formed basically by cells which can be interconnected or isolated depending if the structure is open or closed-celled. On the other hand, solid phase can be divided into struts or Plateau borders which are the intersection of three or more cells and cell walls or films, which separate two adjacent cells.

Conventionally, features corresponding to the gaseous phase are typically considered to understand the physical properties of polymeric foams. However, the characterization of the solid phase, less considered in the literature, becomes critical in order to understand certain physical properties [5, 6].

The main characteristic of a foam is the foam density ( $\rho$ ) or alternatively the relative density or solid fraction ( $\rho^*$ ), which is defined as the ratio between the foam density and the solid material density. The key structural parameters are the cell size distribution, the cell size ( $\phi$ ) and the cell anisotropy ( $R_i$ ). Other

important characteristics are topological aspects such as cell density ( $N_v$ ) that accounts for the number of cells per unit volume as well as average cell geometry - dodecahedral, tetrakaidecahedral, etc.- which is represented by the number of neighbours or coordination number ( $n_i$ ) of each cell. Additionally, there are different parameters related to the solid phase of the cellular structure. One of the most relevant is the average solid material thickness ( $t$ ), which is related to solid fraction and cell size. In addition, this thickness can be studied more in detail if we distinguish between cell wall and strut thickness ( $\delta$  and  $\xi$  respectively). Finally, the fraction of mass in the struts ( $f_s$ ), which is defined as the ratio between the amount of material in the struts and the total amount of material in the solid phase is also a very relevant parameter.

Conventional imaging techniques, such as optical microscopy and scanning electron microscopy (SEM) have been used to elucidate the structure of foams by analysing cross sections of the materials [7, 8]. In addition, nowadays several models in the literature suggest stereological corrections to obtain values in three dimensions (3D) from the 2D data [9-11]. Further, user-friendly tools have been developed in order to carry out fast and simply analysis of 2D SEM images [12]. However, all these 2D methods present some drawbacks such as sample preparation that can modify the structure [13], the challenge of obtaining 3D accurate data from 2D images and the intrinsic difficulty and inaccuracy of

measuring the main parameters of the solid phase using these 2D techniques.

Taking into account these constraints, X-ray micro-tomography ( $\mu$ -CT) becomes an adequate non-destructive technique to study the structure of cellular materials due to its high spatial resolution, no need of specific sample preparation and the possibility to obtain data in 3D [14-16].

A specific difficulty when X-ray tomography is used to characterize foams is the large dimensional disparities between the different elements. Cell sizes are in the range of  $10^2$ - $10^3$   $\mu\text{m}$  whereas the cell wall thickness is around  $10^0$ - $10^1$   $\mu\text{m}$ . Due to this, it is not possible to use an unique  $\mu$ -CT resolution to analyse the whole structure. At a voxel (volumetric pixel) size of 5 microns it is possible to obtain enough statistics regarding the cell morphology but identification/binarization of the solid-phase in the cell wall regions is generally not possible. Watershed wall reconstruction [17, 18] becomes an invalid process giving as a result an inexact reconstruction of those missed cell walls during the binarization which precludes an accurate characterization of the solid phase. A smaller voxel size, around 0.5 microns, nearly 2 times smaller than the minimum cell wall thickness of the material [19, 20], is needed to resolve these thin entities. At this resolution the main inconvenience yields in the fact of getting very poor cell statistics (only 6-10 complete cells are inside the analysed volume).

Consequently, we have performed two sets of experiments using two X-ray systems with the purpose of achieving a multi-scale and accurate characterization of the total structure of the selected foams. Firstly, in order to determine the gaseous phase a laboratory  $\mu$ -CT device, which was designed to obtain an optimum contrast in polymeric materials has been used [21, 22]. Additional  $\mu$ -CT measurements were performed at a synchrotron facility with the objective of solving the limitations in spatial resolution [23, 24]. Although there is nowadays in the market laboratory equipments with equivalent voxel sizes to our experiments, the use of synchrotron radiation improves the contrast and therefore the quality of high resolution  $\mu$ -CT.

The aim of this work is to evaluate in three dimensions and with a high level of resolution, the main descriptors of the two phases (gaseous and solid) of a collection of low density foams establishing a relationship between the foaming process and the structure. For this purpose, two groups of samples with structural differences linked to the particularities of the foaming processes were selected (see materials section). Nowadays, several works have been published studying the gaseous phase of low density foams by using tomographic methods [21, 25-27], being the solid phase less considered in the literature. In this work, we have analysed the solid phase with the required spatial resolution. In addition, although the solid phase is

topologically separated in cell walls and struts, it is usually difficult to select a suitable criterion to distinguish them. For this reason, we have developed a novel methodology for solid classification in low density cellular solids, which allows identifying both parts of the solid phase. This new approach could become an ideal characterization route for the cellular materials scientific community.

## 2. Experimental

### 2.1 Materials

Closed-cell rigid polyurethane foams and cross-linked closed-cell polyolefin foams are comparatively analysed in this work. Polyurethane (PU) foams have been fabricated by a reactive foaming process [28]. In this type of process two different reactants are mixed in order to obtain a foamed solid specimen. In our particular case, the two reactants are di- or polyisocyanate (part A) and a polyol blend (part B) provided by BASF Poliuretanos Iberia S.A. Polyol blends are composed by catalysts (amines), surfactants to stabilize the foam structure, the base polyol, which can be a polyether polyol, a polyester polyol or a blend of different types of polyols, and finally,

water as blowing agent (that decomposes during the reaction generating  $\text{CO}_2$ ). According to the supplier technical data sheet parts proportion were fix to 100 (part B)/160 (part A) for the polyol and isocyanate. The mixture of the two components was carried out using an overhead stirrer (EUROSTAR Power control-visc P1), equipped with a 50 mm diameter propeller stirrer from IKA. The mixing process (25s at 1200 rpm) was carried out in order to promote the blowing and curing reactions. By using four different polyol blends supplied by BASF (part B) in which the difference was only the amount of water it was possible to produce PU foams with four different densities between 30 and 100  $\text{kg/m}^3$  (Table 1).

Cross-linked closed-cell polyolefin foams manufactured by a high-pressure nitrogen gas solution process [29] were generously provided by Zotefoams Plc. (Croydon, United Kingdom). They were produced with low density polyethylene (LDPE) as base polymer. In this process, an extruded and cross-linked LDPE sheet was placed in an autoclave, in which it was subjected to a high pressure of nitrogen gas at temperatures above the polymer softening point. Under these

**Table 1.** Summary of the samples in this study.

Sample	Density ( $\text{kg/m}^3$ )	Relative density	Sample	Density ( $\text{kg/m}^3$ )	Relative density
PU-1	32.5	0.028	LDPE-1	16.4	0.018
PU-2	54.8	0.046	LDPE-2	20.2	0.022
PU-3	76.0	0.064	LDPE-3	31.2	0.034
PU-4	94.9	0.080	LDPE-4	41.3	0.045

conditions, the nitrogen dissolved into the polymer matrix. At the end of the solution stage and after cooling, the pressure was reduced to ambient pressure. Then, the materials were placed in a second autoclave under low pressure and again heated above the polymer melting point. The release of the pressure resulted in full expansion. Finally, the slabs were cooled down to room temperature. For this study we have analysed four samples with densities in the range of 15-45 kg/m<sup>3</sup> (Table 1). A more detailed description of the production process of these foams can be found elsewhere [30, 31].

These two collections of foams were selected for this study due to their structural differences. On the one hand, the microstructural solid distribution of PU foams shows a high concentration of polymer in the struts, (rounded-edge polyhedral pores) whereas, on the other hand, LDPE foams owe a likely sharp-edge polyhedral structure since the material is distributed all over the solid foam structure, and is not concentrated in

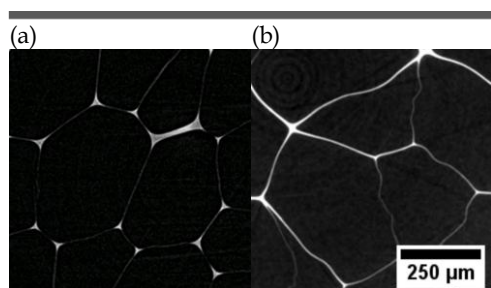


**Fig 1.** Representative tomographic slices of (a) rigid PU foams -PU-2- and (b) cross-linked LDPE foams -LDPE-4-.



**Fig 2.** 3D rendering of X-ray μ-CT device at CelMat Laboratory

the struts (Fig. 1). The density and names of the samples characterized in this study are summarized in Table 1.

#### 2.2 Experimental set-up

Two different series of tomographies were carried out. The samples were analysed in a laboratory system (Fig. 2). The set-up consists of a micro-focus cone-beam X-ray source L10101 from Hamamatsu (spot size: 5 μm, Voltage: 20-100 kV, Current: 0-200 μA) with a maximum output power of 20W and a flat panel detector C7940DK-02 also from Hamamatsu (2240x2344 pixels<sup>2</sup>, 50 μm of pixel size). A rotation stage is mounted over a linear stage with a total travel of 600 mm thus varying the magnification factor,  $M$ , as described in Eq. 1 – $SDD$ : source-detector distance,  $SOD$ : source-object distance–.

$$M = \frac{SDD}{SOD} \quad (1)$$

In our experiments the linear stage was placed in a position to achieve a magnification value  $M=10$  ( $SDD=581.8$  mm,  $SOD=58.18$  mm) and thus an effective pixel size of 5 microns was

reached. A tube voltage of 55 kV and current of 150  $\mu\text{A}$  were found to be optimal for the selected samples characterization. The detector exposure time was 1500 ms and the rotation step was  $0.4^\circ$ . In order to enhance the contrast in the reconstructed images each projection was the result of integrating two consecutive images. The samples were cylinders of 6 mm in diameter and 15 mm in height.

Once all the projections were acquired, the reconstruction process of the tomogram was carried out using Octopus reconstruction package [32].

High resolution X-ray synchrotron  $\mu\text{-CT}$  experiments were performed using the same samples. Measurements were performed at BAM-Line [33], a beam line located at Bessy II facility in Berlin (Germany). In this case, the detector of the X-rays was a PCO 4000 camera ( $4008 \times 2672$  pixels<sup>2</sup>, 9  $\mu\text{m}$  of pixel size) near to a CWO scintillator. The analysed sample was placed very near the scintillator (9 mm) in order to minimize phase contrast artefacts. A specific optical system between scintillator and camera yielded a final pixel size of 0.438  $\mu\text{m}$ . The energy of the X-rays in the line was fixed in a value of 9.8 keV. The selected exposure time of the detector was 3000 ms and the rotation step in this case was  $0.08^\circ$ . Samples with a reduced size (prisms of less than 1 mm<sup>2</sup> of base and 4 mm in height) were used due to the limited field of view of  $1.8 \times 1.2$  mm<sup>2</sup> at such resolution.

### *2.3 Density characterization*

Density ( $\rho$ ) for all the samples was determined over five cubes of  $30 \times 30 \times 30$  mm<sup>3</sup> using the geometric method [1]. Values of 1160 kg/m<sup>3</sup> and 910 kg/m<sup>3</sup> respectively for PU and LDPE solid matrixes were used to calculate the relative density ( $\rho^*$ ).

### *2.4 Laboratory $\mu\text{-CT}$ analysis*

Quantitative data analysis of the gaseous phase was carried out using Octopus Analysis package [2]. Sub-volumes of  $650^3$  voxels were analysed for each sample after a previous 3D median filter of 1 pixel of radius.

Image analysis under this software leads several steps (Fig. 3): image binarization, removal of isolated pixels, cells identification, cells separation by a watershed-based algorithm [3] and, finally, quantitative computation of every cell and its neighbourhoods [4-6]. In addition, the incomplete cells touching the limit of the analysed volume were removed. It is important to remark that watershed algorithm was required at this resolution since the cell walls of the foam present lower contrast than bulky regions (strut).

Once this procedure is applied, several cellular and topological descriptors of the foams such as cell size distribution, cell size, anisotropy, coordination number and cell density can be extracted.



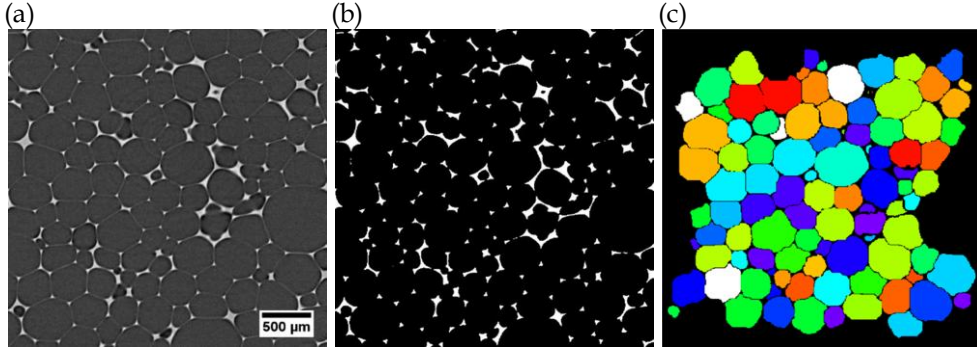


**Fig. 3.** Graphical representation of software workflow. (a) Filtered grey-level (b) binarized without non-resolved cell walls and (c) final individual cell identification with suppressed border cells.

The mean cell diameter corresponds with the *equivalent diameter* which can be defined as the diameter of a sphere containing the same number of voxels than the current cell. In addition, the anisotropy of each individual cell was determined using the *bounding box* descriptor which represents the smallest prism that includes all the voxels of the object/cell. This descriptor outputs 3 cell dimensions (width, depth and height) referred to the Cartesian space directions (X, Y, Z). Moreover, the cell coordination number is defined as the number of cells in contact with a specific one. Finally, cell density informs about the number of cells per unit volume. It can be calculated by using Eq. 2. As several cells in contact with the border of the volume are removed during the analysis, only the foam volume occupied by the analysed cells is considered in this calculation. To calculate this volume, the total volume of gas ( $V_{gas}$ ) calculated as a sum of all the volumes of the individual cells is corrected by using the gaseous fraction of the material ( $1-\rho^*=V_{gas}/V_{foam}$ ). Once the

foam volume is determined,  $N_v^{TOMO}$  is directly calculated considering the involved number of cells ( $n$ ).

$$N_v^{TOMO} = \frac{n(1-\rho^*)}{V_{gas}} \quad (2)$$

### 2.5 Synchrotron $\mu$ -CT data analysis

Quantitative data analysis of the solid phase was carried out using the open source image analysis application ImageJ/Fiji [7, 8]. Three different sub-volumes of  $1300^3$  voxels were analysed for each sample after a previous 3D median filter of 2 pixel of radius.

The method of analysis is different for this type of images (Fig. 4). Volumes were carefully binarized selecting a binarization level that preserves completely the cell walls in the binarized images (Fig 4(b)). Euclidean Distance Transform procedure (in 3D) [9] was applied (Fig. 4(c)) to determine the thickness distribution of the solid phase. Thickness histogram reveals that the thickness distribution of the mentioned constituents of the solid phase –struts and

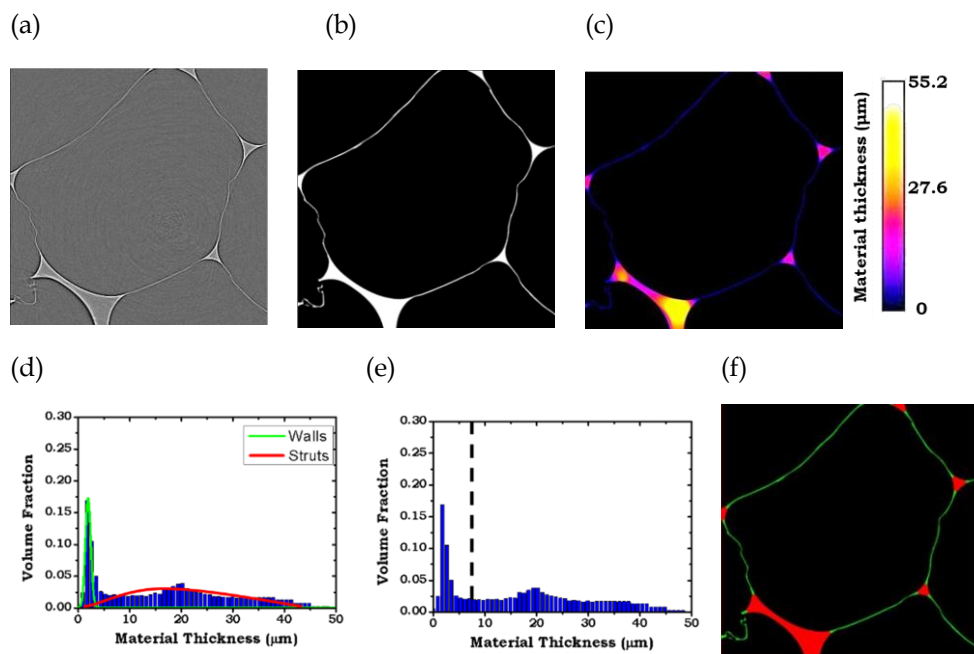


**Fig. 4.** Graphical scheme of the procedure for the analysis of high-resolution tomography volumes. (a) Filtered grey level slice. (b) Binarized slice including the cell walls (c) 3D local thickness with scale bar (d) two curves fitting of the material thickness distribution for the determination of  $f_s$  (Method-1) (e) thickness threshold selected for the determination of  $f_s$  (Method-2) and (f) final separation between cell walls –green– and struts –red– after Method-2.

cell walls- is overlapped. To separate these two contributions, two different strategies have been implemented. The first one consists in fitting the thickness histogram data by using a two-peak deconvolution process, using one peak for each constituent of the solid phase (Fig 4(d)). Considering the distinctly different thickness distributions for PU and LDPE foam materials, Log-normal or Gaussian fitting were used respectively. The correlation coefficient was better than 0.95 in all cases.

With this methodology the determined area of these two peaks ( $A_w$  and  $A_s$  respectively) represents the fraction of

each constituent. Then, the fraction of mass in the struts can be accurately calculated using the expression of Eq. 3 (Method-1). In addition, using the fitted data for these two overlapped thickness distributions it is possible to calculate the mean thickness values for cell walls and struts.

$$f_s^{Method-1} = \frac{A_s}{A_w + A_s} \quad (3)$$

Alternatively, a simpler thickness threshold method (Fig. 4(e)) has been applied to classify struts and cell walls obtaining reasonably good results as observed in Fig. 4(f) (Method-2). The thickness value was selected in each case



in order to reproduce the results of the erosion-dilation methodology, extensively applied in the literature [4, 10]. In this case,  $f_s$  is calculated as the ratio between the area of the thickness distribution above the selected thickness threshold and the total area of the material thickness distribution.

Finally, the mean thickness of the structure ( $t$ ) is obtained calculating the weighted average of the original thickness distribution without fitting process.

These methodologies improve the proposed methods for solid classification in foams described elsewhere [4, 11].

### 3. Results and discussion

The cellular structure descriptors are analysed here in three different sections.

In the first section we discuss the characteristics of the individual entities of the gaseous phase. In the second section, we will analyse the topology of the cells. Finally, the descriptors of the solid phase are examined.

#### 3.1 Gaseous phase descriptors

Fig. 5 shows the analysed cell structure of two of the foams under study, PU-2 and LDPE-4, in order to exemplify the structural differences between them at the two scales analysed. These two foams have been selected for most of the comparisons in this work since they present nearly the same relative density (Table 1). Evident differences can be observed comparing these two materials. On the one hand, the cells of PU foams are slightly oriented in the Z-direction while LDPE foams show nearly isotropic

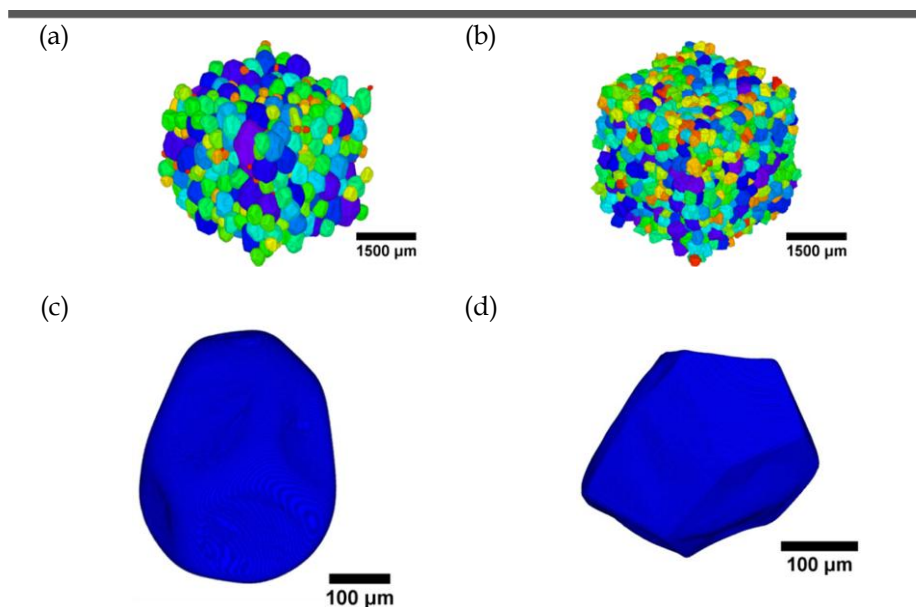


**Fig. 5.** Tomographic 3D renderings of the gas phase for PU-2: (a) and (c), and LDPE-4: (b) and (d). Laboratory resolution: (a) and (b), and synchrotron resolution: (c) and (d).

cells (figures 5(a) and 5(b)). On the other hand, (figures 5(c) and 5(d)), it is possible to elucidate a different shape of the cells. PU cells are rounded-edge polyhedral pores whereas LDPE pores are sharp-edge polyhedrons.

Analysing the dependence of cell size with the foam density it is possible to find two different trends (Fig. 6). For PU foams, in which mean cell sizes are between 310 and 390  $\mu\text{m}$ , there seem to be a relation between cell size and foam density, the cell size decreases as the foam density increases, whereas in the case of LDPE foams there is no correlation between these two parameters. The mean cell size in these materials is ranged between 260 and 320  $\mu\text{m}$ . The different behaviour is caused by specific particularities of each foaming process. On one hand, in reactive foaming (PU foams) when the mixing conditions are fixed (pale, stirring velocity and time) the density can only be controlled by the amount of blowing agent. If stabilizing additives are also kept the constant coarsening and coalescence effect should take place similarly too [12, 13]. As a result, final cell size is slightly higher for less-dense samples and decreases with sample density. On the other hand, for gas dissolution foaming process the most important parameters to control cell size are the first stage pressure (in addition to the pressure release rate) and the temperature during the different steps. As a consequence, it is known that this process allows controlling in a precise

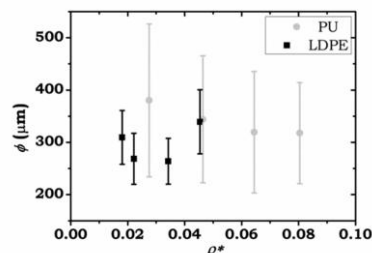


Fig 6. Mean cell size versus relative density for all the samples under study.

and independent way density and average cell size and for this reason it is not expected to find out a relation between these parameters [14, 15].

Furthermore, foaming process also affects the cell size distributions (Fig. 7). All the specimens are likely mono-disperse because the cell size distributions contain a single peak. PU foams present wider distributions. This might be caused intrinsically by the reactive foaming process used to produce these foams, in which cells are nucleated at slightly different times and degeneration mechanisms (coalescence, coarsening, and drainage) promote the apparition of smaller (due to delayed nucleation) and larger cells (due to degeneration mechanisms). On the other hand, in gas-dissolution foaming process nucleation of all the cells occurs in a very short period (when the pressure is released) and the high melt strength of the polymer (that is cross-linked before foaming) reduces the intensity of the degeneration mechanisms, leading to a more homogeneous cellular structure.

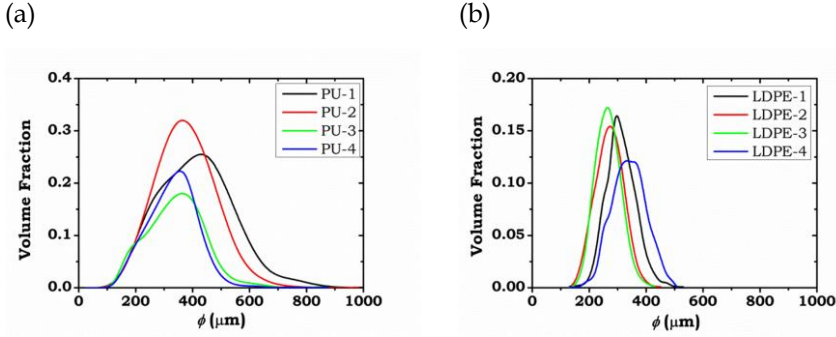


Fig. 7. Cell size distributions for all the samples under analysis. (a) PU foams and (b) LDPE foams.

As it is shown by the error bars of Fig. 6 PU foams have in average a normalized standard deviation (ratio between standard deviation of the cell size distribution and average of a distribution) of 0.35 whilst it is only 0.17 for LDPE foams. In addition, PU foams show a cell size distribution that contains a tail at larger cells. These large cells might be caused by inclusion of external air bubbles during the mixing process of the two components.

In addition, the anisotropy of the cells in the Z-direction has been analysed. We have selected this direction because it corresponds with the growing direction in the analysed foams. As it has been indicated before, we have employed the *bounding box* in order to calculate this parameter. To this end, we calculate the ratio between the cell size in Z direction - height- and the average value of two remaining (and equivalent) cell sizes- X and Y directions- to calculate the anisotropy of every cell considered within the analysed volume. Then, the average value of the cell anisotropy

considering all the cells in the analysed volume is calculated. As it is shown in Fig. 8, LDPE foams are isotropic in this direction but also in the other directions (results not shown). This fact is explained, once again, taking into account the specific foaming process. In this process the material expands in a free expansion process without any physical constrains. As a consequence, the foam is fully isotropic. However, PU foams are anisotropic with cells oriented in Z direction since the expansion in these materials takes place in a cylindrical mould that limits the expansion of the foam in the horizontal plane [15]. In addition there is a clear dependence with

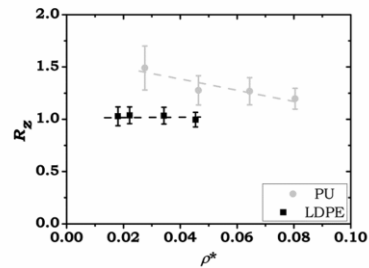


Fig 8. Anisotropy in Z-direction versus relative density for all the specimens in this work.

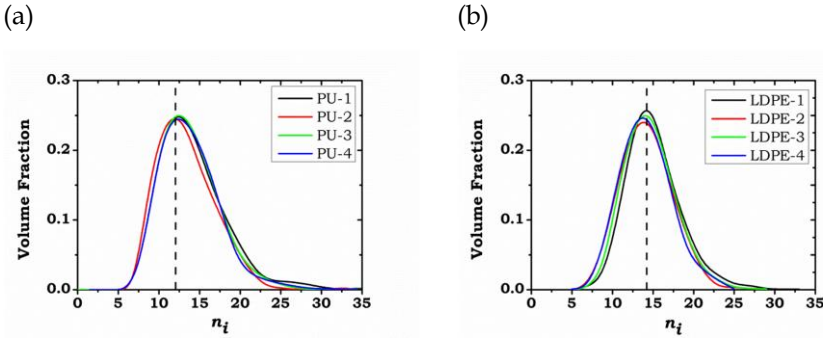


Fig. 9. Coordination number distributions for (a) PU foams and (b) LDPE foams under study. The dashed line corresponds to a coordination number of 12 in PU foams and 14 in LDPE foams.

density. Anisotropy increases when density is reduced. This dependence is explained since different amounts of blowing agent –water- were included in polyol blends in order to obtain specimens with different density. Thus, less dense foams contain a higher amount of water that promotes quicker foaming process and in consequence a higher elongation of the cells in the growing direction of the foam.

3.2 Topological features

The coordination number, which represents the number of neighbours of every single cell, is closely connected with the shape and size in-homogeneity of the cells. In our particular case (Fig. 9), there are clear disparities in the coordination number. In both cases, foams contain cells with a high variation of cell shapes. It is possible to detect cells with geometries such as cubic ( $n_i=6$ ), octahedral ( $n_i=8$ ), dodecahedral ( $n_i=12$ ), tetrakaidecahedral ( $n_i=14$ ), or even icosahedral ( $n_i=20$ ). The most probable value of the coordination number is around 12 or 14, for PU or LDPE foams

respectively (Fig. 9). This interesting result indicates that in average cells in PU foams can be modelled as pentagonal dodecahedrons while a likely tetrakaidecahedral shape should be considered for modelling LDPE foams [16]. In contrast to the precedent parameters, foam density does not affect the cell geometry since all the distributions are very similar in shape.

Calculated values of cell density via tomographic methods ( $N_v^{TOMO}$ ) are ranged between  $10^4$ - $10^5$  cells/cm<sup>3</sup> (Table 2), which are expected values for cell sizes previously measured [17]. In addition, LDPE foams contain a higher number of cells per unit volume due to both its lower density and reduced cell sizes in comparison with PU samples.

Table 2. Cell density values determined by X-ray $\mu$ -CT of samples of this study.			
Sample	$N_v^{TOMO}$ (cells/cm <sup>3</sup> )	Sample	$N_v^{TOMO}$ (cells/cm <sup>3</sup> )
PU-1	$2.2 \cdot 10^4$	LDPE-1	$5.4 \cdot 10^4$
PU-2	$3.1 \cdot 10^4$	LDPE-2	$8.0 \cdot 10^4$
PU-3	$3.8 \cdot 10^4$	LDPE-3	$8.6 \cdot 10^4$
PU-4	$4.1 \cdot 10^4$	LDPE-4	$4.1 \cdot 10^4$

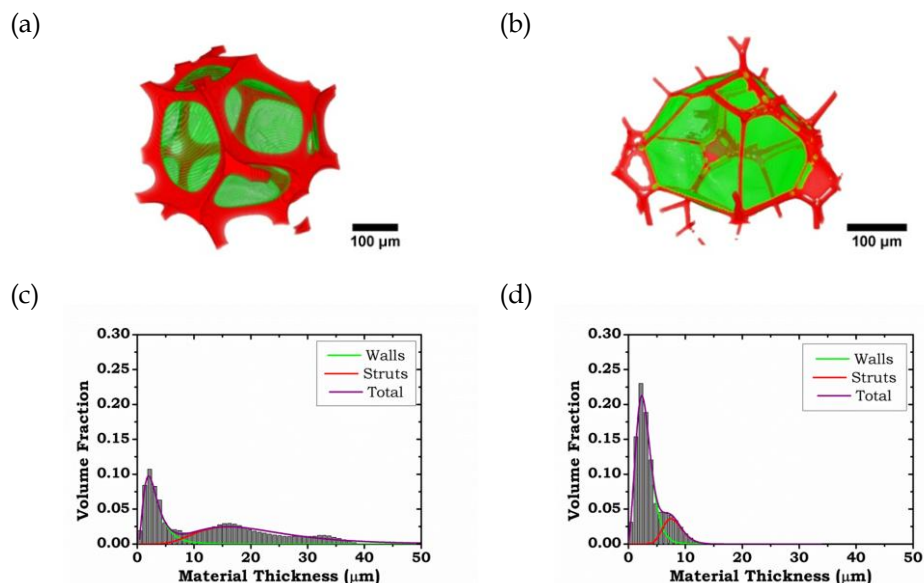


**Fig. 10.** 3D rendering of the separated solid phase (a) and (b), and material thickness distributions (c) and (d) for PU-1 and LDPE-3 samples respectively.

Also packing of the sharp-edged polyhedral cells is expected to be higher complementary contributing to a higher cell density.

### 3.3 Solid phase analysis

Clear differences in the solid material distribution can be observed in Fig. 10 (a) and (b) in the 3D rendering of the solid phase of typical cells. We will use the extracted data for material thickness distribution (Fig. 10, (c) and (d)) to objectively compare the specimens in this work. Results for two foams with similar densities based on a different polymer matrix are shown in this figure.

It can be observed that PU foams present much more asymmetric material thickness distributions. Due to this reason, we have used asymmetric log-

normal functions for processing peak deconvolution and final data fitting. The high amount of material concentrated in the struts will output high values for  $f_s$  next to one. In the case of LDPE foams, the thickness distributions are concentrated in much lower values, having a higher weight in the zone of low thickness with rather overlapped peaks. As a consequence, the solid material is well distributed along the entire structure of the foam, resulting in low fractions of mass in the struts. In addition, for LDPE foams it is possible the use of symmetric functions (combination of two Gaussian curves) to have a more accurate fitting of the experimental data. This difference in the structure of the solid phase and therefore between material thickness distributions for the two kinds of foams under study is explained again

considering the particularities of the foaming processes. In PU samples, the presence of degeneration mechanisms is more intense than in the case of LDPE samples. In particular, drainage of material in PU from cell walls to struts provokes the thickening of the struts and, consequently, broader material thickness distributions appear.

The results corresponding to the Method-1 procedure are shown in Fig. 10 (c) and (d) where the fitting curves are also included. The green curve is associated to cell walls, red distribution represents struts and the purple line is the result of the total fit.

The dependence with density using the results of Method-1 can be seen in Fig. 11(a). The differences between the two types of foams are clearly observed. For the LDPE foams under study fraction of mass in the struts is in the range of 0.1-0.4 whilst in the case of PU specimens this characteristic is between 0.5 and 0.9. Our first method for the determination of this parameter is truly innovative since the conventional procedures to determine

this parameter are based on 2D techniques [18, 19] and/or in 3D analysis by processes based on the application of successive binary erosions and dilations [4, 20] which are not valid in the case of LDPE samples due to the very small difference in thickness between cell walls and struts. Solid classification methods based on local moments of inertia have been complementarily evaluated in our research group reaching successful results for LDPE materials but at the cost of high computation times [11]. Expected computing times for our high resolution data sets would be higher in comparison to the method proposed in this paper. As an example, for a representative volume of  $650 \times 650 \times 650 \text{ pix}^3$ , local thickness algorithm leads to 1-2h of computation whereas solid classification methods leads to 12-16h, in the same computer.

Our threshold-based methodology (Method-2), predicts values of fraction of mass in the struts reasonably well correlated with those values obtained following the first methodology. Nevertheless Method-2 seems to

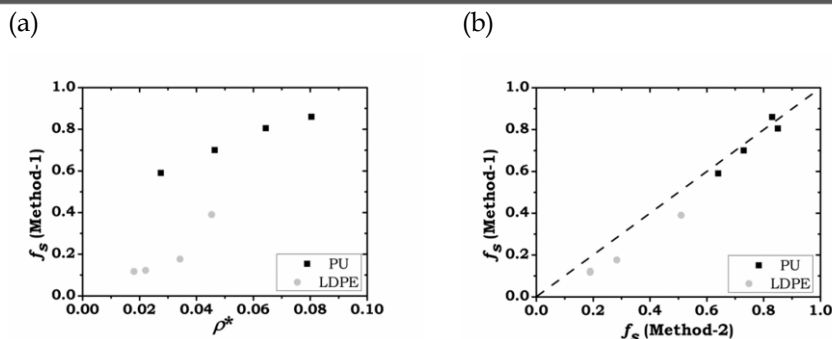


Fig. 11. (a) Dependence of fraction of mass in the struts obtained by Method-1 with foam density. (b) Comparison between both methods of determination of  $f_s$ .



overestimate  $f_s$  for LDPE materials while reach similar values in the case of PU samples (Fig. 11b). This is a logical result taking into account that the differences in thickness between walls and struts are smaller in the LDPE foams (overlapped peaks). Due to this, Method-2 is more inaccurate in these materials while  $f_s$  estimation by both methods is rather similar for PU materials.

The results obtained could be also explained considering the particularities of both foaming processes. In the case of PU, the liquid (low-viscous) material is able to drain from cell walls to struts until the complete gelling of the polymer is reached [21]. Surfactants act as excellent cell-wall stabilizers and as a consequence cell-walls in the micron and even submicron range are still stable. The consequence of this physical process is that most of the solid material is located in the struts (high  $f_s$  value). In fact, varying the amount of blowing agent, i.e., without changing any of other formulation component (basically catalysts and surfactants), promotes the observed result. The higher is the foam density, the higher is the fraction of mass in the struts. In addition, as gel time is similar (same catalyst amount) it results into the same drainage time. Consequently, the amount of material located in cell-wall ( $\delta$ ) is kept constant with density variation (Fig 12(a)) while struts thickness ( $\xi$ ) grows and consequently  $f_s$  (Fig. 12(b)). Figure 12 show the compared results for cell-wall thickness ( $\delta$ ), struts thickness ( $\xi$ ), and

material thickness ( $t$ ). Additional calculations show that structural ratio ( $\xi/\delta$ ) in PU strongly varies with density from 8 to 13.5 with a similar linear trend to  $f_s$ .

In the case of LDPE the foams under study, the cells are created simultaneously during pressure release and the material has a higher melt strength during growing which hinders local drainage and subsequent cell wall thinning. This fact leads to a more

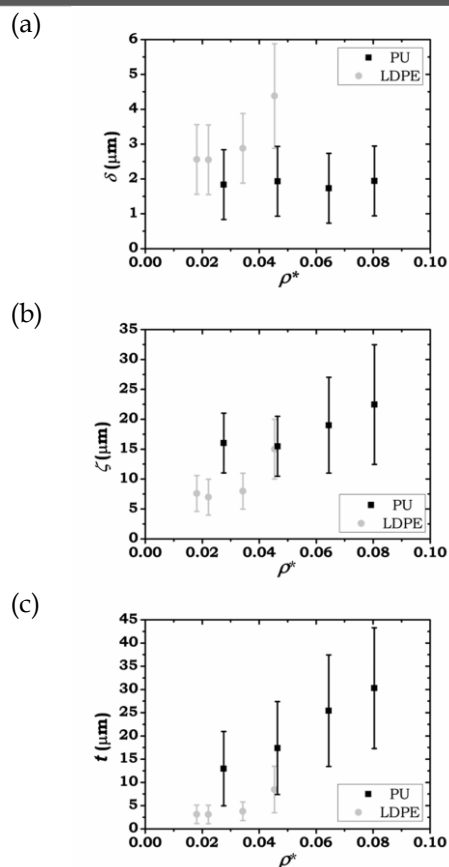


Fig 12. Diverse parameters related to the solid structure thickness for all the samples. (a) Mean cell wall thickness (b) Strut thickness and (c) Average thickness of the total structure.

homogeneous repartition of material throughout the solid architecture and therefore in lower values of  $f_s$ . As shown in Figure 12 both cell wall and strut thickness vary in a similar way and structural ratio is kept nearly constant with struts nearly 3 times thicker than cell walls.

At last, the average value of thickness of the structure increases with foam density (Fig. 12(c)). This fact is probably caused by the higher effect in the average of the thicker structures in the solid foam architecture, the struts.

#### **4. Conclusions**

The cellular structure of two different kinds of low density foams -PU and LDPE foams- have been accurately resolved by laboratory and synchrotron X-ray  $\mu$ -CT. A voxel size of 5 microns has been used to analyse the gaseous phase while an order of magnitude lower voxel size (0.438 microns) has been used to analyse the solid phase. To this end, specific 3D image analysis workflows have been developed getting precise 3D structural information difficult to obtain with the same accuracy with just one resolution level. In addition, a novel methodology for solid classification in low density cellular solids has been developed, this new approach allows performing a detailed characterization of the solid phase.

LDPE foams are characterized for presenting homogeneous distributions of cell size, an isotropic cellular structure and statistically with a higher number of

cells presenting tetrakaidecahedral geometry. In addition, a low fraction of mass in the struts ( $<0.5$ ) is also characteristic of these structures and nearly constant structural ratio ( $\xi/\delta$ ) with values around 3.

On the other hand, PU foams have broader distributions of cell sizes, and cells slightly elongated in the Z-direction (growing direction). The most probable structure geometry corresponds to pentagonal dodecahedrons. In this case, mean cell wall thickness remains constant for all the materials as a result of the physical mechanisms during the foaming process. These materials have a high fraction of mass in the struts ( $>0.5$ ) and their structural ratio ( $\xi/\delta$ ) is not constant (ranging 8-13.5).

#### **5. Data availability**

The raw/processed data required to reproduce these findings cannot be shared at this time as the data also forms part of an ongoing study.

#### **Acknowledgements**

Pre-doctoral contract of S. Perez-Tamarit by University of Valladolid (E-47-2015-0094701) and co-financed by Banco Santander is acknowledged. In addition, financial support from MINECO, FEDER, UE (MAT2015-69234-R) and the Junta de Castile and Leon (VA011U16) are gratefully acknowledged. Joan Ferrer and Luis Vela from BASF Spain are also acknowledged for supplying the materials used in this investigation. Finally, we acknowledge the support



from Bessy II (HZB, Berlin, Germany) to complete this work (proposal 14100497-ST).

### References

- [1] L.J. Gibson, M.F. Ahsby, *Cellular Solids: Structure and Properties*, Pergamon Press, Oxford, England, 1988.
- [2] A. Cunningham, N.C. Hilyard, *Low Density Cellular Plastics: Physical Basis of Behaviour*, Ed. Chapman and Hall, London, 1994.
- [3] M.A. Rodriguez-Perez, The effect of Chemical composition, density and cellular structure on the dynamic mechanical response of polyolefin foams, *Cellular Polymers*, 21 (2002) 117-136.
- [4] A.E. Simone, L.J. Gibson, Effects of solid distribution on the stiffness and strength of metallic foams, *Acta Materialia*, 46 (1998) 2139-2150.
- [5] M. Marvi-Mashhadi, C.S. Lopes, J. Llorca, Modelling of the mechanical behavior of polyurethane foams by means of micromechanical characterization and computational homogenization, *International Journal of Solids and Structures*, 146 (2018) 154-166.
- [6] P. Ferkl, M. Toulec, E. Laurini, S. Pricl, M. Fermeiglia, S. Auffarth, B. Eling, V. Settels, J. Kosek, Multi-scale modelling of heat transfer in polyurethane foams, *Chemical Engineering Science*, 172 (2017) 323-334.
- [7] ASTM-D3572, *Annual Book of ASTM standards*, 1994.
- [8] J. Kuhn, H.P. Ebert, M.C. Arduini-Schuster, D. Büttner, J. Fricke, Thermal transport in polystyrene and polyurethane foam insulations, *International Journal of Heat and Mass Transfer*, 35 (1992) 1795-1801.
- [9] M.D. Montminy, A.R. Tannenbaum, C.W. Macosko, The 3D structure of real polymer foams, *Journal of colloid and interface science*, 280 (2004) 202-211.
- [10] J.C. Russ, R.T. Dehoff, *Practical Stereology*, 2nd Edition ed., Plenum Press, New York, 1999.
- [11] D.L. Sahagian, A.A. Proussevitch, 3D particle size distributions from 2D observations: stereology for natural applications, *Journal of Volcanology and Geothermal Research*, 84 (1998) 173-196.
- [12] J. Pinto, E. Solorzano, M.A. Rodriguez-Perez, J.A. de Saja, Characterization of the cellular structure based on user-interactive image analysis procedures, *Journal of Cellular Plastics*, 49 (2013) 555-575.
- [13] M.D. Montminy, A.R. Tannenbaum, C.W. Macosko, *New Algorithms for 3-D Imaging and Analysis of Open-Celled Foams*, *Journal of Cellular Plastics*, 37 (2001) 501-515.
- [14] L. Salvo, P. Cloetens, E. Maire, S. Zabler, J.J. Blandin, J.Y. Buffiere, W. Ludwig, E. Boller, D. Bellet, C. Jossierond, X-ray micro-tomography an attractive characterisation technique in materials science, *Nuclear Instruments and Methods in Physics Research Section B*, 200 (2003) 273-286.
- [15] E. Maire, P. Colombo, J. Adrien, L. Babout, L. Biasetto, Characterization of the morphology of cellular ceramics by 3D image processing of X-ray tomography, *Journal of the European Ceramic Society*, 27 (2007) 1973-1981.
- [16] S. Youssef, E. Maire, R. Gaertner, Finite element modelling of the actual structure of cellular materials determined by X-ray tomography, *Acta Materialia*, 53 (2005) 719-730.
- [17] K. Mader, R. Mokso, C. Raufaste, B. Dollet, S. Santucci, J. Lambert, M. Stampanoni, Quantitative 3D characterization of cellular materials: Segmentation and morphology of foam, *Colloids and Surfaces A: Physicochemical and Engineering Aspects*, 415 (2012) 230-238.
- [18] L. Vincent, P. Soille, Watersheds in digital spaces: An efficient algorithm based on immersion simulations, *IEEE Transactions on Pattern Analysis and Machine Intelligence*, 13 (1991) 583-598.
- [19] M. Santiago-Calvo, J. Tirado-Mediavilla, J.L. Ruiz-Herrero, M.A. Rodríguez-Pérez, F. Villafañe, The effects of functional nanofillers on the reaction kinetics, microstructure, thermal and mechanical properties of water blown rigid polyurethane foams, *Polymer*, 150 (2018) 138-149.
- [20] R.A. Campo-Arnáiz, M.A. Rodríguez-Pérez, B. Calvo, J.A. de Saja, Extinction coefficient of polyolefin foams, *Journal of Polymer Science Part B: Polymer Physics*, 43 (2005) 1608-1617.
- [21] Y. Ma, R. Pyrz, M.A. Rodriguez-Perez, J. Escudero, J.C. Rauhe, X. Su, X-ray microtomographic study of nanoclay-polypropylene foams, *Cellular Polymers*, 30 (2011) 95-110.
- [22] E. Solórzano, J. Pinto, S. Pardo, F. Garcia-Moreno, M.A. Rodriguez-Perez, Application of a microfocus X-ray imaging apparatus to the study of cellular polymers, *Polymer Testing*, 32 (2013) 321-329.
- [23] A. Elmoutaouakkil, G. Fuchs, P. Bergounhon, F. Peyrin, Three-dimensional quantitative analysis of polymer foams from synchrotron radiation x-ray microtomography, *Journal of Physics D: Applied Physics*, 36 (2003) A37-A43.
- [24] P. Weiss, L. Obadia, D. Magne, X. Bourges, C. Rau, T. Weitkamp, I. Khairoun, J.M. Boulter, D. Chappard, O. Gauthier, G. Daculsi, Synchrotron X-ray microtomography (on a micron scale) provides

three-dimensional imaging representation of bone ingrowth in calcium phosphate biomaterials, *Biomaterials*, 24 (2003) 4591-4601.

[25] A. Elmoutaouakkil, L. Salvo, E. Maire, G. Peix, 2D and 3D characterization of metal foams using x-ray tomography, *Advanced Engineering Materials*, 4 (2002) 803-807.

[26] A. Nistor, M. Toulec, A. Zubov, J. Kosek, Tomographic Reconstruction and Morphological Analysis of Rigid Polyurethane Foams, *Macromolecular Symposia*, 360 (2016) 87-95.

[27] F. De Pascalis, M. Nacucchi, M. Scatto, R. Albertoni, Quantitative characterisation of low-density, high performance polymeric foams using high resolution X-ray computed tomography and laser confocal microscopy, *NDT & E International*, 83 (2016) 123-133.

[28] D. Klempner, K.C. Frisch, *Handbook of polymeric foams and foam technology*, Passavia Druckerei GmbH Passau 1991.

[29] M.A. Rodríguez-Pérez, Crosslinked Polyolefin Foams: Production, Structure, Properties, and Applications, *Advances in Polymer Science*, 184 (2005) 97-126.

[30] O. Almanza, M.A. Rodríguez- Pérez, J.A. de Saja, The microstructure of polyethylene foams produced by a nitrogen solution process, *Polymer*, 42 (2001) 7117-7126.

[31] O. Almanza, M.A. Rodríguez- Pérez, J.A. De Saja, Applicability of the transient plane source method to measure the thermal conductivity of low-density polyethylene foams, *Journal of Polymer Science Part B: Polymer Physics*, 42 (2004) 1226-1234.

[32] J. Vlassenbroeck, M. Dierick, B. Masschaele, V. Cnudde, L. Van Hoorebeke, P. Jacobs, Software tools for quantification of X-ray microtomography at the UGCT, *Nuclear Instruments and Methods in Physics Research Section A: Accelerators, Spectrometers, Detectors and Associated Equipment*, 580 (2007) 442-445.

[33] A. Rack, S. Zabler, B.R. Müller, H. Riesemeier, G. Weidemann, A. Lange, J. Goebbels, M. Hentschel, W. Görner, High resolution synchrotron-based radiography and tomography using hard X-rays at the BAMline (BESSY II), *Nuclear Instruments and Methods in Physics Research Section A: Accelerators, Spectrometers, Detectors and Associated Equipment*, 586 (2008) 327-344.

[34] ASTM-D1622-08, *Annual Book of ASTM standards*, 2008.

[35] L. Brabant, J. Vlassenbroeck, Y. De Witte, V. Cnudde, M.N. Boone, J. Dewanckele, L.V. Hoorebeke, Three-Dimensional Analysis of High-Resolution X-Ray Computed Tomography Data with Morpho+, *Microscopy and Microanalysis*, 17 (2011) 252-263.

[36] S. Pardo-Alonso, E. Solórzano, L. Brabant, P. Vanderniepen, M. Dierick, L. Van Hoorebeke, M.A. Rodríguez- Pérez, 3D Analysis of the progressive modification of the cellular architecture in polyurethane nanocomposite foams via X-ray microtomography, *European Polymer Journal*, 49 (2013) 999-1006.

[37] M.D. Abràmoff, P.J. Magalhaes, J. Sunanda, Image Processing with ImageJ, *Biophotonics International*, 11 (2004) 36-42.

[38] C.A. Schneider, W.S. Rasband, K.W. Eliceri, NIH Image to ImageJ: 25 years of image analysis, *Nature Methods*, 9 (2012) 671-675.

[39] T. Hildebrand, P. Rüeggsegger, A new method for the model-independent assessment of thickness in three-dimensional images, *Journal of Microscopy*, 185 (1997) 67-75.

[40] S. Pardo-Alonso, E. Solorzano, J. Vicente, L. Brabant, M.L. Dierick, I. Manke, A. Hilger, E. Laguna, M.A. Rodríguez-Pérez, muCT-Based Analysis of the Solid Phase in Foams: Cell Wall Corrugation and other Microscopic Features, *Microscopy and Microanalysis*, 21 (2015) 1361-1371.

[41] M.M. Bernal, S. Pardo-Alonso, E. Solórzano, M.A. Lopez-Machado, R. Verdejo, M.A. Rodríguez-Pérez, Effect of carbon nanofillers on flexible polyurethane foaming from a chemical and physical perspective, *RSC Advances*, 4 (2014).

[42] S. Pardo-Alonso, E. Solórzano, S. Estravís, M.A. Rodríguez-Pérez, J.A. de Saja, In situ evidence of the nanoparticle nucleating effect in polyurethane-nanoclay foamed systems, *Soft Matter*, 8 (2012) 11262.

[43] J.S. Colton, Nucleation of microcellular foam: Theory and practice, *Polymer Engineering & Science*, 27 (1987) 500-503.

[44] Z.-M. Xu, X.-L. Jiang, T. Liu, G.-H. Hu, L. Zhao, Z.-N. Zhu, W.-K. Yuan, Foaming of polypropylene with supercritical carbon dioxide, *The Journal of Supercritical Fluids*, 41 (2007) 299-310.

[45] A. Kraynik, D. Reinelt, F. van Swol, Structure of Random Foam, *Physical Review Letters*, 93 (2004).

[46] C. Saiz-Arroyo, M.A. Rodríguez-Pérez, J. Tirado, A. López-Gil, J.A. de Saja, Structure-property relationships of medium-density polypropylene foams, *Polymer International*, 62 (2013) 1324-1333.

[47] A. König, U. Fehrenbacher, T. Hirth, E. Kroke, Flexible Polyurethane Foam with the Flame-retardant Melamine, *Journal of Cellular Plastics*, 44 (2008) 469-480.

### 4.2 Corrugation influence on physical properties

Once the structure is studied in detail it was possible to elucidate the effect of the structural particularities on the final physical properties of the cellular materials such as mechanical or thermal properties [3, 4]. In particular, it is well known that the corrugation of the structure strongly affects the mechanical performance since the presence of wrinkles in a flat surface decreases the required force to buckle it [5]. However, the characterization of the corrugation and its influence on the properties of cellular materials has not been deeply studied in the literature.

The following work entitled **“Effect of solid phase corrugation on the thermo-mechanical properties of low density flexible cellular polymers”** deals with two novel methods to determine the corrugation of the solid phase of a collection of low density flexible cellular polymers. The two developed image analysis protocols are based on high resolution X-ray  $\mu$ -CT in order to properly reconstruct all the parts of the solid phase (cell walls and struts). Both methodologies permit extracting parameters directly related with the corrugation of the structure. Firstly, the Additional Surface of a cell (AS) is the result of normalizing the surface to volume ratio (S/V ratio) of the cell with the S/V ratio of the Kelvin cell of the same volume. Furthermore, the Curvature Variation (CV) is the Full Width at Half Maximum of the histograms of mean curvature distributions along the structure calculated by heavy processing and time consuming computations. It is shown in the manuscript how these two parameters are closely correlated.

These two parameters characterizing corrugation are then related with two physical properties of cellular polymers: collapse stress and thermal expansion coefficient.

In this manuscript we have defined the corrugation ratio as the ratio between the experimental and theoretical values of collapse stress and it is shown how this parameter is directly related with both AS and CV values. On the other hand, it is expected that the slight pressure increase due to temperature changes provokes an unexpected increase on thermal expansion coefficient due to the flattening of the

structure. For this reason, we have analysed the change on thermal expansion coefficient at 25 °C (manufacturing and experimentation temperatures) finding again good agreements with both *AS* and *CV* values.

Materials and Design (submitted)

### Effect of solid phase corrugation on the thermo-mechanical properties of low density flexible cellular polymers

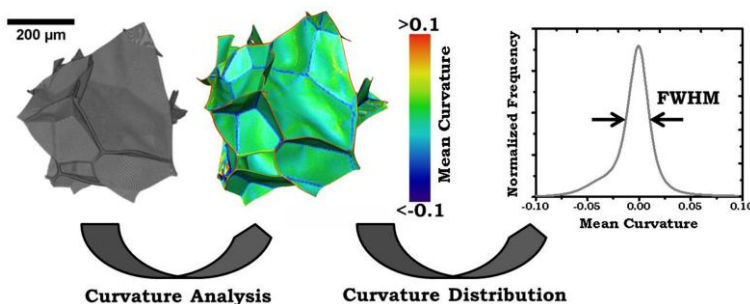
S. Pérez-Tamarit<sup>a,\*</sup>, E. Solórzano<sup>a</sup>, A. Hilger<sup>b</sup>, I. Manke<sup>b</sup>, M.A. Rodríguez-Pérez<sup>a</sup>

<sup>a</sup> CellMat Laboratory, University of Valladolid, Paseo de Belén 7 47011, Spain

<sup>b</sup> Helmholtz-Zentrum Berlin für Materialien und Energie, Lise-Meitner-Campus, Hahn-Meitner-Platz 1 14109, Berlin, Germany.

\* Corresponding author: [saul.perez@fmc.uva.es](mailto:saul.perez@fmc.uva.es)

Tel.: +34 983 423572; fax: +34 983 433192



#### Abstract

This manuscript presents the effect of the solid phase corrugation of low density flexible cellular polymers on both their mechanical and thermal properties. First, a detailed quantification of solid phase corrugation has been carried out by means of high resolution synchrotron micro-tomography in a collection of polyethylene foams. Subsequently, the collapse stress in compression has been analysed both from the theoretical and experimental points of view achieving a clear relation between the solid phase corrugation and the ratio of theoretically calculated and experimentally measured collapse stress. Finally, solid phase corrugation has been correlated with the thermal expansion coefficient at room temperature.

**Keywords:** synchrotron tomography; Imaging; 3D analysis; cellular polymers; solid phase corrugation; collapse stress; thermal expansion coefficient.

## 1. Introduction

Cellular polymers are biphasic materials in which a gaseous phase is dispersed into a solid phase [1]. As a consequence, the final physical properties of cellular polymers depend, on the one hand, on the amount of gas and its distribution throughout the structure, and, on the other hand, depend on a set of characteristics of the solid phase. Its tuneable structure has allowed cellular polymers becoming a good solution in a wide range of applications in several market sectors such as automotive, packaging, building, etc... [2]. In particular, low density flexible cellular polymers are characterized by relative densities lower than 0.1 and consequently solid architectures owning very thin cell walls (2-4 $\mu\text{m}$ ) [3, 4]. The low stiffness of the matrix polymer, the mentioned thin solid architecture and other factors, such as the reduced inner gas pressure, may cause the presence of wrinkles on the cell walls leading to an overall corrugation of the solid phase (Fig. 1) [3]. Fig. 1 shows tomography slices of two low density flexible polymers. Fig. 1(a) shows the structure of a sample with flat cell walls while Fig. 1(b) shows a foam in which cell walls present a significant degree of corrugation (i.e. the cell walls present wrinkles).

Low density flexible cellular materials are used to package fragile products against impact damage during transportation and in body protection such as helmets, knee pads, shin guards, etc...[5] For this

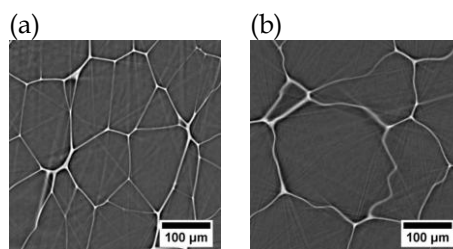


**Fig 1.** Tomography slices of low density cellular polymers with (a) solid phase with flat cell walls and (b) corrugated solid phase.

reason, the mechanical behaviour in compression is one of the most important properties of these materials [6]. Therefore, abundant scientific investigations have been focused on studying the compression behaviour of low density cellular polymers since 1959. Most of these theories consider that mechanical response depends on a multitude of parameters such as relative density, cell size, fraction of material in the foam edges and open cell content and pressure of the gas in cells [7-9]. However, few studies have been carried out in order to understand the effect of the solid phase corrugation on the mechanical properties due to the challenging fact of measuring this structural parameter [10, 11].

In fact, it is well known that the presence of wrinkles in a flat surface reduces the required force need to buckle it, in comparison with a totally flat surface [12]. In the case of low density cellular polymers, little imperfections in the solid phase can reduce the collapse stress of the samples, which is a critical mechanical parameter for the application

of these materials [13]. Therefore, investigating the exact influence of solid phase corrugation is crucial in order to manufacture optimum materials for the above-mentioned applications.

For this purpose, the first step consisted on developing accurate and robust characterization methods to determine the solid phase corrugation. Due to the reduced cell wall thickness of the selected samples we have used synchrotron  $\mu$ -CT data sets to obtain information from the cell walls at this resolution level [10, 14]. The information about solid phase corrugation has been obtained by self-developed methods, some of them requiring time-consuming algorithms (section 2.3). The influence of solid phase corrugation on the collapse stress is determined by comparing both experimental and theoretical values of this parameter (section 2.4). The influence of solid phase corrugation on thermal expansion has been also analysed in this investigation by comparing the slope of the expansion coefficient at 25 °C (section 2.5). It is well known that the thermal expansion coefficient of this type of cellular polymers is influenced by the solid phase corrugation [3, 15]. However, this influence was not studied in detail before due to the inherent difficulty of characterizing accurately this structural parameter.

Consequently, the main objective of this investigation is to determine the solid phase corrugation (presence of wrinkles in the cell walls), validate the indicators

developed in this investigation and quantify the effect of solid phase corrugation on thermo-mechanical properties (collapse stress and thermal expansion coefficient) of low density flexible cellular polymers. To this end, four cellular polymers based on a flexible polymer matrix fabricated by a foaming process which induces corrugation in the cell walls (section 2.1) have been used.

## 2. Experimental

### 2.1 Materials

The materials involved in this investigation are cross-linked closed-cell cellular polymers manufactured by a high-pressure nitrogen gas solution process [2]. The raw material used was a low density polyethylene (LDPE). In this process, an extruded sheet is irradiated and cross-linked and then placed in an autoclave. There, it is subjected to the high pressure of nitrogen gas at temperatures above the polymer softening point. Under these conditions, the nitrogen is dissolved into the polymer matrix. At the end of the solution stage and after cooling, the pressure is reduced to atmospheric pressure. Then, the materials are placed in a second low-pressure autoclave and again heated above the polymer melting point. The release of the pressure in this second step allows the full expansion of the polymeric material than can reach densities as low as 15 kg/m<sup>3</sup>. Finally, the foamed slabs are cooled to room temperature. The foams produced by this technology are isotropic



**Table 1.** Density and cellular structure characteristics of the cellular polymers under study.

Sample	Density ( $\rho_f$ ) [kgm <sup>-3</sup> ]	Cell size ( $\phi$ ) [ $\mu$ m]	Coordination number ( $n_i$ )	Fraction of mass in struts ( $f_s$ )
LDPE-1	16.4 $\pm$ 0.4	310 $\pm$ 50	14.1 $\pm$ 3.3	0.117
LDPE-2	20.2 $\pm$ 0.5	270 $\pm$ 50	13.8 $\pm$ 3.1	0.122
LDPE-3	31.2 $\pm$ 0.8	260 $\pm$ 50	14.1 $\pm$ 3.0	0.176
LDPE-4	41.3 $\pm$ 0.5	340 $\pm$ 60	13.7 $\pm$ 3.1	0.390

closed cell cellular polymers [16]. In this process, the reduction of temperature in the cooling step promotes a reduction of the gas pressure in the cells that results into a corrugation of the cell walls due to the low strength of the solid phase structure, composed of very thin cell walls (thickness 2-4  $\mu$ m) [16] of a flexible polymer (LDPE). Some of the main descriptors of both the gas and solid phases for the materials under study have been measured using a multi-scale characterization based on X-ray tomography [17]. These structural characteristics have been summarized in

Table 1.

2.2 Synchrotron X-ray  $\mu$ -CT

Considering the reduced thickness of cell walls these samples (around 2-4  $\mu$ m) [17], the analysed specimens were scanned using synchrotron X-ray micro-tomography ( $\mu$ -CT) at BAMline (BESSY II synchrotron, HZB, Berlin) [18]. The specific conditions of the tomographic experiments in terms of low energy (9.8 keV), long exposure time (3000 ms), and number of projections (2200) allowed obtaining tomographic results with excellent contrast (Fig. 2 TOP). Further,

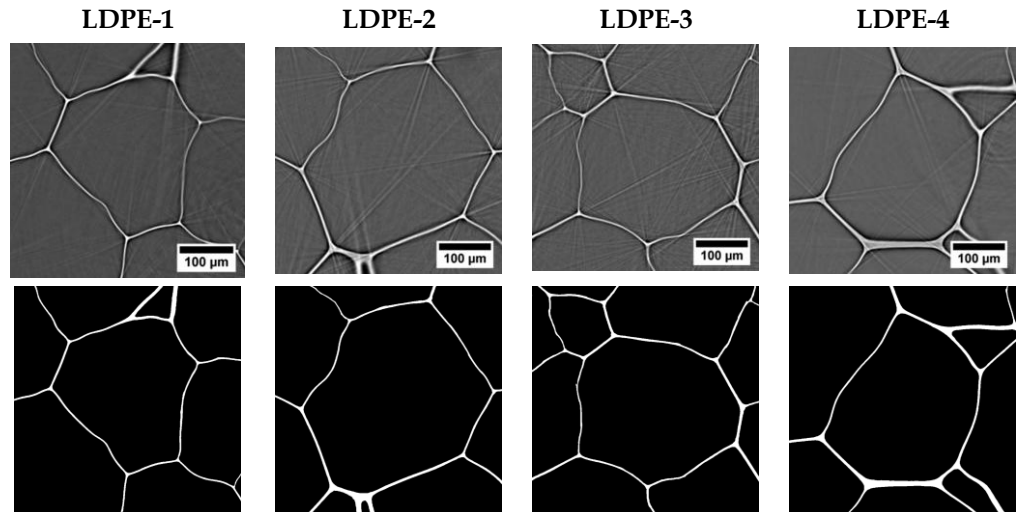


**Fig. 2.** Grey-level slices –TOP– and binarized slices –BOTTOM– for all the foam specimens under study.



the reached spatial resolution (0.438  $\mu\text{m}$  of voxel size) permitted reconstructing the thinnest parts of the solid phase of all the tested cellular polymers (Fig. 2 BOTTOM). The tomography-scanned volumes corresponded to approx. 3  $\text{mm}^3$ .

##### 2.3 Curvature analysis

We have selected two different methods to obtain quantifiable values of the solid phase corrugation.

On the one hand, several pores have been analysed calculating their volume and surface and directly obtaining their surface/volume ratio  $((S/V)^{\text{cell}})$  by using Avizo software package [19]. Then, since the cell geometry for this type of materials is mainly tetrakaidecahedral (average coordination number of 14 (Table 1), i.e. an average of 14 walls per cell) and the cells are isotropic [16, 17], the surface/volume ratio has been normalized considering the surface/volume ratio of a regular Kelvin cell containing the same volume  $((S/V)^{\text{Kelvin}})$  [1, 20]. The normalization of the surface/volume ratio allowed us eliminating the influence of pore size in the surface/volume ratio values. Finally, the Additional Surface (AS) due to cell wall corrugation is calculated as expressed in Eq. (1).

$$AS(\%) = 100 \cdot \left( \frac{(S/V)^{\text{cell}}}{(S/V)^{\text{Kelvin}}} - 1 \right) \quad (1)$$

This simple parameter reveals differences between materials and seems to be a good indicator of the presence of

wrinkles in the solid structure, as it will be shown in the results section. In fact, other works in the literature have dealt with a similar parameter but considering the equivalent sphere to normalize the S/V ratio of the cells finding values for AS around 120% (normalized S/N 2.2) [10]. Consequently, it is proved in this work that the election of the corresponding Kelvin cell as reference for normalization and the selection of AS as the representing parameters seems to be more appropriate.

On the other hand, a more complex method based on surface discretization by means of surface meshing has been used. It uses triangles and a method for local surface approximation by continuous mathematical functions [21, 22]. Several geometrical parameters can be calculated from this analysis, all of them based on the two principal radii of curvatures of the surface,  $r_1$  and  $r_2$ . Among all the possible curvatures definition (mean, maximum, minimum, Gaussian, etc.) we have selected the mean curvature ( $C_a$ ) as a quantifiable indicator of the presence of wrinkles. Mean curvature is defined in Eq. (2) as a function of the above mentioned radii.

$$C_a = \frac{1}{2} \left( \frac{1}{r_1} + \frac{1}{r_2} \right) \quad (2)$$

A negative value of the local mean curvature corresponds to strictly concave regions whereas local positive values of this parameter are located in strictly convex surfaces. The main advantage of computing mean curvature instead of

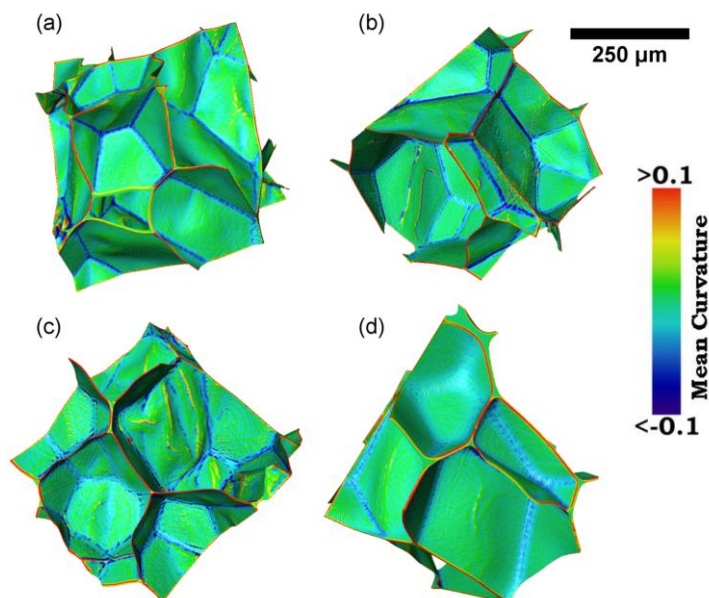


**Fig. 3.** Surface mean curvature maps for a volume of  $900 \times 900 \times 900$  voxels<sup>3</sup>. (a) LDPE-1 (b) LDPE-2 (c) LDPE-3 and (d) LDPE-4

Gaussian curvature is its wider distribution and higher sensitivity to local variations [23, 24].

The curvature computation was carried out using Avizo software package [19]. The method uses a marching-cubes algorithm to create a triangular mesh in the cellular polymer structure surface [25, 26]. This mesh is smoothed by an iterative computational process so the local pixel “roughness” is almost eliminated. Smoothing is accomplished by shifting the triangular vertexes to average positions, considering the neighbours. Maximum shifting of 50% (rather low value) and a high number of iterations (10) were the parameters considered to remove local variations without significantly modifying the original surface. The mean curvature analysis was accomplished considering a surface field

including a significant number of neighbouring triangles. After proper optimization we considered 20 neighbouring triangles in the computations. The high compliance reached by using such neighbourhood conditions made it unnecessary to iterate and refine the mean curvature calculation. The typical computation time under these conditions was between 6 and 8 hours. In order to eliminate local effects in the different samples three different volumes of interest ( $900 \times 900 \times 900$  voxels or  $0.4 \times 0.4 \times 0.4$  mm<sup>3</sup>) were analysed obtaining similar results in all zones. The results for one of the analysed zones in each material are shown in Fig. 3. The final output is represented as histograms of mean curvature distribution using the same representation range and number of bins.

#### 2.4 Collapse stress

One of the most critical physical properties of low density flexible cellular polymers is the collapse stress which is defined as the strain at which elastic buckling of the cell walls of the cellular materials occurs [27]. From a theoretical point of view this property depends on density, properties of the solid phase, cell geometry, fraction of material in the struts and corrugation of the solid phase [9, 28]. However, this last parameter has never been considered in the traditional models described at the beginning of section 2.4.1. It is expected that the presence of wrinkles on the cellular structure should lead to a significant reduction of collapse stress and therefore we have proposed a semi-empirical parameter which takes corrugation into account.

##### 2.4.1 Geometrical modelling of collapse stress

Gibson and Ashby (1988) suggested an analytical model [1] to account for the collapse stress ( $\sigma_c$ ) of cellular polymers (Eq. (3)). They considered isothermal conditions with short timescales, and hence no gas diffusion, in a cubic cell structure.

$$\sigma_c = E_s G \left( \rho_f / \rho_s \right)^2 \quad (3)$$

Where  $\rho_f$  is the density of the cellular polymer,  $\rho_s$  is the density of the matrix polymer and  $E_s$  is the Young modulus of the solid polymer. In addition,  $G$  is a

geometric constant whose value, proposed by Gibson and Ashby, is 0.05.

But instead of using the simple cubic geometry a better approximation is reached if cells are modelled as tetrakaidecahedrons. In the case of a cell face with width  $w$ , side  $a$  and thickness  $\delta$ , the compression force required to initiate the elastic buckling of a cell face ( $F_c$ ) is given by Euler's formula:

$$F_c = \left( \frac{2\pi}{a} \right)^2 E_s \frac{w\delta^3}{12} \quad (4)$$

In addition, we need to take into account the relationship between the cellular structure characteristics and the cellular material density [29]:

$$\frac{\rho_f}{\rho_s} = \frac{C}{1-f_s} \left( \frac{\delta}{\phi} \right) \quad (5)$$

Where  $C$  is a constant that depends on cellular geometry and  $f_s$  is the fraction of material in the struts. Combining Eqs. (4) and (5) the collapse stress can be described as follows:

$$\frac{\sigma_c}{E_s} = G \left( \frac{\rho_f}{\rho_s} \right)^2 = \frac{1}{12} \left[ \frac{2\pi(1-f_s)B}{C} \right]^2 \left( \frac{\rho_f}{\rho_s} \right)^2 \quad (6)$$

Where  $B$  is a constant that condensates other geometric constants. Assuming that cells have the geometry of tetrakaidecahedrons the constants  $B$  and  $C$  can be calculated [1] taking the following values:  $B=2.828$  and  $C=3.348$ .

Eq. (6) accounts for the collapse stress assuming flat cell walls. In order to introduce the solid phase corrugation the previous equation was modified

introducing the so-called “corrugation ratio” ( $\xi$ ) (Eq. (7)) [30]. This term is related to the cellular structure and more specifically to the presence of wrinkles in the cellular polymer structure. Further, this parameter varies between 0 and 1; i.e., a value of 1 indicates that cell faces are flat whereas lower values indicate that the solid phase presents some degree of corrugation.

$$\frac{\sigma_c}{E_s} = \frac{1}{12} \left[ \frac{2\pi(1-f_s)B}{c} \right]^2 \left( \frac{\rho_f}{\rho_s} \right)^2 \xi \quad (7)$$

Then, a simple way to estimate this corrugation ratio is to compare the experimental values of the collapse stress ( $\sigma_c^{exp}$ ) with the theoretical values given by Eq. (4) ( $\sigma_c^{theo}$ ), as indicated in Eq. (8).

$$\xi = \frac{\sigma_c^{exp}}{\sigma_c^{theo}} \quad (8)$$

#### 2.4.2 Experimental measurement of the collapse stress

In order to measure experimentally the collapse stress of the materials under study a collection of compressive mechanical tests have been carried out by

using a universal testing machine (Mod. 5.500R6025, INSTRON) at room temperature (25 °C) and low deformation rate. At these experimental conditions, the required stress ( $\sigma$ ) in order to achieve a determined strain ( $\epsilon$ ) is calculated by the following expression [31]:

$$\sigma = \sigma_c + \frac{p_{atm}\epsilon(1-2\nu)}{1-\epsilon-\rho_f/\rho_s} \quad (9)$$

Where  $p_{atm}$  is the atmospheric pressure during the experiment and  $\nu$  is the material Poisson' ratio. A typical stress-strain curve of this type of materials (sample LDPE-3) is shown in Fig. 4(a). The collapse stress can be measured as the intercept of the straight line with the y axis when plotting the stress in the post collapse zone (strain from 0.2 to 0.5) versus  $\epsilon/(1-\epsilon-\rho_f/\rho_s)$  (so-called volumetric strain) as it is shown in Fig. 4(b).

#### 2.5 Thermal expansion coefficient

On the other hand, linear thermal expansion coefficient has been determined by Eq. (10):

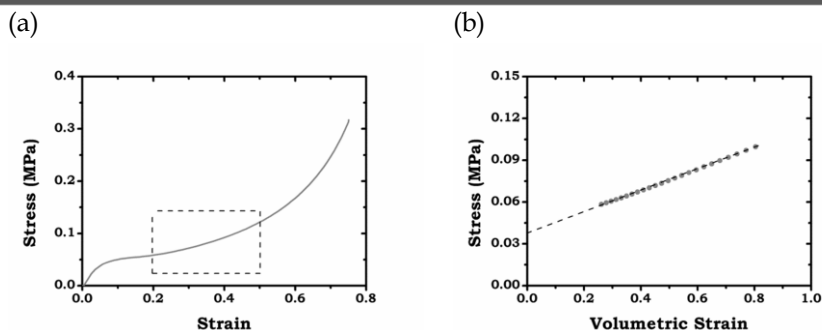


Fig. 4. Stress vs strain compression curve (a) and (b) stress vs volumetric-strain in the post collapse zone for sample LDPE-3.

$$\alpha = \frac{1}{l_0} \frac{dl}{dT} \quad (10)$$

Where  $l_0$  is the original length (or height) at a reference temperature (25°C in this work) and  $l$  is the length (or height) of the sample at temperature  $T$ . It is known that this parameter is very sensitive to the presence of wrinkles in the structure of elastic cellular polymers [3]. As it will be shown in the results section, by analysing the variation of this parameter at 25°C it is possible to elucidate the presence of cell-wall wrinkles and determine an approximate magnitude of corrugation in the solid phase of these materials. The enclosed-gas suffers a pressure increase due to the temperature rise which promotes that the wrinkles of the structure disappear at increasing temperature. This can be detected analysing the derivative value of the thermal expansion coefficient at temperature near 25 °C, i.e. the punctual slope of the thermal expansion coefficient at 25 °C. This temperature is selected since it corresponds to the temperature at which synchrotron  $\mu$ -CT and mechanical

tests were performed.

In our case, the thermal expansion coefficient has been experimentally determined by using a thermo-mechanical analyser (TMA, Perkin-Elmer TMA7) equipped with quartz parallel plate probe in order to measure the material changes in height over a temperature range from -20°C to 100°C with a heating rate of 3°C/min. The analysed samples in this case were cylinders of 10 mm in diameter and 10 mm in height. In addition, at least three different experiments for each foam sample were carried out. Fig. 5 shows a typical thermal expansion curve (sample LDPE-1) of normalized sample length ( $l/l_0$ ) and the linear thermal expansion coefficient (calculated using Eq. (10)) as a function of temperature.

### 3. Results and discussion

#### 3.1 Solid phase corrugation

As mentioned above in the manuscript, two different methods of analysis for the solid phase corrugation have been

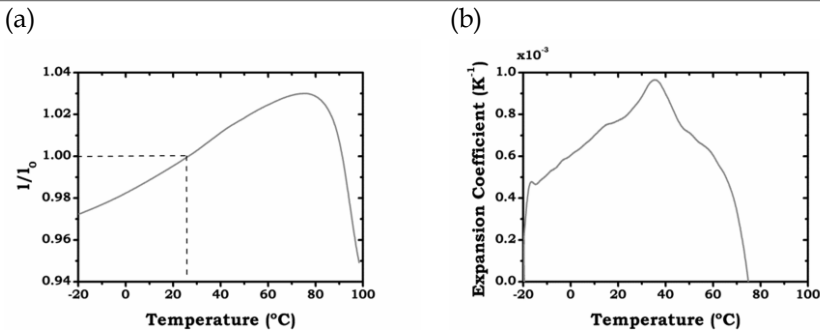


Fig. 5. (a) Normalized sample thickness ( $l/l_0$ ) and (b) thermal expansion coefficient as a function of temperature for LDPE-1 sample.

employed. On one hand, mean curvature distributions of three different volumes of interest for each material have been suitably averaged. These histograms are shown in Fig. 6. All the curves presented a slight asymmetry to negative values due to the concavities of the cells in the material. In this case, we have defined the Curvature Variation (CV) as the parameter characterizing the solid phase corrugation. This parameter corresponds to the full-width at half-maximum (FWHM) of the mean curvature histograms. A higher degree of corrugation in the solid structure promotes a wider curvature distributions and vice versa. Table 2 shows the results for this selected corrugation indicator. There is a clear difference between materials (up to 34% between LDPE-3 and LDPE-4).

In addition, Table 2 shows the obtained values for the Additional Surface (AS). Once again, differences between materials can be appreciated, although the maximum differences are smaller (23% between LDPE-3 and LDPE-4).

It is important to mention that both

**Table 2.** Summary of results on solid phase corrugation for the materials under study.

Sample	Additional Surface (AS) (%)	Curvature Variation (CV)
LDPE-1	4.74±0.38	0.02377
LDPE-2	4.30±0.3	0.02180
LDPE-3	4.84±0.5	0.02666
LDPE-4	3.87±0.26	0.01783

parameters are directly correlated, as demonstrated in Fig. 7. According to the results, AS parameter is less sensitive to changes than CV, with nearly 30% higher maximum variation.

### 3.2 Collapse stress

The relation between the experimental and theoretical values of collapse stress (corrugation ratio) is determined in this section and compared with the geometrically-extracted parameters. To this end, experimental values are determined as explained in section 2.4.2. Moreover, the theoretical values of collapse stress are calculated using Eq. (6) and considering the Young modulus of

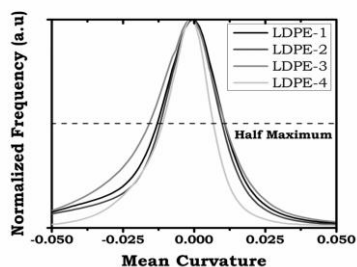


**Fig 6.** Mean curvature distributions for the four analysed cellular materials.

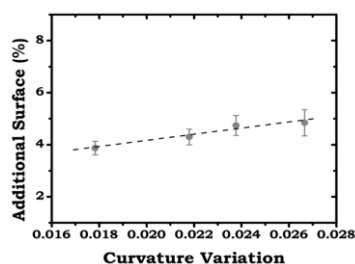


**Fig 7.** Relationship between the AS and CV, the two parameters extracted from the tomographic data and used to quantify the solid phase corrugation.



the solid LDPE,  $E_s$ , of 200 MPa. Both theoretical and experimental values of collapse stress are presented in Fig. 8.

As a consequence, the defined corrugation ratio (Eq. (8)) for the analysed samples takes values between 0.4 (LDPE-3) to 0.6 (LDPE-4). Fig. 9 shows that there is clear relation between the corrugation ratio and both Additional Surface and Curvature Variation. In the proposed trend (dashed line) the corrugation ratio tends to one when the CV tends to zero. A very similar trend is also observed for AS parameter including the validation that corrugation ratio tends to one when AS tends to 0. Both parameters are equally correlated with corrugation ratio. These results confirm our hypothesis; the solid phase corrugation is playing a clear role on the collapse stress of the foams.

## 3.3 Thermal expansion coefficient

Fig. 10 shows the results thermal expansion coefficient for all the materials under study. In all cases, the absolute value of thermal expansion coefficient for each temperature value is inversely

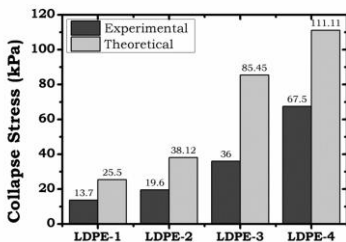


Fig 8. Experimental and theoretical values of collapse stress

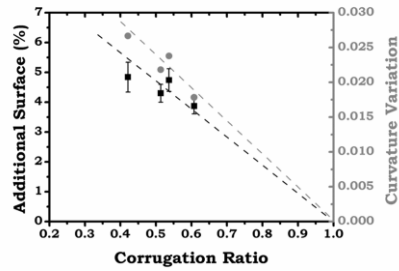


Fig 9. Experimental relationship of corrugation ratio with AS and CV.

related with the density of the foamed materials due to the higher gas volume percentage and the higher capacity of expansion of this gaseous phase in comparison with the solid phase [15]. For this reason, the higher thermal expansion coefficients are observed for LDPE-1 (density 16.4 kg/m<sup>3</sup>) whereas the lower values are for LDPE-4 (density 41.3 kg/m<sup>3</sup>). This tendency is maintained almost up to 40°C. At temperatures above that values do not follow a clear trend since the polymeric matrix softens and other effects take place.

The slope of the thermal expansion coefficient curve at 25 °C is determined to

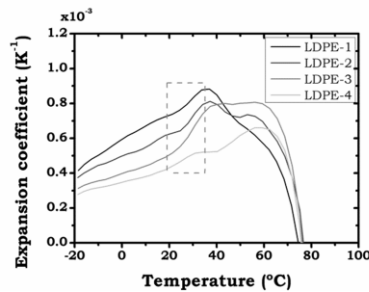


Fig 10. Thermal expansion coefficient values of the analysed samples. The dashed square marks the temperature region in which the cell-wall flattening is taking place.

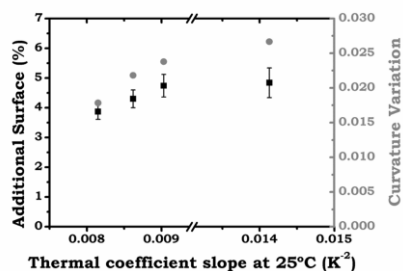


Fig 11. Dependence of thermal expansion coefficient slope at 25°C with AS and CV.

evaluate the influence of solid phase corrugation on thermal expansion coefficient. The results of this analysis can be observed in Fig. 11. The material showing the greatest slope of the thermal expansion coefficient corresponds with the material with the highest solid phase corrugation, being therefore sample LDPE-3, whereas sample LDPE-4, which is the sample with the less corrugated structure, is the sample with a lower variation of thermal expansion coefficient at the mentioned temperature.

As it has been previously discussed the parameter CV allows obtaining higher differences between materials than the AS (34% of variation *vs.* 23%) and seems to be slightly better correlated. As a consequence, this parameter is a more sensitive indicator of corrugations than the Additional Surface. For this reason, we consider that Curvature Variation is the most recommended microstructural indicator of solid phase corrugation. It has also to be taken into account inherent technical (synchrotron  $\mu$ -CT at 0.438 microns resolution) and computational (complex computation method, long

computing times) difficulties to determine it.

#### 4. Conclusions

We have determined the effect of solid phase corrugation in low density flexible foams on two representative physical properties, the collapse stress and the thermal expansion coefficient. To this end, two different image analysis protocols applied to synchrotron  $\mu$ -CT data sets with enough spatial resolution were developed. The two parameters defined to evaluate the solid phase corrugation are the Additional Surface, linked to the surface of the real cell in comparison to a model cell with the same volume but with flat cell walls and the Curvature Variation which corresponds to the FWHM of mean curvature distributions. It has been proved that these two parameters are mutually correlated and that Curvature Variation is slightly more sensitive to the presence of wrinkled cell walls in these foam specimens.

The results obtained for these two parameters can be well correlated with the two physical properties selected. An increase of the solid phase corrugation reduces the collapse stress of the foams and increases the slope of the thermal expansion curve at a temperature of 25 °C.

#### 5. Data availability

The raw/processed data required to reproduce these findings cannot be



shared at this time as the data also forms part of an ongoing study.

### Acknowledgements

Financial assistance from MINECO, FEDER, UE (MAT2015-69234-R) and the Junta de Castile and Leon (VA011U16) are gratefully acknowledged. Predoctoral contract of S. Perez-Tamarit by University of Valladolid (E-47-2015-0094701) and co-financed by Banco Santander is also acknowledged. Finally, we acknowledge the support from Bessy II (HZB, Berlin, Germany) to complete this work (proposal 14100497-ST).

### References

- [1] L.J. Gibson, M.F. Ahsby, *Cellular Solids: Structure and Properties*, Pergamon Press, Oxford, England, 1988.
- [2] M.A. Rodríguez-Pérez, *Crosslinked Polyolefin Foams: Production, Structure, Properties, and Applications*, *Advances in Polymer Science*, 184 (2005) 97-126.
- [3] O. Almanza, Y. Masso-Moreu, N.J. Mills, M.A. Rodríguez-Pérez, Thermal expansion coefficient and bulk modulus of polyethylene closed-cell foams, *Journal of Polymer Science Part B: Polymer Physics*, 42 (2004) 3741-3749.
- [4] M.A. Rodríguez-Pérez, J.I. Gonzalez-Peña, J.A. de Saja, Modifying the structure and properties of polyethylene foams using thermal treatments, *Polymer International*, 58 (2009) 620-629.
- [5] N.J. Mills, M.A. Rodríguez-Pérez, Modelling the glass-loss creep mechanism in EVA foam from running shoes, *Cellular Polymers*, 20 (2001) 79-99.
- [6] V. Bernardo, E. Laguna-Gutierrez, A. Lopez-Gil, M.A. Rodríguez-Pérez, Highly anisotropic crosslinked HDPE foams with a controlled anisotropy ratio: Production and characterization of the cellular structure and mechanical properties, *Materials & Design*, 114 (2017) 83-91.
- [7] A.N. Gent, A.G. Thomas, The Deformation of Foamed Elastic Materials, *Journal of Applied Polymer Science*, 1 (1959) 107-113.
- [8] A.N. Gent, A.G. Thomas, Mechanics of foamed elastic materials, *Rubber Chemistry and Technology*, 36 (1963) 597-610.
- [9] L.J. Gibson, Modelling the Mechanical Behavior of Cellular Materials, *Materials Science and Engineering: A*, 110 (1989) 1-36.
- [10] S. Pardo-Alonso, E. Solorzano, J. Vicente, L. Brabant, M.L. Dierick, I. Manke, A. Hilger, E. Laguna, M.A. Rodríguez-Pérez, *muCT-Based Analysis of the Solid Phase in Foams: Cell Wall Corrugation and other Microscopic Features*, *Microscopy and Microanalysis*, 21 (2015) 1361-1371.
- [11] A.E. Simone, L.J. Gibson, The effects of cell face curvature and corrugations on the stiffness and strength of metallic foams, *Acta Materialia*, 46 (1998) 3929-3935.
- [12] J.L. Grenestedt, Influence of wavy imperfections in cell walls on elastic stiffness of cellular solids, *Journal of the Mechanics and Physics of Solids*, 46 (1998) 29-50.
- [13] D. Klempner, K.C. Frish, *Handbook of Polymeric Foams and Foam Technology*, in: Hanser (Ed.), 1991.
- [14] E.M. Stokely, S.Y. Wu, Surface Parametrization and Curvature Measurement of Arbitrary 3-D Objects: Five Practical Methods, *IEEE Transactions on Pattern Analysis and Machine Intelligence*, 14 (1992) 833-840.
- [15] M.A. Rodríguez-Pérez, O. Alonso, A. Duijens, J.A. De Saja, Thermal expansion of crosslinked closed-cell polyethylene foams, *Journal of Polymer Science Part B: Polymer Physics*, 36 (1998) 2587-2596.
- [16] O. Almanza, M.A. Rodríguez-Pérez, J.A. de Saja, The microstructure of polyethylene foams produced by a nitrogen solution process, *Polymer*, 42 (2001) 7117-7126.
- [17] S. Pérez-Tamarit, E. Solórzano, A. Hilger, I. Manke, M.A. Rodríguez-Pérez, Multi-scale tomographic analysis of polymeric foams: A detailed study of the cellular structure, *Soft Matter*, (submitted) (2018).
- [18] A. Rack, S. Zabler, B.R. Müller, H. Riesemeier, G. Weidemann, A. Lange, J. Goebbels, M. Hentschel, W. Görner, High resolution synchrotron-based radiography and tomography using hard X-rays at the BAMline (BESSY II), *Nuclear Instruments and Methods in Physics Research Section A: Accelerators, Spectrometers, Detectors and Associated Equipment*, 586 (2008) 327-344.
- [19] <https://www.fei.com/software/amira-avizo/>.
- [20] W.E. Warren, A.M. Kraynik, Linear elastic behavior of a low-density kelvin foam with open cells, *Journal of Applied Mechanics*, 64 (1997) 787-794.
- [21] H. Jinnai, T. Koga, Y. Nishikawa, T. Hashimoto, S.T. Hyde, Curvature Determination of Spinodal Interface in a Condensed Matter System, *Physical Review Letters*, 78 (1997) 2248-2251.

- [22] D. Kammer, P. Voorhees, The morphological evolution of dendritic microstructures during coarsening, *Acta Materialia*, 54 (2006) 1549-1558.
- [23] E. Magid, O. Soldea, E. Rivlin, A comparison of Gaussian and mean curvature estimation methods on triangular meshes of range image data, *Computer Vision and Image Understanding*, 107 (2007) 139-159.
- [24] J. Alkemper, P.W. Voorhees, Three-dimensional characterization of dendritic microstructures, *Acta Materialia*, 49 (2001) 897-902.
- [25] A. Lopez, K. Brodlie, Improving the robustness and accuracy of the marching cubes algorithm for isosurfacing, *IEEE TRANSACTIONS ON VISUALIZATION AND COMPUTER GRAPHICS*, 9 (2003).
- [26] W.E. Lorensen, H.E. Cline, Marching cubes: A high resolution 3D surface construction algorithm, *Computer Graphics*, 21 (1987).
- [27] L.J. Gibson, Biomechanics of cellular solids, *Journal of biomechanics*, 38 (2005) 377-399.
- [28] M.A. Rodríguez- Perez, J. Lobos, C.A. Perez-Muñoz, J.A. De Saja, L. Gonzalez, B.M.A. del Carpio, Mechanical Behaviour at Low Strains of LDPE Foams with Cell Sizes in the Microcellular Range: Advantages of Using These Materials in Structural Elements, *Cellular Polymers*, 27 (2008).
- [29] R.A. Campo-Arnáiz, M.A. Rodríguez-Pérez, B. Calvo, J.A. de Saja, Extinction coefficient of polyolefin foams, *Journal of Polymer Science Part B: Polymer Physics*, 43 (2005) 1608-1617.
- [30] E. Laguna Gutiérrez, E. Solórzano, S. Pardo-Alonso, M.A. Rodríguez- Perez, Modelling the compression behaviour of low-density flexible foams with a partially inter-connected cellular structure, *SPE FOAMS*, 2012.
- [31] Y. Masso Moreu, N.J. Mills, Rapid hydrostatic compression of low-density polymeric foams, *Polymer Testing*, 23 (2004) 313-322.

### 4.3 4D monitoring of the foaming process

This chapter presents the description of the main results obtained during the experimental campaign carried out at TOMCAT beamline at Swiss Light Source (SLS) in the Paul Scherrer Institute (PSI). The current setup at TOMCAT allows obtaining a temporal resolution below 1s and pixel size of a few microns ( $<5\mu\text{m}$ ) and consequently it was possible to monitor the full expansion process of several PU pure and composite foams.

Bi-component BASF rigid PU system was a suitable choice for this type of experiment. Long cream time and relatively slow expansion are desired since samples expansion and internal movement are one of the main aspects to avoid motion artefacts such as blurring in tomograms. Furthermore, a special care was taken during setup design to allow in-situ mixing during a few seconds to promote the reaction between isocyanate and polyol, in the same container tomography will be performed. Subsequently, an automatism for mixing and promoting the rising of liquids was designed since we were mainly interested in the very first foaming stages when cells are starting to nucleate.

The campaign was basically focused on studying samples of the same rigid BASF PU formulation with different nanofillers at different contents. Increasing contents of Cloisite 30B, Aerosil R812 and Aerosil A200 were selected for this purpose. The reactants were carefully placed inside the mould by a syringe (0.23 grams of polyol containing the particles and 0.36 grams of isocyanate). For the experiments, we set a pixel size of 3.333  $\mu\text{m}$ , 0.5ms exposure time for every radiogram and a total of 300 projections around the  $180^\circ$ . This results in a total scan time for every single tomogram of 156.8ms. 50 flatfields and 20 darkfield images were acquired for image correction purposes. Field of view was an area of 11.28  $\text{mm}^2$  with the configuration used.

The experimental results concerning the nucleation and growth on both a pure PU and a nanosilica composite PU sample are detailed addressed in the following work

entitled “In-situ understanding of pore nucleation and growth in polyurethane foams by using real-time synchrotron X-ray tomography”.

Physical Review Letters (submitted)

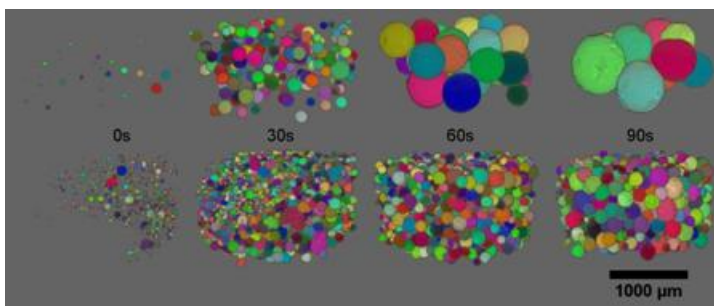
### In-situ understanding of pore nucleation and growth in polyurethane foams by using real-time synchrotron X-ray tomography

S. Pérez-Tamarit<sup>a,\*</sup>, E. Solórzano<sup>a</sup>, R. Mokso<sup>b</sup>, M.A. Rodríguez-Pérez<sup>a</sup>

<sup>a</sup> CellMat Laboratory, University of Valladolid, Paseo de Belén 7 47011, Spain

<sup>b</sup> Swiss Light Source, Paul Scherrer Institute, Villigen, Switzerland

\* Corresponding author: [saul.perez@fmc.uva.es](mailto:saul.perez@fmc.uva.es)  
Tel.: +34 983 423572; fax: +34 983 433192



#### Abstract

The nucleation and growth of pores in polyurethane foams have been visualized for the first time in 4D by using time-resolved X-ray tomography at maximum speed of 7Hz. Homogeneous and heterogeneous nucleation and subsequent bubble growth dynamics has been studied for materials with and without nucleating nanoparticles. Analysis of the tomographic sequences allowed determining the bubble nucleation rate, bubble density and bubble size evolution. A comparison with theoretical models for nucleation and growth has been carried out finding reliable correlations.

Bubble nucleation and growth are critical steps in any foaming process. They are linked to a thermodynamic instability in a specific gas-liquid system. Gas is dissolved into the liquid phase until the solubility limit is reached. At this moment, it precipitates in form of sub-micron metastable nuclei that may both collapse or grow upon a critical diameter. As part of this process a thermodynamical energy barrier must be overcome according to the classical homogeneous nucleation theories [1-3]. Moreover, the presence of particles and/or impurities in the liquid phase may significantly alter the homogeneous bubble nucleation of purified media due to further physical interactions. Under this situation, the local perturbations at gas/liquid interface could facilitate the formation of bubble nuclei increasing consequently the total number of nucleated bubbles. This is the so-called heterogeneous nucleation process [4] that typically reduces the nucleation energy barrier yielding superior bubble densities [5]. Furthermore, it is well known that both size and shape of nucleating particles influence their nucleation potential. The higher is the shape irregularity and lower the size of the particles, the higher is the expected nucleation capability [6]. Therefore, nanoparticles seem to be ideal nucleating agents for bubbles [7]. Nevertheless, interfacial compatibility plays also important role. In this sense the most interesting nucleating agents are those with chemically-modified surface, thus enhancing the interaction between

additive and matrix [8]. This surface compatibilization may affect apparent viscosity and surface tension among other rheological properties [9]. After nucleation has taken place, bubble growth occurs. The equations governing these interactions depend, among other factors, on the diffusion equations considering the available amount of gas and the kinematic characteristics of the fluid [10,11]. In addition, degeneration mechanisms of the cellular structure such as film drainage, coarsening or coalescence may occur [12,13].

The fragility of these systems and the complexity of physico-chemically coupled mechanisms need from advanced nondestructive techniques with sufficient temporal and spatial resolution. Our research group has used time-resolved X-ray imaging (so-called radioscopy to study the bubble nucleation and growth in different polymer/gas systems with considerable success [14-18]. These studies were performed in 2D, at a rather low speed (2Hz) and with a considerable time span from mixing to X-ray monitoring of typically 40-50 seconds.

Last developments at synchrotron facilities, with X-ray intensities  $10^6$  higher than lab systems, open the possibility of performing time-resolved X-ray tomography experiments reaching up to 20 Hz micro-tomography ( $\mu$ -CT) scans [19-21]. In this study we make use of these recent advances to perform time resolved X-ray tomography experiments

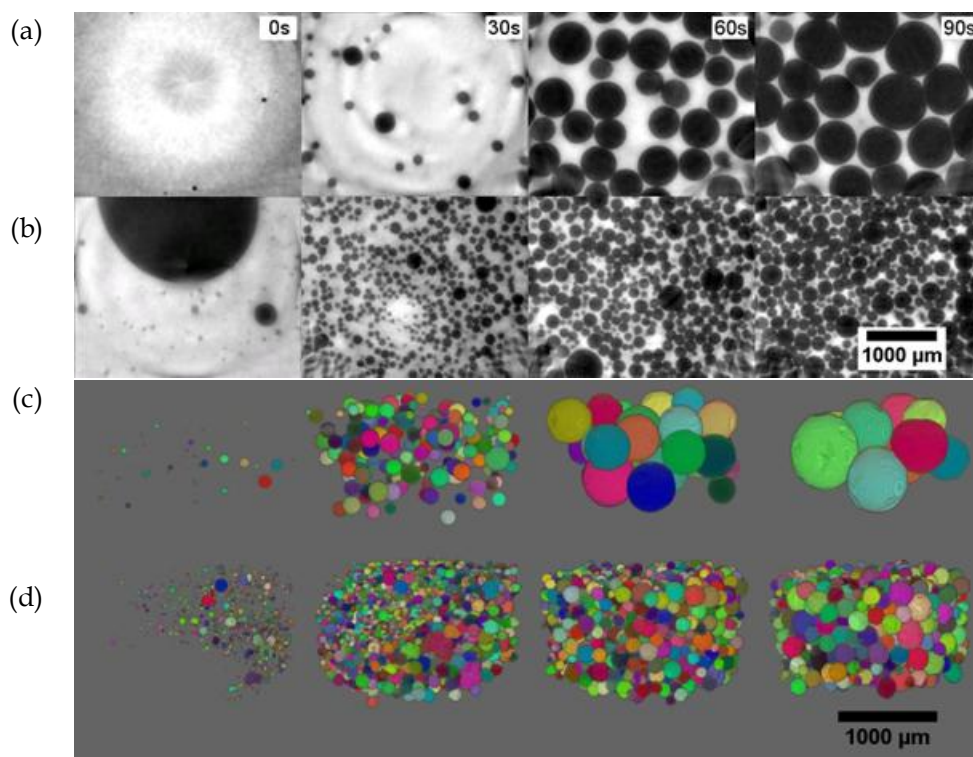


**Fig. 1.** Reconstructed slices for the two scanned systems at different times of the foaming process. Neat PU (a) and PU containing silica nanoparticles (b). 3D rendering of the analyzed cells at the same times in Neat PU (c) and PU containing silica nanoparticles (d).

analyzing the bubble generation and growth in reactive polyurethane (PU) foams in absence/presence of silica nanoparticles reaching temporal resolutions of 156ms per scan and with a high 3D spatial resolution of 3.2 μm. One of the additional innovations included in our study was the design of an *in-situ* mixing system to eliminate the span time and scan the samples immediately after mixing.

A bi-component PU formulation from BASF was selected for this investigation. Previous research has proved this system is stable, not showing degeneration

mechanisms such as coalescence or coarsening [15]. The mixing of two components, isocyanate (IsoPMDI 92140) and polyol blend (Elastopor H 1501/1) (which contains catalyst, surfactants, blowing agent and polyol) promotes simultaneous blowing and gelling reactions that results into a solid cellular polymer after few minutes (gel time  $145 \pm 18$  s) [22]. The nanoparticle selected for the comparative study was a hydrophobic fumed nanosilica (R812 from Evonik Industries, Germany) post-treated with hexamethyldisilazane [23]. 3%wt of nanosilica was previously dispersed (120s) in the isocyanate

component. A miniature specific mixing system was designed and used in order to *in-situ* promote the chemical reactions. Both PU components were placed inside a 75  $\mu\text{m}$  thickness kapton cup ( $h=40$  mm,  $\varnothing=12\text{mm}$ ) coupled to the tomography rotation table (Aerotech ABRT-200). The mixture was stirred during 15s at 1500rpm, and then the first tomography of the sequence was acquired. In this study, we have analyzed only the first 90s of the process in which both nucleation and approximately 70% of the total expansion take place.

Experiments were performed at the TOMCAT beamline of the Swiss Light Source at the Paul Scherrer Institute (Villigen, Switzerland). The experimental end-station incorporates a PCO.Dimax camera coupled with LuAg:Ce 100  $\mu\text{m}$  thick scintillator by 90° optical system and monochromatic beam (20 keV, no filter). During acquisition, 300 projections over 180° of rotation with a total scan time of 156ms are captured. Analyzed data considers 1.4s between scans. Once the tomography sequences were acquired, reconstructions were performed by using a Fourier-based GRIDEC algorithm [24]. Slices of the comparatively scanned materials at several moments of the foaming process are shown in FIG. 1. This figure already shows a clear difference between the two materials, where nucleation is enhanced in the nanocomposite material.

Data collected at TOMCAT were then quantitatively analyzed using the

MorphoLibJ plugin library [25] of ImageJ/FIJI software tool [26,27]. Firstly, an edge preserving filter was applied in order to facilitate the separation between gas and liquid. After that, the separation was carried out by using an adaptive binarization algorithm. As the cell walls are extremely thin in this kind of cellular polymers [28], a 3D distance transform watershed algorithm [29] was used in order to separate bubbles after binarization. As a result, we were able to study 3D descriptors of cellular material such as material density, bubble number (cell density) and its average size (cell size). This image analysis protocol was applied to 33 intercalated scans in the two materials covering approximately the initial 90s of the foaming process.

FIG. 2 shows the foam relative density as a function of time. Relative density was calculated as the ratio between the volume occupied by the binarized liquid phase after watershed algorithm and the total volume. The inclusion of nanoparticles in the evolving liquid promotes a clear acceleration of the

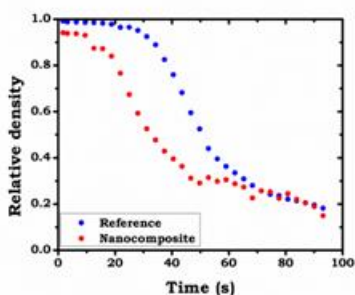


Fig 2. In-situ relative density evolution for the two materials under study



foaming process. A similar result was found when the foaming behavior of the same system was studied using in-situ FTIR. It was proved that this type of silica promotes a significant increase of the isocyanate consumption during the reaction increasing the reaction speed [23]. However final expansion factor is similar in both systems, reaching also similar final values of relative density ( $\sim 0.2$ ). Observed incomplete expansion should be accomplished after reaching gel time of 145s.

By analyzing the number of bubbles in each tomographic volume, cell nucleation density ( $N_0$ ) seems to become nearly constant after few seconds which is in congruence with nucleation theory (FIG. 3). In addition, it is clear that the inclusion of nanoparticles in the expanding liquid enhances the bubble nucleation density by two orders of magnitude (from  $10^4$  to  $10^6$  cells  $\cdot \text{cm}^{-3}$ ) due to the aforementioned free energy barrier reduction. In the literature, nucleation

dynamics are usually modeled according to Arrhenius laws [2,30,31]. Both homogeneous and heterogeneous nucleation rates can estimate, at every instant, according to exponential equations from the classical nucleation theory as described in EQ. 1-2. However, these models do not consider evolving conditions. In a real situation, it would be expected that the combination with other coupled not constant kinetics such as temperature, pressure or surface tension may finally lead to not constant nucleation rates. Nonetheless, in our particular case, we have demonstrated experimentally that the examined systems present constant nucleation rates of 1500 and 20000  $\text{cm}^{-3} \cdot \text{s}^{-1}$  for homogeneous and heterogeneous nucleation respectively (FIG. 3). Presence of nucleating particles has modified the nucleation rate of the original system in more than one order of magnitude.

$$\left(\frac{dN_0}{dt}\right)^{hom} = C_{hom} f_{hom} \exp\left(-\frac{W}{k_B T}\right) \quad (1)$$

$$\left(\frac{dN_0}{dt}\right)^{het} = C_{het} f_{het} \exp\left(-\frac{k W}{k_B T}\right) \quad (2)$$

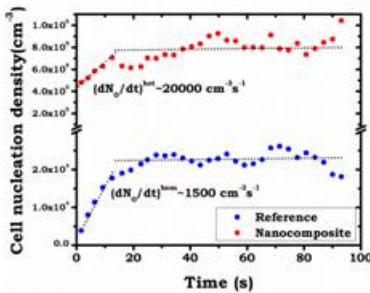


Fig 3. Evolution of the three-dimensionally calculated cell density in the two scanned materials and the two calculated nucleation rates for both homogeneous and heterogeneous nucleation systems.

In our two scanned materials, it looks clear that cell nucleation follows a linear trend until approx. 15s, therefore validating the consideration of constant nucleation rate. In addition, after the first 15s in which the nucleation takes place, it is remarkable that the cell nucleation becomes constant for both homogeneous and heterogeneous systems.

Focusing on the evolution of the average size ( $\phi$ ) of the bubbles several authors proposed in the literature that the initial growth of spherical bubbles in an expanding liquid should fit well with  $t^{1/2}$  [10,11,32] (EQ. 3).

$$\phi = 6\left(\frac{3}{4\pi}\right)^{1/3}(Dt)^{1/2} \quad (3)$$

where  $D$  is the diffusion coefficient of the gas molecules within the polymer liquid phase.

In both systems (FIG. 4) cell size remains nearly constant during early instants of the process ( $t < 15$  s) while nucleation is taking place. Once the nucleation has been accomplished, the gas dissolved in the polymeric matrix starts to fill the bubbles at a nearly constant rate at this square-root scale, thus obtaining good linear fit of average bubble size versus  $t^{1/2}$ . However, this trend is only maintained until  $\sim 65$  s and  $\sim 50$  s for the neat PU and the formulation with nanoparticles respectively. At these times, both systems reach relative densities around 0.3 (FIG. 2). At this approximate value -so called wet-dry transition- cell shape changes from spherical to polyhedral shape [33]. In the wet regime (high relative density) the rounded bubbles are isolated in the liquid whereas in the dry regime (low relative density) the bubbles start touching and create three-dimensional polyhedral network. As a consequence, growth rate is slightly reduced after this reference value.

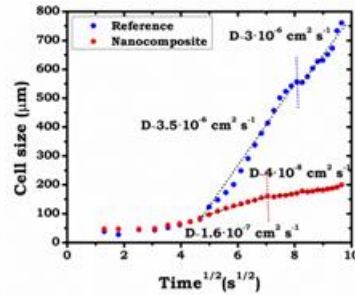


Fig 4. Evolution of the average bubble size vs. the square root of time showing the commented regimes for the two scanned systems.

Therefore, the diffusion coefficient ( $D$ ) can be determined in each case from the observed trends (FIG. 4). In this sense, it has been demonstrated that, in addition to enhance the bubble nucleation, the inclusion of nanosilica particles into PU foam seems to decrease the gas diffusion through the liquid phase of the growing PU ( $1.6 \cdot 10^{-7}$  vs.  $3.5 \cdot 10^{-6}$   $\text{cm}^2 \text{s}^{-1}$  for nanocomposite and neat PU respectively), commented broadly in the literature [34-36]. In fact, diffusion coefficient of  $\text{CO}_2$  in different kinds of PU has been measuring obtaining similar values using the high vacuum technique [37], by sorption weight comparison [38] or by gas permeability measurements [39]. Furthermore, when the cells start touching each other, in the wet-dry transition, the diffusion coefficient seems to decrease from  $3.5 \cdot 10^{-6}$  to  $3 \cdot 10^{-6}$   $\text{cm}^2 \text{s}^{-1}$  and from  $1.6 \cdot 10^{-7}$  to  $4 \cdot 10^{-8}$   $\text{cm}^2 \text{s}^{-1}$  for Neat and nanocomposite PU respectively. However, the change in the diffusion coefficient due to this transition is much lower than the one caused by the inclusion of nanoparticles into the

evolving system. In this case, the decrease in growing rate (and thus in the diffusion coefficient) is caused by the absence of physical space that hinders the expansion of cells.

In conclusion, our 4D X-ray tomography study has provided us a unique insight to understand nucleation and growth processes the analyzed polyurethane formulations. Our analysis allowed us evaluating comparatively the evolution of critical characteristics such as foam density, cell nucleation density and cell size focusing on the early stages of the foaming process ( $t < 90$ s). We have found three differentiated regimes: nucleation, growth and wet-dry transition. Dynamics of these processes are highly influence by the presence of nanoparticles. Firstly, in the nucleation stage ( $t < 15$ s) the density slowly decreases, the cell nucleation density increases at constant rate and the cell size remains practically constant. In a subsequent stage, the growth takes place until the moment in which cells start touching each other (50-65s). In the analyzed remaining 75 seconds relative density drops up to nearly 70% of the final value, cell nucleation density remains constant and cell size increases following a  $t^{1/2}$  rule in which the slope represents the diffusion coefficient of gas within the liquid polymer and obtaining similar values to those from literature for the PU-CO<sub>2</sub> system. In this sense we have found that the inclusion of nanosilica particles seems to decrease the diffusion coefficient. After the wet-dry transition (50s and 65s for nanocomposite and neat

PU respectively), both the density and the cell size evolution speed decrease whereas cell nucleation density still remains constant due to the reduction of physical space to grow. In addition, we have compared the obtained trends with those from nucleation and growth theories reaching valuable correlations. Up to our knowledge, this is the first work dealing with this kind of study on polymeric foams. In fact, in-situ studying the nucleation and growth of cells in 3D is of vital importance to evaluate experimentally these mechanisms and the reliability of the existing theoretical models. In this sense, this work has demonstrated that nucleation and growth are almost uncoupled mechanisms. In addition, both examined systems present almost constant nucleation and growth when the mechanisms take places, in good agreement with theoretical models.

#### Acknowledgements

Financial assistance from MINECO and FEDER program (MAT2015-69234-R) and the Junta de Castile and Leon (VA011U16) are gratefully acknowledged. Predoctoral contract of S. Perez-Tamarit by University of Valladolid (E-47-2015-0094701) and co-financed by Banco Santander is also acknowledged. Finally, we acknowledge the support from Paul Scherrer Institut (Villigen, Switzerland) to complete this work.

## References

- [1] S.F. Jones, G.M. Evans, K.P. BGalvin, Bubble nucleation from gas cavities - a review, *Advances in Colloid and Interface Science*, 80 (1999) 27-50.
- [2] M. Blander, J.L. Katz, Bubble nucleation in liquids, *AIChE Journal*, 21 (1975) 833-848.
- [3] F.F. Abraham, *Homogeneous Nucleation Theory*, Academic Press, New York, 1974.
- [4] J.J. Feng, Prediction of bubble growth and size distribution in polymer foaming based on a new heterogeneous nucleation model, *Journal of Rheology*, 48 (2004).
- [5] W.L. Ryan, E.A. Hemmingsen, Bubble formation in water at smooth hydrophobic surfaces, *Journal of Colloid and Interface Science*, 157 (1993) 312-317.
- [6] J.S. Colton, N.P. Suh, The nucleation of microcellular thermoplastic foam with additives: Part I: Theoretical considerations, *Polymer Engineering and Science*, 27 (1987) 485-492.
- [7] L. Lee, C. Zeng, X. Cao, X. Han, J. Shen, G. Xu, Polymer nanocomposite foams, *Composites Science and Technology*, 65 (2005) 2344-2363.
- [8] M.M. Bernal, M.A. Lopez-Manchado, R. Verdejo, In situ Foaming Evolution of Flexible Polyurethane Foam Nanocomposites, *Macromolecular Chemistry and Physics*, 212 (2011) 971-979.
- [9] R. Verdejo, F.J. Tapiador, L. Helfen, M.M. Bernal, N. Bitinis, M.A. Lopez-Manchado, Fluid dynamics of evolving foams, *Physical chemistry chemical physics : PCCP*, 11 (2009) 10860-10866.
- [10] R.D. Pattel, Bubble growth in a viscous Newtonian liquid, *Chemical Engineering Science*, 35 (1980) 2352-2356.
- [11] M. Favelukis, R.J. Albalak, Bubble growth in viscous newtonian and non-newtonian liquids, *The Chemical Engineering Journal*, 63 (1996) 149-155.
- [12] D. Weaire, S. Hutzler, *The physics of foams*, First Edition ed.2001.
- [13] I. Cantat, S. Cohen-Addad, F. Elias, F. Graner, R. Höhler, O. Pitois, F. Rouyer, A. Saint-Jalmes, *Foams Structure and Dynamics*, Oxford University Press 2013.
- [14] M.M. Bernal, S. Pardo-Alonso, E. Solórzano, M.A. Lopez-Machado, R. Verdejo, M.A. Rodriguez-Perez, Effect of carbon nanofillers on flexible polyurethane foaming from a chemical and physical perspective, *RSC Advances*, 4 (2014).
- [15] S. Pardo-Alonso, E. Solórzano, S. Estravis, M.A. Rodriguez-Perez, J.A. de Saja, In situ evidence of the nanoparticle nucleating effect in polyurethane-nanoclay foamed systems, *Soft Matter*, 8 (2012) 11262.
- [16] E. Solórzano, S. Pardo-Alonso, J.A. de Saja, M.A. Rodriguez-Perez, X-ray radioscopy in-situ studies in thermoplastic polymer foams, *Colloids and Surfaces A: Physicochemical and Engineering aspects*, 438 (2013) 167-173.
- [17] E. Solórzano, S. Pardo-Alonso, J.A. de Saja, M.A. Rodríguez-Pérez, Study of aqueous foams evolution by means of X-ray radioscopy, *Colloids and Surfaces A: Physicochemical and Engineering Aspects*, 438 (2013) 159-166.
- [18] E. Solórzano, J. Pinto, S. Pardo, F. Garcia-Moreno, M.A. Rodriguez-Perez, Application of a microfocus X-ray imaging apparatus to the study of cellular polymers, *Polymer Testing*, 32 (2013) 321-329.
- [19] E. Maire, C. Le Bourlot, J. Adrien, A. Mortensen, R. Mokso, 20 Hz X-ray tomography during an in situ tensile test, *International Journal of Fracture*, 200 (2016) 3-12.
- [20] P.H. Kamm, F. García-Moreno, T.R. Neu, K. Heim, R. Mokso, J. Banhart, Fast Synchrotron X-Ray Tomography of Dynamic Processes in Liquid Aluminium Alloy Foam Advanced Engineering Materials, 19 (2017) 1600550.
- [21] G. Lovric, R. Mokso, C.M. Schlepütz, M. Stampanoni, A multi-purpose imaging endstation for high-resolution micrometer-scaled sub-second tomography, *Physica medica : PM : an international journal devoted to the applications of physics to medicine and biology : official journal of the Italian Association of Biomedical Physics*, 32 (2016) 1771-1778.
- [22] S. Estravis, J. Tirado-Mediavilla, M. Santiago-Calvo, J.L. Ruiz-Herrero, F. Villafañe, M.A. Rodríguez-Pérez, Rigid polyurethane foams with infused nanoclays: Relationship between cellular structure and thermal conductivity, *European Polymer Journal*, 80 (2016) 1-15.
- [23] M. Santiago-Calvo, J. Tirado-Mediavilla, J.L. Ruiz-Herrero, M.A. Rodríguez-Pérez, F. Villafañe, The effects of functional nanofillers on the reaction kinetics, microstructure, thermal and mechanical properties of water blown rigid polyurethane foams, *Polymer*, 150 (2018) 138-149.
- [24] F. Marone, C. Hintermüller, R. Geus, M. Stampanoni, Towards real-time tomography fast reconstruction algorithms and GPU implementation, *IEEE Nuclear Science Symposium Conference Proceedings*, 1-9 (2009).
- [25] D. Legland, I. Arganda-Carreras, P. Andrey, MorphoLibJ: integrated library and plugins for mathematical morphology with ImageJ, *Bioinformatics*, 32 (2016) 3532-3534.
- [26] M.D. Abràmoff, P.J. Magalhaes, J. Sunanda, Image Processing with ImageJ, *Biophotonics International*, 11 (2004) 36-42.
- [27] C.A. Schneider, W.S. Rasband, K.W. Eliceiri, NIH Image to ImageJ: 25 years of image analysis, *Nature Methods*, 9 (2012) 671-675.

- [28] S. Pardo-Alonso, E. Solórzano, L. Brabant, P. Vanderniepen, M. Dierick, L. Van Hoorebeke, M.A. Rodriguez- Perez, 3D Analysis of the progressive modification of the cellular architecture in polyurethane nanocomposite foams via X-ray microtomography, *European Polymer Journal*, 49 (2013) 999-1006.
- [29] L. Vincent, P. Soille, Watersheds in digital spaces: An efficient algorithm based on immersion simulations, *IEEE Transactions on Pattern Analysis and Machine Intelligence*, 13 (1991) 583-598.
- [30] J.S. Colton, The Nucleation of Microcellular Foams in Semicrystalline Thermoplastics, *Materials and Manufacturing Processes*, 4 (1989) 253-262.
- [31] J.S. Colton, N.P. Suh, The Nucleation of Microcellular Thermoplastic Foam with Additives: Part II: Experimental Results and Discussion, *Polymer Engineering and Science*, 27 (1987) 493-499.
- [32] M. Amon, C.D. Denson, A study of the dynamics of foam growth: Analysis of the growth of closely spaced spherical bubbles, *Polymer Engineering and Science*, 24 (1984) 1026-1034.
- [33] Y. Furuta, N. Oikawa, R. Kurita, Close relationship between a dry-wet transition and a bubble rearrangement in two-dimensional foam, *Scientific reports*, 6 (2016) 37506.
- [34] E. Rio, W. Drenckhan, A. Salonen, D. Langevin, Unusually stable liquid foams, *Adv Colloid Interface Sci*, 205 (2014) 74-86.
- [35] A. Stocco, E. Rio, B.P. Binks, D. Langevin, Aqueous foams stabilized solely by particles, *Soft Matter*, 7 (2011) 1260.
- [36] B.P. Binks, R. Murakami, Phase inversion of particle-stabilized materials from foams to dry water, *Nature materials*, 5 (2006) 865-869.
- [37] J.S. McBride, T.A. Massaro, S.L. Cooper, Diffusion of gases through polyurethane block polymers, *Journal of Applied Polymer Science*, 23 (1979) 201-214.
- [38] D. Hu, L. Yan, T. Liu, Z. Xu, L. Zhao, Solubility and diffusion behavior of compressed CO<sub>2</sub> in polyurethane oligomer, *Journal of Applied Polymer Science*, 135 (2018) 47100.
- [39] N. Cao, M. Pegoraro, F. Bianchi, L. Di Landro, L. Zanderighi, Gas transport properties of polycarbonate-polyurethane membranes, *Journal of Applied Polymer Science*, 48 (1993) 1831-1842.



### References

---

- [1] S. Pardo-Alonso, E. Solórzano, L. Brabant, P. Vanderniepen, M. Dierick, L. Van Hoorebeke, M.A. Rodríguez- Perez, 3D Analysis of the progressive modification of the cellular architecture in polyurethane nanocomposite foams via X-ray microtomography, *European Polymer Journal*, 49 (2013) 999-1006.
- [2] S. Pardo-Alonso, E. Solorzano, J. Vicente, L. Brabant, M.L. Dierick, I. Manke, A. Hilger, E. Laguna, M.A. Rodríguez-Perez, muCT-Based Analysis of the Solid Phase in Foams: Cell Wall Corrugation and other Microscopic Features, *Microscopy and Microanalysis*, 21 (2015) 1361-1371.
- [3] A. Cunningham, N.C. Hilyard, *Low Density Cellular Plastics: Physical Basis of Behaviour*, Ed. Chapman and Hall, London, 1994.
- [4] L.J. Gibson, M.F. Ahsby, *Cellular Solids: Structure and Properties*, Pergamon Press, Oxford, England, 1988.
- [5] J.L. Grenestedt, Influence of wavy imperfections in cell walls on elastic stiffness of cellular solids, *Journal of the Mechanics and Physics of Solids*, 46 (1998) 29-50.





## Chapter 5

# **Theory of Light Scattering Applied to Cellular Materials**



Scattering is a general physical process in which radiation is forced to deviate from a straight trajectory by one or more paths due to localized non-uniformities in the medium through which they pass [1-3]. This also includes deviation of reflected radiation from the angle predicted by the law of reflection. Reflections that undergo scattering are often called diffuse reflections and unscattered reflections are called specular reflections [4, 5]. Scattering joins reflexion, refraction and diffraction as one more of the possible processes the radiation can suffer passing through materials.

The types of non-uniformities which can cause scattering so-called scatterers or scattering centres are numerous. For instance, a sample can include particles, bubbles, density fluctuations, crystallites in polycrystalline solids, defects in mono-crystalline solids, surface roughness, etc. The effects of such features on the path of almost any type of propagating wave or moving particle can be described in the framework of scattering theory. Scattering theory is important in areas such as particle physics, atomic, molecular, and optical physics, nuclear physics and astrophysics. Some additional areas where scattering is significant include radar sensing, medical ultrasound, semiconductor wafer inspection, polymerization process monitoring, acoustic tiling, free-space communications and computer-generated imagery.

A particular case of scattering is the so-called **Light Scattering**, referred as the electromagnetic scattering with radiation with wavelength in the visible range [6, 7].

This chapter summarizes the main concepts about Light Scattering and its application for the characterization of cellular materials. Firstly, a clear definition of light scattering is addressed. Then, the main theoretical frameworks studying the scattering phenomena are described. Once these theories are explained, the specific application of Light Scattering to the case of cellular materials is undertaken, from the classical characterization of aqueous foams to the attempts in the case of solid cellular materials. Finally, the ins and outs of the methodology developed during this PhD. Thesis for the characterization of cellular polymers by means of Light Scattering are explained.

## 5.1 Light Scattering

Light scattering means the redirection of light when the radiation beam encounters an obstacle or non-homogeneity. If the majority of the scattered light maintains the same frequency as the incident beam, the scattering is considered “**elastic**”. In the opposite case, the scattered light reduces its frequency thus losing energy during the scattering mechanism, leading to the “**inelastic scattering**”. Furthermore, the **extinction** of the radiation through a material involves the decrease of intensity (or number of photons) in the forward direction of observation, i.e., scattering angle  $0^\circ$ , due to both scattering and absorption of the radiation by the crossed material (Figure 5-1).

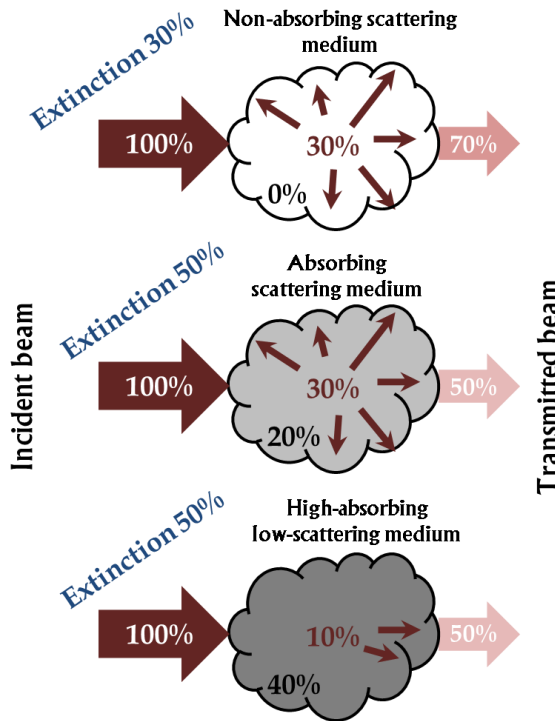


**Figure 5-1.** Extinction phenomena as a contribution of both scattering and absorption within a medium.

This phenomenon is typically modelled using the Beer-Lambert extinction law that relates the incident ( $I_0$ ) and transmitted intensities ( $I$ ) by an exponential equation using

the thickness ( $L$ ) and extinction coefficient of the crossed material ( $k$ ) (Equation 5-1) [8, 9].

$$I = I_0 \exp(-kL) \quad \text{Equation 5-1}$$

From the atomic point of view, the incident electromagnetic wave (light) interacts with the electron orbits of the constituent molecules of the obstacles. As a result, the oscillation or perturbation of the electron clouds results in a periodic separation of charge within the molecule thus becoming a source of electromagnetic radiation, i.e., the source of scattered light [10]. The critical parameter in scattering theories is the so-called scattering cross section ( $\sigma$ ) that encounters the effective area of scattering of the selected scattering centres.

Depending on the nature of the scattering medium, scattering mechanism is usually divided into two main groups: *single scattering* and *multiple scattering*.

### 5.1.1 Single and Multiple scattering

**Single scattering** occurs when radiation is only scattered by one localized scattering centre or a small group of them in which the separation between different scattering centres is much higher than their size [11] (Figure 5-2). As a consequence, the light is only scattered once within the medium resulting typically in a random phenomenon. Single scattering is therefore modelled by probability distributions. This type of scattering mechanism prevails in optically thin and/or strongly absorbing medium since under these conditions the probability of multiple photon collisions is minimized.

If the radiation scatters many times within the medium, it is known as **multiple scattering** mechanism. In this case, the separation between scattering centres is in the range of their size thus leading multiple interactions radiation-material during the radiation travel through the scattering medium [12] (Figure 5-2). Since the number of scattering events is much higher, the process tends to average the trajectory of the scattered beam. As a result, multiple scattering can be modelled using

deterministic distributions of transmitted intensity. Further, it is well known that multiple scattering is strongly analogous to diffusion, and thus interchangeable in many contexts. In fact, optical elements manufactured to provoke multiple scattering are known as diffusers. This type of mechanism dominates in systems optically thick composed by non-absorbing media that promote a strong scattering in which photons may be scattered hundreds of times before emerging from the material.

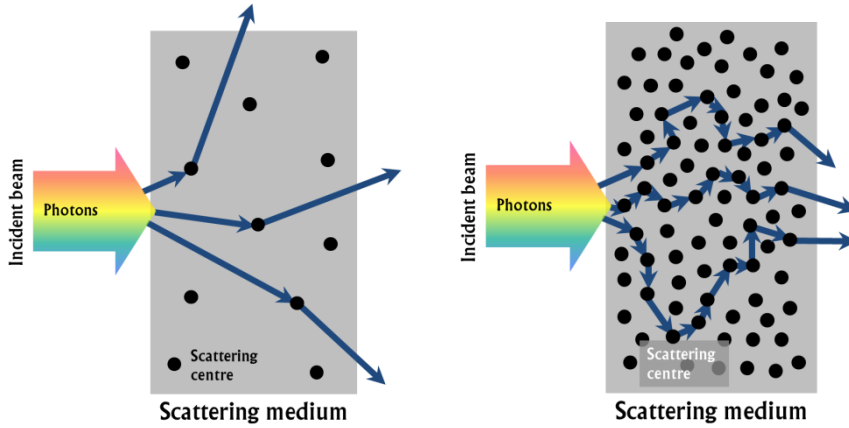


**Figure 5-2.** Example of single -left- and multiple -right- scattering mechanisms.

## 5.2 Principles of Light Scattering

Three mayor theories have been developed to the formal study of light scattering, Rayleigh, Mie and geometrical scattering (i.e. geometric optics). The criteria in order to differentiate between them is established around the so-called size parameter ( $\alpha$ ) that depends on the dimensions (radius) of the illuminated particles, considered as spheres ( $a$ ) and the wavelength of the employed radiation ( $\lambda$ ) (Equation 5-2).

$$\alpha = \frac{2\pi a}{\lambda} \quad \text{Equation 5-2}$$

Under this parameter, the most suitable theoretical framework to study the scattering process is the following (Figure 5-3) [1, 7, 10]. In this figure, considering visible light ( $\lambda \sim 500$  nm), several vertical lines have been included to represent the different types of cellular materials depending on the cell size. **Nanocellular** ( $\phi < 300$  nm), **submicrocellular** ( $0.3 \mu\text{m} < \phi < 1 \mu\text{m}$ ), **microcellular** ( $1 \mu\text{m} < \phi < 10 \mu\text{m}$ ) and **conventional** cellular materials ( $\phi > 10 \mu\text{m}$ ) are included. In this sense, it is possible to discern, in principle, what scattering formalism is more suitable for the tested material. However, in practice, as explained hereinafter, the Mie theory, which includes both geometric and Rayleigh scattering considering specific conditions, is considered as the main theory to study scattering phenomena.

$\alpha \ll 1$ (small particle compared to wavelength)	Rayleigh
$\alpha \approx 1$ (particle similar to wavelength)	Mie
$\alpha \gg 1$ (particle much larger than wavelength)	Geometric

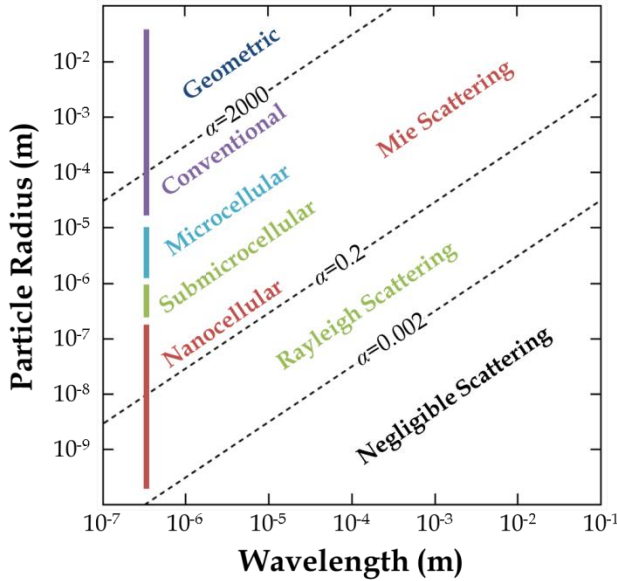


**Figure 5-3.** Different applicable scattering theories depending on both the wavelength and particle radius considering only single scattering and spherical particles. Vertical lines located in the visible range ( $\sim 500$  nm) to represent the different kinds of cellular materials depending on cell size (Chapter 2).

In addition, these theories consider mainly single scattering processes. However, most of the real processes occur involving multiple scattering. In such cases, the theory becomes harder to solve analytically and due to this different approximations are used to reach valuable solutions. In this sense, considering that multiple light scattering is similar to diffusion process, the most used approach is the so-called the *diffusion approximation*. The following paragraphs address the main insights about the three main scattering theories: Rayleigh Scattering, Mie Scattering and Geometric Scattering as well as the basis of the Diffusion Approximation.

### 5.2.1 Rayleigh Scattering

Rayleigh scattering, as commented before, is the dominantly elastic scattering of light by dielectric (non-absorbing) particles much smaller than the wavelength of the radiation, typically a factor  $1/10$ , and optically soft, i.e., with a refractive index close to



1 [13]. In other words, this assumption corresponds physically a situation where the particles are sufficiently small to encounter an uniform electric field at any moment, i.e., the penetration time is much smaller than oscillation period. The oscillating electric field of the incident radiation provokes the charges within a particle to move at the same frequency. The particle therefore becomes a small radiating dipole emitting as a result scattered light. Considering all these specific conditions, the intensity of the scattered light at an angle  $\theta$  ( $I_s$ ) can be calculated knowing the characteristics of both the scattering particles (mainly size  $-a-$  and refractive index  $-n-$ ) and the used radiation (wavelength  $-\lambda-$ ) (Equation 5-3). In addition, it is clear that this intensity depends on the distance between the scattering medium and observer ( $d$ ) [13].

$$I_s = I_0 \left( \frac{1 + \cos^2 \theta}{2d^2} \right) \left( \frac{2\pi}{\lambda} \right)^4 \left( \frac{n^2 - 1}{n^2 + 2} \right)^2 a^6 \quad \text{Equation 5-3}$$

The strong dependence with wavelength of this scattered intensity ( $\lambda^{-4}$ ) has a great importance in several everyday phenomena and technological aspects. Firstly, it is the responsible of the blue appearance of the sky since the blue light corresponds to the minor wavelength visible light received by the sun and scattered by the air gas constituent particles (Figure 5-4). In this figure, as a typical example of application of Rayleigh theory, the proportion (expressed in %) of sun scattered light by molecules of gas present in air is presented. As the blue light has lower wavelength ( $\sim 400$  nm) than red light ( $\sim 650$  nm), the appearance of the sky is blue.

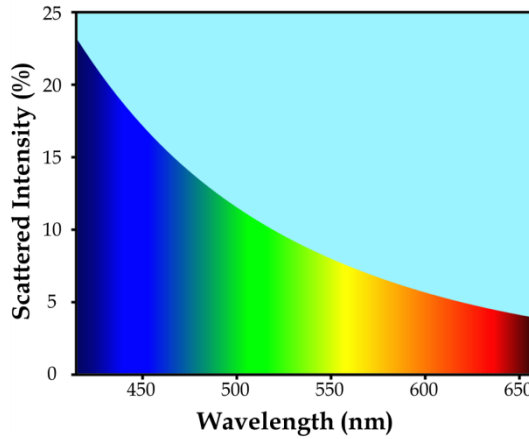


**Figure 5-4.** Dependence with wavelength in the optical range of the scattered intensity by molecules present in air.

Other aspects in which Rayleigh scattering takes importance are the transmission of energy through optical fibres or in nano-porous metals in which the scattering coefficients follow the law  $\lambda^{-4}$  [14].

Integrating the scattered intensity over a sphere surrounding the particle it is possible to determine the scattering cross section ( $\sigma_R$ ) corresponding to the Rayleigh regime (Equation 5-4).

$$\sigma_R = \frac{4\pi^5}{3} \frac{a^6}{\lambda^4} \left( \frac{n^2-1}{n^2+2} \right)^2 \quad \text{Equation 5-4}$$

This cross section is required to determine the total scattered energy ratio ( $dE/dt$ ) striking a surface ( $dA$ ) located at a distance from the scattering event ( $r$ ) (Equation 5-5).

$$\frac{dE}{dt} = I_0 \sigma_R \frac{dA}{r^2} = I_0 \sigma_R d\omega \quad \text{Equation 5-5}$$

### 5.2.2 Mie Theory

Mie scattering is the straightforward application of Maxwell's equations to an isotropic, homogeneous, dielectric sphere [1, 10, 15, 16]. In fact, Rayleigh scattering is

only a simple particular solution of the more general case addressed by Mie theory. This theory is equally applicable to spheres of all sizes, refractive indices and for radiation of all wavelengths. Although this theory is applicable in all cases, it is typically used for the cases in which the size of the scatters is comparable to radiation wavelength. In addition, this theory tends to the limit of geometric optics for large scattering particles. Figure 5-5 shows the trend of normalized scattering cross section ( $\sigma/\pi a^2$ ) according to Mie theory as a function of the ratio between particle radius and radiation wavelength. In the optical region, in which the Geometric Scattering is considered, is characterized by a constant scattering cross section  $\sigma_G = \pi a^2$  and thus normalized scattering cross section tending to 1. On the other part of the figure, since Rayleigh cross section depends on  $(a^6/\lambda^4)$ , the normalized cross section depends on  $(a/\lambda)^4$ , represented as a almost perfect linear fit on the logarithmic scale of the Figure 5-5. In the middle of both extremes, the Mie region, also called resonance region is located. The oscillation on the normalized scattering cross section in this zone is the result of the decomposition of the electromagnetic plane wave in an infinite series of spherical multi-pole partial waves (Legendre polynomials) to determine the scattering cross section.

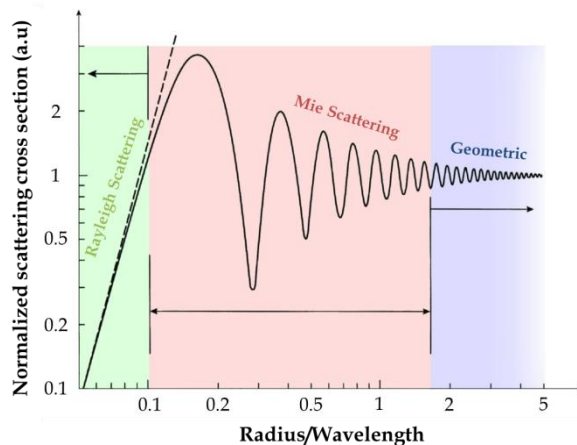


**Figure 5-5.** Variation of normalized scattering cross section according to Mie calculations showing the three ranges depending on the relation between scattering particle radius and radiation wavelength.

According to this formalism, Maxwell's equations are solved in spherical coordinates through separation of variables. To this purpose, the incident plane wave is expanded in Legendre polynomials ensuring that the internal and external solutions match at the particle frontier (or boundary). The solution in the far-field, i.e., at a distance much greater than wavelength, is a combination of two scattering functions result of infinite series. These infinite series can be physically interpreted as a multiple expansion of scattered light [17]. As a consequence, the first term specifies the amount of scattered dipole radiation, the second the quadrupole radiation, etc... If only the first term (dipole) is required to describe the scattering process the Mie theory reduces to Rayleigh scattering.

As a result, the scattering cross section corresponding to the Mie scattering formalism is also an infinite sum of combinations of scattering coefficients depending on Ricatti-Bessel functions. For this reason, analytical treatments of this phenomena are usually not possible thus introducing the numerical computation as the unique possibility [18]. This permits also expanding the range of application to particles of other shapes like ellipsoids or even cylinders.

The applications of Mie theory are several and varied as well as in the case of Rayleigh scattering. It is very important in meteorological optics since clouds are formed by particles (water droplets, dust, smoke...) similar in size than visible light wavelength. In addition, thanks to selective scattering, nowadays it is possible to discern between healthy and cancerous cell nuclei using low-coherence interferometry, based on the theoretical formalism indicated by Mie theory. Among others, it is important to cite that Mie theory is also applied in laser diffraction to inspect the particle sizing effect [19] because Mie theory offers more accurate results than simpler Fraunhofer approximation. However, due to the high computation requirements of the Mie calculations this kind of analysis were not possible until the 1990s.

### 5.2.3 Geometric Scattering

In the limit of large scattering particles ( $\alpha \gg 1$ ) Mie theory reduces to geometric scattering. Under this condition, ray tracing (geometric optics) can be applied to study light scattering by spherical and non-spherical particles. In this situation, the light can be considered as a collection of separate rays with width of rays much larger than wavelength but smaller than the scatter. In this formalism, the scattering cross section is referred as the projected surface of the sphere ( $\sigma_G = \pi a^2$ ). Rays hitting the particle undergoes reflection, refraction and diffraction. These rays exit in various directions with different amplitudes and phases. Such ray tracing techniques are used to describe optical phenomena such as rainbow or halo on hexagonal ice crystals for large particles.

### 5.2.4 Diffusion Approximation

As already mentioned, explained scattering theories only deal with single scattering processes. However, in practice almost all the real scattering processes involve multiple light scattering events. This fact is maximized in systems with a high concentration of scattering centres such as colloids or cellular materials. Light propagation in a multiple scattering medium is governed by the theory of radiative transport [11, 12]. This theory takes into account absorption and scattering due to inhomogeneities in the propagating medium. The radiative transport equation is a partial differential/integral equation. Due to its inherent complexity, analytical solutions only exist for simple problems and the large number of independent variables in the equation provokes that even numerical solutions of this equation are challenging. For this reason, the most used strategy is seeking approximations to simplify the radiation transfer equation. One of the most used is the so-called *diffusion approximation* [20, 21]. This approach is suitable considering the great similarity between multiple scattering and diffusion processes (Figure 5-6).

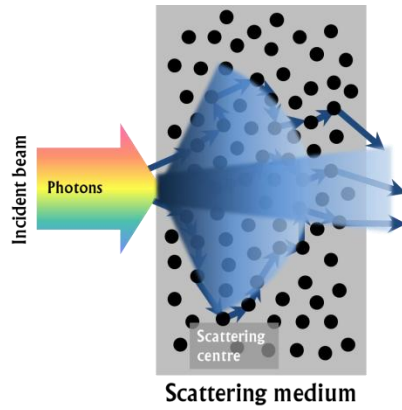


**Figure 5-6.** Schematic representation of the duality between multiple light scattering and diffusion processes.

This approximation applies to light propagation in optically thick mediums, i.e., all the light entering the sample is scattered many times before exiting. Moreover, it assumes that light becomes nearly isotropic due to strong multiple light scattering since as the number of scattering events increase, the angular dependence tends to be smoothed out. For this reason, the phase correlations of the scattered waves within the medium are ignored and only the scattered intensities are considered. Thus, the path followed by an individual photon can be described as a random path. Under this consideration, the density of transported radiated energy ( $U$ ) is modelled by the corresponding diffusion equation (Equation 5-6).

$$\frac{\partial}{\partial t} U(\vec{r}, t) = D \nabla^2 U(\vec{r}, t) \quad \text{Equation 5-6}$$

The diffusion coefficient in this case ( $D$ ) is related to the length scale over which the randomization occurs, the so-called transport mean free path ( $l^*$ ), so that  $D=cl^*/3$  [22]. As a consequence, in order to assure the applicability of the diffusion approximation into a scattering problem, the scattering system should be thick enough to guarantee that the travel of light within the medium is much larger than transport mean free path.

Finally, according to this approximation, the information about the size, shape, composition, etc... of scatter centres is contained within the transport mean free path. Consequently, the determination of this parameter is crucial in order to use this kind of techniques for the characterization of cellular material. This task is described in the following section.

### 5.3 Modelling the Light Scattering in Cellular Materials

Cellular materials are random dispersions of gas bubbles separated by solid or liquid material with varied thickness depending on the relative density and particular cellular structure of the material [23, 24]. Therefore, these materials are a composition of a large amount of gas-material interfaces from the point of view of the light scattering which provides a significant scattering. This gives bulk samples of conventional cellular materials their familiar white opaque appearance even in the case that the solid material is transparent. This special structure provokes the multiple light scattering of light in the internal structure of these materials opening the possibility to characterize them by techniques involving light scattering.

In this regard, one of the simplest optical quantities to measure is the static transmission or transmissivity ( $T$ ) of light through a thickness ( $L$ ) of cellular material defined as the ratio between transmitted ( $I$ ) and incident light ( $I_0$ ) intensities (Equation 5-7) considering identical solid angles for both intensities.

$$T = I/I_0 \quad \text{Equation 5-7}$$

One important goal is to relate the measured transmissivity to characteristics of the tested specimen such as relative density, mean cell size of and/or thickness. The solution of the diffusion equation (*diffusion approximation*) permits relating the transmissivity ( $T$ ) to the transport mean free path ( $l^*$ ), absorption length ( $l_a$ ) and sample thickness ( $L$ ) (Equation 5-8) [11, 25, 26]. Transport mean free path is the length that light travels inside the material until its direction is randomized and absorption length indicates the absorption character of the sample. The shorter is the absorption length, the higher is the light absorption within the material.

This approximation is valid in the case of conventional cellular materials observing the diffused character of the transmitted intensity (Figure 5-7).

$$T \approx \frac{(5l^*/L)\beta}{[1+(4l^*/3L)\sinh\beta]} ; \quad \beta = \sqrt{\frac{3L^2}{l^*l_a}} \quad \text{Equation 5-8}$$



Once the transport mean free path is suitably inferred from the previous equation, its relation with both mean cell size ( $\phi$ ) and relative density ( $\rho_r$ ) has been broadly studied in the literature [25, 27-29]. In fact, proportionality between transport mean free path and mean cell size is usually proposed until the final equation that links all these mentioned parameters (Equation 5-9) [27].

$$l^* = \phi / \sqrt{\rho_r} \quad \text{Equation 5-9}$$

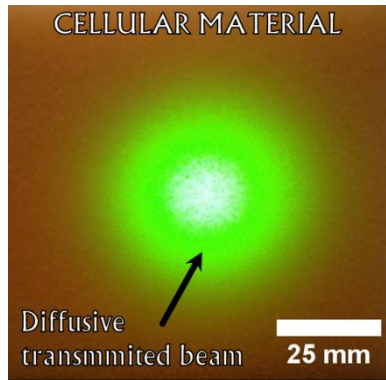


**Figure 5-7.** Aspect of the transmitted light pattern of a green laser (532 nm, 2 mm incident beam diameter) after 25 mm travel within a solid cellular polymer ( $\phi=500 \mu\text{m}$ ,  $\rho_r=0.025$ ).

From the point of view of the constituent matrix, cellular material can be separated into *aqueous* and *solid*. This separation strongly affects the final structure and stability of the corresponding cellular materials and thus the behaviour of light (scattering and absorption) within the medium. For this reason, the application of Light Scattering techniques (solving the equation 5-8) on each type of material is addressed separately in the following paragraphs. In addition and as a separate case, the particularities of *nanocellular polymers*, linked to the change on the spatial scale, are also described.

### 5.3.1 Aqueous foams

These materials are porous structures in which the matrix (or non-gaseous phase) is liquid. As a result, the material is difficult to characterize since the delicate structure cannot be manipulated and evolves with time. For these reasons, the structural

characterization of such kind of materials should be accomplished using a fast non-invasive technique. To overcome these issues, light scattering methods have been developed and applied in these systems since 80s and 90s.

Furthermore, it is well known that the liquid matrix of aqueous foams is formed by very thin liquid films (with thickness around 100-500 nm) [30]. Under this perspective, scattering is the only interaction of light with cellular materials constituents, thus it is reasonable to consider the light absorption within the material negligible. As a consequence, the absorption length becomes several times higher than sample thickness ( $l^* \ll L \ll l_a; \beta \ll 1$ ) allowing simplifying the equation 5-8 (Equation 5-10).

$$T \approx 5l^*/3L \quad \text{Equation 5-10}$$

In fact, values of  $l_a=200$  cm have been estimated in the literature to fit the behaviour of equation 5-8 in slabs of liquid foams of 1 cm in thickness [25]. Combining this last equation with the simple relation between transport mean free path and mean cell size (Equation 5-9) it is possible to obtain a very simple relation to determine mean cell size by light scattering ( $\phi_{LS}$ ) considering sample thickness, density and light transmissivity (Equation 5-11).

$$\phi_{LS} \approx \frac{3}{5}LT\sqrt{\rho_r} \quad \text{Equation 5-11}$$

This equation is the basic relation for the characterization of liquid foams by means of light scattering working in the forward direction transmission. Further, additional studies have been developed in order to study in deep the influence of light absorption in this kind of materials [31, 32]. To this purpose, high density aqueous foams ( $\rho_r \sim 0.8$ ) were selected in order to maximize the probabilities of light absorption. Nonetheless, the absorption length in those materials was around 700 mm. As a consequence, eliminate absorption within the theoretical model of light scattering for these materials is a valid consideration even for materials in which the absorption can be inferred as maximum.

### 5.3.2 Solid cellular polymers

All the work accomplished for aqueous foams can be tested in solid matrix cellular materials (and cellular polymers in particular). As the cellular structure of these materials can be characterized using classical techniques, it will be possible to compare the obtained Light Scattering cell size with well-established 2D (microscopy) and 3D (tomography) results. However, there are several structural differences between solid cellular polymers and liquid foams that should be taken into account for this modelling.

- Polymers are amorphous or semicrystalline. It is clear than the molecular structure of an amorphous polymer is similar to a solidified liquid. However, the ordered structure present on the semicrystalline polymers can play a crucial role non-considered within the models.
- In contrast to thin structures present in liquid foams, solid cellular polymers own cell wall thickness in the micrometre range (1-20  $\mu\text{m}$ ) [33, 34] even for low density materials. As a consequence, in this case light absorption within the material could be significant.

Considering these previous factors, in solid cellular polymers the absorption length is in the range of sample thickness thus avoiding the simplifying of the equation 5-8 as demonstrated in one of the research papers included in **Chapter 6**. Consequently, for the correct modelling of Light Scattering in solid cellular polymers it is required to solve a transcendental equation (Equation 5-8) involving both transport mean free path and absorption length. The particular strategy and obtained solution to this challenge is fully described in the paper "*Efficient prediction of cell size in solid polymeric foams by numerically solving the diffusion approximation of light scattering equation*" (**Chapter 6**).

### 5.3.3 Nanocellular polymers

The case of nanocellular polymers is totally different. For conventional foams, the wavelength of radiation is much lower than the mean cell size of materials (Figure 5-8). As a consequence the spatial frequency of solid barriers on the material (either struts or walls) is much lower than the vibration frequency of light. Under this perspective the radiation can be considered as illumination rays thus enabling the application of the described theoretical framework.

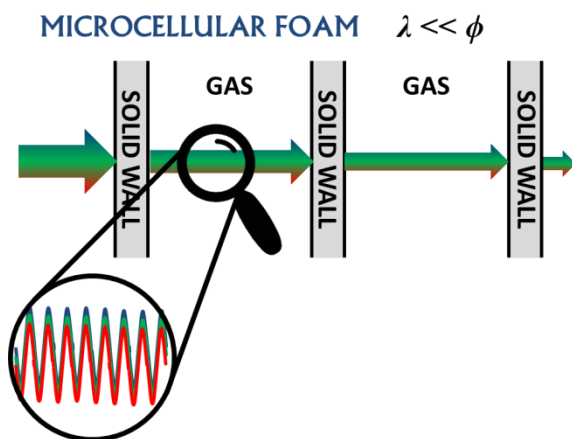


**Figure 5-8.** Schematic representation of the wavelength-mean cell size relationship in conventional foams.

On the other hand, in the case of nanocellular polymers the reduced cell size of these materials provokes that the wavelength of visible light is higher than cell size (Figure 5-9). In these materials the spatial frequency of solid barriers is higher than the vibration frequency of visible light. As a result the scattering behaviour changes varying the tendency of light transmission with the variation of mean cell size. A detailed description of this phenomenon is presented in the paper “*Light transmission in nanocellular polymers: Are semi-transparent cellular polymers possible?*” (**Chapter 7**).

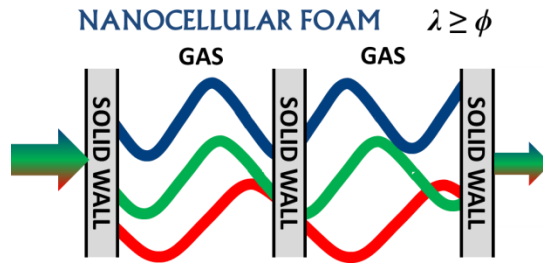


**Figure 5-9.** Schematic representation of the wavelength-mean cell size relationship in nanocellular polymers.

## **5.4 Practical aspects of implementation**

Once the theoretical principles of light scattering have been suitably established we describe the experimental particularities of the application of this kind of technique to conventional cellular polymers. Firstly, a description of the self-developed and assembled system for the transmissivity characterization is presented. After that, several methodological details found during the experimentation are addressed. Finally, we carried out a collection of experiments to demonstrate the influence of light absorption on cellular polymers, i.e., the non-validity of equation 5-11 for the characterization of solid cellular polymers. To this end, each of the involved parameters (cell size, density and thickness) was varied independently. The experimental details about the used samples and result are detailed hereinafter.

### *5.4.1 Transmission measurements setup*

The device for this study (Figure 5-10) consists of a white 50x50 mm backlight LED used as light source and a 12 bit camera used as light detector. The backlight LED provides homogeneous illumination throughout its surface. Nevertheless, a diaphragm ( $\varnothing = 14$  mm) was placed in front of the LED surface with the objective of creating a nearly point-source and limiting the eventual spread of the light out of the sample. During the experiments the samples are positioned in contact with the LED diaphragm so the light is not dispersed before entering in the foam. The distance between the light source and camera lens was fixed at 152 mm. The detection lens-camera system consisted of an IDS-Ueye camera mod. UI-5480CP and a 6 mm lens (1:1.18) providing a field of view of 140x105 mm at the mentioned working distance (152 mm). As a result, all the light emerging from the surface of the sample is acquired in the images and therefore considered to obtain the total transmitted intensity.

At the outset a flatfield image ( $I_0$ ) is acquired at an exposure time of 280 ms. At this exposure time the light does not saturate the camera greyscale. Subsequently, for every sample, three images are recorded and averaged – in order to reduce noise – at an exposure time of 1700 ms. The extended exposure time allows us increasing the

grey scale (intensity) resolution of the camera system when registering the transmitted light. Transmissivity is then calculated as the ratio between the intensity in the sample image and the flatfield corrected intensity (Equation 5-7). The corrected intensity of the flatfield is calculated after checking the camera linearity and thus extrapolating the expected intensity to an exposure time of 1700ms.

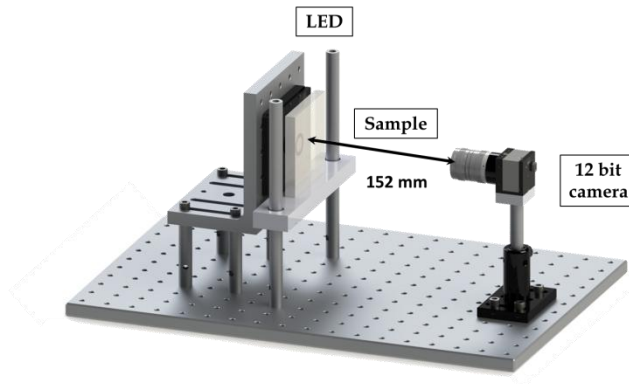


**Figure 5-10.** CAD drawing of the experimental set-up consisting in backlight LED, diaphragm, sample and camera.

Variations of this experimental set-up have been also considered. Different light sources, such as lasers of different wavelengths, have been employed in order to carry out the experiments. However, the impossibility to measure direct illumination with the camera hindered their use for this purpose. In addition, a photodiode joined to an integrating sphere with 12.5 mm window (PRW 0505, Gigahertz-Optik) connected to a photometer (X94, Gigahertz-Optik) has been also used as light detector. Nevertheless, in this case, the spread of the light inside the sample (Figure 5-7) provoked that the transmitted beam was higher than detector windows thus losing part of the transmitted light. Using the camera as light detector this inconvenience was overcome since it permitted acquiring all the light emerging from the sample by adjusting the source-detector distance, and thus the effective FOV by means of an infinite-focus lens. The higher is the distance, the higher is the effective FOV of the camera. A fully description of the different set-ups are addressed in the corresponding papers.

### 5.4.2 Methodological details

Sample dimensions and aspect ratios (relation between transversal dimension  $w$  and thickness  $L$  of the sample) require some additional considerations. We carried out tests over specially produced foams with fixed foam thickness (25 mm) and varying foam surface (50x50 mm, 80x80 mm, 110x110 mm and 200x200 mm) (Figure 5-11). In these experiments the transmitted light increased with sample surface reaching a constant value when  $w/L \sim 4$ . This result can be understood if we consider that part of the scattered light escapes out through the lateral sides of the sample if the surface is not large enough [22].

As a result we recommend the use of slab geometries with sufficiently large surface-to-thickness ratio in order to avoid transmissivity losses which could yield non-linear effects when varying the sample characteristics (mainly mean cell size and relative density). The final accuracy of the results will also depend on this effect and it is important to avoid lateral losses in order to increase the total amount of light transmitted maintaining enough thickness to accomplish the conditions of the diffusion approximation ( $L \gg l^*$ ).

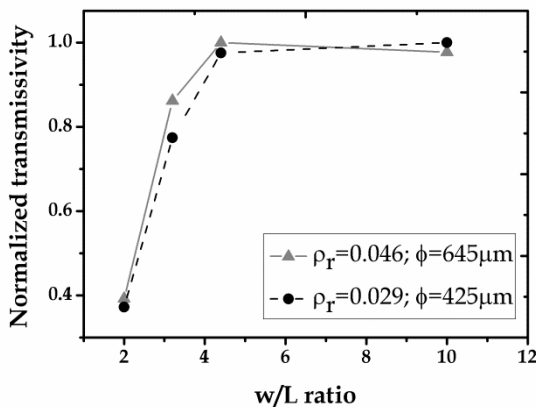


**Figure 5-11.** Variation of the normalized transmissivity response with the slab aspect ratio for samples with two different characteristics.



### 5.4.3 Systematic studies

In order to test the reliability equation 5-11 on solid cellular polymers a collection of materials with varied characteristics (mean cell size, density and thickness) was manufactured. The raw material selected was polyurethane. The possibility of controlling the final material density and cell size changing the amount of blowing agent in the polyol blend and the mixing conditions (rpm and time) respectively permitted us obtaining a chart of 16 samples with varied controlled characteristics (Figure 5-12). Four different densities (30, 55, 70 and 100 kg/m<sup>3</sup>) were selected and four different mean cell sizes (approx. 400, 500, 600 and 700  $\mu\text{m}$ ) were obtained, as explained in **Chapter 2** (Table 2-1).

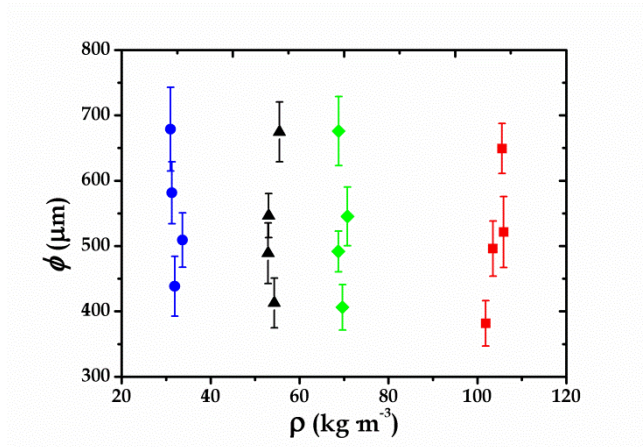


**Figure 5-12.** Cell size versus density of the samples produced showing the independency of both characteristics.

Samples with reduced dimensions (65x65x35 mm<sup>3</sup>) were cut from the central part of the produced foams. The specimens were then progressively sliced to different thickness (33, 27, 21, 15 and 11 mm) to verify the influence of this parameter in the modelling. As a result, a collection of 80 samples were tested the set-up of figure 5-10.

In principle, equation 5-11 proposes a simple prediction of cell size. In addition, according to this equation the cell size estimation should be independent of thickness and/or density variations and all the results should be over the same trend line.

Nevertheless the results are far from the expected ones. Evaluating the results for two different slab thickness (11 and 27 mm) with all the manufactured densities, the cell size predictions correlate with the microscopy cell size ( $\phi$ ) but they are shifted to lower values with increasing density (Figure 5-13). In this case, for the cell size determination optical microscopy (OM) was used. A first step consisted of ink-dyeing in order to highlight the cell edges, making them clearly visible. Then, a collection of three or four micrographs were acquired and analysed. The optical microscope used was Nikon SMZ-U with CMOS digital camera Ueye 1485LE. The image analysis process considers 150-200 cells identified over the 3-4 micrographs. These cells were identified and overlaid manually over a digital screen. The identified masks were analysed in ImageJ/Fiji [35, 36] and a cell size distribution was obtained. The mean value of the equivalent diameter (the diameter of a circular pore with a same area to the one identified) was the parameter selected as mean cell size in this case.

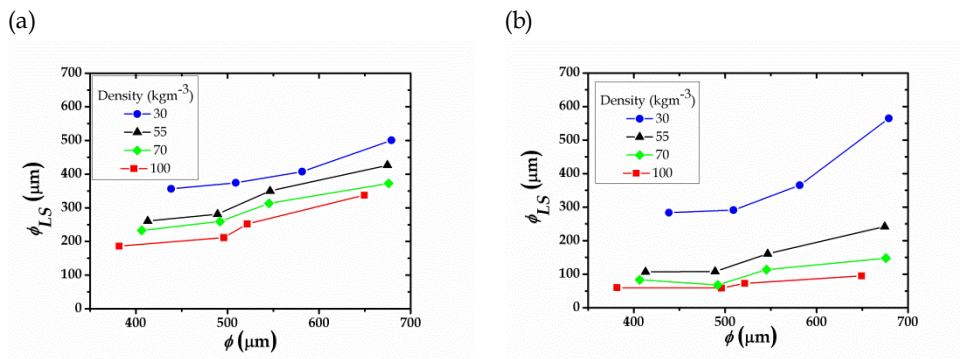


**Figure 5-13.** Cell size estimations for two selected sample thickness (a) 11 mm and (b) 27 mm.

The results for thicker slabs (27 mm) show an increase of differences in the predicted cell size. As an example, samples with a similar cell size present variations of nearly 200% (from 200-250  $\mu\text{m}$  to 400-500  $\mu\text{m}$ ) in the case of slab thickness of 11 mm and 550% (from less than 100  $\mu\text{m}$  to 500  $\mu\text{m}$ ) in the case of slab thickness of 27 mm. The most plausible explanation for these results considers an important influence of light absorption empowered by sample density (cell wall thickness) and/or slab thickness (number of interacted cell walls). Another remarkable aspect is that the increase of sample thickness leads to a detriment of resolution of the final results due to the lower

transmissivity and, therefore, slabs thinner than 20 mm are recommended for high densities.

On the other hand it is also possible to investigate the model compliance in terms of sample thickness for foams with two different densities (30 and 100 kg/m<sup>3</sup>) (Figure 5-14). The results show that cell size predictions show a similar trend but are, again, shifted. The shifting position is related with thickness leading, in general, to apparent smaller cell sizes predictions with increasing density. This result confirms that the classical light scattering model – which neglects absorption – fails for solid cellular polymers.

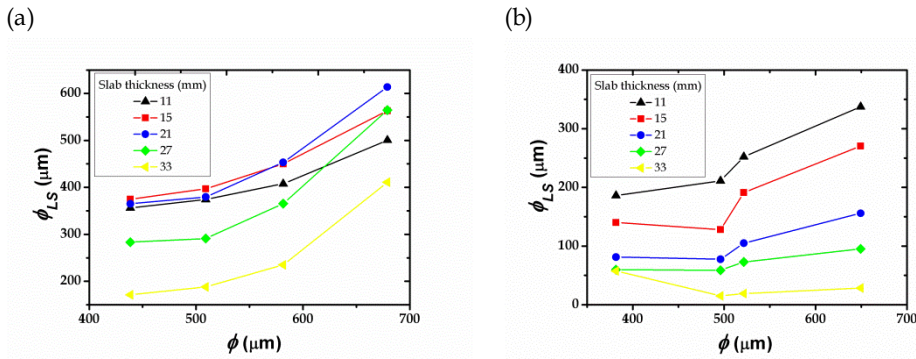


**Figure 5-14.** Cell size estimations for two selected foam densities (a) 30 kg/m<sup>3</sup> and (b) 100 kg/m<sup>3</sup>.

The two presented results indicate a large influence of light absorption for the modelling of Light Scattering on solid cellular polymers. As a consequence the absorption length should be considered within the model forcing to solve the full diffusion equation of Light Scattering. This task, as well as the development of a novel model of Light Scattering is addressed in the **Chapter 6**, in which the possibilities of measuring also the cell anisotropy with light transmission images are also presented.

**References**

---

- [1] C.F. Bohren, D.R. Huffman, *Absorption and Scattering of Light by Small Particles*, WILEY-VCH Verlag GmbH & Co. KGaA1983.
- [2] D. Colton, K. Rainer, *Inverse Acoustic and Electromagnetic Scattering Theory*, Springer1998.
- [3] M. Kerker, E.M. Loeb, *The scattering of light and other electromagnetic radiation*, Academic Press1969.
- [4] K.E. Torrance, E.M. Sparrow, *Theory for off-specular reflection from roughened surfaces*, *Journal of the Optical Society of America A*, 57 (1967) 1105-1114.
- [5] L.B. Wolff, *Relative brightness of specular and diffuse reflection*, *Optical Engineering*, 33 (1994) 285-293.
- [6] P. Debye, *Light Scattering in Solutions*, *Journal of Applied Physics*, 15 (1944) 338-342.
- [7] S. Asano, G. Yamamoto, *Light Scattering by a Spheroidal Particle*, *Applied Optics*, 14 (1975) 29-49.
- [8] T.G. Mayerhofer, H. Mutschke, J. Popp, *Employing Theories Far beyond Their Limits-The Case of the (Boguer-) Beer-Lambert Law*, *Chemphyschem : a European journal of chemical physics and physical chemistry*, 17 (2016) 1948-1955.
- [9] D.F. Swinehart, *The Beer-Lambert law*, *Journal of Chemical Education*, 39 (1962) 333-335.
- [10] D.W. Hahn, *Light Scattering Theory*, in: D.o.M.a.A. Engineering (Ed.), 2009.
- [11] A. Ishimaru, *Wave Propagation and Scattering in Random Media. Volume 1. Single Scatterig and transport theory*, 1978.
- [12] A. Ishimaru, *Wave Propagation and Scattering in Random Media. Volume 2. Multiple scattering, turbulence, rough surfaces and remote sensing*, 1978.
- [13] A.T. Young, *Rayleigh scattering*, *Applied Optics*, 20 (1981) 533-535.
- [14] T. Svensson, Z. Shen, *Laser spectroscopy of gas confined in nanoporous materials*, *Applied Physics Letters*, 96 (2010) 021107.
- [15] G. Mie, *Beiträge zur Optik trüber Medien, speziell kolloidaler Metallösungen*, *Annals of Physics*, 3 (1908).
- [16] R.M. Drake, J.E. Gordon, *Mie scattering*, *American Journal of Physics*, 53 (1985) 955-962.
- [17] J.E. Hansen, L.D. Travis, *Light scattering in planetary atmospheres*, *Space Science Reviews*, 16 (1974) 527-610.
- [18] J.R. Frisvad, N.J. Christensen, H.W. Jensen, *Computing the scattering properties of participating media using Lorenz-Mie theory*, *ACM Transactions on Graphics*, 26 (2007) 60.
- [19] M.R. Rashidian Vaziri, A. Omidvar, B. Jaleh, N. Partovi Shabestari, *Investigating the extrinsic size effect of palladium and gold spherical nanoparticles*, *Optical Materials*, 64 (2017) 413-420.
- [20] V. Venugopalan, J.S. You, B.J. Tromberg, *Radiative transport in the diffusion approximation: An extension for highly absorbing media and small source-detector separation*, *Physical Review E*, 58 (1998) 2395-2407.
- [21] O. Lehtikangas, T. Tarvainen, A.D. Kim, *Modeling boundary measurements of scattered light using the corrected diffusion approximation*, *Biomedical Optics Express*, 3 (2012) 552-571.
- [22] D.J. Pine, D.A. Weitz, J.X. Zhu, E. Herbolzheimer, *Diffusing-wave spectroscopy: dynamic light scattering in the multiple light scattering limit*, *Journal of Physics of France*, 51 (1990) 2101-2127.
- [23] L.J. Gibson, M.F. Ahsby, *Cellular Solids: Structure and Properties*, Pergamon Press, Oxford, England, 1988.
- [24] A.J. Wilson, *Foams: Physics, Chemistry, and Structure*, Springer-Verlag, New York, 1989.
- [25] D.J. Durian, D.A. Weitz, D.J. Pine, *Multiple Light-Scattering Probes of Foam Structure Dynamics*, *Science*, 252 (1991) 686-688.

- [26] A.P. Nefedov, O.F. Petrov, O.S. Vaulina, Analysis of particle sizes, concentration, and refractive index in measurement of light transmittance in the forward-scattering-angle range, *Applied optics*, 36 (1997) 1357-1366.
- [27] M.U. Vera, A. Saint-Jalmes, D.J. Durian, Scattering optics of foam, *Applied optics*, 40 (2001) 4210-4214.
- [28] A. Saint-Jalmes, M.U. Vera, D.J. Durian, Uniform foam production by turbulent mixing: new results on free drainage vs. liquid content, *The European Physical Journal B*, 12 (1999) 67-73.
- [29] Z. Sadjadi, M. Miri, H. Stark, Diffusive transport of light in three-dimensional disordered Voronoi structures, *Physical Review E*, 77 (2008).
- [30] D. Weaire, S. Hutzler, *The physics of foams*, First Edition ed.2001.
- [31] A.S. Gittings, R. Bandyopadhyay, D.J. Durian, Photon channelling in foams, *Europhysics Letters (EPL)*, 65 (2004) 414-419.
- [32] M. Schmiedeberg, M.F. Miri, H. Stark, Photon channelling in foams, *The European physical journal. E, Soft matter*, 18 (2005) 123-131.
- [33] S. Pardo-Alonso, E. Solórzano, L. Brabant, P. Vanderniepen, M. Dierick, L. Van Hoorebeke, M.A. Rodriguez- Perez, 3D Analysis of the progressive modification of the cellular architecture in polyurethane nanocomposite foams via X-ray microtomography, *European Polymer Journal*, 49 (2013) 999-1006.
- [34] S. Pardo-Alonso, E. Solórzano, J. Vicente, L. Brabant, M.L. Dierick, I. Manke, A. Hilger, E. Laguna, M.A. Rodriguez-Perez, muCT-Based Analysis of the Solid Phase in Foams: Cell Wall Corrugation and other Microscopic Features, *Microscopy and Microanalysis*, 21 (2015) 1361-1371.
- [35] M.D. Abramoff, P.J. Magalhaes, J. Sunanda, Image Processing with ImageJ, *Biophotonics International*, 11 (2004) 36-42.
- [36] C.A. Schneider, W.S. Rasband, K.W. Eliceiri, NIH Image to ImageJ: 25 years of image analysis, *Nature Methods*, 9 (2012) 671-675.



Chapter 6

# **Light Scattering in Solid Cellular Polymers**





This Chapter is focused on the application of Light Scattering as a valid technique for the structural characterization of solid conventional cellular polymers. However, as shown in the precedent Chapter the common approach used in aqueous foams is not applicable since the light absorption is not negligible in the case of solid foams.

To this purpose, the first step consisted on the solution of the Diffusion Approximation equation of Light Scattering, but as a transcendental equation [1, 2], this solution was found by numerical methods. After that solution is determined it is required relate all the involved parameters to simplify the Diffusion Approximation equation and thus obtaining a direct equation that permits the determination of cell size by measuring relative density, sample thickness and optical transmissivity.

Finally, as an additional application of LS we show how the cellular anisotropy, crucial for understanding most of the physical properties of cellular materials [3, 4], can be calculated also by using LS measurements.

### 6.1 Solution of the Diffusion Approximation equation

Since the non-absorbing approach of Light Scattering (Equation 5-11) to calculate cell size is not applicable in the case of cellular materials with solid matrix, the only option as a first step to study the viability of this technique for this characterization is considering the full Diffusion Approximation equation of Light Scattering (Equation 5-8).

This equation, in addition to be transcendental, owns two variables, mean free path and absorption length, fact that hinders further the solving of the LS process in solid foams. Moreover, the use of digital cameras as light detectors precludes the direct determination of incident intensity if the light source is a laser, as it was in our case.

As shown in the next work **“Efficient prediction of cell size in solid polymeric foams by numerically solving the diffusion approximation of light scattering equation”**, to overcome these two limitations, several measurements of the transmitted intensity were performed sequentially slicing the thickness of the sample. In this way, thanks to

Lambert-Beer law [5] it was possible extrapolate the incident intensity and thus calculate transmissivity. Finally, the multiple measurements enable solving the Diffusion Equation varying in a broad range absorption length to finally obtain transport mean free path. This process is explained in detail in the following paper. As a result, the mean free path is successfully calculated in a collection of conventional low density microcellular polymers based on PU, PE and PS and consequently the mean cell size of all the samples is determined finding good correlations with SEM characterizations.

Colloids and Surfaces A 534 (2017) 130-137  
<https://doi.org/10.1016/j.colsurfa.2017.07.076>

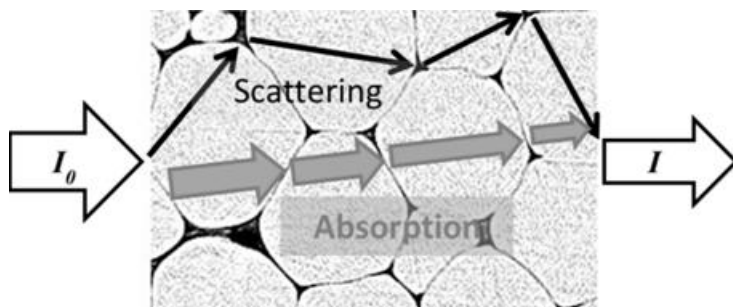
## Efficient prediction of cell size in solid polymeric foams by numerically solving the diffusion approximation of light scattering equation

S. Pérez-Tamarit\*, E. Solórzano, M.A. Rodríguez-Perez

*CellMat Laboratory, University of Valladolid, Paseo de Belén 7 47011, Spain*

\* Corresponding author: [saúl.perez@fmc.uva.es](mailto:saúl.perez@fmc.uva.es)

Tel.: +34 983 423572; fax: +34 983 433192



### Abstract

This paper investigates alternative approaches to accurately calculate the cell size of solid polymeric foams by means of light scattering (LS) experimental data. To this end, static optical transmission measurements have been carried out in foams with different densities, cell sizes and based on different polymers. Using these data cell size has been calculated by solving numerically the diffusion approximation equation of LS that takes into account both scattering and absorption mechanisms. From the analysis performed we have proved that light absorption becomes significant in solid polymeric foams.

**Keywords:** light scattering; solid foams; polyurethane foams; polystyrene foams; polyethylene foams.

## **1. Introduction**

Solid foams are used in hundreds of applications due to their wide range of properties. These materials combine low density, high specific mechanical properties [1-3], improved thermal and acoustic insulation [4-8], high specific surface, etc...

It is well known that the properties of solid foams depend on the properties of the solid matrix and features such as the foam density and the cellular architecture [4]. It is, therefore, important to develop techniques allowing a simple, straightforward and reliable characterisation of these foam characteristics. Density measurements are fast and direct, while a fast quantitative measurement of the cell size is still a challenge. Different techniques are currently used to determine the average cell size but most of them present several inconveniences. Optical methods are tedious; it is necessary to prepare the sample, they evaluate only the foam surface and therefore the results of these techniques are a biased 2D value of the cell size. Alternatively, other methods require complex devices and heavy data treatment (X-ray tomography) or need particular foam characteristics; mercury and gas porosimetry can only be used for open-cell materials.

Aqueous foams research has faced similar challenges, with the additional inconvenience of studying a delicate system that cannot be manipulated. To solve this challenge, a collection of

techniques based on the interaction of light with this dispersive media were developed in the 80's and 90's. These techniques are known as light scattering methods and several variations are described in the literature. These methods are based on correlating the intensity of collected light with the size of objects that interact with light contained within the sample [9]. One of application of these methods allows calculating the cell size by measuring the light transmitted through the foam sample [10, 11].

From a theoretical point of view the correlation between light transmitted and cellular structure is carried out by approximating the light scattering by a diffusion equation for the light that propagates in a media containing a high concentration of dispersion centres, such as colloids or foam bubbles. In this approximation the diffusion of light is characterized by the transport mean free path  $l^*$ , which corresponds to the average distance that a photon can travel before its direction is randomized. Its value is directly related to the diffusion coefficient of light,  $vl^*/3$ , where  $v$  is the speed of light in the medium. In addition, in this model light absorption is also considered through the parameter absorption length ( $l_a$ ). The solution for the diffusion equation in aqueous foams and colloidal systems is rather well known [10] (eq. 1). This equation relates transmissivity ( $T$ ), defined as the ratio between transmitted and incident light intensities, transport mean free path ( $l^*$ ), sample thickness ( $L$ ) and absorption length ( $l_a$ ):

$$T \approx \frac{(5l^*/3L)\beta}{[1+(4l^*/3L)]\sinh\beta} ; \beta = \sqrt{\frac{3L^2}{l^*l_a}} \quad (1)$$

One of the most used approximations in aqueous foams assumes that light absorption is negligible. In fact values of 200 cm [10] for the absorption length has been estimated, resulting in  $l_a \gg L \gg l^*$ . Therefore for the systems with negligible absorption ( $\beta \ll 1$ ), the equation for the transmissivity is:

$$T \approx 5l^*/3L \quad (2)$$

This assumption works properly for liquid foams due to the small dimensions of cell walls, typically in the nanometric range (approx. 100-500 nm) [12]. For these particular materials, light scattering is the only light-material interaction that has to be taken into account. This scattering is mainly produced in the Plateau borders in which almost the totality of the liquid fraction is contained.

In addition, eq. 2 can be modified by using the relation between mean pore size and light transport mean free path proposed by Vera et al. [11].

$$l^* = \phi / \sqrt{\varepsilon} \quad (3)$$

where  $\varepsilon$  is the solid fraction.

Combining eq. 2 and eq. 3, it is possible to obtain a simple final expression relating mean cell size ( $\phi_{LS}$ ), transmissivity ( $T$ ), solid fraction ( $\varepsilon$ ) and sample thickness ( $L$ ).

$$\phi_{LS} = LT\sqrt{\varepsilon} \quad (4)$$

The previous concept (the use of LS experiments to determine cell size) can be tested in solid foams. One important advantage with these materials is the possibility of manipulating these solid foams. Therefore, it would be possible measuring the cell size by 2D or 3D methods and comparing the results obtaining with LS experiments.

However, there are a few aspects that should be considered when applying the previous developed model for aqueous foams or colloids. First, polymers can be amorphous and semicrystalline, and the ordered structure of the polymer in the crystalline phase of these last polymers can play a role.

In addition, solid foams present a mean cell wall thickness in the micrometric range (1-20  $\mu\text{m}$ ), i.e. 1-2 orders of magnitude thicker than that of aqueous foams. As a consequence, light absorption by the solid phase of the material needs to be considered.

Nowadays, the influence of light absorption in liquid foams has been widely investigated [13, 14]. In these studies, liquid foams with liquid fractions of 0.78 have been tested finding absorption lengths values around 700 mm. As a result, the absorption in this type of materials plays a minor role and it is not considered in the theoretical models. In our case, the calculated absorption lengths for the materials

included in this investigation were around 25-110  $\mu\text{m}$ . Therefore it is expected that light absorption plays an important role in the light-material interaction even for low values of the solid fraction.

The main objective of this paper is to determine the cell size of solid polymeric foams by using an experimental data of LS tests and a numerical solution of the LS equation. Taking into account the previous discussion we will use as a starting point equation 1, in which both scattering and light absorption mechanisms are considered. The research is carried out using solid foams based on three different solid polymers: polyurethane -PU (amorphous) -, polystyrene -PS (amorphous) - and polyethylene -PE (semicrystalline)- and with different solid fractions and average cell sizes.

## 2. Experimental

### 2.1 Materials

A collection of solid foams based on three

polymers have been used. . Two of these polymers are amorphous: polyurethane -PU- and polystyrene -PS- and the other one is semicrystalline; polyethylene -PE-. The foams selected covered a wide range of solid fractions (from 0.023 to 0.089) and cell sizes (from 250 to 850 microns) as can be observed in Table 1.

### 2.2 Determination of density, pore size and solid fraction

As mentioned, one of the main advantages of using solid foams in this investigation is the possibility of manipulating the specimens to obtain a detailed characterization of the cellular structure by conventional methods.

The solid fraction is defined as the ratio between foam density and the solid material density. In our case, the foam density for all the materials was measured by the gravimetric method using a high precision balance and considering the sample dimensions. The densities of the solids were 1160  $\text{kg}/\text{m}^3$ , 1050  $\text{kg}/\text{m}^3$  and 910  $\text{kg}/\text{m}^3$  for PU, PS and PE foams respectively.

**Table 1.** Summary of foam specimens included in this investigation.

Matrix type	Reference	$\epsilon$	$\phi$ ( $\mu\text{m}$ )
Polyurethane	PU-1	0.023	600 $\pm$ 130
	PU-2	0.042	850 $\pm$ 200
	PU-3	0.047	570 $\pm$ 100
	PU-4	0.089	760 $\pm$ 100
Polystyrene	PS-1	0.034	250 $\pm$ 50
	PS-2	0.033	260 $\pm$ 50
Polyethylene	PE-1	0.018	370 $\pm$ 80
	PE-2	0.022	340 $\pm$ 80
	PE-3	0.059	800 $\pm$ 150

Cellular structure of specimens was determined by using a scanning electron microscope (model JSM 820). Before the SEM analysis, the samples were fractured in liquid nitrogen to keep the micro-structure unaltered and a thin layer of gold was deposited on the samples surface by using a sputter coater (model SCD 005, Blazers Union). Microscopy images were analysed using a self-developed processing application [15] based on ImageJ/Fiji image analysis software [16, 17] that allows obtaining reliable values of mean cell size in 2D and also determines the stereologic projection of cell size in 3D. In addition, the variability on the measured cell size values is determined by the standard deviation of the cell size distributions (table 1).

### 2.3 Light scattering experiments: Experimental set-up

The experimental set-up used is presented in Figure 1. The main elements

are a green laser (wavelength of 532 nm) of 10 mW of nominal power used as light source and a digital camera used as light detector. The green laser provides a coherent and quasi-parallel illumination (divergence angle of the beam less than 1.2 mrad) with tunable power via a TTL port. The distance between the light source and the camera lens was 230 mm. The detection lens-camera system consisted of an IDS-Ueye 12 bit monochrome CMOS camera mod. UI-5480CP-M-GL and an infinite focus lens providing a field of view of 213x160 mm<sup>2</sup> at the mentioned working distance. The linearity response of this camera with both varying incident light intensity and exposure time was verified. The samples used (figure 1) have lateral dimensions of 120x120mm to avoid border effects (i.e. to avoid light losses through the lateral surfaces)

The transmitted intensity was calculated as the mean grey value of a region of interest in the images (ROI) covering the

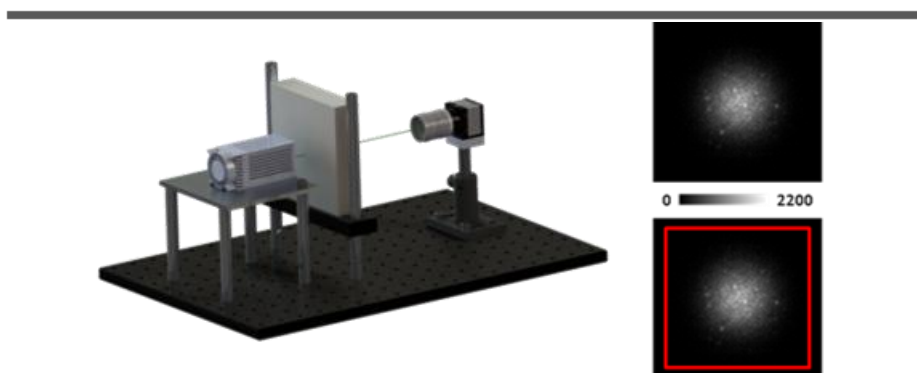
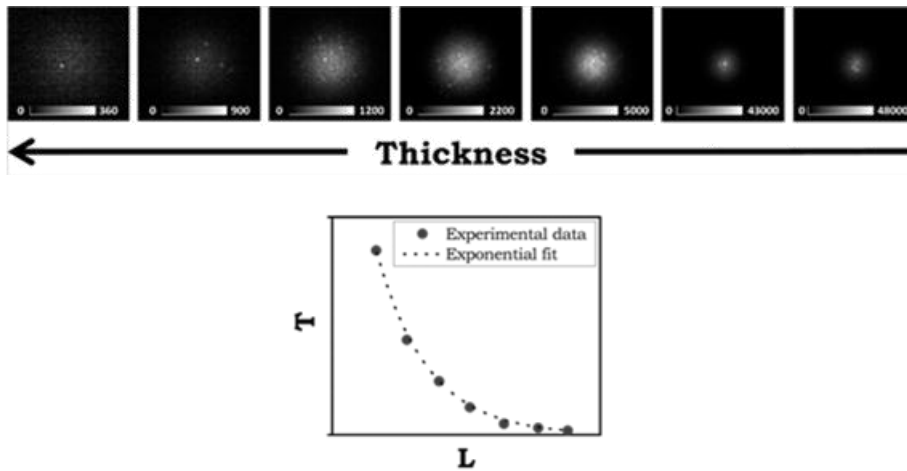


Fig. 1. CAD drawing of the experimental set-up consisting in 532 nm green laser and camera - left- and example of a transmission image with the corresponding ROI -right-.



**Fig. 2.** Complete set of images for the same specimen with different thickness-top- and optical transmission profile versus thickness -bottom- plotted together with the exponential fit.

entire surface of the sample, i.e. collecting the transmitted light from any point of the sample. The area of the ROI for all the samples is basically constant for all the measurements. (Figure 1)

The power of laser beam is tuned at 2 mW and the images are acquired with an exposure time of 5 ms. At this exposure time the transmitted light does not saturate the camera regardless the kind of sample and thickness.

#### 2.4 Optical transmission

As mentioned before, the optical transmission or transmissivity ( $T$ ) is defined as the ratio of the intensity transmitted through the sample ( $I$ ) to the total intensity detected without any sample ( $I_0$ ): (Eq. 5).

$$T = I/I_0 \quad (5)$$

In our particular case, the use of laser as light source precludes the direct measurement of incident intensity using a digital camera. We have determined this value through the extrapolation of the transmitted intensity variation with sample thickness. Any inaccuracy in this calculation may distort the absolute value of the predicted cell size, but should not affect the trends observed for the different examined samples.

The initial specimen for all the materials was a foam slab of 120x120x30 mm<sup>3</sup>. The samples were sequentially sliced from the initial thickness of 30 mm to approximately 5 mm acquiring images for every intermediate thickness (*ca.* 30, 25, 20, 15, 10 and 5 mm). Five consecutive images of the transmitted pattern were acquired and averaged to reduce noise. Therefore, for each sample we obtained a set of images that allowed obtaining the curves intensity versus sample thickness



$$T = \frac{(5l^*/3L) \sqrt{3L^2/l^*l_a}}{[1 + (4l^*/3L)] \sinh\left(\sqrt{\frac{3L^2}{l^*l_a}}\right)} \Rightarrow T [1 + (4l^*/3L)] \sinh\left(\sqrt{\frac{3L^2}{l^*l_a}}\right) = (5l^*/3L) \sqrt{3L^2/l^*l_a}$$

Transcendental equation

Mean free path ( $l^*$ ) results chart

	$L_i$ / mm	...	$L_n$ / mm		
$l_a$ / mm	$T_i$	...	$T_n$	$\bar{l}^*$ / mm	$SD_{l^*}$ / mm
1	$l^{*1}_1$	...	$l^{*n}_1$	$\bar{l}^*_1$	$SD_{l^*_1}$
...	...	...	...	...	...
200	$l^{*1}_{200}$		$l^{*n}_{200}$	$\bar{l}^*_{200}$	$SD_{l^*_{200}}$

**Fig. 3.** Transformation of the diffusion equation to be solved by numerical methods –up- and scheme of the obtained results by using the solving strategy reported –down-.

(figure 2). As it can be observed in the top of the figure 2 the image intensity increases when the thickness is reduced (see greyscale values range). Considering an exponential dependence of the intensity with sample thickness the value of incident intensity was determined and therefore also the transmissivity by using the eq. 5 (figure 2 bottom).

### 3. Numerical methods

As we explained in the introduction the classical solution equation of light scattering (equation 2) does not account for systems in which there is a high absorption. Therefore, in our case it is necessary to solve the diffusion equation (eq. 1). However, this equation is transcendental further and it is not possible to find an analytical solution. Therefore, we have solved this equation numerically by computing results with different sample thickness (pairs of

thickness and transmissivity). In this equation, both absorption length and mean free path are unknown and therefore cell size could not be determined. To overcome this issue, we vary the absorption length in a broad range –from 1 to 200 mm–, and introduce all the variables in the diffusion equation (eq. 1).

We solved then numerically this equation by using the symbolic language for solving equations in MatLab obtaining finally a value of transport mean free path (which is the independent variable in order to find the solution) for every value of absorption length and transmissivity-thickness pair. We calculated the average value ( $\bar{l}^*$ ) and the standard deviation ( $SD_{l^*}$ ) (eqs. 6 and 7) from mean free path corresponding to all the thickness-transmissivity pairs for each absorption length of the selected range (figure 3). Moreover, the samples

are homogeneous in cell size and density and consequently in mean free path (eq. 4). Therefore the most suitable value of absorption length for each sample was one that minimized the variation in the mean free path (see figure 4).

$$\bar{l}^* = \frac{1}{n} \sum_{i=1}^n l^{*i} \quad (6)$$

$$SD_{l^*} = \sqrt{\frac{1}{n-1} \sum_{i=1}^n (l^{*i} - \bar{l}^*)^2} \quad (7)$$

where  $n$  is the number of analysed slabs with different thickness and the superindex indicates thickness-transmissivity pair.

Using both the standard deviation and average values of mean free path we defined a new parameter: the relative variation of transport mean free path ( $\Delta l^*$ ) which is the ratio of the standard deviation and the average value of mean free path (eq. 8).

$$\Delta l^* = 100 \cdot \left( \frac{SD_{l^*}}{\bar{l}^*} \right) \quad (8)$$

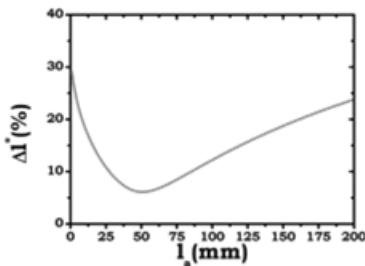


**Fig 4.** Relative variation of transport mean free path as a function of absorption length obtained by the numerical process developed in this investigation (sample PU-3).

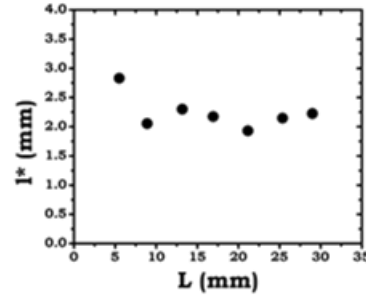


**Fig 5.** Calculated mean free path values as a function of sample thickness for the sample PU-3 obtained from the numerical solution of light scattering equation (equation 1).

This parameter was plotted versus the absorption length and a minimum was found in all cases (fig. 4). The selected value for absorption length is the minimum of the curve in figure 4 since it minimizes the standard deviation of the transport mean free path calculated over the 7 slab thickness of a homogeneous sample, as showed in figure 4.

Once the absorption length is determined the final step consisted in the determination of the transport mean free path at the 7 different thickness values experimentally collected, as shown in figure 5. The calculated value for the material will be the average of these 7 values  $\bar{l}^*$  (figure 3). After having obtained transport mean free path it is possible to calculate cell size ( $\phi_{NS}$ ) using equation 3.

## 4. Results and discussion

### 4.1 Sample characterization

A summary of the characterised features of the analysed samples is shown in table 1. In all cases the solid fraction is lower

than 0.1. Therefore the samples under study are low density solid foams.

The typical cellular structure of the materials under study can be observed in figure 6. All of them are closed cell isotropic foams. The analysed samples have cell sizes ranging 250-850 micrometres as shown in table 1.

The variation in solid fraction with respect to the average solid fraction is higher than 50%. Consequently, the group of selected samples comprises a broad range of solid fractions. From the point of view of cell size this variation is higher than 40%.

PE foams are based in a semicrystalline polymer, while PU and PS are amorphous. This fact might cause significant differences considering the different optical properties of these polymers [18, 19]. In addition, focusing on the cellular architecture, a critical parameter in these materials is the fraction of solid phase in Plateau borders  $-f_s-$ . It represents the fraction of solid

material constituting the Plateau borders (edges and vertexes). It becomes a crucial parameter in the case of mechanical [1], thermal [20] and radiative properties [21, 22]. Therefore, regarding the similarities between IR radiative and light scattering processes this parameter may also strongly affect light scattering behaviour. In the case of the involved specimens in this study, PU foams present a high solid fraction percentage concentrated in Plateau borders resulting in a high value of  $f_s$  [23] whereas in the case of PE and PS foams this parameter is low or even ultra-low [24]. These differences can be shown in figure 7 (slice of high resolution tomographies for two of the included foams). In this figure Plateau borders are represented in red whereas the cell walls are highlighted in green.

### 4.2 Cell size values obtained by LS

The already explained procedure allowed us estimating mean cell sizes for all the analysed samples ( $\phi_{NS}$ ). It is now possible to compare these results with bubble sizes determined by microscopy methods

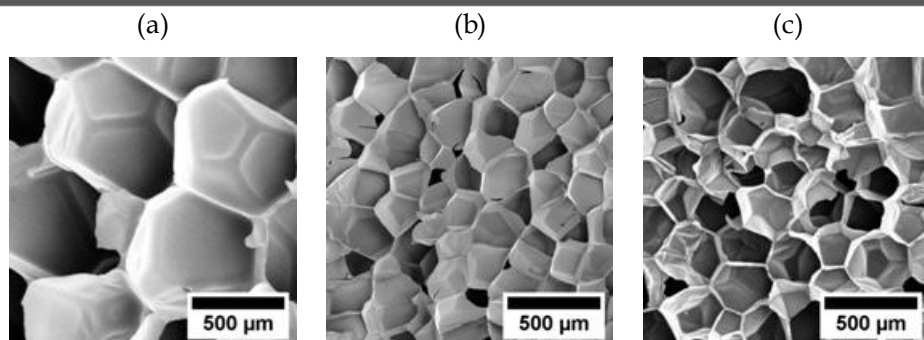


**Fig. 6.** Electron microscopy images of specific samples included in this investigation. (a) PU-1 (b) PS-1 (c) PE-1.

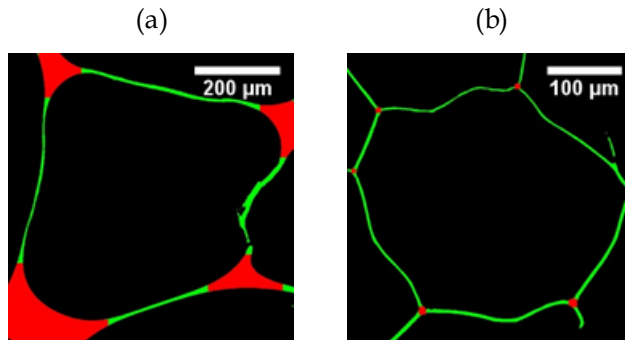


**Fig. 7.** Separated foam structure. Plateau Borders (red) and cell walls (green) for two foam specimens. (a) PU -high  $f_s$ - (b) PE -low  $f_s$ -.

(table 1). Figure 8 shows this comparison. In this figure the black dashed line corresponds to the equality line (slope 1) between the two involved characterization methodologies. As it can be appreciated most of the data are close to this line, in fact the discrepancies between methods do not exceed 20% (grey dashed lines in figure 8) resulting in acceptable differences considering the typical width of cell size distributions in this type of cellular polymeric foams [25].

Moreover, as indicated before, values of absorption length and transport mean free path were also calculated (see table 2). In the case of absorption length, all the values are in the range 25-110 mm certifying the influence of light absorption in low density solid foams. On the other hand, transport mean free path values are around 1.5-4.5 mm for all the samples. Transport mean free path values are lower than sample thickness even for the thinnest tested samples. This fact

confirms that it is possible the application of the diffusion approach for this system.

#### 4.3 Comparison with classical solution

In order to show the differences between the results obtained by using the classical solution of light scattering  $-\phi_{LS}-$  (eq. 4) and the experimental results achieved in this investigation using equation 1  $-\phi_{NS}-$  we have calculated the mean cell size using the two approaches for three samples (figure 9).

Taking into account the displayed results

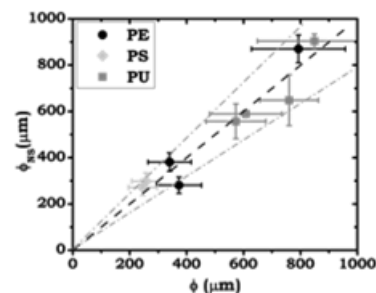


**Fig. 8.** Cell size estimations according to the applied numerical solution compared with cell size measured by scanning electron microscopy.

**Table 2.** Calculated values of transform mean free path and absorption length for all the materials under study.

Matrix type	Reference	$l_a$ (mm)	$l^*$ (mm)
Polyurethane	PU-1	54	3.85±0.07
	PU-2	27	4.43±0.11
	PU-3	45	2.56±0.15
	PU-4	38	2.18±0.37
Polystyrene	PS-1	33	1.48±0.18
	PS-2	35	1.63±0.20
Polyethylene	PE-1	57	2.09±0.26
	PE-2	108	2.56±0.26
	PE-3	45	3.57±0.24

the differences are clear. The classical solution of light scattering that assumes that there is no light absorption seems to be not applicable for several reasons. Firstly, this approach considers an inverse dependence between optical transmission and sample thickness (eq. 2) and we have demonstrated experimentally that this dependence is mainly exponential (similar to a Lambert-Beer law (figure 2)). Moreover, in the literature the corresponding absorption length that allow assuming that light absorption is negligible must be around 200 cm [10] whereas the calculated absorption length values in this investigation are in the range 25-110 mm.

The results figure 9 also confirms that the light absorption in solid foams must be considered since the numerical solution of equation 1 provides a satisfactory outcome. Once the absorption is considered the cell sizes obtained offers reasonable values for all the tested specimen thickness, even for the thicker

samples (~30 mm) in which the amount of transmitted light is small.

Finally is it important to mention that according to the values obtained for the absorption length and transport mean free path (table 2) it is recommendable to exclude those results for thickness below 10 mm since the number of interactions is not sufficient according to the theory. Actually if we remove these points we can see a lower deviation of predicted cell size for the numerical approach and a clearer trend for the classical simplified model.

#### 4.4 Influence of foams characteristics in absorption length and transport mean free path

In this final section, we have analysed the influence of matrix and foam architecture on both characteristic lengths of light scattering -absorption length and transport mean free path-. To this end and in order to eliminate the effect of mean cell size and solid fraction the two characteristic lengths are corrected by a

factor ( $\varepsilon/\phi$ ) and the values obtained are averaged for foams based on the same polymer matrix (figure 10).

The results for corrected transport mean free path indicate that average value for PU and PS is similar whereas in the case of PE the value is 15-20% lower. This is probably connected with the fact that PE

is a semicrystalline polymer with crystallinity index  $-X_c-$  around 40% whereas PS and PU are amorphous polymer (table 3). This result seems to indicate that transport mean free path is likely affected by the optical properties of the solid phase.

On the other hand, the corrected absorption length shows a strong difference for PU foams in comparison to PE and PS. The value for PU foam is about 40% lower in average. Accordingly to the radiative transport literature [20] the size of Plateau borders and more specifically the amount of material constituting these entities are highly associated to scattering process. As observed in figure 3 PU samples possess a larger fraction of mass in the Plateau borders which may be the cause of this reported difference. Curiously both PE and PS present low  $f_s$  values which are within the expected trend. As a consequence the absorption length seems to be strongly correlated with the foam structure and particularly with the  $f_s$  value.

Nevertheless, the variability of the results hinders extracting definitive conclusions

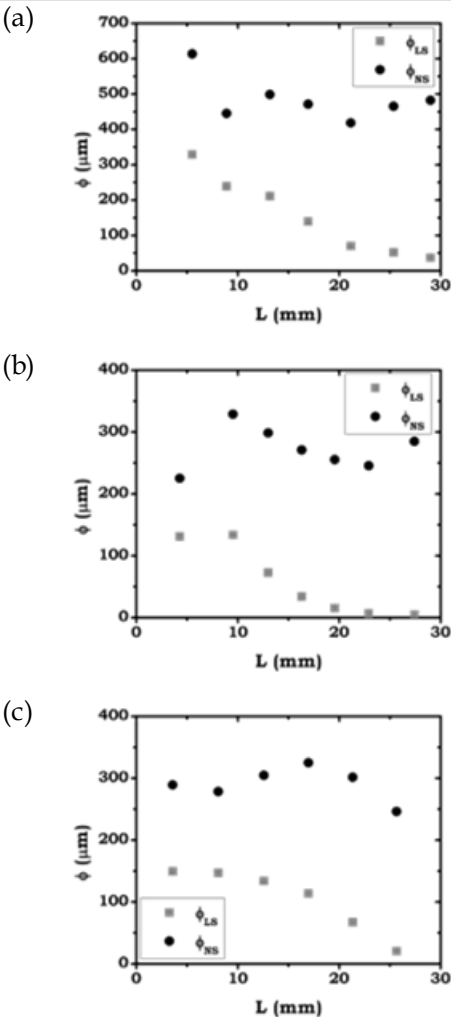


Fig. 9. Comparison of “simplified” light scattering solution (eq. 4) and the numerical solution obtained in this study for three different samples. (a) PU-3 (b) PS-2 (c) PE-1.

Table 3. Fraction of polymer in the Plateau Borders  $-f_s-$  and cristallinity index  $-X_c-$  for the foams under study.

Solid Matrix	$f_s$	$X_c$
PU	0.7-0.9	1-2%
PS	0.1-0.2	1-2%
PE	0.2-0.4	~40%

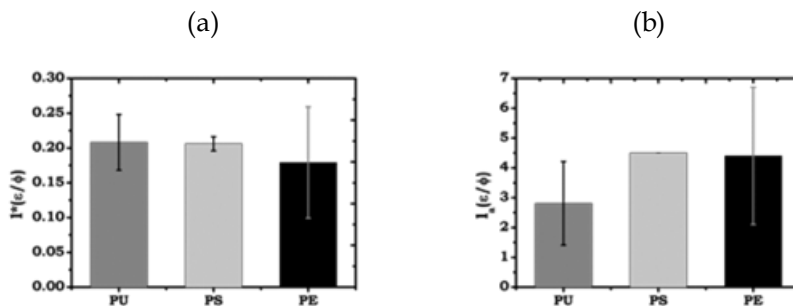


Fig. 10. Average normalized characteristic lengths for samples included in this study. (a) Transport mean free path and (b) absorption length.

on the effects discussed in this section.

### 5. Conclusions

The results of this paper indicate that it is possible to obtain accurate predictions of the cell size of polymeric foams by measuring the optical transmission of foamed slabs of different thickness and by solving the light scattering equation that takes into account both scattering and absorption. The developed approach has been proved in foams within a significant density and cell size range and based on both amorphous and semicrystalline polymers.

Further work and refinements in the experimental set-up are required to develop a theoretical model allowing a direct prediction of cell size without the need of testing foams with different cell sizes. In addition, the influence of other foam and/or matrix characteristics should be studied in detail.

There is an important potential of the results presented in this paper to develop a fast and non-destructive technique to

measure the average cell size of cellular plastics. Due to the simplicity of the set-up this could also be a useful technique for the in-situ characterisation of the evolution of cell size during the production process.

### Acknowledgements

We acknowledge Anniina Salonen and Clément Honorez from the Laboratoire de Physique des Solids of Université Paris Sud for their suggestions and support when we started this research.

In addition, financial assistance from MINECO and FEDER program (MAT 2012 - 34901) MINECO, FEDER, UE (MAT2015-69234-R) and the Junta de Castile and Leon (VA035U13) are gratefully acknowledged. Predoctoral contract of S. Perez-Tamarit by University of Valladolid (E-47-2015-0094701) and co-financed by Banco Santander is also acknowledged.



## References

- [1] L.J. Gibson, M.F. Ahsby, *Cellular Solids: Structure and Properties*, Pergamon Press, Oxford, England, 1988.
- [2] M.A. Rodriguez- Perez, J. Lobos, C.A. Perez-Muñoz, J.A. De Saja, L. Gonzalez, B.M.A. del Carpio, *Mechanical Behaviour at Low Strains of LDPE Foams with Cell Sizes in the Microcellular Range: Advantages of Using These Materials in Structural Elements*, *Cell. Polym.*, 27 (2008).
- [3] M.A. Rodriguez-Perez, *The effect of Chemical composition, density and cellular structure on the dynamic mechanical response of polyolefin foams*, *Cell. Polym.*, 21 (2002) 117-136.
- [4] J.A. Reglero Ruiz, C. Saiz-Arroyo, M. Dumon, M.A. Rodriguez-Perez, L. Gonzalez, *Production, cellular structure and thermal conductivity of microcellular (methyl methacrylate)-(butyl acrylate)-(methyl methacrylate) triblock copolymers*, *Polym. Int.*, 60 (2011) 146-152.
- [5] M.A. Rodriguez- Perez, O. Alonso, J. Souto, J.A. De Saja, *Thermal Conductivity of Physically Crosslinked Closed Cell Polyolefin Foams*, *Polym. Test.*, 16 (1997) 287-298.
- [6] M. Alvarez-Lainez, M.A. Rodriguez-Perez, J.A. De Saja, *Thermal conductivity of open-cell polyolefin foams*, *J. Polym. Sci. Part B: Polym. Phys.*, 46 (2008) 212-221.
- [7] X. Wang, T.J. Lu, *Optimized acoustic properties of cellular solids*, *J. Acoust. Soc. Am.*, 106 (1999).
- [8] A. Cunningham, S.P. Beadle, *Acoustic properties of reticulated plastic foams*, *J. Sound and Vibration*, 175 (1993) 115-133.
- [9] A.P. Nefedov, O.F. Petrov, O.S. Vaulina, *Analysis of particle sizes, concentration, and refractive index in measurement of light transmittance in the forward-scattering-angle range*, *Appl. Opt.*, 36 (1997) 1357-1366.
- [10] D.J. Durian, D.A. Weitz, D.J. Pine, *Multiple Light-Scattering Probes of Foam Structure Dynamics*, *Science*, 252 (1991) 686-688.
- [11] M.U. Vera, A. Saint-Jalmes, D.J. Durian, *Scattering optics of foam*, *Appl. Opt.*, 40 (2001) 4210-4214.
- [12] D. Weaire, S. Hutzler, *The physics of foams*, First Edition ed.2001.
- [13] A.S. Gittings, R. Bandyopadhyay, D.J. Durian, *Photon channelling in foams*, *Europhys. Lett.*, 65 (2004) 414-419.
- [14] M. Schmiedeberg, M.F. Miri, H. Stark, *Photon channelling in foams*, *The European physical journal. E, Soft Matter*, 18 (2005) 123-131.
- [15] J. Pinto, E. Solorzano, M.A. Rodriguez-Perez, J.A. de Saja, *Characterization of the cellular structure based on user-interactive image analysis procedures*, *J. Cell. Plast.*, 49 (2013) 555-575.
- [16] M.D. Abràmoff, P.J. Magalhaes, J. Sunanda, *Image Processing with ImageJ*, *Biophotonics Intern.*, 11 (2004) 36-42.
- [17] C.A. Schneider, W.S. Rasband, K.W. Eliceiri, *NIH Image to ImageJ: 25 years of image analysis*, *Nat. Methods*, 9 (2012) 671-675.
- [18] D. Mileva, R. Androsch, H.-J. Radusch, *Effect of structure on light transmission in isotactic polypropylene and random propylene-1-butene copolymers*, *Polym. Bull.*, 62 (2009) 561-571.
- [19] X.F. Xu, P.J. Bates, G. Zak, *Effect of glass fiber and crystallinity on light transmission during laser transmission welding of thermoplastics*, *Opt. Laser Technol.*, 69 (2015) 133-139.
- [20] A. Cunningham, N.C. Hilyard, *Low Density Cellular Plastics: Physical Basis of Behaviour*, Ed. Chapman and Hall, London, 1994.
- [21] O.A. Almanza, M.A. Rodriguez- Perez, J.A. de Saja, *Prediction of the Radiation Term in the Thermal conductivity of crosslinked closed cell polyolefin foams*, *J. Polym. Sci. Part B: Polym. Phys.*, 38 (2000) 993-1004.
- [22] R.A. Campo-Arnáiz, M.A. Rodríguez-Pérez, B. Calvo, J.A. de Saja, *Extinction coefficient of polyolefin foams*, *J. Polym. Sci. Part B: Polym. Phys.*, 43 (2005) 1608-1617.
- [23] S. Pardo-Alonso, E. Solórzano, L. Brabant, P. Vanderniepen, M. Dierick, L. Van Hoorebeke, M.A. Rodriguez- Perez, *3D Analysis of the progressive modification of the cellular architecture in polyurethane nanocomposite foams via X-ray microtomography*, *Eur. Polym. J.*, 49 (2013) 999-1006.
- [24] O. Almanza, M.A. Rodriguez- Perez, J.A. de Saja, *The microstructure of polyethylene foams produced by a nitrogen solution process*, *Polymer*, 42 (2001) 7117-7126.
- [25] S. Estravís, J. Tirado-Mediavilla, M. Santiago-Calvo, J.L. Ruiz-Herrero, F. Villafañe, M.Á. Rodríguez-Pérez, *Rigid polyurethane foams with infused nanoclays: Relationship between cellular structure and thermal conductivity*, *Eur. Polym. J.*, 80 (2016) 1-15.

## Glossary:

- $\phi$ : mean pore size
- $\rho$ : sample density
- $\varepsilon$ : solid fraction
- $l^*$ : transport mean free path
- $L$ : slab thickness
- $l_a$ : absorption length
- $T$ : transmissivity
- $f_s$ : fraction of mass in Plateau Borders
- $X_c$ : crystallinity index



## 6.2 Novel theoretical modelling in solid cellular polymers

Once the methodology is validated for calculating the mean cell size the next step consist on the relationship between all the involved parameters (transport mean free path, absorption length and the extinction coefficient calculated in the Beer-Lambert equation). As a result, the simplification of the Diffusion Approximation equation can be carried out to finally obtain a theoretical model to determine directly the mean cell size.

In fact, it is well known the solution of the Fick law in case of a semi-infinite diffusing medium with a quasi-parallel illumination, rather similar to our systems, with slab geometries in which the surface/thickness ratio is enough to minimize the light loses by the edges and light laser as light source [6] (Equation 6-1). The resulting equation is similar to the Beer-Lambert equation.

$$I(L) = I(0)\exp\left(-(\mu_a/D)^{1/2}L\right) = I(0)\exp(-kL) \quad \text{Equation 6-1}$$

Where  $\mu_a$  is the absorption coefficient. Considering the relation between diffusion coefficient and transport mean free path ( $D=vl^*/3$ ) the previous equation can be transformed to include mean free path (Equation 6-2).

$$I(L) = I(0)\exp\left(-\left(3\mu_a/vl^*\right)^{1/2}L\right) = I(0)\exp\left(-\sqrt{\frac{3L^2\mu_a}{vl^*}}\right) \quad \text{Equation 6-2}$$

In fact, the last argument within the exponential is similar to  $\beta$  value on the Diffusion Approximation equation. Under this perspective, the relation between all the calculated parameters in the precedent paper was accomplished on the next work entitled **“Semi-empirical modified light scattering model for cell size characterization of solid cellular polymers”**.

In this work, the same samples than in the precedent paper in order to demonstrate those relationships and finally a modified model of LS is developed for the suitable study of solid cellular polymers by means of Light Scattering methodologies. The cell size values obtained thanks to the developed theoretical model are compared with

those determined by means of X-ray Tomography therefore validating the semi-empirical obtained modelling.

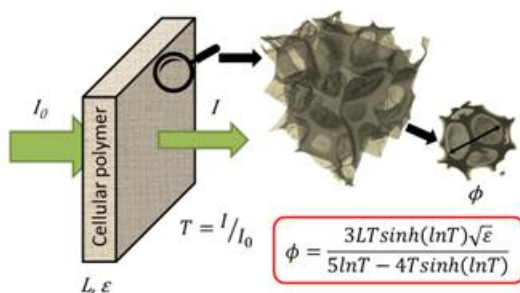
### Semi-empirical modified light scattering model for cell size characterization of solid cellular polymers

S. Pérez-Tamarit\*, E. Solórzano, M.A. Rodriguez-Perez

*CellMat Laboratory, University of Valladolid, Paseo de Belén 7 47011, Spain*

\* Corresponding author: [saúl.perez@fmc.uva.es](mailto:saúl.perez@fmc.uva.es)

Tel.: +34 983 423572; fax: +34 983 433192



#### Abstract

This paper shows the development of a novel modified modelling of light scattering (LS) in solid matrix cellular polymers that will allow directly determining the average cell size of this materials. To this end, empirical data obtained in a previous investigation have been considered and correlated to finally obtain an equation that permits calculating the cell size of solid cellular polymers.

The developed model has been successfully tested in a collection of solid cellular polymers based on polyethylene (PE), polystyrene (PS) and polyurethane (PU) with different characteristics (density and cell size). As an additional consequence, with the results addressed in this paper it will be possible also the monitoring of the in-situ evolution of cell size, for industrial QA purposes for example.

**Keywords:** light scattering; solid cellular polymers; cell size characterization.

## **1. Introduction**

It is well known that the applicability of cellular polymers depends mainly on their structural features (solid matrix characteristics and cellular architecture) [1-3]. For this reason, it is crucial to obtain a straightforward description of the cellular structure of these materials to understand the structure-properties-applications relationship. Density measurements are fast and direct, while a fast quantitative measurement of the cell size is still a challenge. In fact, there are several options nowadays to characterize the cell size of these materials, but involving also several inconveniences. On one hand, optical methods like optical or electronic microscopy are the most extended option to accomplish this task. However, they lead to a tedious process. The tested material must be carefully prepared to maintain the structure unaltered. In addition, these techniques only evaluate the surface of the samples, resulting in 2D skewed results that only could be approximated by 3D stereological extrapolations [4, 5]. On the other hand, X-ray tomography provides accurate structural characterization in 3D [6-8], but requires specific equipment and heavy and time-consuming data treatment.

Another option employed for the characterization of aqueous foams since several decades is a collection of techniques based on the interaction of light with this dispersive media, known as light scattering (LS) methods in the

literature. In these methods the light interacting with the scattering entities within the sample is collected and correlated allowing the determination of the size of these entities [9]. As a result of these basic concepts, this kind of techniques allows a simple, fast and straightforward characterization of scattering objects size. In addition, the extension to in-situ measurements of entities size is almost automatic. Nevertheless, nowadays these modelling options have been only applied in aqueous foams and colloids. Due to the small dimensions of cell walls in these materials, typically in the nanometric range (approx. 100-500 nm) [10], the light absorption is considered negligible and the model is automatically simplified. However, light absorption should be considered in the case of solid cellular polymers.

Therefore, the main objective of this paper is to develop a novel modified modelling of LS which allows determining directly the cell size of solid cellular polymers by using a semi-empirical adaptation of previous experimental results of LS tests. The research is carried out using cellular polymers based on three different solid matrixes: polyurethane -PU -, polystyrene -PS - and polyethylene -PE - and with different relative densities and average cell sizes.

## 2. Experimental

### 2.1 Materials and characteristics

This work was accomplished by using cellular materials based on three different solid matrixes, polyurethane (PU), polystyrene (PS) and polyethylene (PE). The density of the samples was calculated considering their weight and geometrical dimensions. This information allowed us determining the relative density ( $\epsilon$ ) of the involved materials taking into account that the densities of the solid matrixes are 1160, 1050 and 910 kg/m<sup>3</sup> for PU, PS and PE respectively. The cell size was characterized by means of X-ray tomography. This technique allowed us obtaining 3D values of cell size by using our own X-ray equipment and image analysis procedures deeply described elsewhere [11-15]. These two characteristics of the tested samples are summarized in Table 1.

On the other hand, a common practice for

solving the light scattering problem in systems containing high amount of scattering centres (like cellular polymers or colloids) is to approximate the scattering as a diffusion process. In this approximation the diffusion of light is characterized by the transport mean free path ( $l^*$ ) which corresponds to the average distance that a photon can travel before its direction is randomized. Further, light absorption is also considered in this approach by properly including the absorption length ( $l_a$ ). The solution for the diffusion equation according to these conditions is well known [16] (Eq. 1). This equation relates transmissivity ( $T$ ), defined as the ratio between transmitted and incident light intensities, transport mean free path ( $l^*$ ), sample thickness ( $L$ ) and absorption length ( $l_a$ ):

$$T \approx \frac{(5l^*/3L)\beta}{1 + (4l^*/3L)\sinh\beta}; \quad \beta = \sqrt{\frac{3L^2}{l^*l_a}} \quad (1)$$

Moreover, it is broadly known the

**Table 1.** Summary of materials included in this investigation. Both physic characteristics -relative density ( $\epsilon$ ) and microscopy cell size ( $\phi$ )- and scattering characteristic lengths - absorption length ( $l_a$ ) and transport mean free path ( $l^*$ )- are also summarized.

Matrix type	Reference	$\epsilon$	$\phi$ ( $\mu\text{m}$ )	$l_a$ (mm)	$l^*$ (mm)
Polyurethane	PU-1	0.023	530 $\pm$ 110	54	3.85 $\pm$ 0.07
	PU-2	0.042	760 $\pm$ 180	27	4.43 $\pm$ 0.11
	PU-3	0.047	490 $\pm$ 80	45	2.56 $\pm$ 0.15
	PU-4	0.089	690 $\pm$ 90	38	2.18 $\pm$ 0.37
Polystyrene	PS-1	0.034	200 $\pm$ 40	33	1.48 $\pm$ 0.18
	PS-2	0.033	210 $\pm$ 40	35	1.63 $\pm$ 0.20
Polyethylene	PE-1	0.018	310 $\pm$ 70	57	2.09 $\pm$ 0.26
	PE-2	0.022	270 $\pm$ 60	108	2.56 $\pm$ 0.26
	PE-3	0.059	720 $\pm$ 130	45	3.57 $\pm$ 0.24

relation between transport mean free path ( $l^*$ ), relative density ( $\varepsilon$ ) and mean cell size ( $\phi$ ) [17]:

$$l^* = \phi / \sqrt{\varepsilon} \quad (2)$$

Therefore, in order to characterize the mean cell size by LS measurements it is imperative to solve the Eq. 1 to obtain the transport mean free path. As this equation contains also the absorption length as independent variable, our precedent investigation was focused on solving this equation using numerical methods [18]. To this end several transmissivity measurements in the same sample (changing only its thickness) were carried out and correlated. This process allowed us determining both the absorption length and transport mean free path, summarized also in Table 1.

### 2.3 Semi-empirical modified modelling of LS

Once calculated the mean free path it was possible determine the mean cell size of samples (Eq. 2). However, the multiple

measurements required for obtaining these results should be reduced to only one to broadly expand the range of application of the developed technique. To this purpose, relationships between the calculated parameters should be determined to eliminate at least one independent variable. Moreover, as multiple measurements of optical transmissivity were carried out varying sample thickness, we could calculate the extinction coefficient ( $k$ ), as expressed by Lambert-Beer law [19] (Eq. 3).

$$T = e^{-kL} \quad (3)$$

Our objective was thus finding a relationship between the extinction coefficient and the scattering characteristic lengths (transport mean free path and absorption length). Since the extinction coefficient has units of  $\text{length}^{-1}$ , our first attempt was to correlate both this parameter and its reciprocal with an adequate combination of transport mean free path and absorption length ( $(l_a \cdot l^*)^{1/2}$ ). We called this new parameter the condensed light scattering

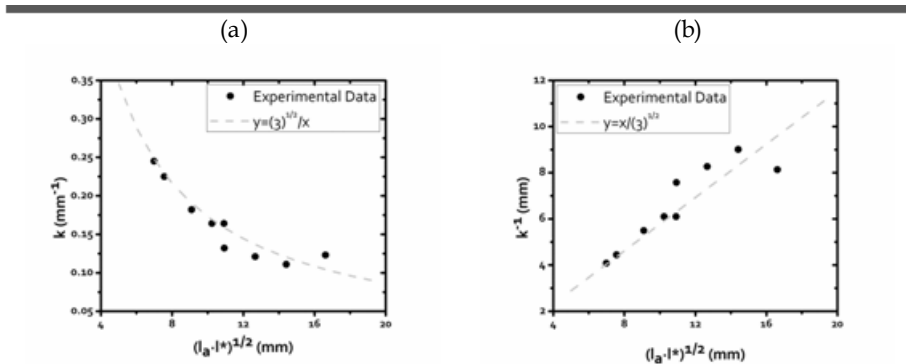


**Fig. 1.** Relationships of the calculated extinction coefficient (a) and its reciprocal (b) with the condensed light scattering length. In addition, the same theoretical trend is plotted in both graphs showing the good agreement of the experimental data to that equation.

length. The explained correlations are shown in Fig. 1.

Therefore, it is clear that the extinction coefficient may be related with the condensed light scattering according to the next expression (Eq. 4):

$$k = \sqrt{\frac{3}{l_a l^*}} \quad (4)$$

In fact, taking into account the definition of  $\beta$  in Eq. 1 and the Beer-Lambert law (Eq. 3) it is possible to simplify the Eq. 1 and extract the novel modified modelling of LS (Eq. 5).

$$\begin{aligned} \beta &= \sqrt{\frac{3L^2}{l_a l^*}} = kL \rightarrow T = e^{-\beta} \rightarrow \\ &\rightarrow \beta = -\ln T \rightarrow \\ &\rightarrow T = \frac{(5l^*/3L)\ln T}{[1+(4l^*/3L)]\sinh(\ln T)} \quad (5) \end{aligned}$$

Converting properly the precedent equation it is possible to determine transport mean free path knowing only sample thickness and transmissivity (Eq. 6). Furthermore, using (Eq. 2), the final expression for the mean cell size could be addressed, depending only on sample thickness, relative density and optical transmissivity (Eq. 7).

$$l^* = \frac{3LT\sinh(\ln T)}{5\ln T - 4T\sinh(\ln T)} \quad (6)$$

$$\phi = \frac{3LT\sinh(\ln T)\sqrt{\varepsilon}}{5\ln T - 4T\sinh(\ln T)} \quad (7)$$

These two equations are quite complicated in comparison with the classical solution of LS. In this approach the light absorption is considered

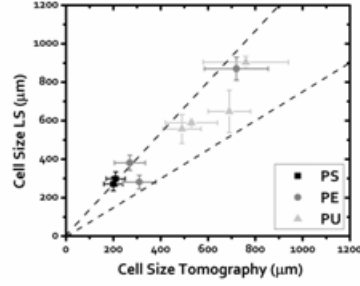


Fig. 2. Representation of average cell size calculation by means of the modified modelling of LS developed during this investigation in comparison to X-ray tomography cell size values.

negligible [16], i.e.,  $l_a \gg L \gg l^*$  and  $\beta \ll 1$ . Under this consideration, Eq. 1 is automatically simplified, obtaining thus the values of both transport mean free path (Eq. 8) and mean cell size (Eq. 9) for the non-absorption (N-A) modelling of light scattering. However, this modelling is not applicable in case of solid cellular polymers, as shown in Results and Discussion section (section 3.2).

$$l^* = \frac{3}{5}LT \quad (8)$$

$$\phi = \frac{3}{5}LT\sqrt{\varepsilon} \quad (9)$$

### 3. Results and discussion

#### 3.1 LS cell size vs. tomography cell size

Once the novel LS model has been obtained, it was possible to calculate the cell size for all the tested materials. Figure 2 shows the relationship between the cell size calculated by using the novel LS equation (Eq. 7) and the cell size characterized by X-ray tomography (summarized in Table 1). As several

thicknesses have been tested in all the materials, we were able also to determine the uncertainty of the LS cell size results. The dashed lines in Figure 2 corresponds to a variation on the cell size from the average value of 25%, which is typical in cell size distributions for this type of microcellular polymers [20]. As a result, the cell size outputs from the model developed during this investigation suitably correlate with cell size values characterized by X-ray tomography.

### 3.2 Developed model vs. non-absorption model

The next step in this investigation consisted on compare the results of the novel modelling (Eq. 6) with the results of the well established model for non-absorbing materials (Eq. 8). To eliminate the effect of sample thickness, firstly we evaluated the evolution of the  $(l^*/L)$  with transmissivity as described by Eqs. 10 and 11 for the new and classical modelling respectively.

$$l^*/L = \frac{3T \sinh(\ln T)}{5 \ln T - 4T \sinh(\ln T)} \quad (10)$$

$$l^*/L = \frac{3}{5}T \quad (11)$$

The comparison is shown in Fig. 3. A first appreciation on the two plotted graphs is that the difference between the two outputs is higher while the transmissivity increases. Therefore, it is clear that the  $(l^*/L)$  behaves quite differently depending on the modelling. In addition, one of the basic aspects of the diffusion approach of light scattering is the existence of enough scattering events

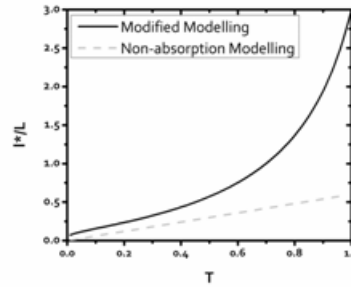


Fig. 3. Evolution of the transport mean free path independent of sample thickness with transmissivity for the developed model and the non-absorption classical modelling of LS.

within the material, i.e., transport mean free path must be sufficiently lower than sample thickness. Consequently, regarding the  $(l^*/L)$  values for the new modelling, we can conclude that this modelling is not suitable if the transmissivity on the sample is higher than around 0.3-0.4. In the case of classical modelling, this constraint is not applicable until transmissivity values around 0.6-0.7.

Moreover, due to the simplicity of the classical non-absorption approach, it could be interesting to extract direct relationships between the two modelling options.

In fact, it is possible to compare both outputs for the same value of transmissivity (Fig. 4). It is clear that the relationship between them is not lineal, due mainly to the presence of hyperbolic sinus in the developed modelling. However, we could discern a little range in which the response of the two models is linearly correlated. This zone is highlighted by a dashed square in Fig. 4a.



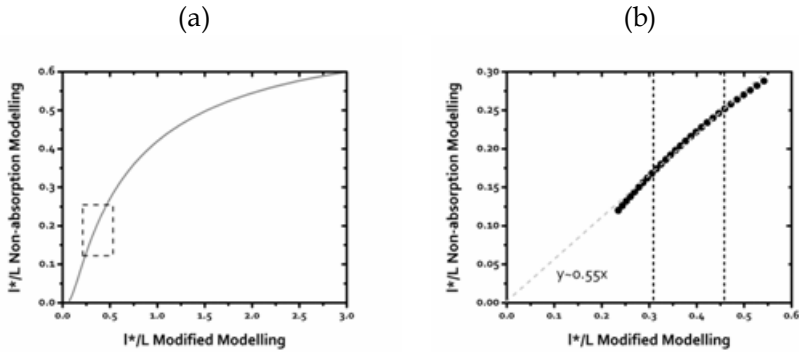


**Fig. 4.** Relationship of the mean free path independent of sample thickness between the developed modelling in this investigation and the classical non-absorption modelling of LS. (a) Complete range and (b) reduced range in which the outputs of two models are almost proportional.

As shown in Fig. 4b, the two models allowed obtaining proportional outputs if the calculated ( $l^*/L$ ) in the new modelling is between 0.31 and 0.46. These two limits correspond roughly to transmissivity values of 0.29 and 0.42 respectively. Therefore, a direct relationship could be established between the two different outputs by using the proportionality constant displayed in Fig. 4b. Nevertheless this is possible only if the optical transmissivity measured in the sample ranges 0.29-0.42.

Finally, as we had to measure the optical transmission for different sample thicknesses to determine the transmissivity (as explained in the experimental section) we were able to calculate the cell size of samples for different sample thickness. Thus we could discern the effect of sample thickness in the output of the two involved modelling equations of LS (Eqs. 7 and 9 for developed and classical modelling respectively).

The calculated results for all the tested samples are included in Fig. 5. On one hand, the results concerning the novel modified modelling of LS are reasonably acceptable (only little variations inside the range of the width of a typical cell size distribution) for sample thickness between around 10 and 30 mm. Below 10 mm the transmissivity was in general higher than 0.4 and above 30 mm the amount of light reaching the camera was almost negligible. Even with these two situations, there is no evidence that these two facts affect largely the cell size outputs.

On the other hand, the cell size results for the classical non-absorption modelling of LS (with N-A in the legends of Fig. 5) clearly show that this one is not an accurate option to explain the LS behaviour in solid matrix cellular polymers. The increase of sample thickness provokes an exponential decrease in transmissivity that could not be explained by using this modelling. As

a consequence, the resulting cell size is more inaccurate as the tested samples become thicker. Further, the numerical value of cell size is not accurate in almost any case regardless the analysed sample thickness. In addition, it is always lower in comparison to the developed model in this investigation (as an indirect consequence of the result shown in Fig. 3).

#### 4. Conclusions

In conclusion, this paper shows a novel equation that permits determine directly the cell size of solid cellular polymers by measuring the sample thickness and density and also the optical transmission thought the materials. It has been tested in a broad collection of cellular polymers based on different polymers (PE, PS and PU), with different densities and cell sizes obtaining good results for sample thickness between 10 and 30 mm.

Further work is required in order to refine the modelling to include both the influence of other physical characteristics of the samples (corrugation of the solid structure, anisotropy of the pores, repartition of solid material between the different parts of the structure...) and the effect of the inclusion of particles of different types in the solid matrix of the materials.

With the results presented in this paper it could be possible to develop a fast and non-destructive technique to measure the average cell size of cellular plastics applicable also for the *in-situ* characterisation of the evolution of cell size during the production process.

#### Acknowledgements

Financial assistance from MINECO and FEDER program (MAT2012-34901) MINECO, FEDER, UE (MAT2015-69234-R) and the Junta de Castile and Leon (VA011U16) are gratefully acknowledged. Predoctoral contract of S.

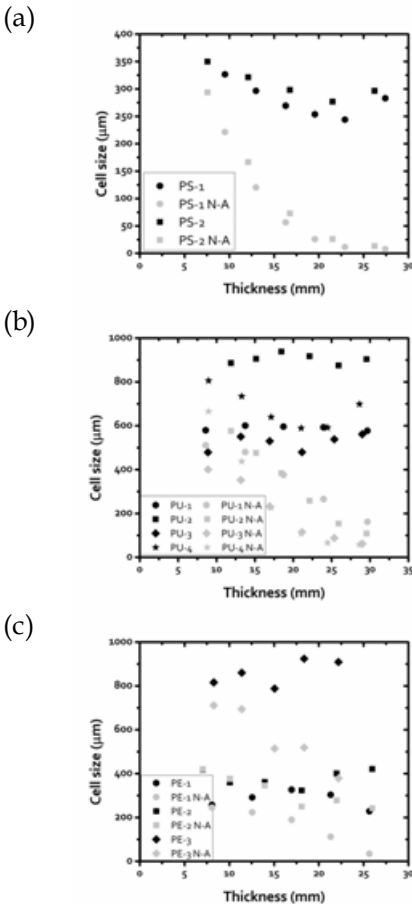


Fig. 5. Cell size for several thicknesses of all the analysed samples calculated using both the new modelling and classical non-absorbing modelling of LS. (a) PS samples (b) PU samples and (c) PE samples.

Perez-Tamarit by University of Valladolid and Banco Santander (E-47-2015-0094701) is acknowledged.

### References

- [1] L.J. Gibson, M.F. Ahsby, *Cellular Solids: Structure and Properties*, Pergamon Press, Oxford, England, 1988.
- [2] J.A. Reglero Ruiz, C. Saiz-Arroyo, M. Dumon, M.A. Rodriguez-Perez, L. Gonzalez, Production, cellular structure and thermal conductivity of microcellular (methyl methacrylate)-(butyl acrylate)-(methyl methacrylate) triblock copolymers, *Polymer International*, 60 (2011) 146-152.
- [3] M.A. Rodriguez-Perez, The effect of Chemical composition, density and cellular structure on the dynamic mechanical response of polyolefin foams, *Cellular Polymers*, 21 (2002) 117-136.
- [4] J.C. Russ, R.T. Dehoff, *Practical Stereology*, 2nd Edition ed., Plenum Press, New York, 1999.
- [5] D.L. Sahagian, A.A. Proussevitch, 3D particle size distributions from 2D observations: stereology for natural applications, *Journal of Volcanology and Geothermal Research*, 84 (1998) 173-196.
- [6] J. Lambert, I. Cantat, R. Delannay, A. Renault, F. Graner, J.A. Glazier, I. Veretennikov, P. Cloetens, Extraction of relevant physical parameters from 3D images of foams obtained by X-ray tomography, *Colloids and Surfaces A: Physicochemical and Engineering Aspects*, 263 (2005) 295-302.
- [7] M.D. Montminy, A.R. Tannenbaum, C.W. Macosko, The 3D structure of real polymer foams, *Journal of colloid and interface science*, 280 (2004) 202-211.
- [8] E. Sadek, N. Fouad, Finite element modeling of compression behavior of extruded polystyrene foam using X-ray tomography, *Journal of Cellular Plastics*, 49 (2013) 161-191.
- [9] A.P. Nefedov, O.F. Petrov, O.S. Vaulina, Analysis of particle sizes, concentration, and refractive index in measurement of light transmittance in the forward-scattering-angle range, *Applied optics*, 36 (1997) 1357-1366.
- [10] D. Weaire, S. Hutzler, *The physics of foams*, First Edition ed. 2001.
- [11] E. Solórzano, J. Pinto, S. Pardo, F. Garcia-Moreno, M.A. Rodriguez-Perez, Application of a microfocus X-ray imaging apparatus to the study of cellular polymers, *Polymer Testing*, 32 (2013) 321-329.
- [12] S. Pardo-Alonso, E. Solórzano, L. Brabant, P. Vanderniepen, M. Dierick, L. Van Hoorebeke, M.A. Rodriguez-Perez, 3D Analysis of the progressive modification of the cellular architecture in polyurethane nanocomposite foams via X-ray microtomography, *European Polymer Journal*, 49 (2013) 999-1006.
- [13] K. Mader, R. Mokso, C. Raufaste, B. Dollet, S. Santucci, J. Lambert, M. Stampanoni, Quantitative 3D characterization of cellular materials: Segmentation and morphology of foam, *Colloids and Surfaces A: Physicochemical and Engineering Aspects*, 415 (2012) 230-238.
- [14] A. Elmoutaouakkil, L. Salvo, E. Maire, G. Peix, 2D and 3D characterization of metal foams using x-ray tomography, *Advanced Engineering Materials*, 4 (2002) 803-807.
- [15] K.S. Lim, M. Barigou, X-ray micro-computed tomography of cellular food products, *Food Research International*, 37 (2004) 1001-1012.
- [16] D.J. Durian, D.A. Weitz, D.J. Pine, Multiple Light-Scattering Probes of Foam Structure Dynamics, *Science*, 252 (1991) 686-688.
- [17] M.U. Vera, A. Saint-Jalmes, D.J. Durian, Scattering optics of foam, *Applied optics*, 40 (2001) 4210-4214.
- [18] S. Pérez-Tamarit, E. Solórzano, M.A. Rodriguez-Perez, Efficient prediction of cell size in solid polymeric foams by numerically solving the diffusion approximation of light scattering equation, *Colloids and Surfaces A: Physicochemical and Engineering Aspects*, 534 (2017) 130-137.
- [19] R.A. Campo-Arnáiz, M.A. Rodríguez-Pérez, B. Calvo, J.A. de Saja, Extinction coefficient of polyolefin foams, *Journal of Polymer Science Part B: Polymer Physics*, 43 (2005) 1608-1617.
- [20] S. Estravís, J. Tirado-Mediavilla, M. Santiago-Calvo, J.L. Ruiz-Herrero, F. Villafañe, M.Á. Rodríguez-Pérez, Rigid polyurethane foams with infused nanoclays: Relationship between cellular structure and thermal conductivity, *European Polymer Journal*, 80 (2016) 1-15.



### 6.3 Characterization of the cellular anisotropy

The use of light detectors with spatial resolution (digital cameras) instead of photon counters opens the possibility of investigating the geometry and distribution of the transmitted light on the outgoing surface of the sample. In this respect, we have realized that the size of the transmitted beam increases with sample thickness due to diffusive behaviour of the transmission process (Figure 6-1).

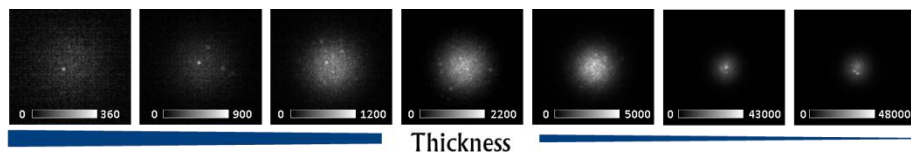


**Figure 6-1.** Variation of transmitted beam size with sample thickness (in addition to intensity exponential decrease).

Furthermore, we have observed that the shape of the transmitted beam, the so-called “halo”, is not perfectly circular. For this reason we have decided to study the anisotropy of these halos finding at the end a clear trend between the observed anisotropy in the transmitted beam and the anisotropy of the cellular structure in the perpendicular plane to the light propagation direction.

The next work, entitled “**Light transmission as a novel tool for the characterization of cell anisotropy in cellular polymers**”, summarizes all the details about the experimentation that allowed us establishing this procedure as a valid tool for the characterization of cellular anisotropy, at least until values of anisotropy similar to 1.2-1.3. Three samples (PU, PE and PS) with similar density but different cellular elongations were tested finding good results in comparison to X-ray Tomography characterizations.



Materials Letters (submitted)

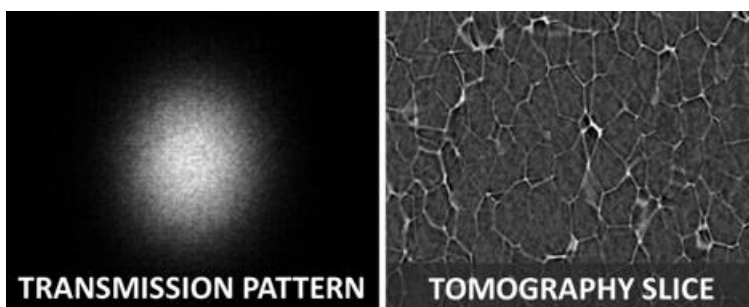
### Light transmission as a novel tool for the characterization of cell anisotropy in cellular polymers

S. Pérez-Tamarit\*, E. Solórzano, M.A. Rodriguez-Perez

*CellMat Laboratory, University of Valladolid, Paseo de Belén 7 47011, Spain*

\* Corresponding author: [saúl.perez@fmc.uva.es](mailto:saúl.perez@fmc.uva.es)

Tel.: +34 983 423572; fax: +34 983 433192



#### Abstract

This paper presents how the relative dimensions of the transmitted light pattern through a slab of microcellular polymers is related with the geometry of the pores inside the material. To this end three samples with different characteristics (raw polymer and cellular architecture) have been selected obtaining the transmission pattern corresponding to the three Cartesian planes. Further, the pore anisotropy in all cases has been characterized by classical methods (microscopy visualization) obtaining good agreements in the outputs of both procedures. Consequently, the method developed during this investigation could become a good characterization technique in order to obtain a simple, fast and reliable value of pore anisotropy of solid microcellular polymers.

**Keywords:** porous materials; polymers; light transmission; cell anisotropy.

## **1. Introduction**

Microcellular polymers are used nowadays in a wide collection of applications due to their extensive and tunable range of properties. It is well known that physical properties of cellular materials depend mainly on both the particular characteristics of the matrix and the cellular architecture of the material [1, 2]. Focusing on the latter aspect, the two key factors are relative density and average cell size. However, cellular anisotropy (elongation of the cells in the space) is another architectural feature that plays an important role in physical properties of cellular materials such as mechanical [3] or thermal properties [4]. For this reason, in recent years the characterization of this parameter has gained importance to elucidate the structure-properties relationship in cellular materials. The determination of this feature is mainly accomplished using microscopy procedures [5, 6]. These techniques are broadly used for the characterization of materials, but the sample preparation could be absolutely tedious. Another possibility for this characterization is using X-ray tomography [7, 8]. However, this technique requires sophisticated experimental devices and subsequent heavy image analysis treatments in order to obtain quantifiable information. Consequently, develop new techniques permitting a fast and accurate characterization of cellular anisotropy could be of great interest for the cellular materials science community.

The main objective of this investigation was thus developing a new experimental route to determine cellular anisotropy in solid cellular polymers. To this end, the relative dimensions of the transmitted pattern through slab geometry samples were analysed. In addition, X-ray tomography values of cellular anisotropy of tested materials were considered in order to verify the novel results obtaining good agreements between both characterization methods.

## **2. Experimental part**

### *2.1 Materials*

Three cellular polymers based on polyurethane (PU), polystyrene (PS) and polyethylene (PE) were selected to carry out this investigation. The particularities of the specific foaming processes, reactive foaming (PU), extrusion foaming (PS) and gas dissolution foaming in autoclave (PE) confer to selected cellular polymers different cellular architecture and therefore different pore geometry and elongations [9]. This fact allowed us evaluating the reliability of the novel anisotropy characterization methodology in a broad range of situations. The density of the three materials was around  $30 \text{ kg/m}^3$ .

### *2.2. Cell anisotropy characterization*

In order to verify the accuracy of the anisotropy results obtained by analysing the transmission patterns, we have characterized the cell anisotropy by means of X-ray tomography. The samples



were scanned in our X-ray tomography system which is optimized for the characterization of low absorbing materials such as polymers [10]. Once the tomographies were reconstructed, a typical image analysis protocol (filter application, binarization, watershed based separation, border objects removal) was applied in order to separate all the cells within the considered volume [7, 11]. After that, the so-called *bounding box* (Fig. 1) -minimum prism that encloses every object- was computed in order to obtain the dimensions in three perpendicular directions (identified as Cartesian coordinates -X, Y, Z-) of every cell. As a result, the cellular anisotropy ( $A$ ) in the three planes (XY, XZ, YZ) was determined dividing the height ( $H$ ) by the width ( $W$ ) of the cells in the

corresponding plane (Eq. 1).

$$A = H/W \quad (1)$$

### 2.3. Light transmission: set-up and anisotropy determination procedure

The experimental set-up used to collect the transmission patterns is presented in Fig. 2a. The main elements were a green laser (wavelength of 532 nm) of 10 mW of nominal power (tunable via TTL port) used as light source and a digital camera used as light detector. The distance between the light source and the camera lens was 150 mm. The detection lens-camera system consisted of an IDS-Ueye 12 bit monochrome CMOS camera mod. UI-5480CP-M-GL and an infinite focus lens. The samples used had slab geometry (dimensions of 30x30x5mm<sup>3</sup>) to

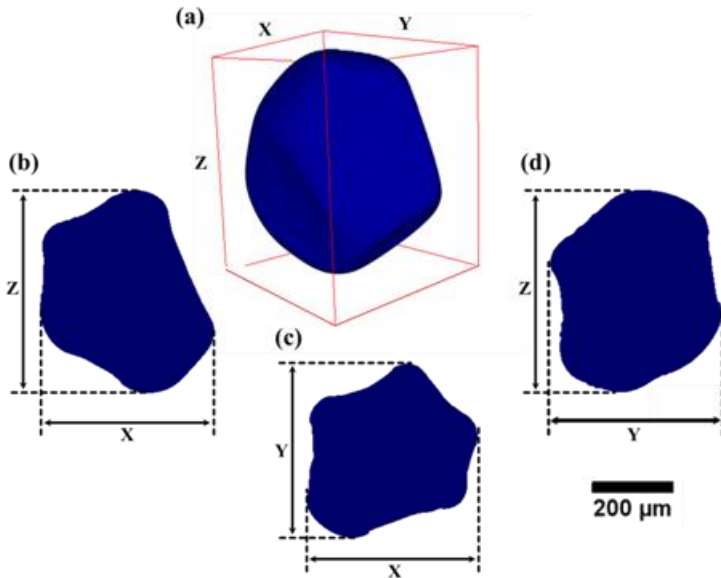


**Fig. 1.** Schematic views of the anisotropy of a PU pore in the different Cartesian planes. (a) 3D rendering of the pore with the corresponding bounding box -in red-. (b) Projection in the XZ plane. (c) Projection in the XY plane. (d) Projection in the YZ plane.

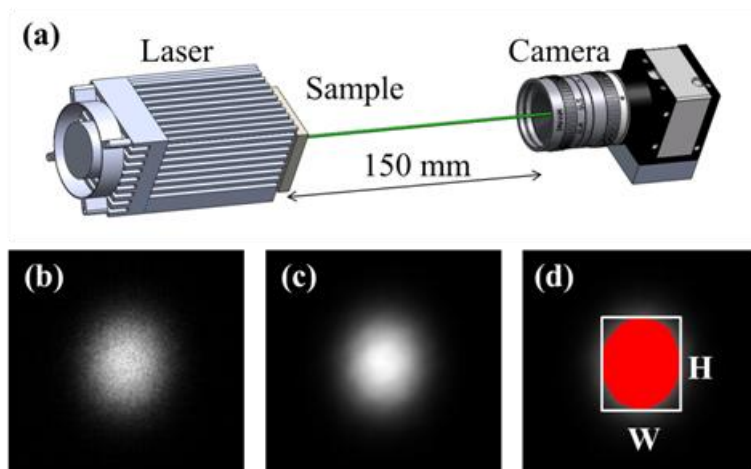


**Fig. 2.** (a) 3D sketch of the experimental set up to record 2D transmission patterns –up-. Main steps of the transmission anisotropy determination –down-. (b) Transmission pattern. (c) Filtered pattern. (d) Binarized pattern and corresponding bounding box.

avoid light losses through the lateral surfaces.

The power of laser beam was tuned at 2 mW and the images were acquired with an exposure time of 500 ms (Fig 2b). After that, an edge preserving filter of 15 pixels of neighbourhood was applied in order to homogenize the grey level on the transmission patterns (Fig. 2c). Finally the filtered patterns were binarized and computing the *bounding boxes* of the resulting masks (in this case in 2D, consequently rectangles instead of prisms) the anisotropy was calculated (Fig. 2d). For the binarization, 7% of grey level histograms were selected as threshold limit in all cases.

### 3. Results and Discussion

First of all, an overview of all the tested samples and planes is shown in Fig. 3. On one hand the tomography slices (Fig. 3a) and on the other hand the corresponding

transmission patterns (Fig. 3b). In addition, the contours of the analysed binarized patterns are highlighted in red in the displayed transmission patterns. Analysing qualitatively the tomography slices (Fig. 3a) we could extract several preliminary results about the measured anisotropy. In the XY plane, both PE and PU cells are almost isotropic whereas for PS the cells are slightly oriented in the Y direction. Moreover, investigating the XZ plane, PE cells are isotropic in opposition to PS and PU cells that are slightly elongated in the Z direction. Finally, in the case of YZ plane the conclusions are complementary. PE cells are also isotropic; PS cells are oriented in the Y direction whereas PU cells are slightly elongated in the Z direction. On the other hand, focusing on the transmission patterns (Fig. 3b) the affirmations are equivalent.

The quantitative comparison of anisotropy determination between both methods is displayed in Fig. 4. The concordance of the results obtained by using both methods is good but not perfect (the black dashed line in the figure 4 indicates equality line –slope 1). However, we have to consider two

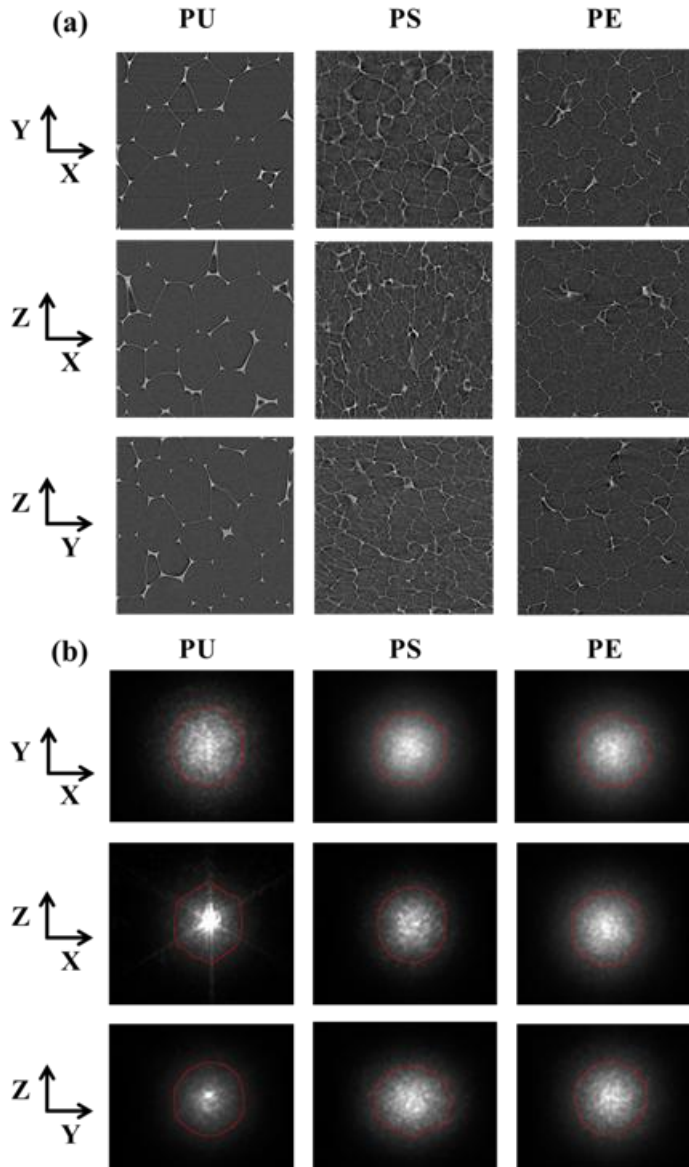


**Fig. 3.** (a) Example tomography slices for the tested samples in the three Cartesian planes. (b) Transmission pattern for all the samples in the corresponding space planes.

separate factors. On one hand, the anisotropy characterized by tomography varies around 10-16% for the samples themselves. On the other hand, the thickness of the tested samples (5 mm) involves the interaction of light with roughly around 13 cells (considering cell sizes of 400  $\mu\text{m}$ , the average value for the selected samples). In this travel through the material, light could encounter cells with different anisotropy values and finally resulting in not perfectly output. In fact, considering these two obstacles the obtained results are so accurate to consider these measurements as a confident methodology to calculate pore anisotropy.

#### 4. Conclusions

In summary, this paper presents the results of characterizing the cell anisotropy by analysing the dimensions of the transmission pattern through cellular polymer slabs. In addition, the cell anisotropy was also determined by means of X-ray tomography in order to evaluate the accuracy of the obtained results. Three different cellular polymers have been tested in the three space planes obtaining reliable relationships between the two characterization methods. Consequently, the methodology presented within this manuscript is valid for a fast, easy and straightforward characterization of cell anisotropy of cellular polymers, even for *in-situ* experiments.

Materials with different densities, thickness and cellular architectures (cell

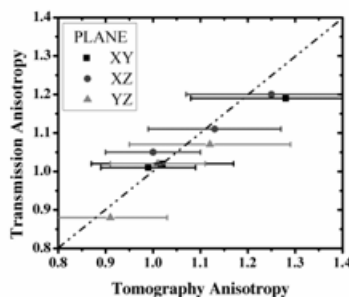


Fig. 4. Relationship for the cell anisotropy using both tomography slices and transmission patterns showing the good agreements of the light transmission anisotropy characterization.

sizes and anisotropies) will be studied in further investigations in order to verify the global applicability of the developed methodology.

#### Acknowledgements

Financial assistance from MINECO and FEDER program (MAT2012-34901) MINECO, FEDER, UE (MAT2015-69234-R) and the Junta de Castile and Leon (VA011U16) are gratefully acknowledged. Predoctoral contract of S. Perez-Tamarit by University of Valladolid and Banco Santander (E-47-2015-0094701) is acknowledged.

#### References

- [1] L.J. Gibson, M.F. Ahsby, Cellular Solids: Structure and Properties, Pergamon Press, Oxford, England, 1988.
- [2] A. Cunningham, N.C. Hilyard, Low Density Cellular Plastics: Physical Basis of Behaviour, Ed. Chapman and Hall, London, 1994.
- [3] L. Oliveira-Salmazo, A. Lopez-Gil, F. Silva-Bellucci, A.E. Job, M.A. Rodriguez-Perez, Natural rubber foams with anisotropic cellular structures: Mechanical properties and modeling, Industrial Crops and Products, 80 (2016) 26-35.
- [4] S. Estravís, J. Tirado-Mediavilla, M. Santiago-Calvo, J.L. Ruiz-Herrero, F. Villafañe, M.Á. Rodríguez-Pérez, Rigid polyurethane foams with

infused nanoclays: Relationship between cellular structure and thermal conductivity, *European Polymer Journal*, 80 (2016) 1-15.

[5] J. Pinto, E. Solorzano, M.A. Rodriguez-Perez, J.A. de Saja, Characterization of the cellular structure based on user-interactive image analysis procedures, *Journal of Cellular Plastics*, 49 (2013) 555-575.

[6] Y. Mu, G. Yao, H. Luo, Effect of cell shape anisotropy on the compressive behavior of closed-cell aluminum foams, *Materials & Design*, 31 (2010) 1567-1569.

[7] S. Pardo-Alonso, E. Solórzano, S. Estravís, M.A. Rodriguez-Perez, J.A. de Saja, In situ evidence of the nanoparticle nucleating effect in polyurethane-nanoclay foamed systems, *Soft Matter*, 8 (2012) 11262.

[8] K.S. Lim, M. Barigou, X-ray micro-computed tomography of cellular food products, *Food Research International*, 37 (2004) 1001-1012.

[9] D. Klemperer, K.C. Frisch, *Handbook of polymeric foams and foam technology*, Passavia Druckerei GmbH Passau 1991.

[10] E. Solórzano, J. Pinto, S. Pardo, F. Garcia-Moreno, M.A. Rodriguez-Perez, Application of a microfocus X-ray imaging apparatus to the study of cellular polymers, *Polymer Testing*, 32 (2013) 321-329.

[11] K. Mader, R. Mokso, C. Raufaste, B. Dollet, S. Santucci, J. Lambert, M. Stamparoni, Quantitative 3D characterization of cellular materials: Segmentation and morphology of foam, *Colloids and Surfaces A: Physicochemical and Engineering Aspects*, 415 (2012) 230-238.



### References

---

- [1] D.J. Durian, D.A. Weitz, D.J. Pine, Multiple Light-Scattering Probes of Foam Structure Dynamics, *Science*, 252 (1991) 686-688.
- [2] M.U. Vera, A. Saint-Jalmes, D.J. Durian, Scattering optics of foam, *Applied optics*, 40 (2001) 4210-4214.
- [3] A. Cunningham, N.C. Hilyard, Low Density Cellular Plastics: Physical Basis of Behaviour, Ed. Chapman and Hall, London, 1994.
- [4] L.J. Gibson, M.F. Ahsby, Cellular Solids: Structure and Properties, Pergamon Press, Oxford, England, 1988.
- [5] D.F. Swinehart, The Beer-Lambert law, *Journal of Chemical Education*, 39 (1962) 333-335.
- [6] C.F. Bohren, D.R. Huffman, Absorption and Scattering of Light by Small Particles, WILEY-VCH Verlag GmbH & Co. KGaA1983.





## Chapter 7

# **X-ray Tomography and Light Scattering in Non-Conventional/ Nanocellular Polymers**



As commented in previous chapters, nanocellular polymers are a novel class of cellular materials with impressive enhanced physical properties [1-4]. These materials have been developed in the recent decades by mainly gas dissolution foaming. As a consequence, the development of novel or modified characterization techniques is required for the accurate study of these materials. In this respect, the two involved techniques during this investigation have been applied for the study of nanocellular polymers. This Chapter deals with the main experimental results of these characterizations. On one hand, two of the main nano-imaging techniques were selected to perform nano computed Tomography (n-CT) [5, 6]. On the other hand, the samples were tested in our equipment to measure optical transmissivity finding the first evidences of the possibility of manufacturing transparent nanocellular polymers.

### 7.1 Nano-tomography applied to nanocellular polymers

As well as in the micrometre range, X-ray Tomography is a powerful technique that allows the structural inspection in 3D. However, the experimental set-up and the involved interaction mechanisms for n-CT are much more complicated than in the case of  $\mu$ -CT. In this respect, two different kinds of techniques dominate in the case of imaging with nanometre spatial resolution: X-ray transmission microscopy (TXM) and coherent diffraction imaging (CDI) depending if the imaging is accomplished in the real or reciprocal space respectively. The main principles of both techniques and the obtained results are addressed in the following paragraphs. These experiments were carried out in I13 beamline at Diamond Light Source synchrotron (Oxford, UK).

#### 7.1.1. *Zernike phase contrast X-ray transmission microscopy (TXM)*

In transmission X-ray microscopy (TXM) Fresnel zone plates (FZP) are employed as high resolution X-ray optics. These are circular diffraction gratings with radially decreasing line spacing. The X-ray beam is condensed onto the object in a region of approx. 50  $\mu\text{m}$  thus increasing the photon density several orders of magnitude. The numerical aperture of the illumination is well matched with the aperture of the objective FZP by means of an order sorting aperture (OSA). The objective FZP guides

the transmitted beam to an image plane in which the detector is located. In order to avoid radiation damage in the high sensitivity detector by the direct undiffracted beam a central stop (CS) manufactured of a high absorption material (of typically 500  $\mu\text{m}$  of diameter) is located before the condenser (Figure 7-1).

The interaction of X-rays with structures in a sample leads to the generation of diffracted light in addition to the direct beam passing through the sample. According to Abbe theory, diffracted light from an object is required for image formation in a microscope. However, the reduced phase shift in typical phase contrast imaging results in a very weak contrast for the sample structure in TXM. For this reason, to obtain valuable contrast it is required according to Zernike to phase shift the undiffracted light [7-9]. This is accomplished with a phase shifting optical element located in the back focal plane of the objective. By these means, the direct beam can be phase shifted either  $90^\circ$  (positive phase shift) or  $270^\circ$  (negative phase shift). This kind of X-ray optical configuration permits reaching effective pixel sizes up to 50 nm.

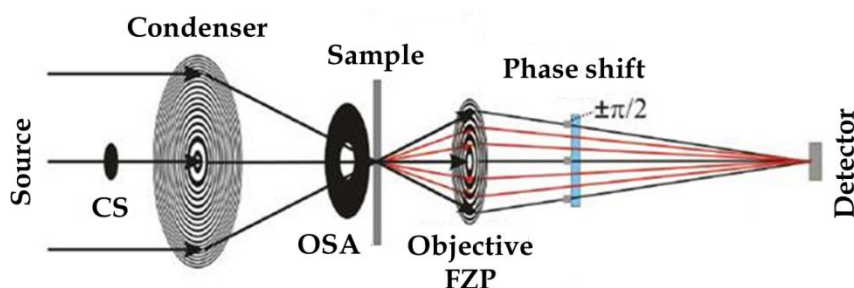


**Figure 7-1.** Basic scheme of a TXM optical equipment.

This configuration, joined to a high precision rotation stage, permits reaching n-CT with effective pixel sizes up to 50 nm.

During the research stay carried out at Diamond synchrotron a collection of TXM tomographies were performed at 100 nm effective pixel size. In those experiments 3 reference images (at  $0^\circ$ ,  $90^\circ$  and  $180^\circ$  of rotation) were acquired before and after the tomography in order to evaluate the stability of the sample during the process. In our case, the high X-ray flux concentrated onto the sample provokes a temperature

increase that provokes the sample expansion and thus drifts in the projections that hindered the correct reconstruction of the tomographies (Figure 7-2).

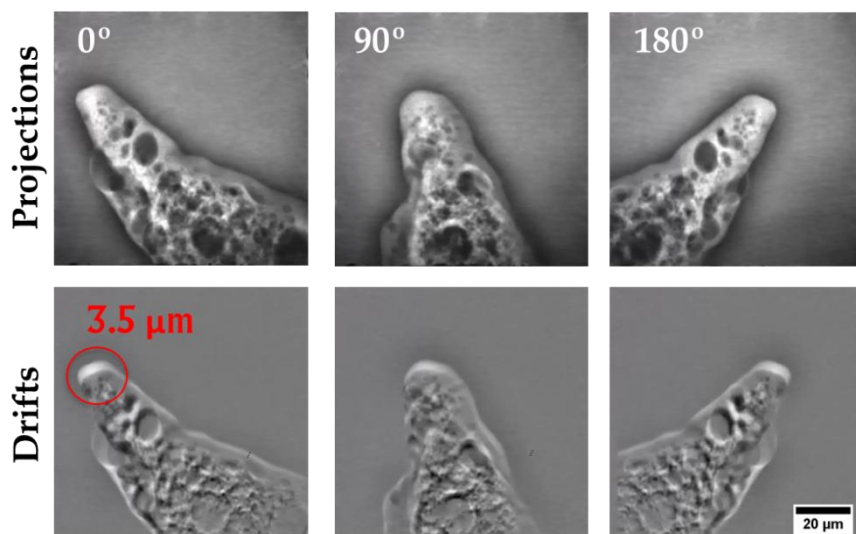


**Figure 7-2.** TXM projections and drift in a nanocellular polymer with 780 nm cell size and 0.5 of relative density.

Only in two samples the induced expansion was as small as required to obtain an acceptable reconstruction. However, in both cases the mean cell size of the samples was 225 nm therefore hindering the correct observation of the cells using 100 nm of effective pixel size (Figure 7-3). For this reason, it is required another technique that does not require the focus of the beam onto the sample, the scanning coherent diffraction microscopy, also called *ptychography*.

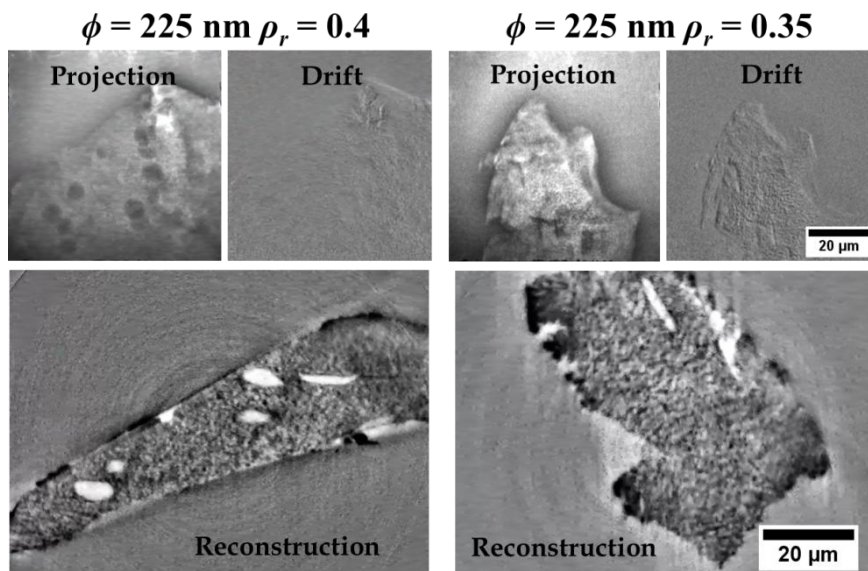


**Figure 7-3.** Projections, drifts and consequent reconstruction of two samples scanned using TXM tomography.

#### 7.1.2 Scanning coherent diffraction imaging (ptychography)

Coherent Diffractive Imaging (CDI) uses a coherent X-ray beam to illuminate a sample and retrieve the phase information on the sample from phase-retrieval analysis of the far-field diffraction pattern. Of the many CDI variants developed ptychography has been shown to be the most robust and is a scanning technique where diffraction information is collected from overlapping regions and used to reconstruct the sample phase properties [10-12]. The advantage of ptychography is that the spatial resolution achieved can be higher than that achieved with conventional optics.

Ptychography does not require sample isolation, and so represents an advance in CDI methods. In a ptychography experiment, the X-ray beam is focused onto a sample so that a small area is illuminated. The sample is then moved with respect to the beam to create a sequential array of overlapping illuminated areas (Figure 7-4). For each area, the light scattered by the sample is recorded as a diffraction pattern. The diffraction patterns are then processed with an iterative algorithm which retrieves the phase information. The output is a pair of images. One is a measure of the extent to which

light has been absorbed by the sample. The other is a measure of the phase delay introduced to the beam as it passed through the sample.

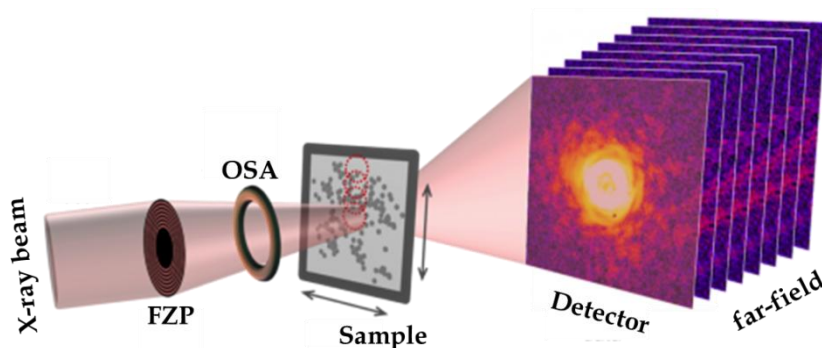


**Figure 7-4.** Basic representation of the typical ptychography experiment.

The lens-less characteristic of this technique permits in principle reach spatial resolutions only limited by the X-rays wavelength according to wavelength limit theory. Further, in combination with high precision equipment for scanning and rotating at the same time it is possible to perform X-ray Tomography using ptychography, the so-called *ptychotomography*.

In the following paragraphs the work entitled **“First 3D characterization of non-conventional cellular polymers by means of X-ray ptychotomography”** is addressed. In this work a detailed description of the characterization technique is included with the experimental particularities adopted for the performance of the experiments. Two different nanocellular polymers with different characteristics were successfully scanned with an effective pixel size of 133 nm. These are, in our knowledge, the first reported 3D characterizations of nanocellular polymers with nanometre spatial resolution.





Macromolecular Communications (submitted)

### First 3D inspection of non-conventional cellular polymers by means of X-ray ptycho-tomography

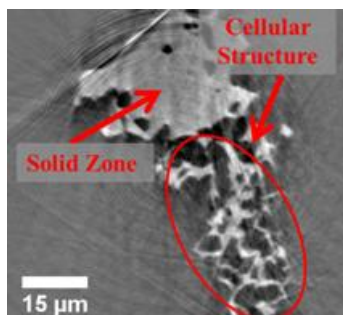
Saúl Pérez-Tamarit,<sup>1,\*</sup> Paula Cimavilla,<sup>1</sup> Judith Martín-de León,<sup>1</sup>  
Victoria Bernardo,<sup>1</sup> Eusebio Solórzano,<sup>1</sup> Darren Batey,<sup>2</sup> Christoph Rau,<sup>2</sup>  
Miguel Angel Rodriguez-Perez,<sup>1</sup>

<sup>1</sup> CellMat Laboratory, University of Valladolid, Paseo de Belén 7 47011, Spain

<sup>2</sup> Diamond Light Source, Harwell Science and Innovation Campus, Didcot OX11 0DE, United Kingdom.

\* Corresponding author: [saul.perez@fmc.uva.es](mailto:saul.perez@fmc.uva.es)

Tel.: +34 983 423572; fax: +34 983 433192



#### Abstract

This work presents the first 3D inspections on non conventional cellular polymers based on poly (methyl methacrylate) (PMMA). These materials have features on the nanometer range and are usually characterized by electron microscopy techniques. However, this kind of techniques always leads to skews due to the inherent 2D characteristics of these techniques and also because the required sample preparation that often hinders the correct visualization of the structure. To solve this X-ray Tomography is commonly used, however, due to the small features present in the samples nano-imaging techniques are required. Among all the possibilities, X-ray ptychography permits extracting phase information of materials with nanometer resolution and with reduced radiation dose to remain unaltered the tested sample. Combining then ptychography with tomography (ptycho-tomography) it is possible obtain 3D reconstructions with nanometer voxel size.

**Keywords:** synchrotron; tomography; ptychography; nanocellular polymers; polymethyl methacrylate.

## **1. Introduction**

Porous polymers, defined as two-phase systems composed of a continuous solid polymeric phase and an either continuous or discontinuous gaseous phase [1-3], are widely used and have a very promising future in important technological sectors such as the automotive and aeronautical industries, renewable energies, construction, cushioning and packaging, and biotechnology. Microporous polymers, characterized by pore sizes on the order of microns, were developed at the Massachusetts Institute of Technology (MIT) in the early 1980s [4]. The key reason that explains the interest in microcellular materials is that these materials improve the physical properties of conventional cellular polymers. This enhancement by reducing the cell size has encouraging reducing even further this characteristic to finally obtain the so-called nanocellular polymers, a novel class of cellular polymers with promising properties [5]. These materials exhibit improved mechanical properties than conventional or microcellular materials [6]. In addition, another interesting fact for these materials is that the cell size reduction allows decreasing the gas conduction contribution to the thermal conductivity due to the Knudsen effect [7]. Further, other physical properties such as dielectric [8], acoustic [9] or optical [10] properties are strongly modified reducing the cell size until the nanometer range. These improvements into the physical properties provoke the

use of these materials on novel applications related to thermal insulation [11], structural applications that require good mechanical properties [12], or to better performances in traditional applications such as impact resistance, dielectric behavior, catalysis, sensing, etc. Due to the novelty of these materials the scientific literature is scarce and mainly connected with methods to produce them [13-15]. Up to now, the characterization of them is performed using 2D SEM images. However, this task can be challenging and tedious. Electron microscopy provides high-resolution 2D-images but it can only be achieved by sectioning. This is very time consuming and it is not always certain whether the initial structure is modified by the sample preparation. In contrast, X-ray tomography provides volume information with easy sample preparation. Laboratory based sources provides micrometer resolution with low intensity X-rays that require specific elements to obtain optimum contrast in low absorbing materials such as polymers [16]. Nevertheless, the nanometer size features present in the novel non conventional cellular polymers preclude the correct characterization of these materials using such kind of system.

In last decades, the development of great third-generation X-ray synchrotron facilities has facilitated the implementation of novel characterization techniques. In particular, regarding X-ray imaging techniques both image quality and spatial resolution have been enhanced by using highly coherent X-

rays. Among all the possibilities we can cite two main techniques in order to finally obtain X-ray imaging with tens of nanometers of resolution: X-ray Transmission Microscopy (TXM) and the so-called Ptychography. Similar to a visible light microscope the main components of an X-ray microscope are the condenser optic and the objective lens. As a result, improved spatial resolution up to 50 nm could be achieved [17, 18]. The condenser optic is matched to the aperture of the objective lens (Fresnel-zone plate) thus providing high spatial resolution. Furthermore, other elements such as phase rings are usually located into the beam to improve the image contrast using Zernike phase contrast imaging [19]. However, under this configuration the beam is concentrated into a reduced zone of the sample (typically of 50-100 microns of diameter) thus increasing the photon density probably inducing radiation damage on the sample or even provoking a temperature increase and thus sample expansion. Consequently, the use of this technique for long experiments in which the sample stability is crucial, such as tomography, becomes totally dependent of the scanned sample. On the other hand, Ptychography (or scanning coherent diffraction imaging) is nowadays one of the most developed synchrotron-based techniques due to its applicability and possible spatial resolution up to 10 nm [20, 21]. The basis of this technique is the acquisition of several diffraction patterns at large distance from the sample produced

under coherent illumination. Original structure of scanned sample and acquired diffraction patterns are related then by Fourier transform and therefore the projection is obtained by iterative reconstruction methods. As the beam is moving along the sample while acquiring diffraction patterns the impact of radiation damage in the sample is, at least locally, lower. However, being a scanning technique, ptychography involves several seconds per projection that results in long experimentation times when tomography is carried out.

The aim of this work is to perform, as a first time, experiments using 3D X-ray ptychography (ptycho-tomography) on non conventional cellular polymers to visualize the structure of these materials in three dimensions with sufficient spatial resolution.

## 2. Experimental section

### 2.1 Materials

The PMMA was kindly provided by Altuglas International (France) in the form of pellets. The material used presents a glass transition temperature ( $T_g$ ) of 114.5 °C measured by DSC, density ( $\rho_s$ ) of 1180 kg/m<sup>3</sup> measured at 23 °C and 50% HR. Medical grade CO<sub>2</sub> (99.9 % purity) was used as blowing agent.

### 2.2 Samples production

The PMMA was processed by extrusion using a twin-screw extruder model COLLIN TEACH-LINE ZK 25T, with L/D of 24 and screw diameter of 25 mm,

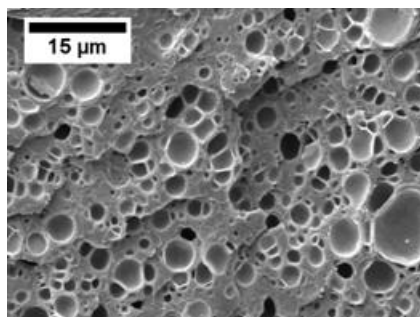


**Fig 1.** SEM micrograph of the sample under study.

with a temperature profile set from 160 °C to 200 °C, and the screw speed equal to 40 rpm. Solid sheets (4 mm thick) from the extruded material were produced by compression molding using a hot plate press provided by Remtex (Spain). The temperature set on the press was 250 °C and processing time was 9.5 minutes, 8.5 for melting the polymer and 1 minute more for compression under pressure (1.7 MPa). From these sheets, squares of 25x25 mm<sup>2</sup> were cut for the foaming experiments.

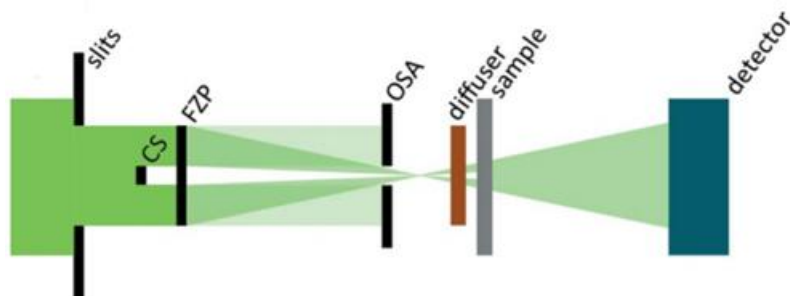
Cellular material was produced using a two-step foaming process in a high-pressure vessel (model PARR 4681) provided by Parr Instrument Company. The pressure was set to 6 MPa and it is controlled via a pressure pump controller (model SFT-10) provided by Supercritical Fluid Technologies Inc. The temperature was fixed at 25 °C, and it was kept constant with a clamp heater controlled with a CAL 3300 temperature controller. The foaming step was carried out in a thermal bath with water. The foaming temperature used to was 40 °C. The foaming time was 1.5 minutes. A SEM

image of foamed specimen is shown in Figure 1.

### 2.3. X-ray ptychography at I13-1 (Diamond Light Source)

Ptychography is a scanning coherent diffraction imaging (CDI) technique in which the sample is scanned perpendicular to the path of X-ray beam, collecting diffraction patterns at each point. As a mandatory condition, there is always enough overlap of probe between adjacent points. The resulting far-field diffraction patterns are then processed through iterative phase retrieval algorithms to obtain high resolution, phase contrast projections [22]. A natural extension of two dimensional ptychographic imaging is the so-called ptycho-tomography, a combination of ptychography with tomography. We exploit the high resolution 2D ptychographic projections obtained at various angles as a starting point which are then taken through the conventional tomographic process of alignment and 3D reconstruction thus obtaining a three-dimensional reconstruction of the sample under study.

Ptychographic imaging was carried out at the I13-1, the coherence branchline of the I13 beamline at Diamond light source, UK [18]. The samples were imaged with X-rays at a photon energy 9 keV and 0.05s exposure time per diffraction pattern. The detector to sample distance was ~7 m. The photon counting Excalibur detector with a pixel size of 55μm and ~2000x1800 pixels<sup>2</sup> was used [23]. Other elements



**Fig. 2.** Schematic of the ptychography elements and geometry present at I13-1 beamline of Diamond Light Source (from [21]).

such as a zone plate (FZP), beam-stop (CS), and order sorting aperture (OSA) were employed to obtain a X-ray probe in order to illuminate the sample (as schematically shown in Figure 2). The effective reconstruction pixel size in this geometry was 133nm. 600 projections were collected to finally reconstruct the 3D volume.

### 3. Results and Discussion

The main characteristics (density and cell size) of scanned sample have been determined by classical procedures and are summarized in Table 1. The bulk density has calculated using the Arquimedes' water-displacement method. Further, the cell size has been obtained analyzing SEM images (Figure 1) by a self developed tool [24] in imageJ/Fiji image analysis environment [25, 26].

Focusing on the ptychography scan, observing the shown projection (Figure 3 left) it is possible to observe several parts on the sample that are totally visible observing the ptycho-tomography reconstruction (Figure 3 right). Due to the high relative density of the sample (0.65)

and the particularities of the gas dissolution foaming, the sample owns both solid and foamed parts, not a continuous foamed specimen with high density. In the case of the cellular part of the sample, we can conclude that even the thinnest parts of the structure are well reconstructed with the selected effective pixel size of 133 nm. In addition, a qualitative inspection of the tomography volume outputs a relative density of 0.7 and a mean cell size of  $(3.1 \pm 1.5) \mu\text{m}$ , which are in concordance with measurements of bulk density and analysis of the cell size by means of SEM images (in 2D).

### 4. Conclusions

A combination of X-ray ptychography and tomography (ptycho-tomography) has been used to visualize the structure of

**Table 1.** Sample included in this study

Density [kg/m <sup>3</sup> ]	Mean cell size [μm]
760	2.3±1.2

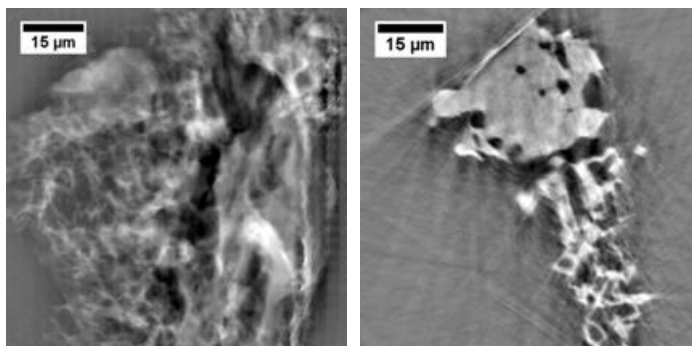


**Fig. 3.** Ptychographic projection -left- and reconstructed slice from ptychotomo experiments of tested sample -right-.

non conventional cellular polymers for the first time. Due to the unique characteristics of the used technique tomography experiments with 133 nm of effective pixel size have been performed. As a result, even the thinnest parts of the solid structure of the scanned samples. In addition, thanks to phase information obtained in ptychographic projections the final reconstructions owned also suitable contrast even for low absorbing and diffracting materials such as amorphous PMMA, used as raw material for the selected cellular materials. With the results of this manuscript in mind and knowing the potential of ptychography to reach spatial resolutions of 10 nm, the inspection presented here will be applicable for scanning more challenging samples with reduced cell size.

### Acknowledgments

Financial assistance from MINECO and FEDER program (MAT2012-34901) MINECO, FEDER, UE (MAT2015-69234-R) and the Junta de Castile and Leon (VA035U13) are gratefully acknowledged. Predoctoral contract of S.

Perez-Tamarit by University of Valladolid and Banco Santander (E-47-2015-0094701) is also acknowledged. Financial support from Junta de Castile and Leon (Grant Paula Cimavilla) (Grant Judith Martín-de León) and from Spanish Ministry of Education (FPU grant FPU14/02050, Victoria Bernardo) is gratefully acknowledged. We thank Diamond Light Source for access to beamline I13 (proposal MT17625-1) that contributed to the results presented here.

### References

- [1] L.J. Gibson, M.F. Ahsby, Cellular Solids: Structure and Properties, Pergamon Press, Oxford, England, 1988.
- [2] D. Klemptner, K.C. Frisch, Handbook of polymeric foams and foam technology, Passavia Druckerei GmbH Passau 1991.
- [3] D. Weaire, S. Hutzler, The physics of foams, First Edition ed. 2001.
- [4] V. Kumar, N.P. Suh, A process for making microcellular thermoplastic parts, Polymer Engineering & Science, 30 (1990) 1323-1329.
- [5] B. Notario, J. Pinto, M.A. Rodríguez-Pérez, Nanoporous polymeric materials: A new class of materials with enhanced properties, Progress in Materials Science, 78-79 (2016) 93-139.
- [6] B. Notario, J. Pinto, M.A. Rodríguez-Pérez, Towards a new generation of polymeric foams: PMMA nanocellular foams with enhanced physical properties, Polymer, 63 (2015) 116-126.



- [7] B. Notario, J. Pinto, E. Solorzano, J.A. de Saja, M. Dumon, M.A. Rodríguez-Pérez, Experimental validation of the Knudsen effect in nanocellular polymeric foams, *Polymer*, 56 (2015) 57-67.
- [8] B. Notario, J. Pinto, R. Verdejo, M.A. Rodríguez-Pérez, Dielectric behavior of porous PMMA: From the micrometer to the nanometer scale, *Polymer*, 107 (2016) 302-305.
- [9] B. Notario, A. Ballesteros, J. Pinto, M.A. Rodríguez-Pérez, Nanoporous PMMA: A novel system with different acoustic properties, *Materials Letters*, 168 (2016) 76-79.
- [10] S. Pérez-Tamarit, B. Notario, E. Solórzano, M.A. Rodríguez-Pérez, Light transmission in nanocellular polymers: Are semi-transparent cellular polymers possible?, *Materials Letters*, 210 (2018) 39-41.
- [11] C. Forest, P. Chaumont, P. Cassagnau, B. Swoboda, P. Sonntag, Polymer nano-foams for insulating applications prepared from CO<sub>2</sub> foaming, *Progress in Polymer Science*, 41 (2015) 122-145.
- [12] D. Miller, V. Kumar, Microcellular and nanocellular solid-state polyetherimide (PEI) foams using sub-critical carbon dioxide II. Tensile and impact properties, *Polymer*, 52 (2011) 2910-2919.
- [13] J. Martín-de León, V. Bernardo, M. Rodríguez-Pérez, Low Density Nanocellular Polymers Based on PMMA Produced by Gas Dissolution Foaming: Fabrication and Cellular Structure Characterization, *Polymers*, 8 (2016) 265.
- [14] V. Bernardo, J. Martín-de León, E. Laguna-Gutiérrez, M.Á. Rodríguez-Pérez, PMMA-sepiolite nanocomposites as new promising materials for the production of nanocellular polymers, *European Polymer Journal*, 96 (2017) 10-26.
- [15] V. Bernardo, J. Martín-de León, M.A. Rodríguez-Pérez, Production and characterization of nanocellular polyphenylsulfone foams, *Materials Letters*, 178 (2016) 155-158.
- [16] E. Solórzano, J. Pinto, S. Pardo, F. García-Moreno, M.A. Rodríguez-Pérez, Application of a microfocus X-ray imaging apparatus to the study of cellular polymers, *Polymer Testing*, 32 (2013) 321-329.
- [17] M. Stampanoni, R. Mokso, F. Marone, J. Vila-Comamala, S. Gorelick, P. Trtik, K. Jefimovs, C. David, Phase-contrast tomography at the nanoscale using hard x rays, *Physical Review B*, 81 (2010).
- [18] C. Rau, U. Wagner, Z. Pešić, A. De Fanis, Coherent imaging at the Diamond beamline I13, *physica status solidi (a)*, 208 (2011) 2522-2525.
- [19] C. Holzner, M. Feser, S. Vogt, B. Hornberger, S.B. Baines, C. Jacobsen, Zernike phase contrast in scanning microscopy with X-rays, *Nature Physics*, 6 (2010) 883-887.
- [20] M. Holler, A. Diaz, M. Guizar-Sicairos, P. Karvinen, E. Farm, E. Harkonen, M. Ritala, A. Menzel, J. Raabe, O. Bunk, X-ray ptychographic computed tomography at 16 nm isotropic 3D resolution, *Scientific reports*, 4 (2014) 3857.
- [21] S. Sala, V.S.C. Kuppili, S. Chalkidis, D.J. Batey, X. Shi, C. Rau, P. Thibault, Multiscale X-ray imaging using ptychography, *Journal of Synchrotron Radiation*, 25 (2018) 1214-1221.
- [22] H.M. Faulkner, J.M. Rodenburg, Movable aperture lensless transmission microscopy: a novel phase retrieval algorithm, *Phys Rev Lett*, 93 (2004) 023903.
- [23] J. Marchal, I. Horswell, B. Willis, R. Plackett, E.N. Gimenez, J. Spiers, D. Ballard, P. Booker, J.A. Thompson, P. Gibbons, S.R. Burge, T. Nicholls, J. Lipp, N. Tartoni, EXCALIBUR: a small-pixel photon counting area detector for coherent X-ray diffraction - Front-end design, fabrication and characterisation, *Journal of Physics: Conference Series*, 425 (2013) 062003.
- [24] J. Pinto, E. Solorzano, M.A. Rodríguez-Pérez, J.A. de Saja, Characterization of the cellular structure based on user-interactive image analysis procedures, *Journal of Cellular Plastics*, 49 (2013) 555-575.
- [25] M.D. Abramoff, P.J. Magalhaes, J. Sunanda, Image Processing with ImageJ, *Biophotonics International*, 11 (2004) 36-42.
- [26] C.A. Schneider, W.S. Rasband, K.W. Eliceiri, NIH Image to ImageJ: 25 years of image analysis, *Nature Methods*, 9 (2012) 671-675.





Several physical properties have been already studied on nanocellular polymers such as mechanical [2], thermal [3], dielectric [4], or even acoustic properties [13]. These novel materials have shown enhanced properties in comparison with similar materials but with cells sized in the micrometre range.

Nevertheless, the optical properties of such kind of materials have been scarcely considered. For this reason, one part of this Thesis has been focused in the study of optical behaviour of nanocellular polymers.

### 7.2 Light Scattering in nanocellular polymers. Transparency

Among all the possible existing parameters in order to characterize the optical properties we have selected the optical transmissivity ( $T$ ). The simplicity for measuring this parameter permitted us evaluating the effect of changing the scale of the cell size in cellular polymers. To this end, a collection of cellular polymers based on PMMA was selected for this work with similar relative density ( $\sim 0.5$ ) and cell sizes from 11  $\mu\text{m}$  to 30 nm.

The experimental details and the obtained results about this investigation are detailed in the following paragraphs. The work entitled “**Light transmission in nanocellular polymers: are semi-transparent cellular polymers possible?**” shows how decreasing the cell size of cellular polymers up to nanometre range it will be possible to manufacture cellular polymers with valuable transparency.



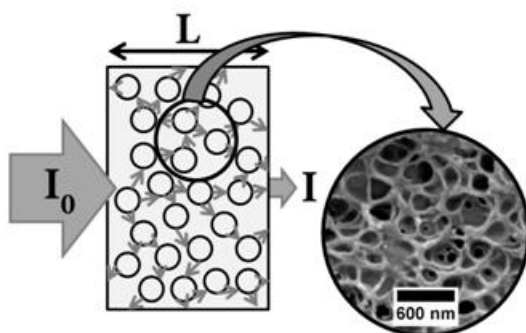
Materials Letters 210 (2018) 39-41  
<http://dx.doi.org/10.1016/j.matlet.2017.08.109>

## Light transmission in nanocellular polymers: are semi-transparent cellular polymers possible?

S. Pérez-Tamarit\*, B. Notario, E. Solórzano, M.A. Rodriguez-Perez

*CellMat Laboratory, University of Valladolid, Paseo de Belén 7 47011, Spain*

\* Corresponding author: [saul.perez@fmc.uva.es](mailto:saul.perez@fmc.uva.es)  
Tel.: +34 983 423572; fax: +34 983 433192



### Abstract

This work presents the light transmission through a collection of solid cellular polymers based on poly (methyl methacrylate) (PMMA) with cells sizes covering the micro and nano-scale. The obtained results showed that the behavior of light transmission when cell size is in the nano-scale is opposite to the one shown by microcellular foams or the one predicted by theoretical models of light scattering (LS). In fact, the expected trend is that a reduction of cell size increases the opacity of the samples. However, for nanocellular polymers based on amorphous polymers reducing the cell size increases the light transmission. Therefore, this result indicates that a further reduction of the cell size could result in cellular polymers optically semi-transparent.

**Keywords:** polymers; poly (methyl methacrylate); light transmission; nanocellular foams; porous materials.

## 1. Introduction

Nano-cellular polymers represent a new kind of materials which have attracted the attention of the scientific community in the last years due to their surprising properties [1, 2]. Nowadays, some papers have been published on the thermal [3], acoustical [4], mechanical [5] or dielectric [6] properties of these materials showing promising results. However, the optical properties of these materials have been less considered [7].

Moreover, similar materials as those studied in this work are silica aerogels [8]. An aerogel is an open-celled, mesoporous, solid cellular material that is composed of a network of interconnected nanostructures. It exhibits a porosity (non-solid volume) greater than 50% and cells with sizes in the nano-scale (*ca.* 50nm) [9]. These materials have a combination of properties that no other cellular material possesses simultaneously [10]. For instance, silica aerogels have very low densities and thermal conductivities (Knudsen effect), among other extraordinary properties [11, 12]. In addition, these materials, produced from transparent solid matrix (silica) and with pores in the nano-scale, are almost transparent to light in the optical wavelength range (400-750nm) [9].

Therefore the aim of this paper is to study the optical properties of nanocellular polymers produced from an amorphous polymer (PMMA) trying to elucidate if reducing the cell size to the nanoscale could induce some transparency in the

materials. To this end light transmission ( $T$ ) through samples has been measured. This property characterizes the transparency of the materials. Transmissivity ( $T$ ) is defined as the ratio between transmitted ( $I$ ) and incident ( $I_0$ ) intensity reaching the light detector (Eq. 1).

$$T = I/I_0 \quad (1)$$

## 2. Experimental

### 2.1 Materials

The PMMA was kindly provided by Altuglas-Arkema Company (France) in the form of pellets. The material used presents a glass transition temperature ( $T_g$ ) of 115°C, density ( $\rho_s$ ) of 1180kg/m<sup>3</sup> and due to its amorphous structure a high transparency.

### 2.2 Samples production

PMMA pellets were first dried in a vacuum furnace (680 mm Hg) at 80°C during 4h. Then, the pellets were molded into precursors of 155x75x4mm<sup>3</sup> by using a two-hot plate press. The temperature of the press was fixed at 250°C. The material was molten without pressure for 9 minutes, then it was compacted under a constant pressure of 21.8bar for another minute and finally it was cooled under the same pressure.

Foaming experiments were performed in a pressure vessel (PARR4681, Parr Instrument Co.). The pressure system comprises an accurate pressure pump controller (SFT-10, Supercritical Fluid Technologies Inc.). The vessel is equipped

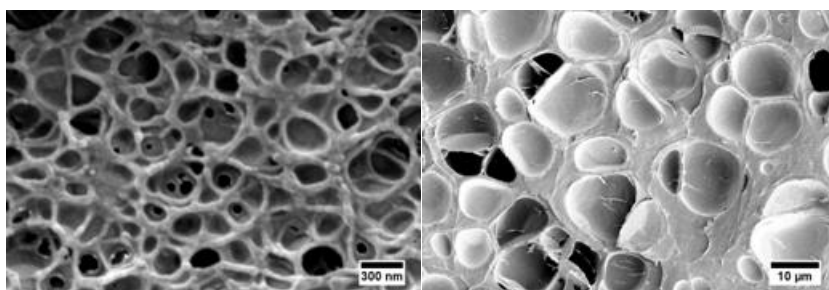


**Fig. 1.** Micrographs of the two kinds of samples. Nanocellular (25-400nm) –left- and microcellular (0.8-11μm) –right-. Samples are Nano-3 and Micro-4.

with a clamp heater (1200W) controlled via a CAL3300 temperature controller. Therefore, a collection of experiments were implemented following the solid state foaming process [3, 13]. The pressure and temperature were selected in order to produce four samples with cells in the micrometer range ( $\phi > 500\text{nm}$ ) and five materials with cells in the nano-scale ( $\phi < 500\text{nm}$ ). The analyzed foamed specimens ( $12 \times 12 \times 1\text{mm}^3$ ) were prepared by using a precision buzz saw.

### 2.3 Characterization techniques

Density of the samples was measured by the water-displacement method using the density determination kit for an AT261 Mettler-Toledo balance. Relative density ( $\rho_r$ ) is calculated as the ratio between cellular material density ( $\rho_f$ ) and solid polymer density ( $\rho_s$ ) resulting for all analyzed samples values close to 0.5 (Table 1). Although the effect of sample density is corrected in transmissivity theoretical models, comparing samples with similar densities is crucial to obtain accurate conclusions.

Cellular structure was determined using a scanning electron microscope (JSM820, Jeol and Quanta 200FEG). Samples were cooled in liquid nitrogen, fractured and finally coated with gold using a sputter coater (SCD005, Blazers Union) for the microscopic visualization. Microscopy images were analyzed using a self-developed application [14] based on ImageJ/Fiji image analysis software [15]. Microcellular materials with cell sizes between 1-11μm have been selected (Fig. 1 right). The nanocellular samples have cell sizes ranging 25-400nm (Fig. 1 left).

**Table 1.** Labels, cell size ( $\phi$ ), density ( $\rho_r$ ) and relative density of samples under study.

Sample	$\phi$ (nm)	$\rho$ (kg/m <sup>3</sup> )	$\rho_r$
Nano-1	25	625.4	0.53
Nano-2	90	568.9	0.48
Nano-3	200	531.5	0.45
Nano-4	350	508.1	0.43
Nano-5	400	519.2	0.44
Micro-1	820	623.3	0.53
Micro-2	1080	638.6	0.54
Micro-3	7000	592.8	0.50
Micro-4	11000	649.0	0.55

Therefore, three orders of magnitude of difference between the materials with the largest and the smallest cell sizes.

#### 2.4 Experimental set-up for transmissivity measurements

The experimental set-up to measure the light transmission by using Eq. 1 is shown in Fig. 2. The device consist of a photodiode joined to an integrating sphere with 12.5mm window (PRW0505, Gigahertz-Optik) connected to a photometer (X94, Gigahertz-Optik) as light detector and three different lasers as light source. The lasers (blue -450nm-, green -532nm- and red -650nm-, 10mW) were selected in order to investigate the influence of light wavelength in transmission. The samples were placed at a distance less than 1mm of the detector window and due to their surface ( $\sim 12 \times 12 \text{ mm}^2$ ) and their thickness ( $\sim 1 \text{ mm}$ ) the totality of light crossing the sample reaches the detector. The laser-detector distance was 30mm fixing the size of the laser beam at the samples surface (2mm).

### 3. Theory

Light scattering models concerning

transmission in porous media with a non-absorbing liquid matrix establish that transmissivity is related with sample thickness ( $L$ ) and transport mean free path of light in the medium ( $l^*$ ) as long as the mean cell size is much larger than light wavelength (Eq. 2) [16]. This condition is accomplished by the analyzed microcellular materials but not in the case of nanocellular materials.

$$T \propto l^*/L \quad (2)$$

Mean free path is the average distance a photon travels before its direction is randomized and is related with mean cell size and relative density (Eq. 3) [17].

$$l^* = \phi / \sqrt{\rho_r} \quad (3)$$

Combining the previous expressions it is possible to define a normalized transmissivity ( $T_N$ ) that includes the influence of sample thickness and density (Eq. 4).

$$T_N = LT\sqrt{\rho_r} \quad (4)$$

### 4. Results

The transmissivity values for the solid

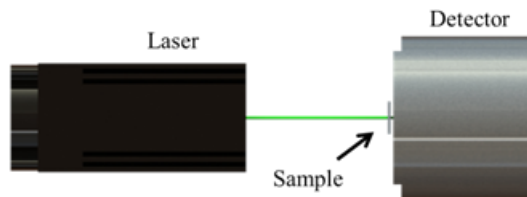


Fig. 2. Sketch of the experimental set-up for transmissivity measurements.

material ( $\rho_r=1$ ) were around 0.85 for the three selected lasers. Consequently, PMMA polymer is a good candidate in order to manufacture semi-transparent nanofoams.

The normalized transmissivity obtained using different laser beams is represented as a function of mean cell size of the samples (Fig. 3). Two opposite trends are visible. On the one hand, for microcellular foams as the mean pore is reduced the normalized transmissivity decreases. This is the expected behavior for a microcellular material (Eq. 3). Under these conditions, considering a one-dimensional cellular material, the lower is the cell size; the higher is the solid barriers (cell walls or edges) inside the material. Consequently, the number of light interactions with solid-gas interfaces of the material increases and the amount of light crossing the sample is smaller.

On the other hand, the results show an opposite trend for nanocellular polymers. In this case, a reduction of the cell size causes a significant increment of the transmissivity. In this range of cell sizes, still considering one-dimensional cellular materials, the frequency of solid barriers is higher than the frequency of oscillation of light. This is a possible explanation of the phenomena observed in the figure. As the mean cell size of the cellular material decreases, the interaction of light with the solid-gas interfaces of the foamed samples also decreases resulting in a higher transmissivity. Moreover, in this range of cell sizes the light wavelength influences the transmissivity response,

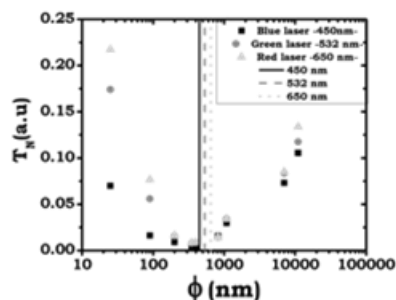


Fig 3. Normalized transmissivity versus the cell size of the tested samples. Vertical lines correspond to the wavelength of lasers -450, 532 and 650nm-

reinforcing the possible explanation presented above that assumes the dependence of transmissivity on the relationship between the cell size and the spatial frequency of light.

Finally, the minimum of the curves (Fig. 3) appears for mean pore sizes close to the light wavelength. However, the lack of samples with cell size in this range prevents knowing the exact minimum of the curves.

## 5. Conclusions

In summary, the paper presents the first experimental data on the light transmission of nanocellular polymers produced from an amorphous polymer. The results showed that reducing the cells below the wavelength of the light used in the experiments modifies the trend in the transmissivity versus cell size curve. The tendency is opposite to that observed for materials with cells in the micro-scale or to that predicted by LS models. The results obtained seem to indicate that by further reducing the size of the cells cellular polymers with a

significant transparency could be produced.

Further work is required to evaluate this effect for the infrared wavelength range due to its influence on the thermal conductivity of these materials.

## Acknowledgments

Financial assistance from MINECO and FEDER program (MAT2012-34901) MINECO, FEDER, UE (MAT2015-69234-R) and the Junta de Castile and Leon (VA011U16) are gratefully acknowledged. Predoctoral contract of S. Perez-Tamarit by University of Valladolid and Banco Santander (E-47-2015-0094701) is acknowledged.

## References

- [1] S. Costeux, CO<sub>2</sub>-Blown Nanocellular Foams, *J. Appl. Polym. Sci.* 131 (2014) 41293.
- [2] B. Notario, J. Pinto, M.A. Rodríguez-Pérez, Nanoporous polymeric materials: A new class of materials with enhanced properties, *Prog. Mater. Sci.* 78-79 (2016) 93-139.
- [3] B. Notario, J. Pinto, E. Solorzano, J.A. de Saja, M. Dumon, M.A. Rodríguez-Pérez, Experimental validation of the Knudsen effect in nanocellular polymeric foams, *Polymer* 56 (2015) 57-67.
- [4] B. Notario, A. Ballesteros, J. Pinto, M.A. Rodríguez-Pérez, Nanoporous PMMA: A novel system with different acoustic properties, *Mater. Lett.* 168 (2016) 76-79.
- [5] B. Notario, J. Pinto, M.A. Rodríguez-Pérez, Towards a new generation of polymeric foams: PMMA nanocellular foams with enhanced physical properties, *Polymer* 63 (2015) 116-126.
- [6] B. Notario, J. Pinto, R. Verdejo, M.A. Rodríguez-Pérez, Dielectric behavior of porous PMMA: From the micrometer to the nanometer scale, *Polymer* 107 (2016) 302-305.
- [7] H. Yokoyama, L. Li, T. Nemoto, K. Sugiyama, Tunable Nanocellular Polymeric Monoliths Using Fluorinated Block Copolymer Templates and Supercritical Carbon Dioxide, *Adv. Mater.* 16 (2004) 1542-1546.
- [8] R. Vacher, T. Woignier, J. Pelous, E. Courtens, Structure and self-similarity of silica aerogels, *Phys. Rev. B* 37 (1988) 6500-6503.
- [9] G.M. Pajonk, Transparent silica aerogels, *J. Non-Cryst. Solids* 225 (1998) 307-314.
- [10] A. Soleimani Dorcheh, M.H. Abbasi, Silica aerogel; synthesis, properties and characterization, *J. Mater. Process. Tech.* 199 (2008) 10-26.
- [11] J.E. Fesmire, Aerogel insulation systems for space launch applications, *Cryogenics* 46 (2006) 111-117.
- [12] R.W. Pekala, J.C. Farmer, C.T. Alviso, T.D. Tran, S.T. Mayer, J.M. Miller, B. Dunn, Carbon aerogels for electrochemical applications, *J. Non-Cryst. Solids* 225 (1998) 74-80.
- [13] A.V. Nawaby, Y.P. Handa, X. Liao, Y. Yoshitaka, M. Tomohiro, Polymer-CO<sub>2</sub> systems exhibiting retrograde behavior and formation of nanofoams, *Polym. Int.* 56 (2007) 67-73.
- [14] J. Pinto, E. Solorzano, M.A. Rodríguez-Pérez, J.A. de Saja, Characterization of the cellular structure based on user-interactive image analysis procedures, *J. Cell. Plast.* 49 (2013) 555-575.
- [15] M.D. Abràmoff, P.J. Magalhaes, J. Sunanda, Image Processing with ImageJ, *Biophotonics Intern.* 11 (2004) 36-42.
- [16] D.J. Durian, D.A. Weitz, D.J. Pine, Multiple Light-Scattering Probes of Foam Structure Dynamics, *Science* 252 (1991) 686-688.
- [17] M.U. Vera, A. Saint-Jalmes, D.J. Durian, Scattering optics of foam, *Appl. Opt.* 40 (2001) 4210-4214.



### References

---

- [1] B. Notario, J. Pinto, M.A. Rodríguez-Pérez, Nanoporous polymeric materials: A new class of materials with enhanced properties, *Progress in Materials Science*, 78-79 (2016) 93-139.
- [2] B. Notario, J. Pinto, M.A. Rodríguez-Pérez, Towards a new generation of polymeric foams: PMMA nanocellular foams with enhanced physical properties, *Polymer*, 63 (2015) 116-126.
- [3] B. Notario, J. Pinto, E. Solorzano, J.A. de Saja, M. Dumon, M.A. Rodríguez-Pérez, Experimental validation of the Knudsen effect in nanocellular polymeric foams, *Polymer*, 56 (2015) 57-67.
- [4] B. Notario, J. Pinto, R. Verdejo, M.A. Rodríguez-Pérez, Dielectric behavior of porous PMMA: From the micrometer to the nanometer scale, *Polymer*, 107 (2016) 302-305.
- [5] A. Diaz, P. Trtik, M. Guizar-Sicairos, A. Menzel, P. Thibault, O. Bunk, Quantitative x-ray phase nanotomography, *Physical Review B*, 85 (2012).
- [6] P.J. Withers, X-ray nanotomography, *Materials Today*, 10 (2007) 26-34.
- [7] P. Gao, B. Yao, I. Harder, N. Lindlein, F.J. Torcal-Milla, Phase shifting Zernike phase contrast microscopy for quantitative phase measurement, *Optics Letters*, 36 (2011) 4305-4307.
- [8] C. Holzner, M. Feser, S. Vogt, B. Hornberger, S.B. Baines, C. Jacobsen, Zernike phase contrast in scanning microscopy with X-rays, *Nature Physics*, 6 (2010) 883-887.
- [9] U. Neuhausler, G. Schneider, W. Ludwig, M.A. Meyer, E. Zschech, D. Hambach, X-ray microscopy in Zernike phase contrast mode at 4 keV photon energy with 60 nm resolution, *Journal of physics D: Applied physics*, 36 (2003) A79-A82.
- [10] M. Holler, A. Diaz, M. Guizar-Sicairos, P. Karvinen, E. Farm, E. Harkonen, M. Ritala, A. Menzel, J. Raabe, O. Bunk, X-ray ptychographic computed tomography at 16 nm isotropic 3D resolution, *Scientific reports*, 4 (2014) 3857.
- [11] F. Pfeiffer, X-ray ptychography, *Nature Photonics*, 12 (2017) 9-17.
- [12] V.S.C. Kuppili, S. Sala, S. Chalkidis, A.M. Wise, A.D. Parsons, I. Zanette, C. Rau, P. Thibault, Ptychotomography at DLS Coherence Beamline I13, *Journal of Physics: Conference Series*, 849 (2017) 012031.
- [13] B. Notario, A. Ballesteros, J. Pinto, M.A. Rodríguez-Pérez, Nanoporous PMMA: A novel system with different acoustic properties, *Materials Letters*, 168 (2016) 76-79.



## Chapter 8

# Conclusions and Perspectives



### 8.1 Conclusions

This final chapter presents the main conclusions that have surged from this thesis as well as the most remarkable achievements of the investigation.

This investigation was built around three main objectives:

- The application of X-ray tomography to reveal the process-structure-properties relationship on microcellular polymers.
- The development and application of a novel non destructive technique for the characterization of cellular polymers based on Light Scattering methodologies.
- The application of both techniques on nanocellular polymers for the first time.

Therefore, the main conclusions of this thesis are closely related with these objectives and separated in three great groups, X-ray Tomography, Light Scattering and Application on nanocellular polymers.

#### *1. X-ray Tomography*

We have design and upgrade the X-ray imaging system located in CellMat laboratory into a  $\mu$ -CT scanner allowing the acquisition of tomograms with up to 2.5  $\mu\text{m}/\text{pixel}$  resolution and optimum image contrast for the study of cellular polymers. In addition, this upgrade is totally compatible with the established radioscopy set-ups of the X-ray imaging system resulting in a unique and versatile characterization equipment of cellular polymers.

With this system it was possible to develop detailed structural characterizations of the cellular structure of several kinds of cellular polymers focusing on the gas phase (cell size, anisotropy, neighbourhood distribution and cell density) due to the limitations of spatial resolution. Moreover, the cell size and anisotropy tomographic values obtained in our X-ray  $\mu$ -CT scanner have been used to evaluate the reliability of the Light Scattering results.

Furthermore, the experimentation has been completed by means of synchrotron campaigns in different European facilities such as Swiss Light Source (SLS, Switzerland) and Bessy II (Germany). On one part of these experiments (Bessy II) we were able to increase the spatial resolution of the acquired tomograms (up to  $0.45\text{ }\mu\text{m}/\text{pixel}$ ), allowing the reconstruction of the thinnest parts of the cellular structure on conventional low density cellular materials. Therefore, by using specific and advanced image analysis protocols developed during this investigation based on analysing the material thickness distributions a detailed characterization of the solid phase of these materials has been carried out. The analysed parameters were the fraction of material in the struts and the thickness of different parts of the structure (walls and struts) and also the full structure average thickness. Combining these results with the in-house system results a full detailed characterization could be obtained nowadays. In addition, by using these tomographies we were able to compute the solid structure corrugation of low density flexible cellular polymers and to evaluate and model its influence on both thermal and mechanical properties of these materials (thermal expansion coefficient and collapse stress respectively). On the other hand, synchrotron experiments on SLS enabled the study of cell nucleation and growth on cellular polymers for the first time in 3D. The increased temporal resolution in this facility allows acquiring tomography sequences at 20 Hz rate. In our particular case, the used rate (6 Hz) was selected in order to follow the foaming dynamics of both nanocomposite and pure PU with suitable temporal (156 ms/tomography) and spatial resolution ( $3.2\text{ }\mu\text{m}/\text{pixel}$ ).

### *2. Light Scattering*

During this investigation it was possible to develop a novel theoretical model of Light Scattering applied to solid cellular polymers in a semi-empirical way. In that model the influence of light absorbed by the material is considered, in opposite to Light Scattering models for aqueous cellular systems in which the absorption is considered negligible. A collection of semi-transparent (non-coloured) cellular polymers based on PE, PU and PS with different cell sizes ( $200\text{--}1000\text{ }\mu\text{m}$ ) and densities ( $15\text{--}110\text{ kg/m}^3$ ) was considered. The experimental output of this model was compared with X-ray

tomography results obtaining good findings in all cases, with variations in cell size below 20%, which is the typical width of cell size distributions on such kind of cellular polymers.

The light diffusion within the material provokes the widening of the light beam forming a light halo in the output of the sample that grows with sample thickening. This fact forced us to change the light detector from a photodiode coupled to an integration sphere to a digital camera. Therefore the field of view of our system changed from 12.7 mm (window size of the photodiode) to the full surface of the sample, registering the transmitted light from all the points of the surface of the sample.

With these findings, a milestone of this investigation was the design and building of a dedicated laboratory equipment for the characterization of solid cellular polymers by means of Light Scattering.

On the other hand, using the digital camera as light detector we were able to measure the spatial dimensions of the transmitted light halo in the surface of the sample. Analysing its anisotropy and the cellular anisotropy of the material on the perpendicular plane to the light beam propagation direction we found that both anisotropy values are closely related. Therefore, cellular anisotropy is obtained also by means of Light Scattering methodologies.

The possibility of measure both cell size (linked to the transmitted light intensity) and cellular anisotropy (linked to the relative geometry of the transmitted beam) encouraged us to patent Light Scattering as a valid methodology for the structural characterization of semi-transparent solid cellular polymers, as final conclusion of this investigation regarding Light Scattering.

### *3. Application on nanocellular polymers*

Nanocellular polymers are a new class of cellular materials. In consequence, novel techniques must be developed or adapted in order to characterize them. In regard to

this fact, this investigation is completed by applying the two used techniques, suitably adapted, to this kind of materials.

On one hand, X-ray n-CT techniques (with spatial resolution around 100 nm/pixel) have been considered for the 3D structural characterization of these materials. These experiments were carried out at Diamond Light Source (United Kingdom) during both the research stay corresponding to this thesis and a synchrotron measurements campaign. The obtained results represent the first reported 3D characterization of nanocellular polymers in which the gas phase of these materials with varied characteristics is analysed in detail.

On the other hand, a collection of nanocellular polymers with constant relative density and different cell size (30-11000 nm) permitted us elucidating that in the micrometer range ( $\phi > 800$  nm), the higher is the cell size, the higher is light transmissivity whereas in the nanometer range ( $\phi < 800$  nm) the tendency is the opposite. The lower is the cell size; the higher is the light transmissivity. This result is one of the first evidences about the possibility of manufacturing transparent nanocellular polymers.



### 8.2 Perspectives

We have presented the capabilities of two different characterization techniques, X-ray and Light Scattering.

In the case of X-ray Tomography, this is a continuation and confirmation of a previous thesis about the application of this kind of technique on cellular materials research. We have demonstrated how this technique is a powerful tool to understand the mechanisms governing the process-structure-properties relationship in cellular polymers, even in novel nanocellular materials. For this reason, we think in the following topic to even extend the capabilities of this technique:

- Develop novel image analysis protocols for the detailed structural characterization of foams in an easier way. In particular, analysis routines that allow calculating parameters concerning the solid phase in conventional X-ray tomographies (subresolution).
- Continue investigating the possibilities on nanotomography for the 3D characterization of nanocellular polymers, in particular, further increasing the spatial resolution.
- Evaluate other features of the solid phase of cellular materials such as tortuosity, connections between cells etc...
- New experiments about 4D imaging could be conceived and carried out thanks to the improvements of synchrotron facilities.
- Apply the developed methodologies to materials based on other solid matrices such as glass, metals, etc...
- Push the limits of the actual X-ray  $\mu$ -CT system to increase the spatial resolution up to 1  $\mu\text{m}$ /pixel.

On the other hand, this is the first investigation in CellMat about Light Scattering applied to the structural characterization of solid cellular polymers. As this technique has been proved to be a powerful tool to extract in an easy way fundamental structure features of cellular polymers, we expect that this dissertation could be a reference

book and a starting point for new research works, focused probably in the following topics:

- Investigate factors none contemplated during this thesis such as the influence of particles (type, size and shape), colour of the samples, etc... on the Light Scattering response and model the corresponding behaviour.
- Combine X-ray radiography and Light Scattering to obtain surface distributions of density and thus cell size.
- Develop a novel theoretical model that allows determining the cell size even in the case of nanocellular polymers.

*Annex*

# **Other Applications of X-ray Imaging Techniques**



In the last Chapter of this Thesis, listed as an additional Annex to the main results of this research, other applications of X-ray imaging techniques are summarized. These two works are none directly related with the main subject of the Thesis but also intends to characterize key factors in the cellular materials scientific framework.

On one hand, as previously commented throughout this Thesis the fast, simple and accurate determination of mean cell size is crucial since most of physical properties of these materials strongly depend on this parameter. For this reason, in addition to Light Scattering, this investigation was focused on developing a novel methodology to extract quantifiable values of mean cell size of X-ray transmission images (radiographies) making use of the Fast Fourier Transform (FFT).

### **A.1 Cell size determination in X-ray transmission images**

It is well known that Fourier transform procedures are capable to determine the size, shape and number density of spherical particles distributed in a projected image in a volumetric monodisperse distribution of particles [1]. In fact, the two dimensional Fourier transform of a circularly symmetric object corresponds essentially to the Hankel transform of order zero [2]. It has been previously demonstrated that the frequency of oscillation of the Hankel transform in such cases corresponds with the size of the entities in the volume [3]. Nevertheless, the polydispersity of the size distribution of particles in the volume hinders the correct visualization of several peaks on the Hankel transform plot and only the first peak is available to extract valuable information.

Making use of the penetration power of X-rays it is simple to obtain 2D projections (radiographies) of a volumetric sample (Figure A-1). In fact, radiographies of cellular materials, adequately treated, seem a non-monodisperse distribution of quasi-circular particles.

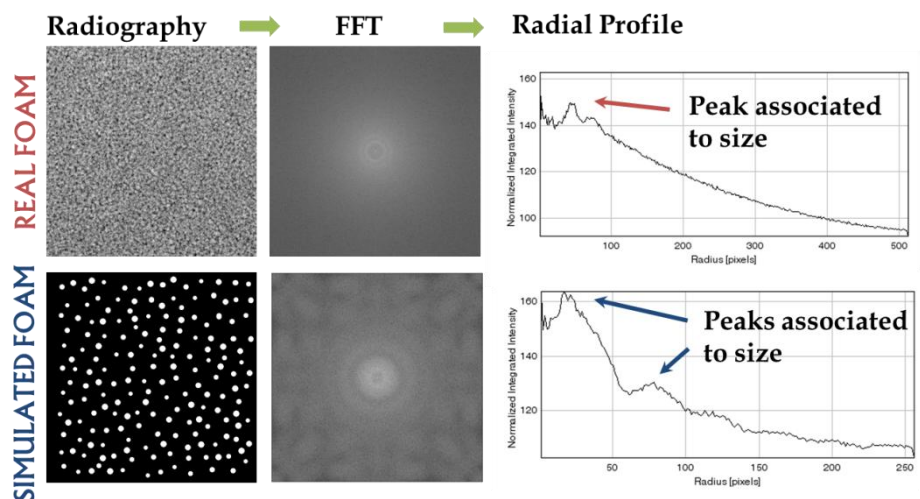


**Figure A-1.** Comparison of the methodology developed for the characterization of the mean cell size in a real foam radiography and in a simulated foam projection. The polydispersity present in the real foam provokes the disappearance of high order peaks in the radial profile of FFT image.

The following work **“Fast Fourier Transform procedures applied to X-ray transmission images”** addresses all the methodology developed and implemented in Matlab language to obtain quantifiable results of mean cell size by means of FFT on X-ray radiographies. To this purpose, a collection of PU samples with controlled characteristics was fabricated and characterized in detail in order to verify this novel approach for measuring cell size in a broad spectrum of samples.

In addition, this methodology has been successfully applied to study the stability of the cellular structure (and thus study cellular structure degeneration mechanisms) in different polypropylene (PP) blends foamed by chemical blowing agent (azodicarbonamide) and monitored by means of neutron radioscopy [4].

Microscopy and Microanalysis (submitted)

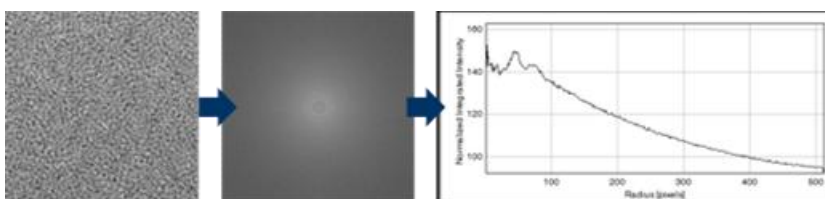
## Fast Fourier Transform procedures applied to X-ray transmission images

S. Pérez-Tamarit<sup>1,\*</sup>, E. Solórzano<sup>1</sup>, A. Kaestner<sup>2</sup>, M.A. Rodríguez-Pérez<sup>1</sup>

<sup>1</sup> CellMat Laboratory, University of Valladolid, Paseo de Belén 7 47011, Spain

<sup>2</sup> Neutron imaging and Activation Group, Paul-Scherrer Institute, LNS WBBA/118 5232 Villigen, Switzerland.

\* Corresponding author: [saul.perez@fmc.uva.es](mailto:saul.perez@fmc.uva.es)  
Tel.: +34 983 423572; fax: +34 983 433192



### Abstract

This paper investigates the applicability of fast Fourier procedures to cell size calculation in solid cellular materials. To this end a collection of closed-cell rigid polyurethane (PU) foams and an X-ray radiography system optimized to soft materials has been used to acquire the required images. A precise complementary determination of cell size and solid fraction of the samples have been accomplished. We can show that the spatial frequency of the first oscillation peak in the radial plot of the reciprocal space image is correlated with the real mean pore size, both in simulated and real images. To this end we propose an algorithm based on MATLAB language that also allows discriminating between isolated samples and samples belonging to a foaming process.

**Keywords:** fast Fourier transform; polyurethane; foam; X-ray imaging; optical microscopy; microstructure.

# 1. Introduction

The fast Fourier transform (FFT) is a computational tool which facilitates data analysis such as power spectrum analysis and filter simulations. It is a method for efficiently computing the discrete Fourier transform (DFT) of a series of data samples. The FFT takes advantage of the fact that the calculation of the coefficients of the DFT can be carried out iteratively, which results in a considerable savings of computation time. Specifically, if the data consists of  $N$  samples, FFT needs  $N \cdot \log_2 N$  arithmetic operations in contrast to  $N^2$  operations that are required to straightforward calculate the DFT coefficients [1]. As an example, it has

been reported that for 8192 samples, the computations require about five seconds for the evaluation of all the DFT coefficients, whereas conventional procedures take on the order of half an hour [2].

Moreover, it is well known that Fourier transform procedures are capable to determine the size, shape and number density of spherical particles distributed in a projected image in a volumetric monodisperse distribution of particles [3]. In fact, the two dimensional Fourier transform of a circularly symmetric object corresponds essentially to the Hankel transform of order zero [4]. As we demonstrate later in this manuscript with

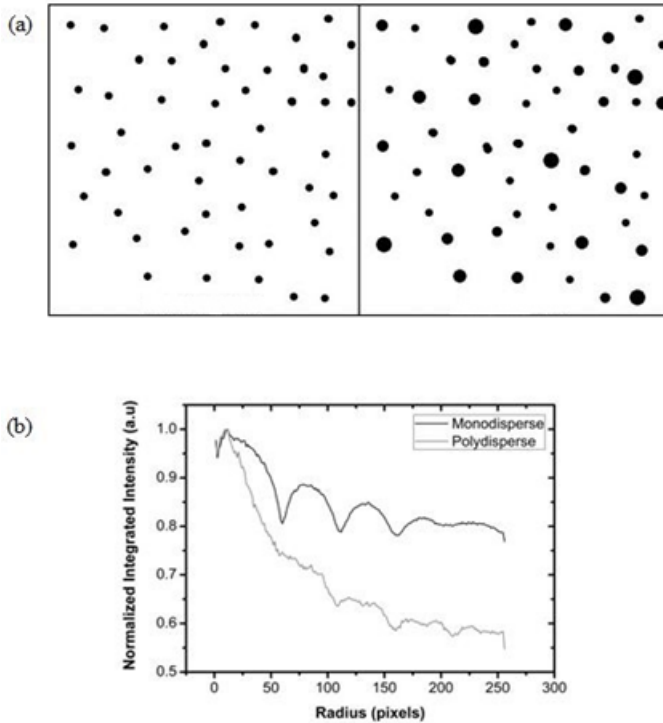


**Fig. 1.** (a) 2D dispersion of particles of monodisperse particle size (left) and polydisperse particle size distribution (right) and (b) resulting radial profiles of 2D Fast Fourier Transform.



the simulations made in a collection of hand-designed distributions of circular entities in 2D images, the frequency of oscillations of the first order Hankel transform [5] is nearly correlated with the particle size in the images. As the monodispersion in particle size in analysed images disappears, the oscillations in the two dimensional Fourier transform are smoothed only remaining oscillations corresponding to a short range order (Fig. 1).

The goal of our work is to investigate the applicability of this methodology to closed-cell solid matrix foams in order to obtain a parameter which may be correlated to mean pore size of the foams under study.

Cellular materials or foams are two phase structures in which a gas is dispersed throughout a solid (or liquid) continuous phase [6, 7]. From a geometric point of view it is helpful to think of a cellular structure as vertices, joined by edges (or struts), which surround faces (or walls), which enclose cells (or pores) [7].

In addition, it is well known that the properties of solid foams depend on the properties of the solid matrix and features such as the foam density and the cellular architecture [8]. It is therefore important to avail of techniques which allow simple, straight forward and reliable characterisation of these foam parameters. Density measurements are fast and direct, while the quantitative measurement of the cell size poses a challenge in terms of time investment

and accuracy. Different techniques are currently used to determine the average cell size but most of them present several inconveniences, such as complex devices or certain required foam characteristics.

For this reason, the methodology presented in this work is of great importance due to the ease of reaching a parameter correlatable with foam average pore size. To this end, the fast Fourier methodology described in the following sections is applied to X-ray transmission images of the foams under study. Furthermore, it is remarkable that the application of this procedure allows characterizing mean cell size both for experiments ex-situ and in-situ via X-ray radioscopy experiments [9, 10].

In this work we use a collection of rigid polyurethane (PU) foams in which we previously characterized the cell size by other methods in order to correlate the 2D real mean pore size of the foam in the orthogonal plane to the X-ray beam, and the signal available after the FFT algorithm implementation. The effects of sample density, real average pore size of foams and sample thickness (or pore overlapping in the X-ray image) have also been studied. In addition, the evolution of apparent cell size of polypropylene (PP) foam during the radioscopy experiment of foaming process in a mould similar to described in [9] is also included in the study.

## 2. Materials and methods

### 2.1 Preparation of foams

Polyurethane foams are commonly produced from reactive bi-component systems using di- or polyisocyanate and polyol blends [11]. Polyol blends include catalyst (amines), surfactants to stabilize the foam structure and water as blowing agent. Varying these polyol blends, it is possible to control the final density, the pore type (open or cell), the matrix rigidity (rigid or flexible) and, partially, the pore size. In this work, foams were produced from four different formulations, kindly provided by BASF (Barcelona, Spain), containing mainly different amounts of water. Due to the varying amount of blowing agent it was possible to produce PU foams with four different densities (30, 55, 70 and 100 kg/m<sup>3</sup>).

In order to avoid further variations of the formulations, the pore size control was accomplished by varying the mixing parameters. For a given density four different stirring conditions of the isocyanate and the polyol blends were used with the aim of obtaining materials with different pore sizes. The mixing conditions were modified by changing

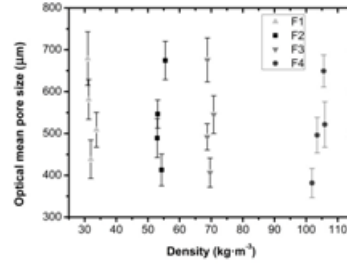


Fig 2. Real sample cell size measured by means of optical microscopy versus geometric sample density for all the formulations included in Table 1.

the stirring time and speed. As a result of this procedure, foams with different cell sizes were obtained (Fig. 2). A summary of different formulations (F) and mixing conditions (MC) used can be found in Table 1.

The mixture of the two components was accomplished by using an overhead stirrer (EUROSTAR Power control-visc P1), equipped with a 50 mm diameter propeller stirrer from IKA. Samples were produced in a large cylindrical container (200 mm height, 120 mm diameter) reaching expansion volumes over 1 litre. Smaller prismatic samples (65x65x35 mm) were prepared from the central foam block. In addition, the samples were sliced to different thicknesses to study the influence of the overlap of pores in the X-ray transmission images. In our particular

**Table 1.** List of samples used in the work. 16 samples in total, 4 formulations (F) and 4 mixing conditions (MC).

	F-1 (30 kg/m <sup>3</sup> )	F-2 (55 kg/m <sup>3</sup> )	F-3 (70 kg/m <sup>3</sup> )	F-4 (100 kg/m <sup>3</sup> )
MC-1 (12 s, 800 rpm)	✓	✓	✓	✓
MC-2 (16 s, 1000 rpm)	✓	✓	✓	✓
MC-3 (20 s, 1200 rpm)	✓	✓	✓	✓
MC-1 (25 s, 2000 rpm)	✓	✓	✓	✓

case, five different thicknesses were selected (33, 27, 21, 15 and 11 mm) which corresponds to approximately 15-80 pores in this direction considering the mean bubble size reached by the specimens during the foaming process (Fig. 2).

Furthermore, a linear PP supplied by Total Petrochemicals (PPH 4070) mixed with a 2 wt.% of a chemical blowing agent, azodicarbonamide (ADC) Porofor M-C1 from Lanxess ( $d_{50}=3.9 \pm 0.6$  micrometers) in order to promote the foam generation at high temperatures was used to verify the validity of FFT procedures in in-situ mold foaming process.

## 2.2 Determination of pore size and foam density

In our particular case, the solid fraction (or relative density) was measured by gravimetric methods using a high precision balance and considering the sample dimensions. For the cell size determination optical microscopy (OM) was used. This is the simplest and fastest technique for obtaining reliable values for the average cell size. A first step consisted of ink-dyeing in order to highlight the pore edges, making them clearly visible (Fig. 3). Then, a collection of three or four micrographs are taken and further analysed. All the micrographs were taken using an optical microscope Nikon SMZ-U with CMOS digital camera Ueye 1485LE. The image analysis process considers 150-200 pores identified over the 3-4 micrographs. These pores are

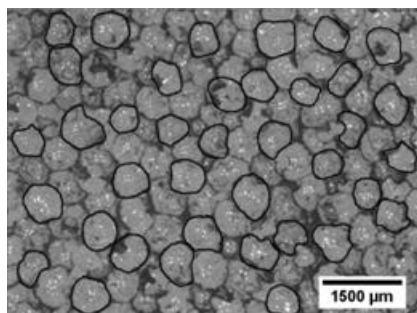


Fig 3. Example of one optical micrograph with highlighted pores selected.

identified and overlaid manually over a digital screen. The identified masks are analysed in ImageJ/Fiji [12,13] and a cell size distribution is obtained. The mean value of the equivalent diameter (the diameter of a circular pore with a same area to the one identified) is the parameter selected as pore size descriptor.

## 2.3 X-ray detection system

The setup used for radiography acquisition includes a micro-focus X-ray source from Hamamatsu (L10101) producing polychromatic X-rays and cone-beam geometry ( $39^\circ$  of aperture) with a spot size 5-20 microns which allows up to 20 times magnification,  $M$ , (Eq. 1) of the irradiated sample [14] – SOD: source-object distance,  $SDD$ : source-detector distance–.

$$M = \frac{SDD}{SOD} \quad (1)$$

The X-ray transmitted radiation is detected by a high sensitivity flat panel also from Hamamatsu (C7940DK-02) ( $2240 \times 2344$  pixels, 12bits and 50 microns pixel size) which allows high speed

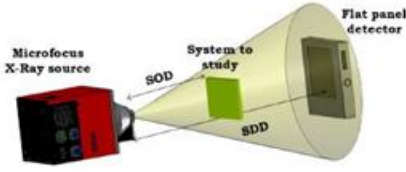


Fig. 4. Microfocus cone beam radiography setup.

imaging up to 9 fps (at 4x4 pixel binning). Finally a frame grabber records the radiography sequences for later image processing. The setup is customized for low absorbing materials such as polymers and typically works at low energies 20-60 kV and high currents 100-200  $\mu\text{A}$  in order to achieve an optimum contrast keeping small exposure times (600ms, typically) and high acquisition rates (1.66 fps). Nonetheless, in the case of very low dense samples (density about 25-30  $\text{kg}/\text{m}^3$ ) the weak absorption of X-rays results low contrast radiographs. Particularly, for this study the X-rays source parameters were 45 kV, 140  $\mu\text{A}$ , the exposure time was 1500 ms and magnification used is 2 times with effective pixel size of 25 microns by using a source-detector distance of 580 mm and source-object distance of 290 mm. Additional measurements have carried out considering a magnification 4 times with effective pixel size of 12.5 microns by using a source-object distance of 145 mm maintaining constant the source-detector distance. A 3D drawing of the X-ray imaging system is shown in (Fig 4).

## 2.4 Fast Fourier algorithm

The methodology is similar to the one described by [3]. In this methodology the pore size ( $\Phi_{FFT}$ ) is analysed in the Fourier space after removing the grey level fluctuations in the background (density in-homogeneities in the meso-scale). This step was done by using a high-pass filter based on large 2D median filter (15 pixels neighbourhood) and subsequently subtracting the original image from the filtered one. The output image was analysed in the reciprocal domain. The radial profile in Fourier space is plotted, then smoothed (5 pixels of Savitzky-Golay filter [15]) and finally, the spatial frequencies corresponding to the average pore size are identified as a broad peak. The peak position is identified by an automatic Gaussian fit, which allows evaluating the peak position with statistical accuracy. To this end, a MATLAB language algorithm was implemented using a commercial software package (MATLAB 8.2, The MathWorks Inc., Natick, MA, 2013). A resume of this procedure can be found in (Fig. 5). In this algorithm, different parameters may be fixed by the user (2D median filter index, smoothing filter index and name of the experiments) and

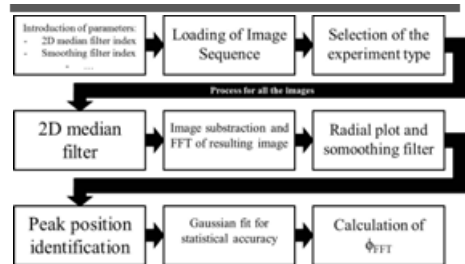


Fig. 5. Scheme of FFT algorithm procedure.

others are required for output calculations (pixel size of the setup of the images in study). In addition, the algorithm permits to select between two different modes to analyse the collection of images, one for foaming experiments (or spatial correlation between consecutive images) and another for a collection of different samples. The maximum of data analysed nowadays is a collection of 507 images with 700x700 pixels size [16] taking 437s of full-process time with successful results.

### 3. Results and Discussion

#### 3.1 Simulation of monodisperse particle distributions

The first step and the main motivation of this methodology concern the simulation of a collection of hand-draw images with the particularity of containing monodisperse distributions of particle size. To this end, the algorithm described

in the previous section was applied ignoring the 2D median filter in order to avoid blurring in the borders of the particles. The images under study consist in five different images varying the particle size in each of them, from 10 to 40 pixels, but not the position of each point in the images. The collection of images is shown in (Fig. 6).

Once implemented the FFT algorithm to these images, radial plots of reciprocal space images can be represented (Fig 7.a) and, by identification of the position of the first oscillation peak in every image, a first correlation between selected particle size and these position can be found (Fig 7.b). Furthermore, due to the foregoing correlation, it is possible to develop a new and better correlation taking into account the inverse value of first position peaks in radial plots (or associated spatial frequency to this point in the Fourier space) (Fig 7.c). The oscillations

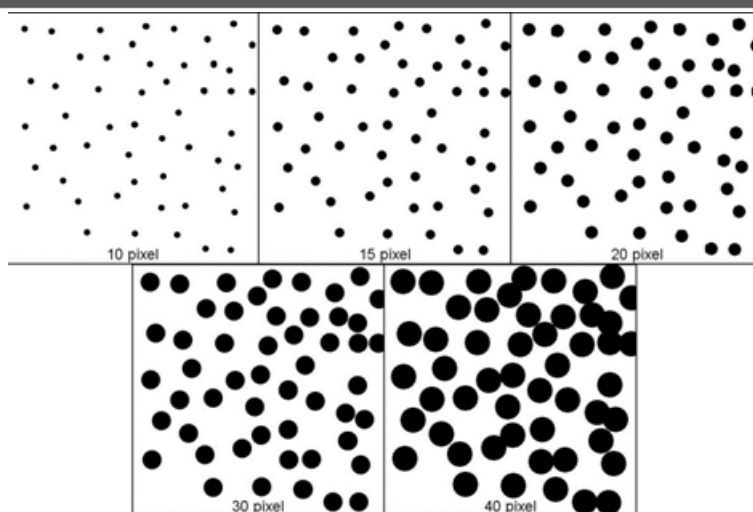


**Fig. 6.** Succession of images used in the simulation in order to verify the validity of FFT procedures to correlate mean particle size with the response measured by the FFT based algorithm.

presented in (Fig. 7.a) corresponds to the first order Hankel transform. In addition, the correlation between particle size and the inverse of the first peak position is almost perfect, which may be principally due to two reasons. First, all the particles in the succession of images are located in the same positions, that introduce less level of noising in the radial profiles and

the second one, as it has been mentioned above in the manuscript, the polydispersion in the particle size distributions provokes that the radial profiles loses the oscillations to become only one peak.

As it is shown in (Fig 7.a) and also in (Fig 7.c) the frequency of spatial oscillations in the reciprocal space increases linearly as the particle size become higher in each image. Therefore, in the case of real foams, it will be possible to correlate mean pore size with the spatial frequency associated to the first oscillation (and single oscillation, due to cell size distribution) in the radial plots of the reciprocal space images. To this end, several parameters of foams were taken separately in the analysis. First of all, the influence of sample density (four groups of samples, depending on described formulations in previous sections) in FFT algorithm response was analysed, secondly, the parameter under study was the mean pore size of the different foams (3 different values, depending mainly on stirring conditions) and finally, the effect of overlapping of pores in the final response was also studied. In addition, the applicability of this procedure in foaming process radioscopy experiments was complementarily analysed.

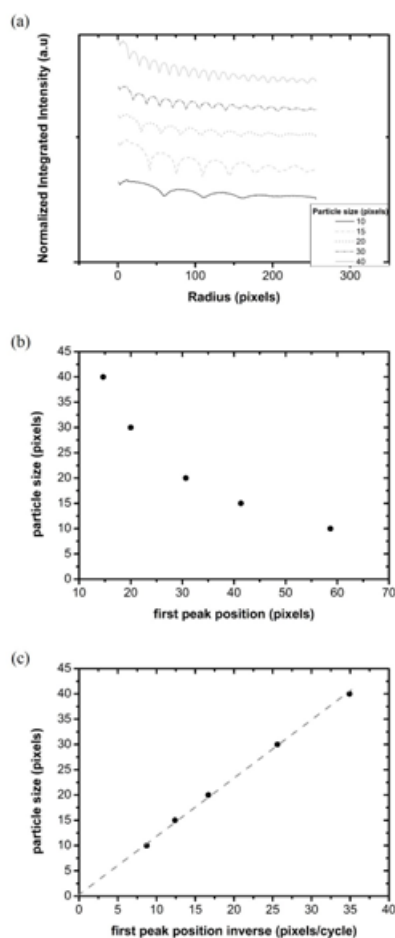


Fig. 7. (a) Radial plots of reciprocal space images of (Fig. 6). (b) Representation of the particle size versus first oscillation peak of the radial plot for each image and (c) Representation of particle size versus the spatial frequency associated to first oscillation peak for every image.

### 3.2 Influence of foam density

In X-ray imaging, contrast in the transmission images is due to differences in X-ray absorbance of the material under study [17]. The absorbance of X-rays of

the material is related with sample density and thickness via Lambert-Beer law [18]:

$$I(x, z) = I_0 e^{-\mu \rho(x, z) t} \quad (2)$$

where  $\rho(x, z)$  is the density of the system,  $t$  is the sample thickness in the beam direction assumed to be constant,  $\mu$  is the attenuation coefficient and  $I_0$  is the initial beam intensity. Thus, higher is the foam density under study; better is the contrast in X-ray transmission images. This fact causes that samples with highest density ( $100 \text{ kg/m}^3$ ) have a superior response in measured cell size by FFT procedures independently of the sample thickness (Fig. 8). In addition, good general trends are achieved both for samples with

thickness 11 mm and 33 mm. Nonetheless, in the case of very low dense samples ( $30 \text{ kg/m}^3$ ) the X-ray absorbance is not enough for obtaining images with a suitable contrast, thus, the FFT response for this type of foams lacks of accuracy.

### 3.3 Influence of real mean pore size

Considering all the samples under study, it is possible to discriminate well three different cell sizes in whole density range although samples with density  $30 \text{ kg/m}^3$  present again deviations from the general trend of the rest of specimens. Furthermore, the slope for the three different pore sizes is almost the same and decreases as the foam thickness increases to the point to turn to zero as it is shown in (Fig. 9). Moreover, it is remarkable that in all cases, ignoring lowest dense samples, the FFT response of different trends concerning each pore size is arranged such that the minor real mean pore size ( $490 \text{ }\mu\text{m}$ ) is located in the bottom of the graphs, the major ( $670 \text{ }\mu\text{m}$ ) in the top, and the remaining one ( $520 \text{ }\mu\text{m}$ ) between them. Finally, as last consideration, taking into account that in our setup the pixel size of the X-ray imaging system is  $25 \text{ }\mu\text{m}$ , the differences between 490 and  $520 \text{ }\mu\text{m}$  are reduced to one pixel, making possible that the response of these two different pore sizes results overlapped.

### 3.4 Influence of pore overlapping

In X-ray transmission imaging, due to high penetration power of the X-rays, it is possible that the surface of the object

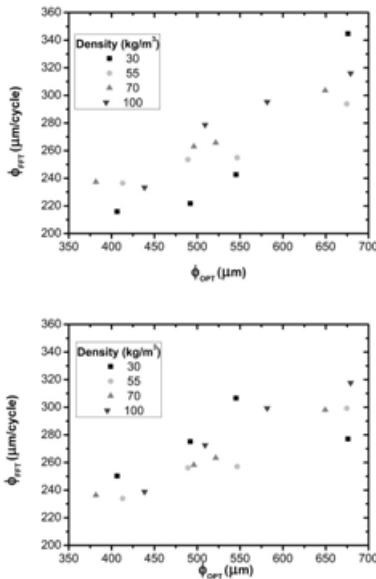


Fig. 8. Measured pore size by FFT procedures versus real mean pore size measured by optical microscopy for samples with 11 mm of thickness (top) and 33 mm of thickness (bottom).

under study may be perturbed by the irregularities inside the material, resulting low quality images. In our case, these irregularities are inherent, and can be disastrous for the study that we are carried out. In fact, the overlapping of pores may result in an effective pore size higher than the original cell size, becoming even more noticeable as the sample thickness increases. In order to alleviate this fact, as well as other

irregularities, the 2D median filter is implemented in the algorithm, as it is mentioned above in the text.

Therefore, as it is shown in (Fig.10), disregarding again samples with 30 kg/m<sup>3</sup> of density, the possibility of overlapping of pores has no effect in the final response of FFT algorithm. Consequently, within the thickness range in which are the samples selected for this work, the FFT signal is not influenced by sample thickness. In addition, in this figure are discernible all the trends involving pore size measured by FFT procedures and real mean cell size measured by optical microscopy.

### 3.5 Study of a foaming process

At this point, it is clear that the real mean pore size of the samples is highly correlated with the mean pore size associated to the spatial frequency of the first oscillation peak in the radial plot of the reciprocal space image of the samples. Thus, by X-ray radioscopy experiments of foaming processes it is possible to discern the relative evolution in real time of mean pore size by means of the procedure implemented in this algorithm. A succession of isolated radiographs of a radioscopy foaming experiment is shown in (Fig. 11) where it can be seen the evolution in time from plastic pellets to foamed by heating structure of the material. In our case, the algorithm is implemented since the foam has been completely formed (this is our time origin for representations) to the final of the

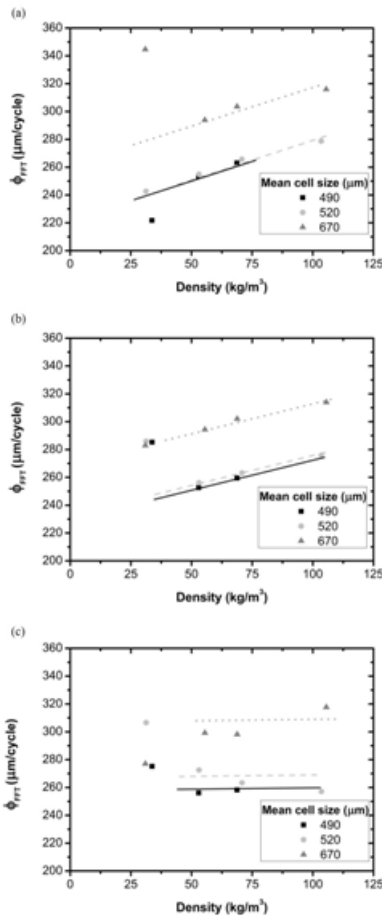


Fig. 9. Measured pore size by FFT procedures versus sample density considering three different real pore sizes. The foam thickness varies between 11 mm (a) to 33 mm (c) considering an intermediate point (21 mm, b).



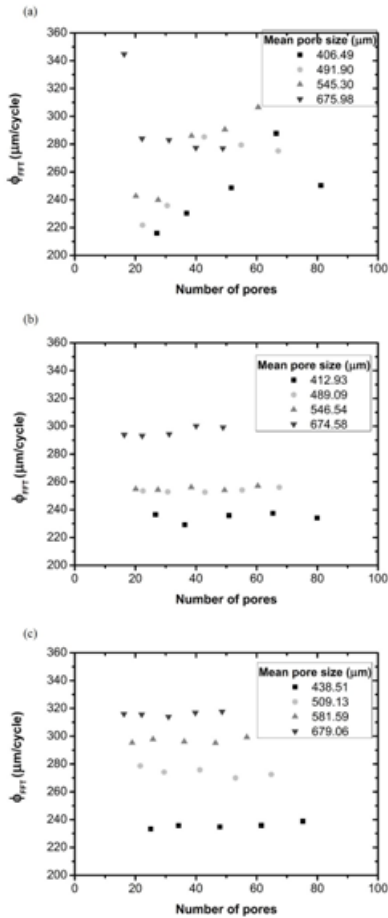


Fig. 10. Cell size measured by means of FFT algorithm versus number of pores in thickness for three different foam densities, (a) 30  $\text{kg/m}^3$ , (b) 50  $\text{kg/m}^3$  and (c) 100  $\text{kg/m}^3$ .

experiment, in 700x700 pixels region of interest (ROI). As it is shown in (Fig. 12), the cell size of the sample under study

increases with time and, although the exact value of real mean pore size is unknown, this is its real evolution, therefore, measuring simply the final value of real mean pore size of the sample it is plausible to calculate the mean cell size in the whole foaming process.

#### 4. Conclusions

Using PU foam samples with a number of different characteristics varied independently (pore size, density, thickness, etc.) and a X-ray imaging system we have been able to show that fast Fourier transform procedures applied to X-ray transmission images allow to correlate real mean pore size of the samples under study. Furthermore, varying independently main characteristics of the foams it is possible to discern which parameters affect in the final response of the FFT algorithm presented in this work.

Thus, concerning foam density, taking into account that the absorption of X-rays by the material is related to material density (via Lambert-Beer law) and the X-ray absorption determines contrast in final images, more dense samples result in more contrasted images, therefore, as

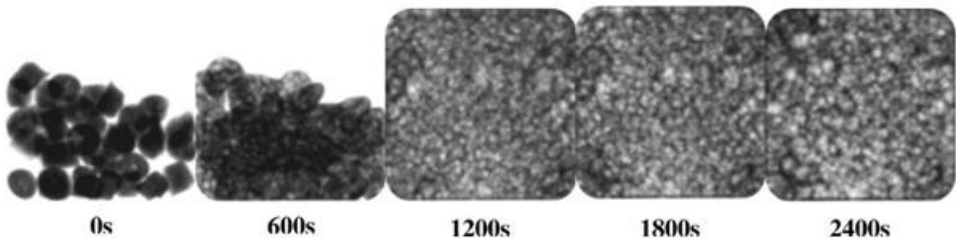


Fig. 11. Isolated radiographs of the whole foaming process.

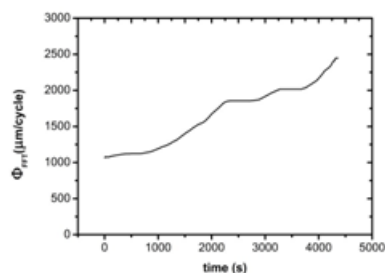


Fig. 12. Measured by FFT algorithm cell size evolution versus foaming experiment time.

higher is sample density, major is the final response of the FFT algorithm.

Moreover, we have shown that for constant mean pore size, the measured cell size by means of FFT algorithm is correctly ordered for every density (excepting very low dense samples under study). Finally, varying sample thickness between 11 and 33 mm, we have demonstrated that in this range of foam thickness the overlapping of pores doesn't affect to FFT signal. A 2D high-pass median filter was applied to all the images under study, eliminating, by subtracting filtered image to original image, the irregularities in original image.

In addition, the applicability of this procedure to real time foaming processes radioscopy has been studied, achieving quite good results concerning relative mean pore size during the foaming process. Further work is required in order to characterize in detail other foam parameters like cell anisotropy that can be studied by identifying the symmetry of the radial plot of the reciprocal space images.

The potential applicability of these results as a fast and non-destructive technique to measure the average cell size is of a capital utility for the cellular plastics scientific and technical community. Due to the simplicity of the set-up this could be a useful technique for the in-situ characterisation of cell size evolution during processing.

## Acknowledgments

Pre-doctoral contract of S. Perez-Tamarit by University of Valladolid (E-47-2015-0094701) and co-financed by Banco Santander is acknowledged. In addition, financial support from MINECO, FEDER, UE (MAT2015-69234-R) and the Junta de Castile and Leon (VA011U16) are gratefully acknowledged. Joan Ferrer and Luis Vela from BASF Spain are also acknowledged for supplying the materials used in this investigation.

## References

- [1] P. Duhamel, M. Vetterli, Fast Fourier Transforms: A tutorial review and a state of the art, *Signal Processing*, 19 (1990) 259-299.
- [2] W.T. Cochran, J.W. Cooley, D.L. Favon, H.D. Helms, R.A. Kaenel, W.W. Lang, G.C. Maling, D.E. Nelson, C.M. Rader, P.D. Welch, What is the fast Fourier transform?, *Proceedings of the IEEE*, 55 (1967) 1664-1674.
- [3] C.D. Chan, M.E. Seitz, K.I. Winey, Disordered spheres with extensive overlap in projection: image simulation and analysis, *Microscopy and microanalysis : the official journal of Microscopy Society of America, Microbeam Analysis Society, Microscopical Society of Canada*, 17 (2011) 872-878.
- [4] Y. Li, Y. Lu, Deriving the integral representation of a fractional Hankel transform from a fractional Fourier transform, *Optics Letters*, 23 (1998) 1158-1160.
- [5] V. Magni, G. Cerullo, S. De Silvestri, High-accuracy fast Hankel transform for optical beam propagation, *Journal of Optical Society of America A*, 9 (1992) 2031-2033.

- [6] A. Cunningham, N.C. Hilyard, *Low Density Cellular Plastics: Physical Basis of Behaviour*, Ed. Chapman and Hall, London, 1994.
- [7] L.J. Gibson, M.F. Ahsby, *Cellular Solids: Structure and Properties*, Pergamon Press, Oxford, England, 1988.
- [8] J.A. Reglero Ruiz, C. Saiz-Arroyo, M. Dumon, M.A. Rodriguez-Perez, L. Gonzalez, Production, cellular structure and thermal conductivity of microcellular (methyl methacrylate)-(butyl acrylate)-(methyl methacrylate) triblock copolymers, *Polymer International*, 60 (2011) 146-152.
- [9] E. Solórzano, S. Pardo-Alonso, J.A. de Saja, M.A. Rodriguez-Perez, X-ray radioscopy in-situ studies in thermoplastic polymer foams, *Colloids and Surfaces A: Physicochemical and Engineering aspects*, 438 (2013) 167-173.
- [10] S. Pardo-Alonso, E. Solórzano, S. Estravís, M.A. Rodriguez-Perez, J.A. de Saja, In situ evidence of the nanoparticle nucleating effect in polyurethane-nanoclay foamed systems, *Soft Matter*, 8 (2012) 11262.
- [11] D. Klempner, K.C. Frisch, *Handbook of polymeric foams and foam technology*, Passavia Druckerei GmbH Passau 1991.
- [12] M.D. Abràmoff, P.J. Magalhaes, J. Sunanda, *Image Processing with ImageJ*, *Biophotonics International*, 11 (2004) 36-42.
- [13] C.A. Schneider, W.S. Rasband, K.W. Eliceri, NIH Image to ImageJ: 25 years of image analysis, *Nature Methods*, 9 (2012) 671-675.
- [14] E. Solórzano, J. Pinto, S. Pardo, F. Garcia-Moreno, M.A. Rodriguez-Perez, Application of a microfocus X-ray imaging apparatus to the study of cellular polymers, *Polymer Testing*, 32 (2013) 321-329.
- [15] R.W. Schafer, What is a Savitzky-Golay filter?, *IEEE Signal Processing Magazine*, (2011) 111-117.
- [16] E. Solórzano, E. Laguna-Gutierrez, S. Perez-Tamarit, A. Kaestner, M.A. Rodriguez-Perez, Polymer foam evolution characterized by time-resolved neutron radiography, *Colloids and Surfaces A: Physicochemical and Engineering Aspects*, 473 (2015) 46-54.
- [17] M.M. Bernal, S. Pardo-Alonso, E. Solórzano, M.A. Lopez-Machado, R. Verdejo, M.A. Rodriguez-Perez, Effect of carbon nanofillers on flexible polyurethane foaming from a chemical and physical perspective, *RSC Advances*, 4 (2014).
- [18] E. Solórzano, S. Pardo-Alonso, J.A. de Saja, M.A. Rodríguez-Pérez, Study of aqueous foams evolution by means of X-ray radioscopy, *Colloids and Surfaces A: Physicochemical and Engineering Aspects*, 438 (2013) 159-166.



On the other hand, it is well known that in the cellular materials manufacturing the inclusion of particles in the polymer matrix serves either as blowing agents and nucleating sites depending on the type of particle. Several aspects influence the optimum performance of additives (both for blowing or nucleating purposes) such as the amount of additive [5], its size [6] or its compatibility with the employed polymer matrix [7]. In addition, the filler dispersion onto the polymer matrix plays an important role to optimize the purpose of the filler (blowing, nucleating or even as enhancer of a determined physical property) [8].

Several works have been performed in order to characterize all these aspects focused on typical characterization techniques such as SEM or SAXS, but owning critical experimental skews such as the 2D information or the compromise between resolution and statistics. Other techniques based on rheology could be considered in order to study the particle dispersion, but they are not applicable in the case of blowing agents due to the decomposition of the filler. For this reason this investigation is focused in obtaining a novel methodology to characterize the particle dispersion in polymer composites by means of high resolution X-ray Tomography.

## **A.2 Quantification of additive dispersion in polymers using X-ray Tomography**

In this work entitled “**Novel quantification methods of fillers dispersion in polymer composites based on high resolution synchrotron X-ray  $\mu$ -CT**” the dispersion quality of azodicarbonamide (ADC) particles in three different polypropylene matrixes is studied by means of synchrotron X-ray  $\mu$ -CT. The high resolution achieved in the performed tomographies (0.438  $\mu\text{m}$  voxel size) permitted reconstructing in detail the ADC particles thanks to phase retrieval (Figure A-2).

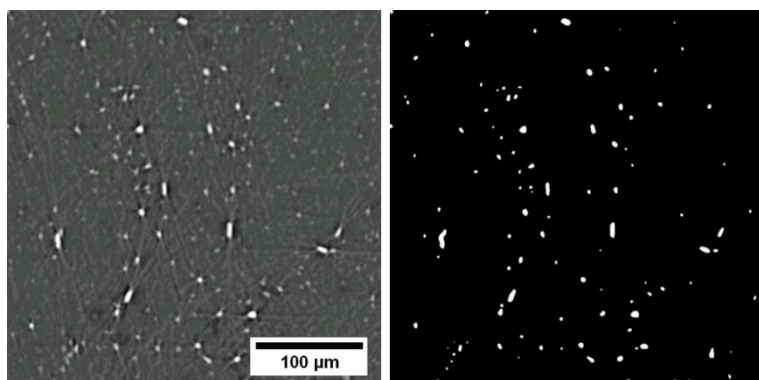


**Figure A-2.** Tomographic slice of ADC particles distributed on Linear PP -LEFT- and corresponding binarization -RIGHT- showing the perfect detection of all the particles in the image.

Two image analysis methodologies have been developed and applied to determine the quality of dispersion in those polymer composites finding minor but crucial differences between the three materials studied. In addition, a statistical method that permits elucidating the type of distribution (Gaussian, Poisson, etc) of the particles within the sine of the polymer has been considered and demonstrate that the ADC particles are distributing according the same type of distribution in all the materials.

This work opens novel possibilities to quantitatively characterize this crucial aspect in polymer composites.

Polymer (submitted)

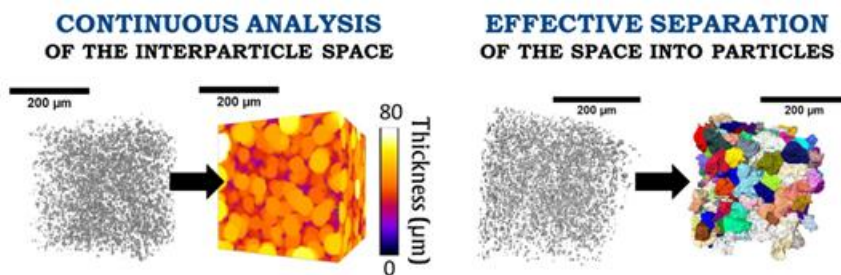
## Novel quantification methods of fillers dispersion in polymer composites based on high resolution synchrotron X-ray $\mu$ -CT

S. Pérez-Tamarit<sup>1,\*</sup>, E. Solórzano<sup>1</sup>, E. Laguna-Gutierrez<sup>1</sup>, A. Hilger<sup>2</sup>  
I. Manke<sup>2</sup>, M.A. Rodriguez-Perez<sup>1</sup>

<sup>1</sup> CellMat Laboratory, University of Valladolid, Paseo de Belén 7 47011, Spain

<sup>2</sup> Helmholtz-Zentrum Berlin für Materialien und Energie, Lise-Meitner-Campus, Hahn-Meitner-Platz 1 14109, Berlin, Germany.

\* Corresponding author: [saul.perez@fmc.uva.es](mailto:saul.perez@fmc.uva.es)  
Tel.: +34 983 423572; fax: +34 983 433192



### Abstract

The inclusion of fillers on polymers is a common practice to accomplish determined requirements for this kind of materials. Nonetheless, one of the critical aspects in these polymer composites in order to achieve the desired effect is to guarantee a good dispersion of the particles included. In addition, there are few experimental methods that allow quantitatively characterizing the quality of dispersion of fillers in polymer composites.

This work investigates new analysis routes of the dispersion of additives in polymer composites by using high resolution X-ray micro computed tomography ( $\mu$ -CT). To this end, three different polymer composites based on polypropylene (PP) and azodicarbonamide (ADC) have been scanned. Three different methods have been developed showing that the polymer viscosity slightly affects particle dispersion. Furthermore, the analysis of the obtained tomographies allowed accurately determined the particle granulometry and concentration within the material.

**Keywords:** polymer composites; polypropylene; synchrotron; X-ray  $\mu$ -CT; 3D image analysis.

## **1. Introduction**

Nowadays, polymer composites industry covers a high range of applications, expanding the own range of raw polymers [1-3]. This expansion occurs in two different ways, by always focusing on a determined physical property. On one hand, specific additives could enhance specific physical properties such as mechanical and thermal properties in order to improve the behaviour of polymer composites for example on structural [4] or safety [5] and flame retardant [6] or energy saving [7] applications respectively. On the other hand, in recent decades fillers with specific properties have been included in polymer composites in order to open new application possibilities to these materials. It is achieved by providing impossible characteristics for the raw polymers such as electricity conduction or magnetic properties. This fact permits the use of polymer composites in applications such as microelectronics [8] or medical applications (for drug delivery capsules) [9].

Nonetheless, in addition to the particular properties of the fillers, it is well-established that the improvement of performance of polymer composites in comparison with the raw polymer relies on the polymer changes on the matrix-additive interface [10-13]. For this reason, there are many factors affecting the properties enhancement in polymer composites. Studying each of them separately, i.e. evaluating their effect

maintaining the rest unaltered, we can discuss their effect on final polymer composites properties. First of all, it is obvious that the amount of used additive affects the polymer composite final performance. However, in not few cases there are optimal amounts of filler [14, 15] because it also affects the other enhancement properties factors (provoking for example percolations) [16]. After that, the size of the additive particles is also crucial. Reducing the size of fillers increases the aspect ratio of the reinforcement and thus habilitating more matrix-additive interfaces. As a result, a higher volume of matrix polymer is affected by the additive and the desired effect in the polymer composite is optimized. This fact has been extremely empowered in recent decades by using nano-sized fillers on polymer composites, creating so-called polymer nano-composites [17, 18]. Further and not less important, the matrix-additive compatibility plays a key role in order to maximize the improvement of properties of polymer composites. In fact, this factor is closely related with the previous one. Non-desired poor matrix-additive compatibility provokes micro-(or even nano-) holes in the matrix-additive interface resulting in non-optimum materials [19]. Finally, two linked factors are the filler dispersion and agglomeration within the polymer matrix. They are connected because optimum particle dispersion should avoid the agglomeration. However, it could be possible to obtain polymer composites with agglomerates but



perfectly dispersed. In the particular case of nano-sized filler the agglomeration or in opposite case the exfoliation of the additives is crucial [20-22]. If the additives agglomerate, the effective particle size increases thus reducing the aspect ratio and also the amount of matrix-additive interfaces. As a consequence the effect of the included filler in the polymer matrix is also reduced.

Since all of these factors are crucial for the final performance of the polymer composites, a lot of studies have been carried out in order to investigate them in different ways and by using several experimental techniques. The most common techniques to analyse these factors are linked with electron microscopy (both scanning and transmission). This kind of techniques allows characterizing the filler size, agglomeration, compatibility and dispersion [10, 23-26] with high spatial resolution in a simple way. Nevertheless, microscopy techniques offer always results in two dimensions obviating the third one including consequently a skew in the results. A quasi-3D option is the confocal microscopy [27], but offering up to day low depths and overlapped information, i.e. the third dimension. In addition, due to the high spatial resolution, the statistical accuracy of the results could be compromised. Furthermore, particle dispersion and/or agglomeration are commonly studied by using X-ray diffraction techniques (both SAXS and WAXS) [28, 29].

Focusing on particle dispersion, which is the main objective of this work, indirect measurements could be obtained by means of the rheological changes provoked in the polymer matrix by additives [30,31]. This technique permits obtaining valuable results about the additive dispersion independently of its size resulting ideal for polymer nano-composites [32-34]. However, it presents also some disadvantages. Regarding the basis of the technique, it could be not applicable to study the particle dispersion if the additive decomposes with temperature, as in the case of the studied materials for this investigation. Moreover, the particle dispersion quantification is based on theoretical models that could be not so accurate for specific materials.

Due to the limitations of existing techniques for investigating the particle dispersion quality within polymer matrixes, the main objective of this investigation is to develop a new methodology to study this feature based on high resolution synchrotron X-ray tomography. This technique allows us obtaining results in 3D with high resolution of any system (whereas the resolution permits) maintaining good statistics. To this end, three systems based on polypropylene (PP) and azodicarbonamide (ADC) have been scanned and then analysed by using specific image analysis methodologies developed for this investigation.

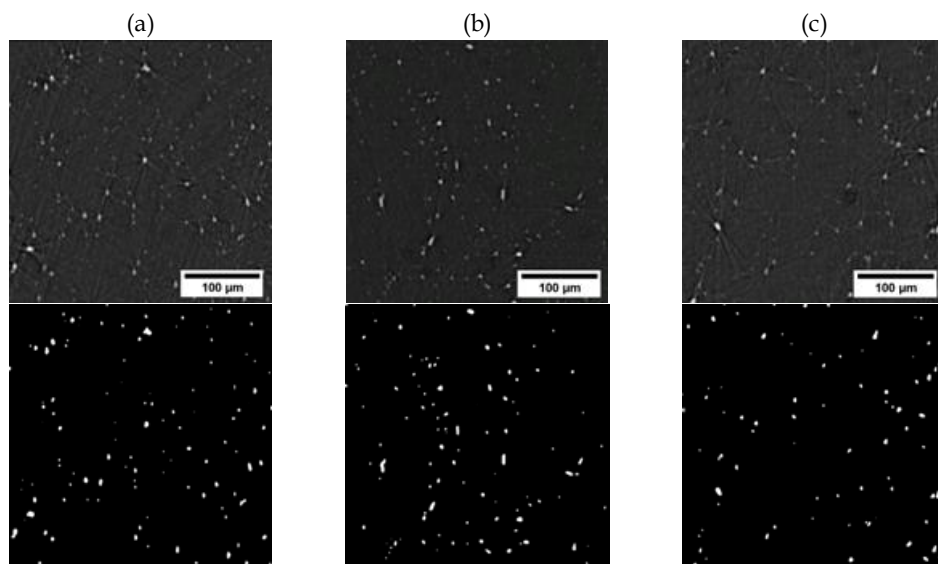


Fig 1. Representative tomographic slices of materials under study. Grey scale -up- and particles binarized -down-. The materials are (a) HMS-PP (b) Linear-PP and (c) 50-50.

## 2. Experimental

### 2.1 Materials

Two different polypropylenes (PPs) have been used. The first PP is a branched high melt strength PP (HMS-PP) supplied by Borealis (PP Daploy WB 135 HMS). The second PP is a linear PP (Linear-PP) supplied by Total Petrochemicals (PPH 4070). The density at room temperature is  $900 \text{ kg/m}^3$  for both PPs.

In addition, a balanced blend of the two PPs (50 wt. % HMS-PP and 50 wt. % Linear-PP, 50-50) has been prepared with a co-rotating twin screw extruder Collin ZK 25T with L/D of 24. The rotational speed used was 80 rpm and the melt temperature was  $190^\circ\text{C}$ .

Antioxidants Irgafos 168 and Irganox 1010 (from Ciba) have also been used to

reduce the thermal degradation of the polymers.

The additive for the three tested polymers was a chemical blowing agent, azodicarbonamide (ADC) Lanxess Porofoor M-C1 with an average particle size of  $3.9 \pm 0.6 \text{ }\mu\text{m}$  and density of  $1650 \text{ kg/m}^3$ .

### 2.2 Samples production

The formulations produced (HMS-PP, Linear-PP and 50-50) were mixed with 2 wt. % of ADC using the same co-rotating twin screw extruder, previously described, with a rotational speed of 100 rpm and a melt temperature of  $180^\circ\text{C}$  avoiding the thermal decomposition of blowing agent. Irgafos 168 and Irganox 1010 were added to the formulation in proportions of 0.08% and 0.02% by weight respectively.

Once the final formulations were fabricated, the pellets were placed in a mould (22 mm of diameter and 1.5 mm in thickness) which is located in a hot-plate press. This process allowed obtaining solid precursors of the three tested materials with these dimensions.

### 2.3 Synchrotron $\mu$ -CT

The analysed specimens were scanned using synchrotron X-ray microtomography ( $\mu$ -CT) at BAMline (BESSY II synchrotron, HZB, Berlin) [35]. The specific conditions of the tomographic experiments, such as low beam energy (9.8 keV), high exposure time (3000 ms), and number of exposers (2200) allowed obtaining tomographic results with excellent contrast by using phase-retrieval reconstruction [36] (Fig. 1). Further the reached spatial resolution (0.438  $\mu\text{m}$  of voxel size) permitted reconstructing almost the totality of the added fillers. Due to spatial resolution, scanned samples were prisms of less than 1 mm<sup>2</sup> of base.

### 2.4 Fillers dispersion evaluation methods

Three different methods allowing discerning the quality of particle dispersion have been developed for this work. Two of them determine the inter-particle space distribution by using image analysis procedures and the last one iteratively discretizes the space analysing the position of the particles into it.

In order to obtain valuable results, three different volumes (800x800x800 pix<sup>3</sup> or *ca.*

350x350x350  $\mu\text{m}^3$ ) were selected and analysed by the methods presented hereinafter. Prior the binarization of the volumes of interest (VOIs), an edge preserving filter in 3D of one pixel of radius was applied in order to enhance the image contrast. For the binarization of particles in all cases the amount of filler (in % V.) included in the formulation was considered as a reference. In order to calculate the % V. the % wt. was transformed by using the density of the components (raw polymer and additive) of the polymer composite.

#### 2.4.1 Continuous analysis of the inter-particle distance

Once the particles were suitably binarized, the local thickness of the inter-particle space was computed by applying the local thickness algorithm based on Euclidean distance transform [37] as shown in Fig. 2. These computations were carried out by using ImageJ/Fiji application [38, 39]. In addition, the computation time was around 6h for the volumes analysed (800<sup>3</sup> voxels). This method allowed determining the minimum distance between particles for every voxel in the inter-particle space and consequently inter-particle distance distributions (inter-particle distance 1).

#### 2.4.2 Effective separation of the space into particles

The image analysis protocol for this type of method was compound of several steps. Once the binarization step is completed (first step, Fig. 3a), the inter-

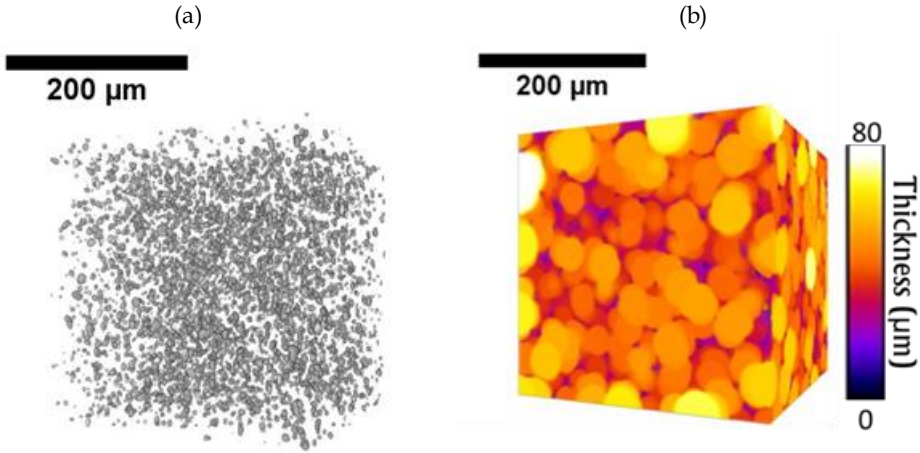


**Fig. 2.** Computation workflow for the continuous analysis of the inter-particle space in one of the analysed VOIs of the HMS-PP polymer composite. (a) 3D rendering of the binarized particles and (b) result of the local thickness algorithm.

particle space was separated in individual objects by means of a 3D distance transform (quasi-Euclidean) watershed algorithm (Fig. 3b) [40]. After that, the objects connected with the edges of the VOI were eliminated in order to improve the statistics of the results (Fig. 3c). Finally, the volume of the remaining objects (around 750 in all cases) was determined. All the workflow steps of this method of analysis were carried out by using MorphLibJ plugin [41] for imageJ/Fiji. The computation time was around 2h in order to complete all the steps of this analysis method. In this case, the inter-particle distance is calculated as the equivalent diameter ( $ED$ ) of the volume ( $V$ ) of the analysed objects (Eq. 1). This parameter represents the average inter-particle distance for groups of particles and allowed also obtaining inter-particle distance distributions (inter-particle distance 2).

$$ED = 2 \sqrt[3]{\frac{3V}{4\pi}} \quad (1)$$

Once the inter-particle distance distributions were determined for the two presented methods, we defined a new parameter characterizing the quality of the particle dispersion based on parameters of these distributions. We called it normalized full width at half maximum ( $NFWHM$ ) and is calculated as the ratio between the full width at half maximum ( $FWHM$ ) and the average value ( $A$ ) of the inter-particle distance distributions (Eq. 2). As a criterion, the lower is the  $NFWHM$  of the inter-particle distance distributions; the better is the filler dispersion in the analysed VOI.

$$NFWHM = FWHM/A \quad (2)$$

In addition, the average values of the inter-particle distributions of the analysed VOIs should be linked to the concentration of particles contained therein (directly obtained from the

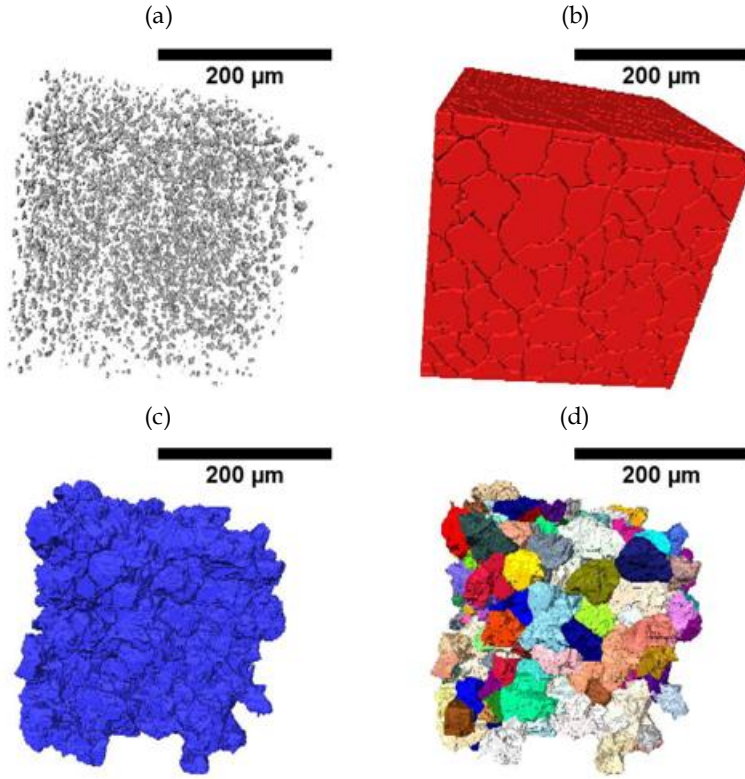


**Fig. 3.** Computation steps for the effective separation of the space into particles method for one VOI of the HMS-PP polymer composite. (a) Binarization of the particles (b) watershed segmentation of the inter-particle space (c) removal of the objects connecting the VOI edges and (d) remaining objects volume analysis.

binarized VOIs). The higher is the particle concentration within a volume; the lower is the inter-particle distance. As a consequence, this relation might allow discriminating the quality of fillers dispersion within a volume. However, as shown below in the manuscript, the latter criterion is less precise than the previous one.

#### 2.4.3 Statistical evaluation of the fillers dispersion on the space

The last developed method consisted on the calculation of the Morishita index ( $I_M$ )

[42] in 3D for the selected volumes. It was usually determined in 2D images but not in 3D. To this end, a selected volume was iteratively subdivided in smaller parts of the same volume. In each iteration ( $n$ ) the number of particles of all the subvolumes was recorded. The Morishita index is then calculated according to Eq. 3.

$$I_M(n) = q \frac{\sum_{i=1}^q n_i(n_i-1)}{N(N-1)} \quad (3)$$

where  $q=3^n$  is the number of subvolumes of the iteration  $n$ ,  $n_i$  is the number of particles contained in the subvolume  $i$

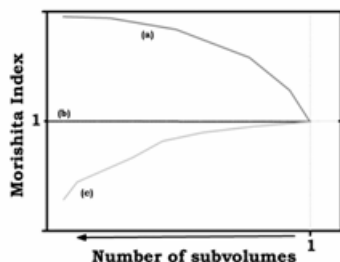


Fig. 4. Examples of the Morishita index outputs. (a) Aggregate distribution (b) Poisson distribution and (c) Normal distribution.

and  $N$  is the initial number of particles. The analysis process ended when the number of subvolumes was equal or greater than the number of particles contained in the initial volume.

In our case, a little script was developed in MatLab language to calculate this index for the selected VOIs. To this end, the mass center of particles was selected as the position reference of every particle in the space. Then, comparing these values with the bounding coordinates of the subvolumes was possible determine all the  $n_i$  values for every iteration and consequently  $I_M$ .

Nevertheless, this index does not permit discerning the dispersion quality, but the type of particle distribution within the material. It is possible analysing its evolution with number of subvolumes (or iterations). Among all the possibilities, we focus on three main cases. Firstly, if the Morishita index increases with the number of subvolumes, the distribution of the particles in the material is Aggregate distribution (Fig. 4a). Moreover, if this parameter remains at a

constant value of 1 independently of the number of subvolumes, the distribution is Poisson distribution (Fig. 4b). Finally, if this index decreases when the number of iterations increases, the particle distribution is Normal (Fig. 4c) [24].

## 2.5 Particle granulometry

Finally, an interesting output of this analysis was the particle granulometry within the material. To this end, the volume of the binarized particles was analysed, again by means of MorphLib plugin. Once the volume was computed, the particle size ( $D$ ) was determined as the equivalent diameter of the particle volume ( $V_P$ ) (Eq. 4) even if these particles are not spherical.

$$D = 2^3 \sqrt{\frac{3V_P}{4\pi}} \quad (4)$$

## 3. Results and Discussion

### 3.1 Continuous analysis of the inter-particle space

First of all, the homogeneity of the particle dispersion within the material was evaluated analysing the inter-particle distributions for the three analysed zones in each material (Fig. 5). In principle, all the distributions corresponding to each material are similar. Therefore, the dispersion quality is similar in all the analysed zones. In addition, HMS-PP is qualitatively the polymer in which there are less differences between zones (Fig. 5b) whereas in the two remaining polymers (50-50 and Linear-PP) the differences between the particle

distribution on the different zones are higher but similar between them (Fig. 5 a and c).

Moreover, we have determined the average inter-particle distance in all the zones calculating the average value of the inter-particle distributions. These distances are related hereinafter with the particle concentration of the analysed

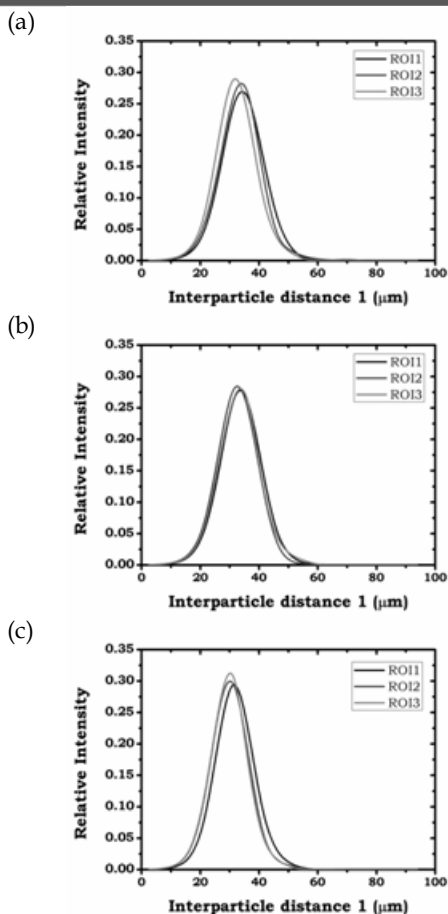


Fig. 5. Inter-particle distance distributions for the continuous analysis of the space (inter-particle distance  $l$ ) showing the homogeneity of the results between the selected ROIs (or VOIs). (a) 50-50 (b) HMS-PP and (c) Linear-PP.

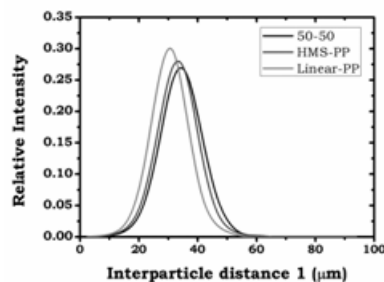


Fig. 6. Average inter-particle distributions obtained by the continuous analysis of the inter-particle space for the three tested polymer composites.

VOIs.

Furthermore, in order to compare between materials, the histograms of the three regions have been suitably averaged (Fig. 6). This fact allowed us to discriminate the dispersion quality of ADC particles in the three analysed materials. Regarding then the *NFWHM* values for the three distributions (Table 1), the particles are slightly better and worse dispersed in the Linear-PP and HMS-PP respectively. In addition, the dispersion quality of the 50-50 is in between of the two precedent limits.

Comparing these results with viscosity values of the raw polymers measured by rheological techniques (Table 1) [43] the relationship is clear. The higher is the zero-shear viscosity of the raw PP; the better is the ADC dispersion in the polymer by the dispersion method employed.

However, the small differences in the *NFWHM* for all the materials (approx. 2%) seem to indicate that the dispersion

**Table 1.** Viscosity characteristics and quantitative results of particle dispersion by the two image analysis methods

Polymer	Zero-shear viscosity (Pa s)	<i>NFWHM</i>	<i>NFWHM</i>
		Continuous analysis	Effective separation
50-50	9700	0.45	0.71
HMS-PP	8800	0.46	0.76
Linear-PP	10700	0.44	0.69

quality is more linked to the manufacture process of the polymer composite and not to the characteristics of raw materials.

3.2 Effective separation of the space into particles

The second method that separated the space into particles allowed extracting similar conclusions. On one hand, the differences in the inter-particle distributions for the analysed zones in the polymer composites are also small (Fig. 7). From the point of view of this method, the polymer in which the particle dispersion is more homogeneous comparing the different zones is the 50-50 (Fig. 7a) whereas the opposite corresponds to the Linear-PP (Fig. 7c).

Furthermore, we have extracted the average inter-particle distance from these distance distributions for this type of analysis. Again, these results allowed us discerning the relationship between the inter-particle distance and the particle concentration within a volume. The inter-particle distributions were then averaged (Fig. 8). Analysing the resulting distributions we were able to calculate the *NFWHM* for this method of analysis (Table 1). In this case the distributions are broader although the average inter-

particle distance is similar. As a result, both the *NFWHM* and the differences in

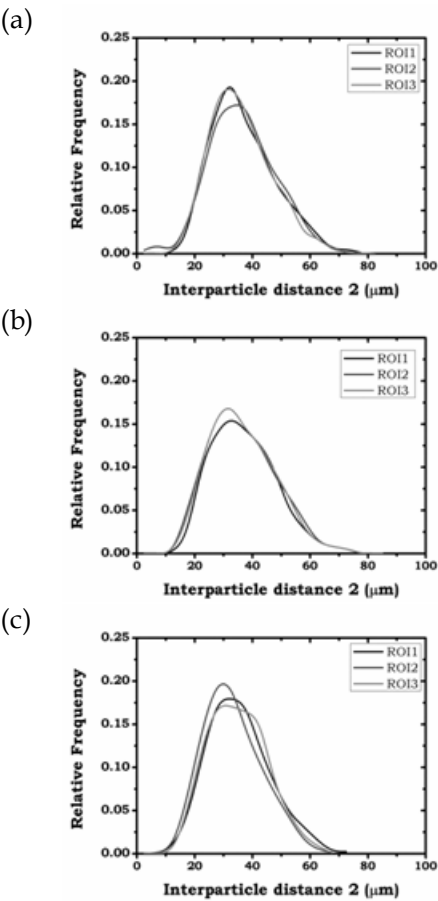


**Fig. 7.** Inter-particle distance distributions for the effective separation of the space (inter-particle distance 2) showing the homogeneity of the results between the selected ROIs (or VOIs). (a) 50-50 (b) HMS-PP and (c) Linear-PP.



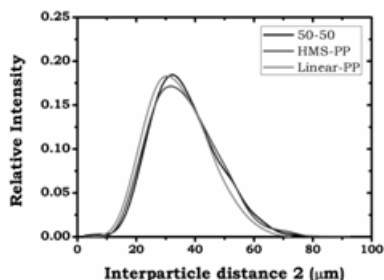


Fig. 8. Average inter-particle distributions obtained by the effective separation of the space into particles for the three tested polymer composites.

this parameter between materials (approx. 6%) are higher in this case as shown in Table 1.

In fact, the same conclusion as before could be addressed from these results relating the particle dispersion and the raw polymer shear zero viscosity. The higher is the zero-shear viscosity of the raw PP; the better is the ADC dispersion in the polymer by the dispersion method employed.

Furthermore, the calculated average inter-particle distances were compared with the obtained particle concentration

within every selected VOI (Fig. 9). The particle concentration was between  $1.5 \cdot 10^8$  and  $2.4 \cdot 10^8 \text{ cm}^{-3}$ . We could see a clear separation between materials regarding the particle concentration. The concentration in the zones corresponding to the HMS-PP and 50-50 is lower than  $1.9 \cdot 10^8 \text{ cm}^{-3}$  whereas the particle concentration in the analysed zones of the Linear-PP is higher than this value. The high shear viscosity of this polymer (Table 1) might provoke that a few amount of particles were fractured during the polymer composite manufacture. As a result, the number of particles within the material was slightly increased and also the average size of the particles was reduced, as shown in the granulometry results.

Investigating the average inter-particle distances, it is clear that the continuous analysis of the space (Fig. 9a) results in lower values of inter-particle distance (between 30 and 35  $\mu\text{m}$ ). On the other hand, the average inter-particle distances determined by means of the efficient

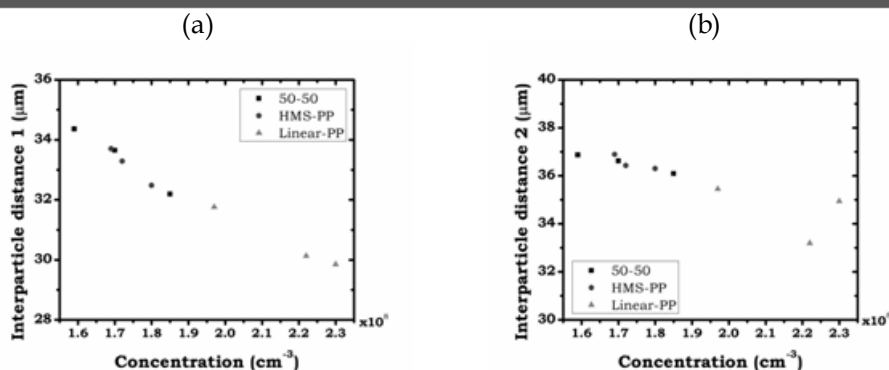


Fig. 9. Inter-particle distance versus particle concentration for the three analysed ROIs of the tested materials. (a) Continuous analysis of the inter-particle space and (b) effective separation of the space into particles.

separation of the space into particles was slightly higher (ranging 33-38  $\mu\text{m}$ ), as shown in Fig. 9b. Furthermore, a clear tendency was established in both cases. The higher is the particle concentration within a volume; the lower is the inter-particle distance in this volume. The only exception to this tendency is one of the selected zones of the Linear-PP by means of the second method of analysis.

### 3.2 Morishita index characterization

By using the same volumes and the procedure described before the Morishita Index was calculated. As explained before, the information related with this parameter is not the absolute value but the tendency when increasing the number of subvolumes. In this case the results concerning the different analysed volumes are not shown since they are essentially identical. For these reasons, only the average result for the three polymer composites is displayed (Fig. 10).

Taking into account that the Morishita index is reduced when the number of subvolumes is increased, the particles are distributed within the polymer matrix according to Normal distributions. In this case there is no difference between materials. The variance of viscosity of the raw polymers is not enough to provoke a critical change in the particle distribution type since both the amount of additive and the production process of the polymer composites were the same.

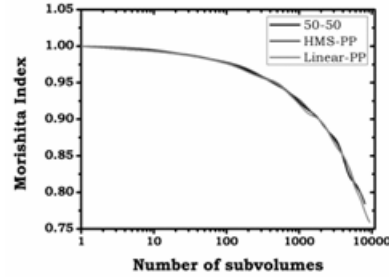


Fig. 10. Morishita Index calculation for several iterations in the analysed volumes and for the three materials under study.

Consequently, the Morishita Index curves are also identical.

### 3.3 Particle granulometry

Finally, analysing the distributions of particle size within the polymer matrixes (Fig. 11) it is possible to elucidate that the particles are slightly modified during the production of the composite precursors. As a result, the main parameters of the size distributions, summarized on Table 2 are also different. Linear PP material provokes a higher shear during production due to higher viscosity leading to smaller particles (both average size and  $d_{50}$ ) whereas in HMS-PP the effect is the inverse. Finally, the PP blend is in the middle of both extreme

**Table 2.** Results of the particle granulometry analysis.

Polymer	Average size ( $\mu\text{m}$ )	Standard deviation ( $\mu\text{m}$ )	$d_{50}$ ( $\mu\text{m}$ )
50-50	4.08	2.15	3.76
HMS-PP	4.11	2.14	3.79
Linear-PP	3.88	2.03	3.56

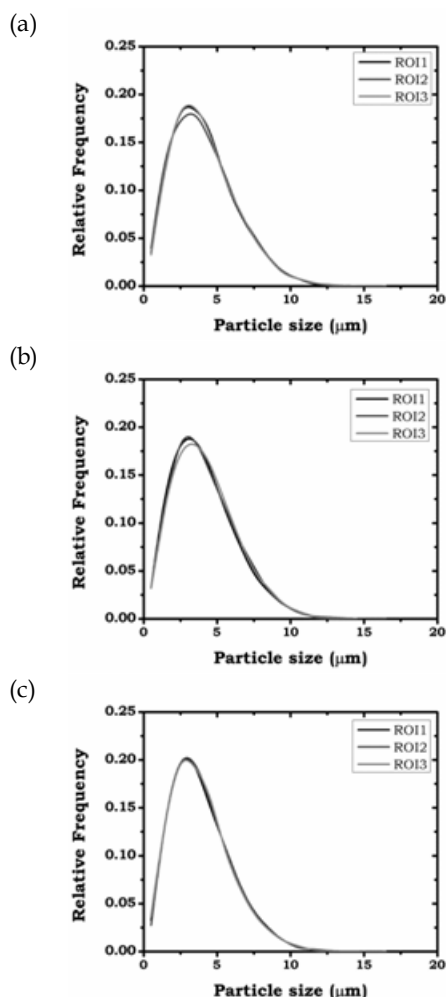


Fig. 11. Particle granulometry characterized by X-ray tomography for the three zones analysed on the materials. (a) 50-50 (b) HMS-PP and (c) Linear-PP.

materials. Particle size is mostly between 0 and 12 μm in all the materials with average values around 4 μm (Fig. 12).

#### 4. Conclusions

In conclusion, we have defined new methodologies to investigate the quality of particle dispersion in polymer

composites by using synchrotron X-ray μ-CT and image analysis.

Two different methods have been developed and applied in three polymer composites based on polypropylene and azodicarbonamide. Both methods investigate the inter-particle space and quantify the inter-particle distance distributions. In addition, independently of the selected method, it was clear that the higher was the viscosity of the matrix polymer; the better was the particle dispersion within the polymer.

Moreover, using the position in the space of the particles (assigned to the center of mass), the Morishita Index was calculated in 3D. Analysing the tendency of this parameter when sequentially dividing the space into subvolumes, we could extract that the particles in these systems were dispersed according to Normal distributions.

Finally, by means of the same tomographies, the particle granulometry inside the materials was characterized. As

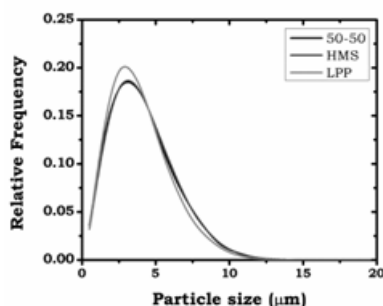


Fig. 12. Particle granulometry on the three analysed polymer composites.

a result, we realized that the higher viscosity value of the Linear-PP provoked that the included particles were slightly fractured. In consequence, the particle size was reduced and particle concentration was increased.

## Acknowledgments

Financial assistance from MINECO and FEDER program (MAT2012-34901) MINECO, FEDER, UE (MAT2015-69234-R) and the Junta de Castile and Leon (VA011U16) are gratefully acknowledged. Predoctoral contract of S. Perez-Tamarit by University of Valladolid and Banco Santander (E-47-2015-0094701) is acknowledged.

## References

- [1] S. Thomas, K. Joseph, S.K. Malhotra, K. Goda, M.S. Sreekala, *Polymer Composites, Volume 1 Macro- and Microcomposites*, Wiley-VCH2012.
- [2] S. Thomas, K. Joseph, S.K. Malhotra, K. Goda, M.S. Sreekala, *Polymer Composites, Volume 2 Nanocomposites*, Wiley-VCH2013.
- [3] S. Thomas, K. Joseph, S.K. Malhotra, K. Goda, M.S. Sreekala, *Polymer Composites, Volume 3 Biocomposites*, Wiley-VCH2014.
- [4] C.E. Bakis, L.C. Bank, F. ASCE, V.L. Brown, M. ASCE, E. Cosenza, J.F. Davalos, A.M. ASCE, J.J. Lesko, A. Machida, S.H. Rizkalla, F. ASCE, T.C. Triantafillou, M. ASCE, *Fiber-Reinforced Polymer Composites for Construction—State-of-the-Art Review*, *Journal of Composites for Construction*, 6 (2002) 73-87.
- [5] G.C. Jacob, J.F. Fellers, S. Simunovic, J.M. Starbuck, *Energy Absorption in Polymer Composites for Automotive Crashworthiness*, *Journal of Composite Materials*, 36 (2002) 813-850.
- [6] C. Bao, Y. Guo, B. Yuan, Y. Hu, L. Song, *Functionalized graphene oxide for fire safety applications of polymers: a combination of condensed phase flame retardant strategies*, *Journal of Materials Chemistry*, 22 (2012) 23057.
- [7] S. Estravís, J. Tirado-Mediavilla, M. Santiago-Calvo, J.L. Ruiz-Herrero, F. Villafañe, M.Á. Rodríguez-Pérez, *Rigid polyurethane foams with infused nanoclays: Relationship between cellular structure and thermal conductivity*, *European Polymer Journal*, 80 (2016) 1-15.
- [8] S. Thomas, V. Deepu, S. Uma, P. Mohanan, J. Philip, M.T. Sebastian, *Preparation, characterization and properties of Sm<sub>2</sub>Si<sub>2</sub>O<sub>7</sub> loaded polymer composites for microelectronic applications*, *Materials Science and Engineering: B*, 163 (2009) 67-75.
- [9] Q.A. Pankhurst, J. Connolly, S.K. Jones, J. Dobson, *Applications of magnetic nanoparticles in biomedicine*, *Journal of physics D: Applied physics*, 36 (2003) R167-R181.
- [10] H.E. Miltner, N. Watzeels, C. Block, N.-A. Gotzen, G.V. Assche, K. Borghs, K.V. Durme, B.V. Mele, B. Bogdanov, H. Rahier, *Qualitative assessment of nanofiller dispersion in poly( $\epsilon$ -caprolactone) nanocomposites by mechanical testing, dynamic rheometry and advanced thermal analysis*, *European Polymer Journal*, 46 (2010) 984-996.
- [11] J. George, M.S. Sreekala, S. Thomas, *A Review on Interface Modification and Characterization of Natural Fiber Reinforced Plastic Composites*, *Polymer Engineering and Science*, 41 (2001) 1471-1485.
- [12] B. Pukanszky, *Influence of interface interaction on the ultimate tensile properties of polymer composites*, *Composites*, 21 (1990) 255-262.
- [13] M.Z. Rong, M.Q. Zhang, S.L. Pan, B. Lehmann, K. Friedrich, *Analysis of the interfacial interactions in polypropylene/silica nanocomposites*, *Polymer International*, 53 (2004) 176-183.
- [14] H. Demir, D. Balköse, S. Ülkü, *Influence of surface modification of fillers and polymer on flammability and tensile behaviour of polypropylene-composites*, *Polymer Degradation and Stability*, 91 (2006) 1079-1085.
- [15] M. Forsyth, D.R. MacFarlane, A. Best, J. Adebahr, P. Jacobsson, A.J. Hill, *The effect of nanoparticle TiO<sub>2</sub> fillers on structure and transport in polymer electrolytes*, *Solid State Ionics*, 147 (2002) 203-211.
- [16] W. Bauhofer, J.Z. Kovacs, *A review and analysis of electrical percolation in carbon nanotube polymer composites*, *Composites Science and Technology*, 69 (2009) 1486-1498.
- [17] J.H. Koo, *Polymer Nanocomposites: Processing, Characterization, and Applications* McGraw-Hill2006.
- [18] S. Puggal, N. Dhall, N. Singh, M.S. Litt, *A Review on Polymer Nanocomposites: Synthesis, Characterization and Mechanical Prop*, *Indian Journal of Science and Technology*, 9 (2016).
- [19] P.M. Borba, A. Tedesco, D.M. Lenz, *Effect of reinforcement nanoparticles addition on mechanical properties of SBS/curauá fiber composites*, *Materials Research*, 17 (2014) 412-419.

- [20] K. Kalaitzidou, H. Fukushima, L.T. Drzal, A new compounding method for exfoliated graphite-polypropylene nanocomposites with enhanced flexural properties and lower percolation threshold, *Composites Science and Technology*, 67 (2007) 2045-2051.
- [21] R. Qiao, H. Deng, K.W. Putz, L.C. Brinson, Effect of particle agglomeration and interphase on the glass transition temperature of polymer nanocomposites, *Journal of Polymer Science Part B: Polymer Physics*, 49 (2011) 740-748.
- [22] D.A. Brune, J. Bicerano, Micromechanics of nanocomposites: comparison of tensile and compressive elastic moduli, and prediction of effects of incomplete exfoliation and imperfect alignment on modulus, *Polymer*, 43 (2002) 369-387.
- [23] R. Herzig, W.E. Baker, Correlations between image-analysed morphology and mechanical properties of calcium carbonate-filled polypropylene, *Journal of Materials Science*, 28 (1993) 6531-6539.
- [24] L. Karasek, M. Sumita, Characterization of dispersion state of filler and polymer-filler interactions in rubber-carbon black composites, *Journal of Materials Science*, 31 (1996) 281-289.
- [25] H.S. Khare, D.L. Burris, A quantitative method for measuring nanocomposite dispersion, *Polymer*, 51 (2010) 719-729.
- [26] S. Pfeifer, P.R. Bandaru, A Methodology for Quantitatively Characterizing the Dispersion of Nanostructures in Polymers and Composites, *Materials Research Letters*, 2 (2014) 166-175.
- [27] H. Yazdani, B.E. Smith, K. Hatami, Multiscale 3D dispersion characterization of carbon nanotube-filled polymer composites using microscopic imaging and data mining, in: U.o. Cambridge (Ed.) *Carbon Nanotechnology* 2014.
- [28] Y. Rao, J.M. Pochan, Mechanics of Polymer-Clay Nanocomposites, *Macromolecules*, 40 (2007) 290-296.
- [29] V. Nigam, D.K. Setua, G.N. Mathur, K.K. Kar, Epoxy-montmorillonite clay nanocomposites: Synthesis and characterization, *Journal of Applied Polymer Science*, 93 (2004) 2201-2210.
- [30] M. Alloncle, J. Lefebvre, G. Llamas, J.L. Doublier, A Rheological Characterization of Cereal Starch-Galactomannan Mixtures, *Cereal Chemistry*, 66 (1989) 90-93.
- [31] S. Bar-Chaput, C. Carrot, Rheology as a tool for the analysis of the dispersion of carbon filler in polymers, *Rheologica Acta*, 45 (2006) 339-347.
- [32] P. Cassagnau, Melt rheology of organoclay and fumed silica nanocomposites, *Polymer*, 49 (2008) 2183-2196.
- [33] J. Zhao, A.B. Morgan, J.D. Harris, Rheological characterization of polystyrene-clay nanocomposites to compare the degree of exfoliation and dispersion, *Polymer*, 46 (2005) 8641-8660.
- [34] M.J. Solomon, A.S. Almusallam, K.F. Seefeldt, A. Somwangthanaroj, P. Varadan, Rheology of Polypropylene/Clay Hybrid Materials, *Macromolecules*, 34 (2001) 1864-1872.
- [35] A. Rack, S. Zabler, B.R. Müller, H. Riesemeier, G. Weidemann, A. Lange, J. Goebbels, M. Hentschel, W. Görner, High resolution synchrotron-based radiography and tomography using hard X-rays at the BAMline (BESSY II), *Nuclear Instruments and Methods in Physics Research Section A: Accelerators, Spectrometers, Detectors and Associated Equipment*, 586 (2008) 327-344.
- [36] J.R. Fienup, Phase retrieval algorithms: a comparison, *Applied Optics*, 21 (1982) 2758-2769.
- [37] T. Hildebrand, P. Rüegsegger, A new method for the model-independent assessment of thickness in three-dimensional images, *Journal of Microscopy*, 185 (1997) 67-75.
- [38] C.A. Schneider, W.S. Rasband, K.W. Eliceiri, NIH Image to ImageJ: 25 years of image analysis, *Nature Methods*, 9 (2012) 671-675.
- [39] M.D. Abràmoff, P.J. Magalhaes, J. Sunanda, Image Processing with ImageJ, *Biophotonics International*, 11 (2004) 36-42.
- [40] J. Roerdink, A. Meijster, The Watershed Transform: Definitions, Algorithms and Parallelization Strategies *Fundamenta Informaticae*, 41 (2000) 187-228.
- [41] D. Legland, I. Arganda-Carreras, P. Andrey, MorphoLib: integrated library and plugins for mathematical morphology with ImageJ, *Bioinformatics*, 32 (2016) 3532-3534.
- [42] J. Golay, M. Kanevski, C.D. Vega Orozco, M. Leuenberger, The multipoint Morisita index for the analysis of spatial patterns, *Physica A: Statistical Mechanics and its Applications*, 406 (2014) 191-202.
- [43] E. Laguna-Gutierrez, R. Van Hooghten, P. Moldenaers, M.A. Rodriguez-Perez, Understanding the foamability and mechanical properties of foamed polypropylene blends by using extensional rheology, *Journal of Applied Polymer Science*, 132 (2015) 42430.



## References

---

- [1] C.D. Chan, M.E. Seitz, K.I. Winey, Disordered spheres with extensive overlap in projection: image simulation and analysis, *Microscopy and microanalysis : the official journal of Microscopy Society of America, Microbeam Analysis Society, Microscopical Society of Canada*, 17 (2011) 872-878.
- [2] Y. Li, Y. Lu, Deriving the integral representation of a fractional Hankel transform from a fractional Fourier transform, *Optics Letters*, 23 (1998) 1158-1160.
- [3] V. Magni, G. Cerullo, S. De Silvestri, High-accuracy fast Hankel transform for optical beam propagation, *Journal of Optical Society of America A*, 9 (1992) 2031-2033.
- [4] E. Solórzano, E. Laguna-Gutierrez, S. Perez-Tamarit, A. Kaestner, M.A. Rodriguez-Perez, Polymer foam evolution characterized by time-resolved neutron radiography, *Colloids and Surfaces A: Physicochemical and Engineering Aspects*, 473 (2015) 46-54.
- [5] H. Demir, D. Balköse, S. Ülkü, Influence of surface modification of fillers and polymer on flammability and tensile behaviour of polypropylene-composites, *Polymer Degradation and Stability*, 91 (2006) 1079-1085.
- [6] S. Puggal, N. Dhall, N. Singh, M.S. Litt, A Review on Polymer Nanocomposites: Synthesis, Characterization and Mechanical Prop, *Indian Journal of Science and Technology*, 9 (2016).
- [7] P.M. Borba, A. Tedesco, D.M. Lenz, Effect of reinforcement nanoparticles addition on mechanical properties of SBS/curauá fiber composites, *Materials Research*, 17 (2014) 412-419.
- [8] R. Qiao, H. Deng, K.W. Putz, L.C. Brinson, Effect of particle agglomeration and interphase on the glass transition temperature of polymer nanocomposites, *Journal of Polymer Science Part B: Polymer Physics*, 49 (2011) 740-748.

